THE COMPUTATION OF BLOOD FLOW WAVEFORMS FROM DIGITAL X-RAY ANGIOGRAPHIC DATA

by

Alexander M Seifalian
M.Sc., PGDip.Com., CPhys., MInstP., MIPSM.

Thesis submitted for the Degree of Doctor of Philosophy for the University of London

June 1993

University Department of Surgery
Royal Free Hospital School of Medicine
London NW3 2QG, UK.

Division of Radiological Sciences
United Medical and Dental School
London SE1 9RT, UK.

ABSTRACT

This thesis investigates a novel technique for the quantitative measurement of pulsatile blood flow waveforms and mean blood flow rates using digital X-ray angiographic data.

Blood flow waveforms were determined following an intra-arterial injection of contrast material. Instantaneous blood velocities were estimated by generating a 'parametric image' from dynamic X-ray angiographic images in which the image grey-level represented contrast material concentration as a function of time and true distance in three dimensions along a vessel segment.

Adjacent concentration-distance profiles in the parametric image of iodine concentration versus distance and time were shifted along the vessel axis until a match occurred. A match was defined as the point where the mean sum of the squares of the differences between the two profiles was a minimum. The distance translated per frame interval gave the instantaneous contrast material bolus velocity.

The technique initially was validated using synthetic data from a computer simulation of angiographic data which included the effect of pulsatile blood flow and X-ray quantum noise. The data were generated for a range of vessels from 2 mm to 6 mm in diameter. Different injection techniques and their effects on the accuracy of blood flow measurements were studied.

Validation of the technique was performed using an experimental phantom of blood circulation, consisting of a pump, flexible plastic tubing, the tubular probe of an electromagnetic flowmeter and a solenoid to simulate a pulsatile flow waveform which included reverse flow.

The technique was validated for both two- and three-dimensional representations of the blood vessel, for various flow rates and calibre sizes. The effects of various physical factors were studied, including the distance between injection and imaging sites and the length of artery analysed.

Finally, this method was applied to clinical data from femoral arteries and arteries in the head and neck.

CONTENTS

FIGURES

thin lines inputs the true waveform, the dotted lines that from the bolus mass tracking algorithm (Swanson et al 1986) and the thick lines the results using our velocity algorithm computing.

Fig. 7.7. Plots of typical contrast concentrations vs time generated from synthetic data at two sites A (dotted lines) and B (solid lines), 40 mm apart, along a blood vessel with an internal diameter of 6 mm and mean blood flow of 367 ml/min.

Fig. 7.8. Scatter plot showing the relationship between true mean velocity and mean velocity estimated by the tracking of bolus mass method (Swanson et al 1986) for a 6 mm diameter vessel and a laminar flow pattern. The results for ramp, constant, 2 and 5 pulse/sec injection techniques are plotted. The line represents the line of identity.

Fig. 7.9. Scatter plot showing the relationship between true mean velocity and mean velocity estimated by our velocity computing algorithm, for a 6 mm diameter vessel and a laminar flow pattern. The results for ramp, constant, 2 and 5 pulse/sec injection techniques are plotted. The line represents the line of identity.

Fig. 7.10. Scatter plot showing the relationship between true mean velocity and the mean velocity estimated by the tracking of bolus mass (Swanson et al 1986) for 2 and 4 mm diameter vessels with a laminar flow pattern. The line represents the line of identity.

Fig. 7.11. Scatter plot showing the relationship between true mean velocity and the mean velocity estimated by our velocity computing algorithm (distance-density curve matching method), for 2 and 4 mm diameter vessels, for a laminar flow pattern. The line represents the line of identity.

Fig. 7.12. Scatter plot showing the relationship between true mean velocity and the mean velocity estimated by the tracking of bolus mass (Swanson et al 1986) for a 4 mm diameter vessel for 'plug' or constant axial flow pattern. The line represents the line of identity.

Fig. 7.13. Scatter plot showing the relationship between true mean velocity and the mean velocity estimated by our velocity computing algorithm, for a 4 mm diameter vessel, for a 'plug' or constant axial flow pattern. The line represents the line of identity.

Fig. 8.1. Block diagram of flow phantom.

Fig. 8.2. Relationship between flow determined from timed fluid (saline) collection and the electromagnetic flowmeter (EMF) mean flow reading.

Fig. 8.3. (a) Parametric image generated by 2D data processing for a 6.6 mm calibre with a mean blood flow of 348 ml/min. (b) Direct comparison of volume flow waveforms measured synchronously using the standard EMF (thin lines) and from the parametric image using our velocity computing algorithm (thick lines).

Fig. 8.4. (a) Parametric image generated by 2D data processing for a 6.6 mm calibre with a mean blood flow of 708 ml/min. (b) Direct comparison of volume flow waveforms measured synchronously using the standard EMF (thin lines) and from the parametric image using our velocity computing algorithm (thick lines).

Fig. 8.5. (a) Parametric image generated by 2D data processing for a 6.6 mm calibre with a mean blood flow of 1705 ml/min. (b) Direct comparison of volume flow waveforms measured synchronously using the standard EMF (thin lines) and from the parametric image using our velocity computing algorithm (thick lines).

Fig. 8.6. (a) Parametric image generated by 2D data processing for a 4.0 mm calibre with a mean blood flow of 339 ml/min. (b) Direct comparison of volume flow waveforms measured synchronously using the standard EMF (thin lines) and from the parametric image using our velocity computing algorithm (thick lines).

Fig. 8.7. Direct comparison of volume flow waveforms measured synchronously using the standard EMF (thin lines) and from the parametric image using our velocity computing algorithm (thick lines) for a tube of 6.0 mm lumen diameter with a mean fluid flow of 586 ml/min (parametric image generated by 3D data processing).

Fig. 8.8. (a) Parametric image generated by 3D data processing for a 6.0 mm calibre with a mean blood flow of 1157 ml/min. (b) Direct comparison of volume flow waveforms measured synchronously using the standard EMF (thin lines) and from the parametric image using our velocity computing algorithm (thick lines).

Fig. 8.9. (a) Parametric image generated by 3D data processing for a 4.0 mm calibre with a mean blood flow of 176 ml/min. (b) Direct comparison of volume flow waveforms measured synchronously using the standard EMF (thin lines) and from the parametric image using our velocity computing algorithm (thick lines).

Fig. 8.10. (a) Parametric image generated by 3D data processing for a 4.0 mm calibre with a mean blood flow of 271 ml/min. (b) Direct comparison of volume flow waveforms measured synchronously using the standard EMF (thin lines) and from the parametric image using our velocity computing algorithm (thick lines).

Fig. 8.11. (a) Parametric image generated by 3D data processing for a 4.0 mm calibre with a mean blood flow of 687 ml/min. (b) Direct comparison of volume flow waveforms measured synchronously using the standard EMF (thin lines) and from the parametric image using our velocity computing algorithm (thick lines).

Fig. 8.12. Direct comparison of volume flow waveforms measured synchronously using the standard EMF (thin lines) and from the parametric image using our velocity computing algorithm (thick lines) for a tube of 3.0 mm lumen diameter with a mean fluid flow of 229 ml/min (parametric image generated by 3D data processing).

Fig. 9.1. X-ray angiogram showing the left femoral arteries. The arrows indicate the positions of the selected arterial segments for generation of the parametric images. a=left common femoral; b=left superficial femoral; and c=left profunda femoris arteries.

Fig. 9.2. Parametric image showing contrast medium concentration (grey scale) at different positions down the blood vessel (the vertical axis) and at different times (the horizontal axis) pre-angioplasty for: (a) the left common femoral, (b) the left superficial femoral with severe stenosis and (c) the left profunda femoris arteries.

Fig. 9.3. As in fig. 9.2 but post-angioplasty.

Fig. 9.4. Plots of the flow velocity waveforms pre-angioplasty derived from the parametric images shown in fig. 9.2. The waveforms were extracted from the parametric images constructed for the left common femoral artery (thick solid lines), the left superficial femoral

artery (dotted lines) and the profunda femoris artery (thin solid lines).

Fig. 9.5. Plots of the flow velocity waveforms post-angioplasty. The waveforms were extracted from the parametric images shown in fig. 9.3 for the left common femoral artery (thick solid lines), the left superficial femoral artery (dotted lines) and the profunda femoris artery (thin solid lines).

Fig. 9.6. Parametric image showing contrast medium concentration (grey scale) at different positions down the blood vessel (the vertical axis) and at different times (the horizontal axis), the left and right common carotid (LCC, RCC), internal carotid (LIC,RIC) and vertebral (LVE,RVE) arteries for patient MB (see table 9.3).

Fig. 9.7. Biplanar X-ray angiogram showing the carotid and vertebral arteries for patient MB (see table 9.3).

Fig. 9.8. Plots of the volume flow velocity waveforms. The waveforms were extracted from the parametric images shown in fig. 9.6 for the left common carotid (LCC), right common carotid (RCC), left internal carotid (LIC), right internal carotid (RIC), left vertebral (LVE) and right vertebral (RVE) arteries.

TABLES

vertebral (LVE) and right vertebral (RVE) arteries.

ACKNOWLEDGEMENTS

The work presented in this thesis was carried out at several sites in the London University Medical Schools. I would like to thank many people for their help during the period of my research and in the production of this thesis.

First and foremost, I would like to thank Dr David J Hawkes for his supervision, advice, encouragement and tremendous support throughout the last five years. I also would like to thank my supervisor Professor K E F Hobbs who encouraged and supported me in my travels around the London Medical Schools during the performance of my research.

I would like to thank all within the Division of Radiological Sciences, United Medical and Dental School, for their support, especially Martin Graves, Derek Hill, Glyn Robinson and Cliff Ruff for assistance in the data handling and support of the SUN station network. I am grateful to radiology and radiography staff at Guy's Hospital for their assistance in collecting the technical data.

I would like to thank all members of the University Department of Surgery, Royal Free Hospital and School of Medicine, for their tolerance of my absences from the department and their support and encouragement over the period of the research on this thesis.

I would like to acknowledge the help of Dr Alan Colchester, Department of Neurology, UMDS, who initially proposed the algorithms for computing blood velocity and blood vessel cross-sectional area.

I would like to thank Mr C R Hardingham for writing the 3D reconstruction program.

I acknowledge collaboration with Dr John Brunt of the Department of Medical Biophysics at Manchester University and Professor George du Boulay of the Institute of Neurology, Queen Square, London (who are investigating the use of gradient operators to derive blood flow from the parametric image).

Many thanks to the Department of Medical Illustration at Royal Free Hospital for photographing and printing some of the images from the computer screen.

Many thanks to friends and colleagues who proofread this thesis and gave me much needed encouragement and support. Many thanks to Stewart Gray for proofreading the final copy of my thesis.

CHAPTER 1

INTRODUCTION

1.1 INTRODUCTION

In research and clinical practice there are many unresolved haemodynamic problems for which quantitative measurements of blood flow could provide some of the solutions. Methods of measurement of blood flow evaluate either tissue perfusion or vascular blood flow. Tissue perfusion is the transmission of blood through the microcirculation and is the ultimate determination of tissue oxygenation; and is usually measured in ml/min/100 gram or ml/min/kg tissue weight. The measurement of tissue perfusion is important in, for example, monitoring tumour tissue perfusion and in dermatological and rheumatological disorders. Vascular blood flow is a measure of the amount of blood passing along a vessel; and is usually measured in ml/min. Applications include assessment of the progression of atheroma, investigation of haemodynamics, and study of the efficacy of vascular bypass operations and angioplasty. The commonest type of vascular disease is atherosclerosis, which tends to affect larger vessels. Measurement of flow or change in flow in the diseased vessel(s), is a more direct assessment of severity of disease than measurements of tissue perfusion in the region of supply of the vessel, which may be spatially ill-defined. Several arteries may supply one territory (collateral supply). Vessel flow measurement may however allow estimation of the relative contribution of particular collateral vessels. Unfortunately no sufficiently accurate non-invasive technique exists at present to measure vascular blood flow. In brief, currently available methods include the electromagnetic flowmeter (EMF) which has been used to estimate blood flow in animals and man. The technique is invasive, requiring the placement of probes on blood vessels. Doppler ultrasound has been used mainly for qualitative analysis of blood flow in vessels near the body surface and can be used to measure aortic flow, but it lacks the necessary resolution in space and time to assess smaller, deep-seated vessels. Magnetic resonance techniques are developing rapidly, but present methods are time consuming and have poor spatial resolution. X-ray angiography remains the imaging modality which gives the highest spatial and temporal resolution and is

widely used in clinical practice for obtaining high quality blood vessel images. The ability to derive quantitative flow data from this procedure would be a useful clinical tool. Numerous publications have shown its potential but it has not been widely used due in part, I believe, to the use of inappropriate algorithms to process the image data.

The objective of this work is to examine the accuracy of using an X-ray angiographic technique to compute blood flow. Hence it concentrates on the derivation and subsequent processing of blood flow waveforms from digital dynamic X-ray angiographic data. It is therefore a methodological study rather than a clinical study. Although limited patient data were acquired and analysed these have mainly been used to demonstrate that the theory and methods developed using synthetic and phantom data may be applicable in clinical studies.

This chapter includes an outline of applications of blood flow measurements, with special reference to arterial blood flow waveform patterns in the detection of vascular diseases. This is followed by a breakdown of the thesis as a whole, chapter by chapter.

1.2 APPLICATIONS OF BLOOD FLOW MEASUREMENTS

Blood flow measurements in individual vessels would be of value in a variety of clinical circumstances:

(1) To confirm the clinical diagnosis.

(2) To achieve a better understanding of the patho-physiology of the disease process.

(3) To document the progression of the disease, for example: (a) the assessment of the effect of atherosclerosis and other sources of vessel narrowing on flow in individual vessels (b) the study of hepatic blood flow for better understanding of the natural history of portal hypertension.

(4) To measure total blood flow to an organ, pre and post kidney or liver transplants.

(5) To predict pressure gradients from the combination of vessel blood flow

measurements with calibre and path length measurements.

(6) To assist the selection of patients for reconstructive surgery.

(7) To assess the immediate and long-term post-operative results of reconstructive surgery, such as the investigation of bypass graft patency.

(8) To assess the haemodynamic effects of percutaneous transluminal angioplasty and other interventional studies.

(9) To assess changes in pulsatile flow waveforms in vascular disease. This is discussed in section 1.2.1.

(10) Finally, there is still much to be learnt about the physics, physiology and pathology of blood flow and vascular resistance in individual vessels.

Flow measurements in individual vessels are a central part of this research.

1.2.1 Arterial Flow Velocity Waveform Patterns

The pattern of flow waveforms can be used to grade the severity of arterial occlusive disease. Individual vessels have different blood flow waveform patterns depending on their location. For example:

(1) The normal flow pattern in the major arteries of the lower limb consists of an initial high-velocity forward-flow phase during cardiac systole, a brief phase of reverse flow in early diastole, and a low-velocity forward-flow phase in late diastole. The factors that modify this normal pattern include the presence of arterial occlusive disease and changes in peripheral vascular resistance. An arterial stenosis acts like a filter which removes rapidly changing components of the flow waveform. This, together with the compensatory decrease in peripheral resistance, results in the disappearance of the reverse-flow phase (see chapter 9). Thus, the waveform obtained distal to a stenotic lesion has a single forward velocity phase, the peak flow velocity is lower than normal and the peak of the waveform is more rounded. Flow waveforms taken from within a haemodynamically significant stenosis have an abnormally high peak systolic velocity that represents the high-velocity jet generated due to the lesion.

(2) Arteries such as the internal carotid, that supply low resistance organs,

normally show forward flow throughout the cardiac cycle and relatively high diastolic flow velocities (see chapter 9).

1.3 STRUCTURE OF THESIS

Chapter 2 critically describes current available methods for measuring blood flow, emphasising their difficulties and relative advantages.

From the review of the literature in chapter 2, it is apparent that there are many problems associated with determining blood flow. X-ray angiography remains the imaging modality which gives the highest spatial and temporal resolution, and, because of its high signal-to-noise ratio, is widely used in clinical practice for obtaining high-quality vessel images. In addition to conventional anatomical information, a timed sequence of digital images also contains useful temporal information which hitherto has been largely ignored.

Chapter 3 describes the main principals of a digital X-ray angiographic system and outlines its individual components.

Chapter 4 discusses in detail the drawbacks of the existing X-ray angiographic techniques of measuring blood flow velocity, introduces approaches to the measurement of pulsatile blood flow waveforms from profiles of injected contrast mass or concentration versus distance, and outlines outstanding problems in their implementation. In this chapter X-ray angiographic techniques to measure cross-sectional area are reviewed emphasising both the value and shortcomings of using geometric or densitometric methods to calculate the cross-sectional area.

Chapter 5 describes in detail a three-dimensional (3D) reconstruction technique for obtaining vascular configurations from biplanar X-ray angiographic images. Such reconstruction is possible on condition that the position and orientation of the X-ray equipment during the data acquisition is known, and that corresponding vessel segments in the vascular configuration in the two projections can be identified. This chapter also includes a validation of the 3D approach for the measurement of vessel cross-sectional area and vascular path lengths.

Chapter 6 describes a new digital X-ray angiographic technique of measuring blood flow waveforms, by matching profiles of injected contrast concentration with respect to distance along a blood vessel (distance-density curves) over a period of time.

Two procedures will be described, in chapters 7 and 8 respectively, that validate the new flow algorithm. The first method uses simulated X-ray angiographic data generated by computer models (details and results of the validation are described in chapter 7). Quantitative comparison with other algorithms is also made using computer generated images. A total of 114 synthetic images were generated by varying the following parameters in the mathematical model of the angiographic imaging chain: flow rate, blood vessel calibre size and injection technique (chapter 7). The second method is a validation of the technique using an experimental model of blood circulation. The results obtained from this system are described in chapter 8.

In order to demonstrate the applicability of the new angiographic technique (as described in chapter 6) in clinical practice, flow was measured in the left femoral arteries of a 69-year-old male patient with severe superficial femoral artery stenosis, pre- and post-percutaneous transluminal angioplasty and, subsequently, in the carotid and vertebral arteries of seven patients. The analysis of the flow in the femoral artery was performed using two-dimensional (2D) image processing, in the plane of the projected radiograph, while the analysis of the vessels in the head and neck was performed using a 3D representation of the vascular network (chapter 9).

The tenth and final chapter provides the conclusion and overall assessment of the work presented in this thesis.

CHAPTER 2

A REVIEW OF EXISTING METHODS OF MEASURING FLOW IN BLOOD VESSELS

2.1 INTRODUCTION

The measurement of blood flow is important in understanding both normal physiology and disease processes as well as assessing the effects of therapeutic procedures such as angioplasty, shunting, bypass and transplantation.

There are several techniques which have been used to measure blood flow. The classification of techniques is to some extent arbitrary and several so-called 'different' methods may share certain common principles. The methods can be classified into two main groups: those primarily concerned with flow through discrete vessels and those used to assess local microcirculatory blood flow (tissue perfusion). All techniques have their advantages and disadvantages and in some situations a combination may provide the most information (Seifalian et al 1991a). In addition, because of the many factors affecting blood flow, measurement in a single subject may vary depending on position, recent food intake, anxiety, anaesthesia and drug therapy. This thesis does not attempt to address these external factors, rather it addresses the technical problem of measuring flow through discrete vessels. The development of a technique to measure intravascular blood flow using digital X-ray angiographic data is described. The technique of digital X-ray angiography is described in chapter 3 and previous approaches to using these data to measure flow are reviewed in chapter 4. This chapter surveys other methods available for assessing intravascular blood flow, examines the different parameters being measured, and outlines problems of applicability and interpretation of the results from each technique.

2.2 METHODS

2.2.1 The Electromagnetic Flowmeter

The measurement of blood flow by electromagnetic induction was first suggested by Fabre in 1932. The principle of the technique is based on Faraday's law of electromagnetic induction. If a magnetic field is applied across a vessel in which blood is flowing then an electric field is induced at right angles to both the induced magnetic field and the flow vector (Webster 1978; Harper et al 1974). The electrical field is detected along its axis from the potential difference across the outside of the vessel. This potential is primarily determined by the velocity of the flowing blood within the vessel. Accuracy demands attention to detail and proper calibration (Khouri and Gregg 1963; Wyatt 1984) using a pump and saline solution. There is no way of checking calibration 'in-vivo' except by vessel clamping for zero flow. Interference from other electrical instruments also reduces the accuracy of the technique (Meisner and Messmer 1970).

In practice the method involves the placement of the device around the vessel to be assessed. For a good signal, close contact is essential. Drapanas et al (1960) and Price et al (1965) compared electromagnetic flowmetry with the bromsulphalein clearance method (Bradley et al 1945) for measuring hepatic arterial and portal vein flow in a dog and found a good correlation between the two methods. Because of the invasive nature of the technique, it is applicable mainly to animal studies and to patients at the time of surgery. These devices are, however, still regarded as the 'gold standard' against which all other methods of measuring flow must be compared. Electromagnetic flowmeters are able to measure instantaneous and mean blood flow in an exposed vessel. They can also detect forward and reverse flow and the temporal resolution is fast enough for flow to be studied during the cardiac cycle. Another advantage of this method is its insensitivity to changes in blood temperature and viscosity.

2.2.2 The Thermodilution Technique

The concept of the thermodilution technique is based on the principle of supplying a known quantity of heat to the blood within a vessel and measuring

the blood temperature at a point downstream. The rate of the injection washout is proportional to the flow. Fegler (1954) injected heated saline solution (the indicator) into the blood stream via a catheter, then applied the Stewart-Hamilton equation (Hamilton et al 1932), describing the relationship between injected volume, the area under the time-dilution curve, and blood flow in thermodilution techniques:

$$F = \frac{Q*(T_b - T_i)*60*K}{A} \qquad (2.1)$$

where F is blood flow, Q is the injected indicator volume, T_b and T_i are the blood and injected indicator temperatures, A is the area under the temperature time curve and K is the fluid constant. The fluid constant is dependent upon specific gravity and heat of blood and indicator, it remains virtually constant and is calculated to be equal to 1.08 when isotonic saline or 5% dextrose solution is used (Nadel et al 1986).

Nadel et al (1986) validated this technique 'in-vitro' for flow ranging from 200 to 700 ml/min, and reported that flows under 200 ml/min had an average error of 28%, while flows above 200 ml/min had an average error of 6%.

The assumptions for this technique are that there is homogeneous mixing between the indicator and the blood, and that the injection of the indicator does not influence flow. Apart from the mixing problem, one of the difficulties of the injection technique is that heat is lost from the fluid during its passage to the catheter tip and this heat passes out into the blood altering its temperature and therefore the temperature recorded by the downstream sensor. In addition injection of hot or cold saline might affect the vascular tone of arteries and hence the arterial blood flow.

2.2.3 Doppler Ultrasound

According to the Doppler principle, the frequency of a sound wave that is reflected from a moving object will increase or decrease depending on the

object's direction and velocity relative to the incident wave. This change in frequency is called the Doppler effect. Using ultrasonic equipment the Doppler shift δF is given by the following equation:

$$\delta F = \frac{2VF\cos\theta}{c} \qquad (2.2)$$

where F is the transmitted frequency (2-10 Mhz), V is the velocity of the moving blood cell, θ is the angle between the transmitted sound and the axis of blood vessel and c is the constant speed of sound in the blood and tissue ($\approx$ 1540 m/sec).

Doppler instrumentation allows for ultrasound to be transmitted continuous wave (CW) Doppler or intermittent (pulsed) wave Doppler.

The advantage of the CW Doppler is its simplicity, no upper limit to the velocity measurable, and a lack of aliasing. Therefore CW Doppler may be used for the analysis of high velocities, particularly across stenotic orifices. These devices are commonly used in obstetrics to obtain umbilical artery waveforms, and have been widely used for many years in the carotid and lower limb arteries.

The disadvantages of the system are that it does not allow determination of the depth at which the frequency shift occurred, it provides little information about flow profile and it is unable accurately to measure a detected stenosis (O'Leary 1985).

In pulsed wave Doppler, several intermittent gated (timed) voltage pulses are applied to the transducer, resulting in a pulsed, rather than continuous, wave transmission. Pulsed Doppler devices usually have a single crystal, operating alternately as transmitter and receiver. The principle of operation is to transmit a short burst of ultrasound towards the target and wait for the backscattered ultrasound to return. By selecting the time between transmission and reception, the depth at which blood velocities are detected can be chosen. This provides discrimination of Doppler signals from different depths, allowing for the detection

of moving interfaces and scatterer from within a well-defined 'sample volume'. The dimensions of the sample volume are defined axially by the pulse length and laterally by the beam width of the combined transmitter-receiver system. The sample volume can be positioned anywhere along the axis of the ultrasound beam, but to obtain a narrow band of frequencies it should be placed in the central stream of the blood vessel (Breslau 1982).

While pulsed Doppler has the considerable advantage of permitting Doppler analysis at precise locations determined by the operator, there are velocity measurement limitations. The highest velocity that can be detected is a function of the transmission frequency, the depth at which the velocity is sampled, and the intercept angle. Altering the intercept angle away from parallel flow may permit velocity measurements that can be corrected to the true velocity by multiplying by the cosine of the intercept angle. Difficulties, however, arise in measurement of the intercept angle.

With simple Doppler ultrasound alone, details of flow are obtained but the vessel and surrounding soft tissues cannot be evaluated and so there is no anatomic reference. Placing the sample volume at a desired anatomical site requires the combination of an imaging device with a Doppler device and is referred to as duplex scanning.

Most commonly, duplex probes contain two piezoelectric transducers positioned in a geometric configuration that allows simultaneous real time sector imaging and pulsed Doppler flow studies (Burns 1987). Therefore it has the advantage of both Doppler spectral analysis and real time imaging which enables the measurement of volume flow in blood vessels. Volume flow is the product of cross-sectional area and mean velocity. The vessel area is estimated from the B-scan, and the mean velocity estimated from the mean velocity shift of the Doppler spectrum. The limitation of the technique is due to the conflict between design considerations optimal for imaging and those that are optimal for Doppler measurement. Doppler frequency shifts are maximal when the axis of the transducer is as near parallel to the axis of flow as possible, whilst imaging is best when the beam axis is perpendicular to the vessel wall. These design constraints make simultaneous collection of Doppler and imaging data difficult.

Although duplex instrumentation is now widely accepted as valid for most vascular applications, there are several disadvantages which have prevented total acceptance of the method (Jaffe 1984). These have been well documented and are summarised by Burns (1987) and Merritt (1986). Briefly, they are as follows:

(a) Sampling problems. When used to measure laminar flow in a vessel with a beam width less than the diameter of the vessel, only the central portion of the vessel lumen will be insonated (Evans 1982 and 1986) leading to an error in estimating velocity and hence flow. Nearly all current pulse mode Doppler machines are based on centre-line measurements of peak velocity and spectral broadening (Langlois et al 1984). Abnormalities may be missed due to failure to sample nearer the wall where flow disturbances are more likely to occur (Switzer and Nanda 1985; Rittgers and Fei 1988).

(b) Errors can arise in estimating blood vessel diameter. These are due to imaging not being perpendicular to the longitudinal axis of the vessel; poor resolution of the imaging transducer; pulsatility of blood flow, causing variation in vessel diameter with time; and observer variability (Zoli et al 1986). Assuming that a vessel is circular can lead to an error of up to 30% in calculating the area of the vessel (Gill 1985).

(c) Errors due to beam angle. The magnitude of velocity is a function of the cosine of the intercept angle between beam direction and the blood vessel. The volume flow rate calculation equation is a trigonometrical function of the angle between the beam direction and the blood flow. Errors vary considerably with that angle, being minimal in the angle range 55-75° (Stacey-Clear and Fish 1984).

To overcome problems of visualisation of flow in small vessels and to improve qualitative analysis, colour-duplex instruments have been developed (Nelson and Pretorius 1988; Powis 1988). Colour-duplex imaging instruments provide the following additional information: (1) with the existence of a Doppler frequency shift, the echo is represented in colour otherwise it is displayed in shades of grey, (2) the magnitude of the Doppler frequency shift is displayed on a colour shading scale, with the direction of blood flow, with reference to the Doppler transducer, displayed in different colours, i.e. red and blue.

The advantages of the colour-duplex is the resultant visualisation of flow, even if the vessel is too small to be resolved on the grey-scale image, and distinction between vascular and non-vascular structures, for instance at the portal hepatis where blood vessels can be distinguished from the extrahepatic bile ducts. It is important to recognise that the flow information illustrated with colour-duplex instruments is qualitative, not quantitative (Zwiebel 1990).

To overcome problems with angle correction and sampling error in duplex ultrasound systems, intra-arterial Doppler catheters have been used to measure blood flow (Wilson et al 1985; Sibley et al 1986). The Doppler catheter has a single crystal mounted 4.5 mm behind the catheter tip and angled at 45° to the long axis of the catheter.

Intra-arterial Doppler catheters are frequently used in the coronary circulation (Sibley et al 1986; Johnson et al 1989), but recently have been used to measure flow in the superior mesenteric artery in patients, with and without portal hypertension, who are undergoing diagnostic splanchnic arteriography (McCormick et al 1992).

We have validated an intra-arterial Doppler ultrasound catheter to test for its accuracy in quantitative measurement of pulsatile blood flow velocity. An experimental model of the arterial circulation was constructed. This consisted of a pump, flexible plastic tubing, and the tubular probe of an EMF (McCormick et al 1992).

In the flow model the catheters were able to reproduce the flow velocity waveforms for a 6.5 mm calibre tube but tended to overestimate the instantaneous flow velocity by an amount ranging from 5.3% to 36.4%. The results showed much poorer agreement for smaller calibre tubes (4.5 and 3.0 mm) in which the errors were as high as 200% (Seifalian et al 1991b). Similar results were observed in the patient femoral artery undergoing bypass graft using intra-arterial Doppler ultrasound and comparison with EMF reading.

In summary, all Doppler devices are subject to the same physical constraints; even the most sophisticated colour flow mapping systems are subject to aliasing

and the angle dependence of the Doppler shift frequency. Duplex scanning potentially provides a non-invasive way of assessing blood flow in many clinical situations. Its accuracy has been validated 'in-vitro' and in experimental animals (Miyatake et al 1984; Seifalian et al 1988a), but problems do exist in using this technique in clinical practice.

2.2.4 Nuclear Magnetic Resonance

Nuclear Magnetic Resonance (NMR) imaging is a non-invasive imaging modality that has rapidly gained clinical acceptance, although widespread introduction has been delayed by the capital cost of installing a NMR scanner. Flow detection with NMR has been explored for more than 40 years (Suryan 1951; Garroway 1974; Hahn 1960). When NMR imaging was first performed in the late 1970s, signal loss was noted within arteries and attributed to high flow rates (Hawkes et al 1980). In the early 1980s, several causes of increased signal intensity were described, generally associated with slow flow in veins and dural sinuses (Waluch and Bradley 1984; Bradley and Waluch 1985). Understanding these flow phenomena has provided the basis for the development of specialised NMR imaging sequences intended to quantify blood flow measurements. Several methods have been proposed to quantify blood flow (Ridgway et al 1987; Shimizu et al 1986; West et al 1988) and a full review of the techniques is described by Smith (1990).

The theory of applications of NMR to measure blood flow is too complex to describe in full here. However, in brief, there are three main approaches to the measurement of blood flow using NMR: (1) measurement of the signal produced by the inflow and outflow of blood in an image selected perpendicular to the vessel axis, (2) time-of-flight techniques, where a bolus of blood is used as an indicator: it is excited and then its progress along the vessel is followed, and finally (3) phase modulation, which utilises the phase of the net magnetic moment. At present the relative merits of each approach in terms of spatial and velocity resolution and image acquisition times have not been completely evaluated. However, this will undoubtably be an area of significant development in the future.

2.3 CONCLUSION

Currently the measurement of blood flow is difficult. There are often large variations in flow measurements between techniques. Some of these differences may be due to the methods and conditions used while others are undoubtedly caused by complexities of the blood flow in the vascular system which are not yet completely understood.

Most importantly, a reliable method of non-invasively assessing blood flow in the clinical context is still required. Duplex Doppler ultrasound offers a non-invasive way of assessing blood flow but its many inaccuracies make it a difficult technique to use in quantitative studies, especially when studying deep seated vessels such as abdominal or cerebral arteries. Intra-arterial Doppler flow probes and NMR may have a role in the future.

In chapter 4, X-ray angiographic techniques of measuring blood flow are reviewed. In chapters 5 and 6 a new technique to measure blood flow using digital X-ray angiographic data is introduced.

CHAPTER 3

PHYSICS AND INSTRUMENTATION OF DIGITAL ANGIOGRAPHY

3.1 INTRODUCTION

Over the years, X-ray film with an intensifying screen has proved to be an excellent medium for the detection and display of images in the majority of conventional radiographic examinations. However, printing the images on film presents several limitations that are becoming more important as interventional techniques make greater demands on X-ray imaging. The first of these limitations is that images are generally not available on cine-film until approximately 15-20 minutes after the procedure compared to two minutes for single X-ray film. As a result, the images cannot be used to guide an interventional study unless the procedure is interrupted for film processing. In addition, the adequacy of the images is not known until film development, so more views than necessary may have to be obtained at a cost of increased contrast dose, radiation exposure, and time.

Other problems related to the use of film are technical, including: the limited dynamic range of X-ray film; a non-linear relationship between optical density and exposure; the inconvenience of film digitisation necessary for most quantitative analysis; and lack of control over image contrast after acquisition.

To overcome these problems, digital radiology has been developed. The basic principle of digital imaging is that an image is stored as rectangular array of numbers, each number relating to image intensity at that point. This digital image can be manipulated or analysed by computer. The numbers are either converted back into a visual image for viewing or quantitative data may be generated such as cross-sectional area of a blood vessel, volume of a particular structure, and flow rate down a blood vessel, etc.

3.2 PRINCIPLES OF DIGITAL FLUOROGRAPHIC IMAGING

A simplified block diagram of the processes involved in digital fluorography is shown in fig. 3.1. The whole system is controlled by a general-purpose computer. Here the concepts involved in each individual component are briefly outlined.

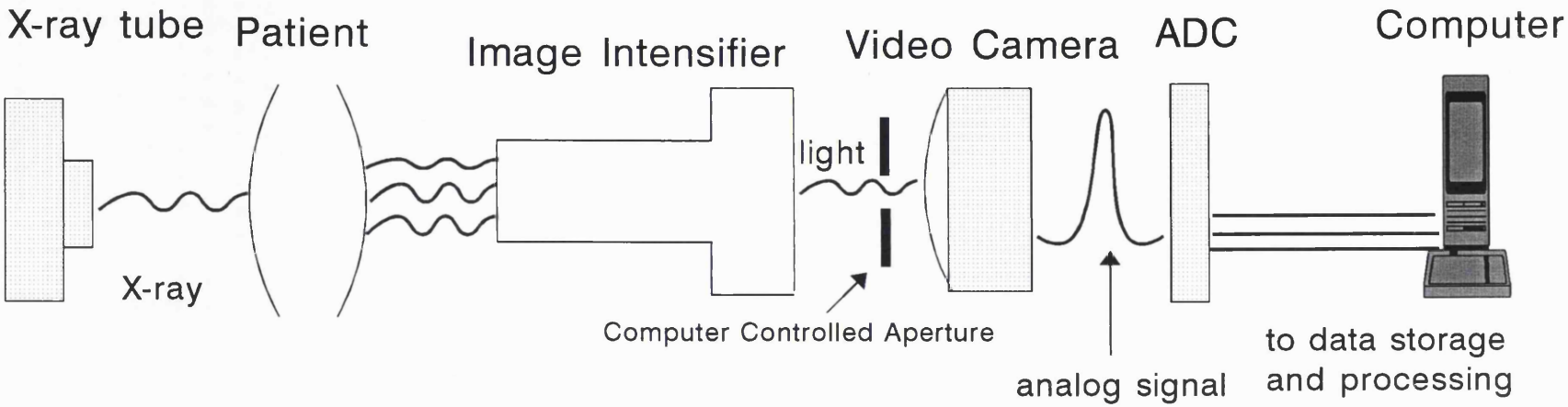

Fig. 3.1. Block diagram of basic system used for digital fluorography. The main imaging components include: X-ray tube, image intensifier, video camera, high speed analogue-to-digital converter (ADC), and a computer.

3.2.1 X-ray Tube and Generator

The standard features and requirement for X-ray sources are well known (Leeuw 1986). In summary, diagnostic application requires: (1) high instantaneous power levels up to 100 Kw, of a short duration; (2) highly stable voltage during each exposure, this is critical for studies which evaluate the temporal variations of contrast material such as vascular flow; (3) provision for pulsing the radiation source at up to 50 pulses per second, short X-ray pulses are essential to avoid blurring of moving structures; (4) a small 'focal spot' to maximise geometric sharpness, because the spatial resolution of images depends on the type of image receptor, the magnification factor, and on the actual focal size of the X-ray tube. Typical focal spots are 0.2-0.6 mm. These X-ray systems can therefore provide diagnostic images for visual interpretation and, in addition, quantitative densitometric data can be derived.

An important factor in digital angiography is the synchronisation of the X-ray generator with the digital video processor. Different systems accomplish this differently; the Siemens Digitron II digital subtraction angiographic (DSA) system used in acquiring the digital X-ray angiographic data used in chapters 8 and 9, use the following methods for synchronising the X-ray exposure and T.V. scan sequence. At 25 frames per second the X-ray exposure is typically 4 ms which is immediately followed by the scan of the T.V. target. The system controller synchronises both X-ray exposure and T.V. scan sequence to mains frequency. At 50 frames per second the exposure times are shorter and only one scan of an interlaced sequence (312 lines) is used.

3.2.2 Image Intensifier

The primary radiological image may be converted instantaneously into a visual image by use of an image intensifier (II). A detailed description of the II has been written by Nalcioglu et al (1986) and Fujita et al (1985). In brief an II has an input phosphor and photocathode, where X-ray photon energy is converted into light energy and hence a release of electrons. The electrons are accelerated by a high voltage and are focused on to an output phosphor, where the electrons are converted back into light photons. Amplification takes place during this

conversion process, so that for every X-ray photon arriving at the input phosphor of the intensifier, many thousands of light photons are generated at the output. Three major factors define the quality of an II:

(1) quantum detection efficiency (*QDE*), this measures the accuracy or quality of data transfer in imaging systems and is defined as:

$$QDE = \frac{(SNR_{out})^2}{(SNR_{in})^2} \tag{3.1}$$

where SNR_{in} and SNR_{out} are the signal-to-noise ratio in and out respectively;

(2) spatial resolution, and

(3) field of view.

The thicker the input phosphor of the II, the higher the *QDE*, but the poorer the spatial resolution; typical values for efficiency are 50% at 50 kev. The spatial resolution varies with field size, typical values are 2 to 5 lp/mm full width half maximum (FWHM) for a field size of 110-400 mm. The other important parameter in assessing quality is geometric distortion. Limitations in the electron optics lead to distortion in the II during the acceleration of electrons from the input phosphor to the output phosphor and due to the curved face of the input phosphor (Chakraborty 1987). This results in a pincushion distortion effect. The result of this distortion is that images are stretched in the radial direction by a factor which increases as the distance from the centre of the image increases. Although it does not degrade the resolution significantly, it may produce error in geometric measurements. This distortion can usually be corrected by imaging a calibrated metallic grid and by applying the subsequent corrections. In a modern II this effect is very small, and we have shown that it can be considered to be negligible in geometric measurements (see chapter 5).

3.2.3 Video Camera

This is the single most important element in the imaging chain. A video camera, more usually of vacuum-tube design, is coupled to the output screen of the image intensifier by a lens system. The primary function of the system is to convert the light intensity image (optical image) produced by the II to an electronic signal that can be digitised. Some of the important properties of the video camera are:

(1) speed of acquisition (frame rate);
(2) signal-to-noise ratio (SNR);
(3) linearity between output video signal and the incident X-ray flux, which is determined by the photoconductivity of the target material used (Sandrik 1984);
(4) spatial resolution;
(5) extent of the 'blooming effect', whereby if a high intensity object is adjacent to a low intensity object, there is in effect some leakage of the high intensity area onto the lower intensity area.

State of the art cameras such as a Plumbicon^{R*} (lead oxide) have a resolution of 1249 or 525-lines for a 1024x1024 or 515x512 pixel matrix respectively, and a SNR of 1000:1 or better, with an acquisition rate of 25 or 30 frames per second (Roehring et al 1981). Other advantages of the lead oxide are that the output video signal is linearly dependent upon the incident X-ray flux (light intensity); whereas, for other types of video camera the video output V is approximately related to the light flux I according to the relationship

$$V=I^{\Gamma} \tag{3.2}$$

where Γ is a constant. For the Plumbicon camera (lead oxide) $\Gamma\approx1$, whereas for typical non-linear fluoroscopic cameras (such as those with an antimony trisulfide target) $\Gamma=0.6$ (Kruger et al 1981a). For digital imaging, a value of $\Gamma=1$ is needed for accurate subtraction and quantisation. Before the digital image is displayed its contrast can be manipulated to match the characteristics of the monitor.

Recently another type of camera has been introduced which is solid-state, this uses the latest integrated circuit (IC) technology. These cameras are manufactured with light sensitive silicon devices called charge-coupled devices (CCDs). Here the image is focused on an array of discrete (digital) CCD elements. The advantages of these cameras are that each pixel is independent of its adjacent neighbours, so that problems with blooming effects are eliminated due to the discrete matrix of tiny light sensitive elements. Another advantage is that this type of camera has excellent geometric stability and frame to frame registration.

3.2.4 Analogue-to-Digital Conversion

The image conversion is performed by the following steps: scanning, sampling, and quantisation. This process of digitisation is performed by an analogue to digital conversion (ADC), the efficiency of which can be defined by the rate of digitisation or conversion time, and intensity resolution or depth of digitisation. Scanning is accomplished by the video camera, which converts the continuous 2D image into a number of horizontal scans, called rows or rasters. The intensity along each raster scan is measured, or sampled, at evenly spaced points. Each of these measured values represents the brightness at one location in the image, known as a picture element, or pixel. Finally, each pixel intensity is converted to an integer between 0 and N_g - 1, where N_g is the number of discrete grey levels the ADC can represent. This conversion is called quantisation. The number of grey levels, N_g, determines the upper limit to the precision with which the original image intensities are represented in the digital image. The precision of the ADC (i.e. the ADC step size) is important, the larger the number of bits per pixel, the greater the dynamic range and the smaller the quantisation error or "quantisation noise". Most systems use 8 or 10 bits per pixel for the ADC. The major difference between 8 and 10 bits conversion can be appreciated only in images that have very large dynamic range. At present time conversions greater than 10 bits probably will not increase accuracy, because the SNR of currently available cameras is 1000:1. Work is in progress to develop a 12 bit ADC coupled to a camera with a SNR of 2000:1.

The maximum resolving power of a digital imaging system is limited by the pixel

size. The information content in images, has been characterised in term of spatial frequency components, for example an object with sharp edges will have higher spatial frequencies than an object that has only smooth edges. The process of digitising an image into discrete pixels is called sampling, and the size of the pixels corresponds to a sampling frequency. According to the Nyquist sampling theorem, an image can be sampled without loss of any information provided that the sampling frequency is at least twice the highest spatial frequency component in the image. Depending on the characteristics of the original image being digitised, there may be two types of quantisation errors. First, if the sampling frequency is too low, there will be loss of image information at high spatial frequency. This introduces image blurring, with loss of spatial resolution. Second, there may be introduction of artefact due to aliasing in which spatial frequencies above the Nyquist frequency in the original image masquerade as lower spatial frequencies.

3.2.5 Image Analysis Workstations

Digital fluorography systems are currently not convenient for reviewing images or quantitative analysis. This is because they lack the appropriate computer hardware and software, and lack an appropriate development environment; additionally, in most centres, the angiography theatres are very busy with the day to day acquisition and basic manipulation of the images.
Consequently, some centres have set up an off-line digital image workstation with full analysis and display facilities. Images can be transferred from the digital fluorography system to an image analysis workstation via magnetic tape, optical disk or by direct transfer via a local area network (LAN).

3.3 DIGITAL SUBTRACTION ANGIOGRAPHY

The concept of the temporal subtraction methods such as the mask mode and time interval difference methods provides an important contribution to the study of vasculature. In the mid 1970s and early 1980s, much research was done in the field of digital image subtraction, particularly as applied to medical imaging (Crummy et al 1980; Enzmann et al 1983; Meaney 1980; Modic et al 1981; Nelson et al 1982; Kruger and Rieder 1984).

It was found that radiologists routinely failed to detect approximately 30% of abnormalities in angiograms (Ziskin et al 1971), and so a technique was sought to improve this situation. At the same time, scientists wished to decrease the amount of contrast material that needed to be administered to patients in order to visualise the blood vessels and heart chambers. A new field, known as 'digital subtraction angiography', emerged.

In angiography, traditionally, contrast material would be injected just proximal to the artery or heart chamber of interest and then an X-ray image of that region would be taken. The arteries and chambers of interest could be visualised in these X-ray images, but so would overlying bone and some tissue structures. These often obscured the structure of interest in the image, e.g. the arteries and heart chambers. A technique was sought that would remove the unnecessary and unwanted structures in the images. The solution was as follows:

1. Take an X-ray of the patient.
2. Inject the contrast material into the patient.
3. Take another X-ray of the patient.
4. Subtract the first image from the second, and display the result.

The theory was that the background structures would appear in both X-ray images and so would not appear in the subtracted image. Only the structures of interest (e.g. those containing the contrast material) would be shown in the subtracted image. Although this approach has been successful, one limitation has emerged: the two images need to be aligned perfectly, or motion artefacts appear in the subtracted image. Several researchers have attempted to find ways of correcting for motion artefacts caused by patient motion (Brody 1981; Kruger et al 1982; Mistretta 1981) but it still remains a problem.

Baily et al (1983) and Kruger et al (1981b) introduced the concept of logarithmic transformation prior to subtraction. That is:

$$f_s(x,y)=A+B\{\log[f_2(x,y)]-\log[f_1(x,y)]\} \qquad (3.3)$$

where:

$f_1(x,y)$ is the pre-injection image intensity,
$f_2(x,y)$ is the post-injection image intensity,
$f_s(x,y)$ is the subtracted image intensity,
A and B are constants to scale the input and output data appropriately (i.e. offset and gain, respectively).

The optical brightness of an image intensifier varies exponentially with the radiographic density of a target placed in a monoenergetic X-ray beam. This effect, known as the Lambert-Beer's law, was originally defined for monochromatic radiation:

$$I = I_0 \exp(-\mu d) \tag{3.4}$$

where I is the transmitted intensity, I_0 is the intensity of the incident monochromatic beam, d is the thickness of the absorbing material, and μ is the linear attenuation coefficient of the material. From equation (3.4):

$$d = \text{const.}\log\left(\frac{I}{I_0}\right) \tag{3.5}$$

which means there is a proportionality between the thickness of the absorbing layer and the logarithmic value of the transmitted intensity.

When the image is obtained digitally instead of photochemically, the intensity at each pixel is transformed logarithmically and stored in a matrix. With logarithmic digital format, the signal defining the image is linearly proportional to the thickness of contrast material traversed by the X-ray beam. Consequently, if the conditions governing these important physical relationships are satisfied, quantitative information can be easily extracted from 2D X-ray projection.

However, the X-ray sources used in diagnostic radiology are not monochromatic,

and the above equation is only a rough approximation of reality. But it has been shown that a monoexponential relationship remains accurate for polychromatic radiation under the typical conditions present during digital fluorography (Lantz and Strid 1973; Nissen et al 1983). Thus, in digital angiography, the digital system performs a logarithmic transformation of image intensity prior to mask mode subtraction to obtain accurate projections of vascular networks.

3.4 ERROR IN FORMATION OF DIGITAL IMAGES

3.4.1 Noise

In digital fluoroscopy the following three sources contribute to digital image noise which limits image quality.

(1) Quantum noise (sometimes called quantum mottle because of the mottling effect this noise produces in film images), resulting from detecting a finite number of X-ray photons in each pixel. The greater the number of X-rays used to form an image the smaller is the relative intensity of the noise. For a beam of monoenergetic X-ray photons the relative error in each pixel is proportional to:

$$\frac{1}{\sqrt{N}} \tag{3.6}$$

where N is the number of detected X-ray quanta contributing to that pixel. Accordingly quadrupling the number of detected X-rays (and hence patient exposure) will decrease the noise twofold. In a dynamic study with X-ray imaging, the noise cannot be made arbitrarily small because there is a practical limit to the acceptable patient dose and the X-ray flux that can be produced by the X-ray tube in the short period of time required to record a sharp image ($\approx$0.04 second).

(2) An exposure-independent electronic noise contribution, which originates primarily in the preamplifier stage of the television. This contribution is termed 'system noise' and enters to a limited degree at all stages of

analogue signal processing.

(3) Digitisation noise, which is due to the discrete increments between grey levels in a digital image, and which can made smaller by increasing the number of grey levels defined by the ADC. Commercially available ADCs provide 1024 grey levels (10 bits) (Shroy 1988).

In general, one of the these three noise sources will dominate a digital fluoroscopy image. In a properly designed and operated image system, the total image noise should be dominated by quantum noise since otherwise the X-ray dose to the patient could be reduced without sacrificing image quality. Low-noise video cameras are used in digital angiography to keep electronic noise well below quantum noise. Quantisation error can be made small compared to overall noise by choosing the grey level assignment to be less than twice the quantum noise (Shroy 1988).

The image subtraction techniques is used to enhance the detectability of low contrast anatomical structures. Subtraction is therefore a method of removing a significant source of noise, patient structure noise due to overlying bone and soft tissue structure. But subtraction does not reduce random noise such as quantum mottle, since this noise changes from one frame to another. Random noise occurs due to the finite number of X-ray photons contributing to the image (quantum noise) and due to random fluctuation in signal in the T.V. pre-amplifier (electronic noise). As this noise is largely un-correlated between successive images the subtracted image will have increased noise. For example, when there is a linear transformation of X-ray intensity to image grey value and the X-ray intensity is approximately the same for mask and opacified images, then the absolute level of the noise will increase by a factor of $\sqrt{2}$ (Keyes et al 1981). i.e. random noise adds in quadrature.

The most basic measure of image quality is the SNR of the final image. It is defined as the range of intensities to be digitised (the signal) divided by the root-mean-square deviation of intensity (noise). The SNR is frequently expressed using the logarithmic decibel (dB) scale. The signal to noise ratio in dB is equal to 20 $\log_{10}$(SNR). Thus, 60 dB correspond to an SNR of 1000:1.

3.4.2 Scatter and Veiling Glare

The X-ray intensity of each pixel in a digital fluoroscopy image is the sum of two components: a primary (direct) component composed of X-rays transmitted straight through the patient; and a secondary (indirect) component composed of X-rays which have been deflected or scattered within the patient before reaching the imaging system. Scattering of light in the output phosphor, or veiling glare, also adds an additional secondary component. With the use of a broad field image intensifier both the primary and scattered X-ray intensity, S_p and S_s, respectively, are detected. This reduces the iodine contrast in a logarithmic difference image by the factor:

$$\frac{S_s+S_p}{S_p} \tag{3.7}$$

compared to the ideal case where only the primary X-ray intensity S_p is detected. Several investigators have tried to estimate and correct scatter and veiling glare (Pfaff et al 1988; Maher et al 1982) but the more practical approach is to calculate an estimated correction from the image by assuming that scatter and veiling glare can be characterised by a point spread function (PSF). Shaw et al (1982) have estimated veiling glare by convolving a fixed PSF with the image and multiplying the result by a weighting factor. Seibert et al (1985) convolved a calibrated inverse filter with the image to remove veiling glare. In our laboratory Arnold and Hawkes (1989) have devised a technique for densitometric calibration using a pair of scanning slits. The technique is designed to remove the effects of X-ray scatter, beam hardening, and veiling glare.

3.5 CONCLUSION

Digital angiography and cine-film angiography employ identical imaging chains from the X-ray tube through to the image intensifier and therefore share the limitations of these systems in terms of resolution, contrast, and noise. The advantages of digital imaging during the angiographic procedure are the speed and ease with which the images can be replayed, the availability of image

enhancement, random access to multiple reference frames from previous views, and increased contrast sensitivity with digital subtraction, allowing a reduction in the volume of injected contrast material. In addition, it is faster to extract quantitative data from digital images than from cine-film.

An important contribution of digital fluorography is the use of subtraction techniques to enhance the detectability of low contrast anatomical structures. Subtraction is therefore a method of removing a significant source of noise, patient structure noise due to overlying bone and soft tissue structure.

The spatial resolution and SNR in digital angiography make this image modality well suited to quantitative studies of the vascular system. The next chapter provides an overview of existing X-ray angiographic techniques of blood flow measurements.

CHAPTER 4

A REVIEW OF QUANTITATIVE X-RAY ANGIOGRAPHIC TECHNIQUES TO MEASURE BLOOD FLOW AND VESSEL CALIBRE

4.1 INTRODUCTION

As discussed in the previous chapter, the spatial and temporal resolution of angiograms is relatively high, which in principle should allow the derivation of both anatomical and physiological information about vascular diseases. But despite the widespread and long-standing use of X-ray angiography in clinical practice, the method of interpretation of angiograms has changed very little in recent years. Image quality continues to improve as a result of higher quality image intensifiers, pulsed fluoroscopy, real-time image enhancement, and high quality image digitisation; however, most angiograms are still viewed visually and therefore subjectively. In the expanding field of interventional catheterisation procedures, including thrombolysis, percutaneous transluminal angioplasty, and other rapidly evolving techniques for transluminal revascularisation, a more detailed and quantitative routine analysis of vascular angiograms is urgently needed for planning and assessment of the outcome of the therapy.

The volume flow rate is the product of the velocity of blood in the direction of the vessel axis, averaged over the vessel cross-section, times the cross-sectional area of the blood vessel.

This chapter provides an overview of techniques of quantitative analysis of X-ray angiograms which have been used to extract blood flow measurements, highlighting the advantages and limitations of the available methods of assessing the volume blood flow. Initially I will discuss the problems involved with the more conventional methods, such as dye-dilution and contrast bolus transport time, which use time-density curves for the measurement of blood flow. I will then introduce a more recently developed technique of blood flow measurement which uses analysis of a distance-density-time representation to extract blood flow waveforms. At the end of the chapter an overview of the various techniques used to measure cross-sectional area is provided.

4.2 METHODS OF MEASURING BLOOD FLOW

Since the early development of angiography, there has been interest in expanding videodensitometric recordings to quantify blood flow. Attempts to quantify blood flow from radiographs of individual vessels were presented as early as the late 1950s (Sinclair et al 1960; Nordenström and Grim 1965; Hilal 1966; Rutishauser et al 1967). Despite a long history of scientific interest in the use of X-ray angiographic techniques in the measurement of blood flow in vessels, progress has been very slow.

Conventionally, there are three main classes of methods used in quantifying blood flow angiographically. The first uses the rate of dilution of contrast material in the blood as a measure of flow rate. The second, the transport time technique, determines the time of transport of a contrast bolus along a predetermined length of vessel. In addition a third approach has been used to measure average and instantaneous blood flow velocities. The main principle behind this approach is to consider changes in the contrast material mass (or concentration) in the blood vessel, rather than using predefined distances as in the bolus transport time method.

The majority of the conventional techniques have been developed for cineangiographic film analysis; however, in the same or a slightly modified format, they are also applicable to digitally acquired data. With rapid improvements in hardware and software for digital systems, and the development of objective and reproducible analysis, the on-line approaches will play an increasingly dominant role in clinical decision making and, possibly in the near future, in the assessment of the efficiency of interventional studies.

4.2.1 Dye-Dilution Technique

This method utilises the theory embodied in the standard Stewart and Hamilton equations, which predicts that the area under an indicator density versus time curve will be directly proportional to the quantity of indicator injected and inversely proportional to flow.

For angiographic applications, the contrast material is used as the indicator, and the density is measured in an arterial region of interest. This method has been used to measure both absolute and relative flow. If cardiac output is known, then absolute flow can be calculated by obtaining indicator dilution curves from both a reference injection into the aorta and a separate injection of the same amount into the artery of interest. The technique requires precise knowledge of the amount of contrast injected and the complete mixing of the indicator with the blood. Alternatively, the measurement of absolute flow from single injections into an artery can be performed if complex corrections are made. These are needed to account for the effects of radiographic scatter, veiling glare, and beam hardening in order to optimise and linearise the effective mass absorption coefficient, the transfer function of the image intensifier system, and the intensity of incident radiation. However, if the same quantity of contrast can be administered under similar conditions, and if the radiographic technique follows a fixed protocol so that any effects are effectively cancelled out, then a much less technically demanding measure of relative flow between two arteries is possible, where relative flow is the ratio of flows along the two arteries.

Two techniques are commonly used to inject the indicator into the vessel: (1) a single bolus injection, and (2) continuous injection at a constant rate.

4.2.1.1 *Bolus injection*

This approach assumes that the indicator is injected into the blood vessel as a single bolus. Let us suppose that a mass of indicator M, such as iodine contrast material, is injected into a vessel, and is diluted with blood flowing in the vessel. The iodine concentration then varies as a function of time following the injection. The concentration at any point downstream from the site of injection is related to the mass of injected contrast material and the volume flow rate F at the injected site by:

$$F = -\frac{V}{C} \cdot \frac{dC}{dt} = -\frac{1}{C} \cdot \frac{dM}{dt} \qquad (4.1)$$

where C is the concentration of indicator at the sampling point, V is volume of the

vessels and t is time. With the assumption of contrast flow, the flow F can be calculated with the knowledge of the quantity of indicator injected by integrating the indicator concentration curve over time for the single injection. This equation is known as the Stewart-Hamilton equation (Stewart 1912; Hamilton et al 1932).

The problem with this method was discussed in detail by Colchester (1984) and can be summarised as follows:

(1) because the blood flow in arteries is pulsatile the assumption of constant flow rate introduces an error;

(2) blood flow at both sites must remain constant for the angiograms of the study to be valid, but the pharmacological effects induced during the first injection of the contrast material are likely to be at their peak when injecting for the second time.

The most important technical prerequisite of this technique is that the administered contrast dose must be known precisely, therefore the catheter should be filled with contrast material before the injection (Holcroft et al 1980). Complete mixing must also be ensured.

Some investigators have attempted to describe the dilution curve (the concentration time curve) by fitting a mathematical model to it. The gamma variate curve has been fitted by the method of least squares to the dilution curves and the variate has been shown to approximate an indicator dilution curve without recirculation (Thompson et al 1964). The indicator concentration, $C(t)$, at time t after injection can be expressed as:

$$C(t)=K(t-t_a)^{\alpha}e^{-(t-t_a)/\beta} \qquad (4.2)$$

where t_a is the indicator arrival time at the site of the measurement, K is a constant scale factor, and α and β are fit parameters.

The flow can be calculated by either using the Stewart-Hamilton equation, as described above, or calculating the mean transit time (MTT) of the contrast

material (Starmer and Clark 1970):

$$MTT=\frac{\int_0^\infty tC(t)dt}{\int_0^\infty C(t)dt} \tag{4.3}$$

$$MTT=t_a+\beta(\alpha+1) \tag{4.4}$$

Bateman and Kruger (1984) similarly computed a time to maximum opacity by setting d*C*/d*t* to zero. This resulted in

$$t_{max}=\alpha\beta+t_a \tag{4.5}$$

It can be seen from equations (4.4) and (4.5) that *MTT*, t_a and t_{max} differ only by constants. Relative flow times *t* (transport time: differences between two transit times) were determined along a length of an artery using two parametric images. In the first parametric image, each pixel represents the maximum value of the dynamic image density, the second parametric image contains the time of maximum opacification. In addition, the curve fitting procedure was performed on a representative portion of the vessel under study to determine the parameters α and ß.

Their assumption was that the shape of the time-density curve along the vessel stays constant. This theory was validated 'in-vitro' (Kruger et al 1983) using a physical model of blood circulation. The calculated velocity differed by up to ±15% from the velocity determined by fluid collection. The range of velocities calculated was from 204 to 373 mm/sec.

4.2.1.2 *Constant rate injection*

This approach uses a variation of the Hamilton-Stewart principle. The volume flow rate *F* can be estimated from the quantity of injected indicator *Mdt* and indicator concentration in the blood over time *Cdt*

$$F=\frac{\int Mdt}{\int Cdt} \tag{4.6}$$

Hilal used the slow continuous infusion method to quantify femoral arterial blood flow in dogs (Hilal 1966). Using a systematic calibration procedure Hilal was able to relate the change in film density due to X-ray beam filtration across a blood vessel image with the mass of contrast material per unit area transradiated. Hilal assumed that 'in-vivo' vessels were circular, and thus equated the width of the vessel image on film with the depth of transradiated contrast material in the centre of the vessel image. By dividing the contrast material mass per unit area by the vessel depth he obtained the contrast material concentration. The mean blood flow was then calculated using equation (4.6). Although Hilal reported reasonable success with the technique, it has not found practical application because of the difficulty in quantifying iodine content.

Korbuly (1973) applied this method to the measurement of pulsatile flow by calculating flow at different stages of the cardiac cycle. The pulsatile flow data was improved by averaging over several cardiac cycles. A physical model was used, consisting of a pulsatile pump and plastic tubing (with an internal diameter of 5 mm) in series with the probe of an EMF. The system was primed with heparinised human blood. EMF data were synchronised with X-ray angiography by recording the exposure time and duration. Data was collected using 6 exposures per second with a 50 msec exposure time. In the physical model studied, the mean flow measured with the EMF was 135 ml/min and the peak flow 325 ml/min. Although the main features of the blood flow waveform were faithfully reproduced, there were errors as large as 30%, with mean error within ±12% (±1 SD) with regards to the EMF reading.

The Stewart-Hamilton technique is potentially the most accurate as it can integrate the entire velocity profile. However, it is limited to arterial segments in which there is no branching or recirculation, and requires that arterial dimensions and the iodine content be accurately quantified.

4.2.2 Bolus Transport Time Technique

The concept of using transport time techniques to measure blood velocity and flow is summarised in fig. 4.1. The time taken for the passage of contrast between two points, a known distance apart in the vessel of interest, has been

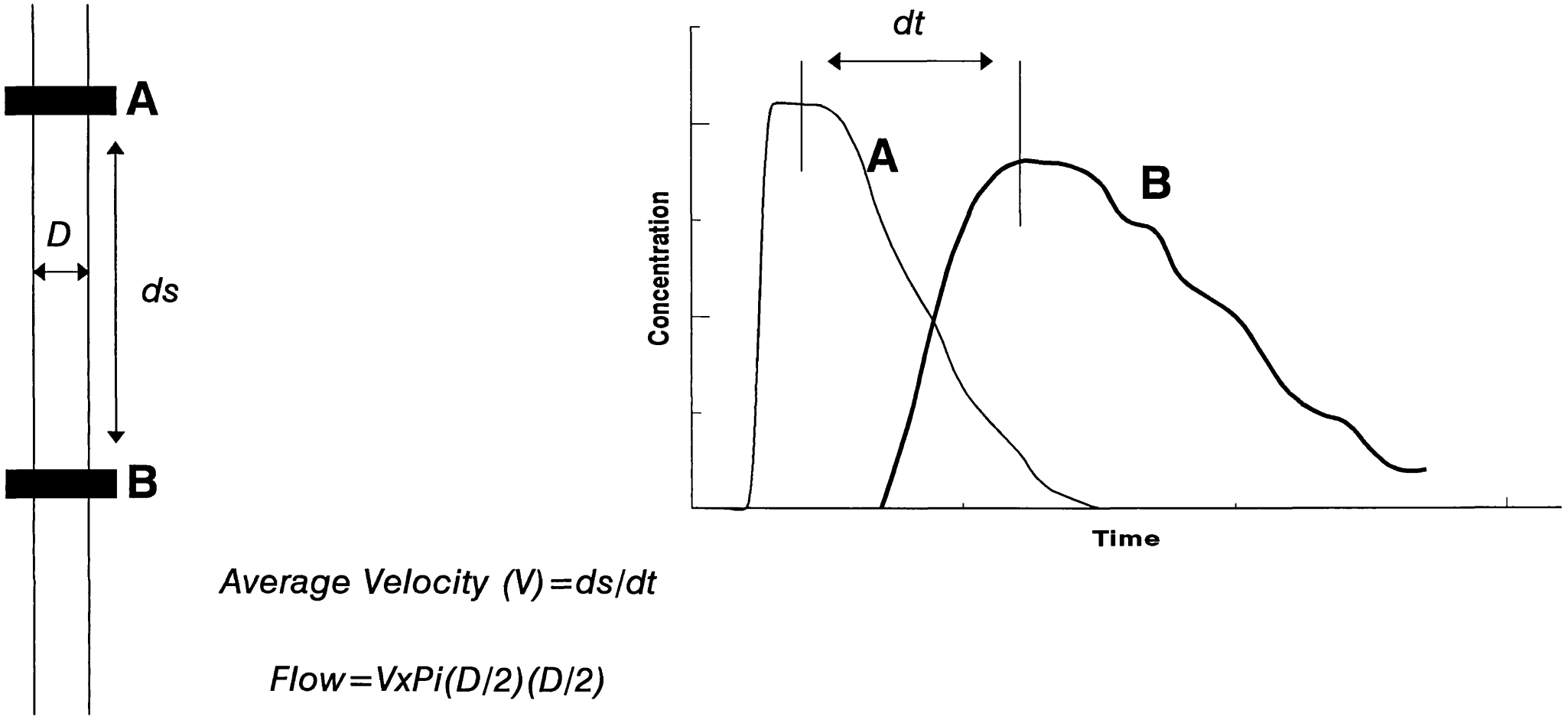

Fig. 4.1. Schematic illustration of the basis for calculation of blood flow from the transport time. The time d*t* for passage of a contrast bolus from a ROI (A) to a ROI (B) is measured. The average velocity *V* and flow can be calculated from the distance d*S* between the ROIs and the diameter (*D*) of the blood vessel segment.

used to calculate the velocity of a bolus of contrast material. Measurement of the mean cross-sectional area of the blood vessel segment allows conversion of the velocity measurement into a flow measurement.

Several methods have been used for processing time-density curves (fig. 4.1) in order to calculate transport time measurements. Distinct features on the profiles, such as the peak, the leading edge or the centre of gravity have been identified. The transport time was taken as the time difference between corresponding points at the two sites under study.

4.2.2.1 *Bolus transport time estimation using part of the time-density curves*
The time separation of the peak, half peak maximum and first appearance (foot) of the two time-density curves are parameters used by Silverman and Rosen (1977); Bürsch et al (1979); Kruger et al (1983) and Forbes (1984) to determine mean bolus transport time.

Probably the most successful method of estimating mean transit time from the initial portion of a time-density curve is that described by Bürsch et al (1979 and 1981). This is referred to by Colchester (1984) as the "equal height square-wave arrival moment". The peak of the curve is identified, and the area under the curve up to this point measured. A square wave of the same height and the same area is then constructed with its right-hand edge coinciding with the peak time-density. The left-hand edge of this square wave, i.e. the area divided by the height of the initial curve and subtracted from the time of the peak, is taken as the arrival moment for each curve.

This method has the advantage of utilizing and averaging all the data from the first part of the curve, and although the method of calculation requires approximate recognition of the peak bolus time, in circumstances where the peak is flat and very hard to define, small errors in its localisation have little effect on the calculated time-parameter.

4.2.2.2 *Bolus transport time estimation using the whole of the time-density curves*
The time (mean transit time) difference between the centres of gravity (cogs) of two time-density curves a known distance apart is taken as the bolus transport

time (Zierler 1962). The mean transit time (*MTT*) is defined according to the following formula:

$$MTT = \frac{\int tC(t)dt}{\int C(t)dt} \tag{4.7}$$

where $C(t)$ is the time-density curve at a region of interest (ROI) as a function of time t.

Rutishauser and colleagues (1967) confirmed the mathematical proof of the above equation experimentally by using a circulation model of constant flow rate. The validation of the cog principal was carried out 'in-vivo' using the carotid artery of a dog. A 20% deviation was reported from the line of identity (Rutishauser et al 1967).

A drifting density background level is one of the main problems influencing the time-density curve. Sakurai et al (1986) tried to overcome this problem by placing background ROIs close to the artery. For correction, the density of the background ROI was then subtracted from the time-density curve of the ROI over the artery. However due to the pulsatility of arterial blood flow, the time-density curves can be very complex in shape, and, therefore, establishing when to begin or end computation of cog is a very difficult task.

Another method is to cross-correlate the time-density curves: the time-density curve at position x is correlated with that at a reference position x_0 as a function of the time shift t_s, i.e.

$$C(x,t_s) = \int_{k_0}^{k_1} F(x,t-t_s)F(x_0,t)dt \tag{4.8}$$

where $F(x,t-t_s)$ and $F(x_0,t)$ are the time-density curves at positions x and x_0 respectively and k_0 and k_1 define the integration interval.

The temporal (time) shift obtained for the maximum of the cross-correlation

function $C(x,t_s)$ (a sum of products of the amplitudes of the integration interval), or from a similar technique relating the time-density curves, is taken as the bolus transport time (Rosen and Silverman 1973; Silverman and Rosen 1977).

The basic operation in correlation is to compute a measure of the 'agreement' between the two time-density curves. The first time-density curve is shifted relative to the second time-density curve along the time axis, and a new cross-correlation is calculated. At some point, the moving curve will contain the same features as the fixed time-density curve. When this happens, the shape of the two time-density curves is approximately overlapped, and the measure of curve agreement is maximised.

The comparison is limited to a certain time interval (integration interval), if the integration interval were reduced in size then the statistical error in the calculation of the cross-correlation would increase significantly due to the pulsatility of the blood flow.

4.2.2.3 *Measurement of the leading edge of the bolus*

Sovak et al (1971) proposed a novel method of measuring constant and pulsatile blood flow by plotting the displacement of lipiodol oil droplets against frame times using cineangiographic data. The validity of this technique was demonstrated using a physical phantom consisting of a 300 ml glass syringe with a metallic piston in series with plastic tubing of 5, 10, or 17 mm diameter. The film was then digitised and for each frame the position of the piston and droplet were plotted against the frame number (time). From the gradient of this curve the mean velocity was calculated. The main problem of this technique is that the oil droplets being insoluble may occlude a number of small vessels. Dependent on their number and location, these embolic obstructions may seriously affect the subject, therefore the technique is not suitable for use 'in-vivo'.

More than a decade later, Schmiel et al (1986) improved the technique of tracking the leading edge of a bolus in two distinct ways. Firstly, they used a soluble and non-invasive contrast material (amidotricoate), injected as a 1.5 ml bolus using a power injector at a rate of 5 ml/sec, and secondly the leading edge displacement of the front of the contrast bolus from frame to frame was detected

manually, after the masking of each frame by the previous frame. The instantaneous velocity was then calculated as the product of the sampling frequency and the displacement of the contrast for each frame. The technique was applied to measure blood flow velocity in the left coronary artery in man, but this technique was not validated against any other method, to assess the accuracy. The problems with this technique are: (1) the leading edges of the contrast material are used to measure blood velocity, which would overestimate the true flow as the velocity of the contrast material in the central laminae is higher than the average velocity, (2) the manual detection of the leading edges of the contrast material is a very difficult task due to back-flow.

The pulsatility of the blood flow waveform produces wide variations in contrast material concentration over time. These variations produce marked features in the time-density curves. Very few of the existing techniques used for angiographic flow measurement have addressed this problem of inaccuracies in mean flow estimation caused by pulsatile flow. Typical time-density curves last for one half to two seconds and transport times are derived from an uncontrolled and asymmetrically-weighted sample of the cardiac cycle.

Figs 4.2 and 4.3 demonstrate clearly why time-density curves may assume a complex shape when flow is pulsatile. The contrast bolus is shown as very short and discrete, and it is assumed there is some forward and backward flow and that the bolus becomes increasing dispersed. Depending on the choice of recording sites of a pair of concentration- (density-) time curves, the simple matching described above may be impossible (Colchester et al 1986). This is the prime reason that none of the existing bolus transport time techniques could produce accurate velocity estimates from the time-density curves. The flow rates calculated from time-density curves using bolus transport time techniques have been found to vary by as much as 100% around the average flow rates, and the average error in the calculated mean flow rates is over 20% (Schmiel et al 1978; Spiller et al 1983).

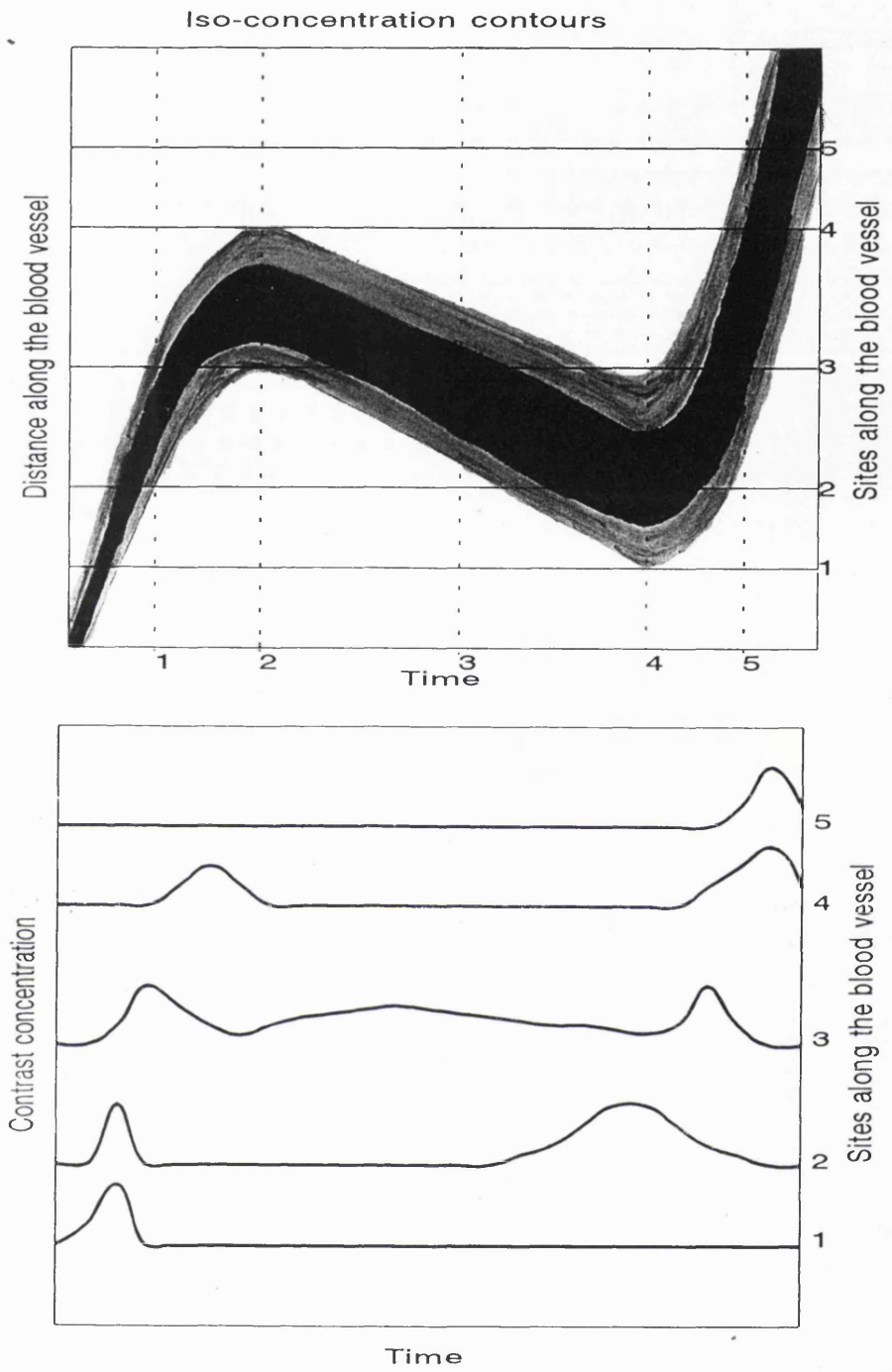

Fig. 4.2. The passage of a bolus of indicator down a vessel during one cardiac cycle. It shows where samples could be taken by previous techniques using time-density curves which would be extremely difficult to match: see text for details. (Reproduced by kind permission of Colchester et al 1986).

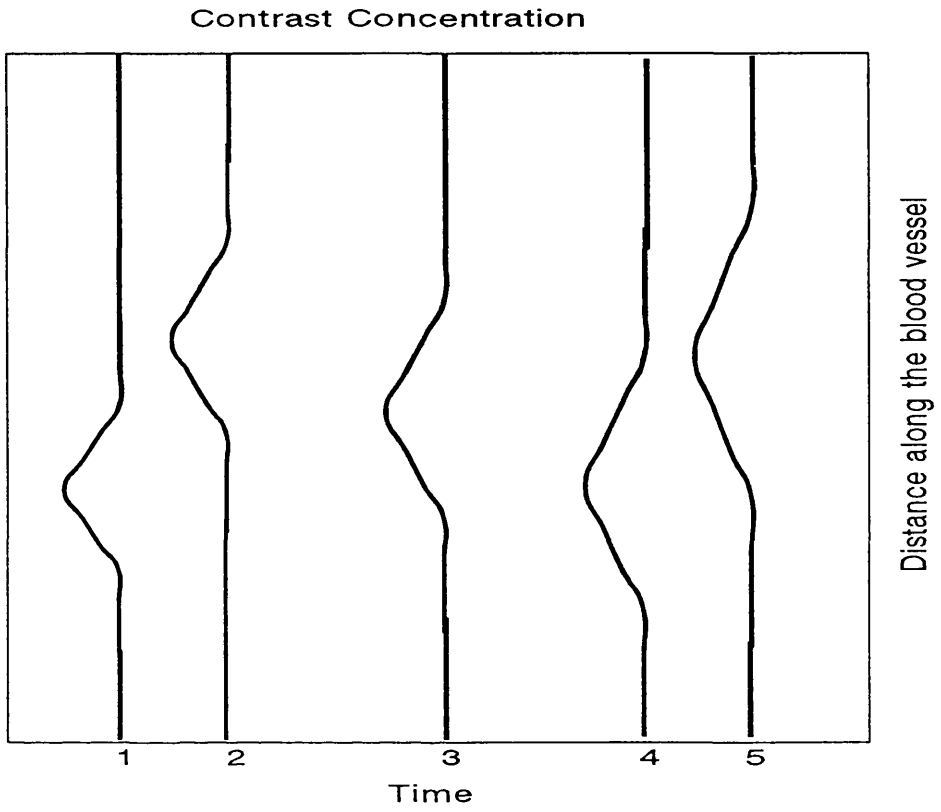

Fig. 4.3. Graphical representation of density-distance curves obtained from sites 1 to 5 from the image of a bolus of indicator down a vessel in fig. 4.2.

4.2.3 Distance-Density Curves

To overcome the inherent problem with bolus transport time estimation in the presence of pulsatile flow, distance down the vessel can be regarded as a continuous function and changes in contrast material mass (or concentration) in the blood vessel tracked as a function of time.

4.2.3.1 *Distance between rapidly pulsed boluses*

In this method the separation along the vessel between rapidly pulsed short boluses of contrast material was measured (Shaw and Plewes 1986). This method could be classified under the transport time technique as it uses the same principles to calculate the velocity of the bolus along the blood vessel. However, contrast material was injected with a specially modified injector at a pulsing frequency as high as 15 Hz, so that two or more boluses could be imaged simultaneously. Contrast injections were gated to the signal from an electrocardiogram. The velocity of flow was determined by measuring the spacing between the boluses using peak-to-peak, maximum leading edge gradient or centre of gravity criteria and multiplying this distance by the pulsing frequency. In this application, therefore, the actual time measurement was not obtained from the time-density curve, as it is in the usual transport time applications. Instead, it was obtained from the known injection frequency. The distance-density curve was analysed solely to determine the distance travelled by each bolus.

For steady flow conditions in a physical model, a good correlation was reported between flow velocities measured using this technique and values determined using graduated fluid collection, although there was a systematic 54 mm/sec overestimation for velocities of 80-600 mm/sec, with a measured tube diameter of 3 mm. Validations 'in-vivo' have not yet been performed with this method, and the physical model used did not represent the clinical situation very closely. The length of plastic tube imaged (380 mm) was much longer than most segments of human blood vessel free from branching, no allowance was made for back-flow and the range of velocities selected (peak 290 mm/sec) were much lower than is found in arterial blood flow 'in-vivo'. In-vivo application would require 3D reconstruction of the true course of the vessel. In addition the method requires a high rate of image acquisition to ensure adequate temporal resolution and high

pulsatile rates of contrast injection. More importantly, pulsatility of the blood flow imposes features on the individual distance-density curves of the small boluses, making the measurement of distance separation between boluses difficult at physiological flow rates.

4.2.3.2 *Tracking of bolus mass*

Swanson et al (1986) suggested a technique for determining the blood velocity by tracking the constant mass of contrast material in time sequences of radiographic images along a fixed length of vessel.

On the first angiographic image the integrated radiographic density was determined along a defined length of the total arterial segment imaged. The integrated radiographic densities of regions of the same length in the next frame were then calculated for all positions from the most proximal site to the most distal site, with single pixel shifts after each calculation. The density value obtained in the first frame was subtracted from all the density values determined in the second frame. The shift for which the absolute difference in the integrated radiographic density was a minimum was then determined. The length between this point and the previous point provided a measure of the distance moved by the blood during one frame period. This blood velocity was then combined with a densitometrically based cross-sectional area calculation (Kruger et al 1983) to establish phasic flow measurements.

Swanson et al (1988) employed this technique to quantify absolute pulsatile and mean flow in a coronary artery bypass graft. In contrast to the method of Shaw and Plewes (1986), only a single contrast injection to measure pulsatile blood flow was required.

This technique was reported after development commenced of our technique of computing the blood flow waveform (see chapter 6) and my assessment of this technique using computer simulated dynamic angiographic data (Seifalian et al 1988 and 1989) highlighted the following points: the tracking of bolus mass method was in fair agreement with the input profile for low blood flow, but it failed at high flow rates, i.e. either no match or incorrect matches were found. Chapter 7 discusses these findings in greater depth.

4.2.3.3 *Calculation of velocity using a grey-level gradient operator*

Colchester and Brunt (1983) proposed a novel way of forming a two-dimensional data structure, a parametric image, and hence extracting blood flow waveforms. In this method the *X*-axis is the frame number (time), the *Y*-axis is the vascular path length, and the parametric image grey value is the concentration of contrast material in the blood vessel lumen at position (*X,Y*). Thus, each pixel in the parametric image represents the concentration of contrast material at a particular position in the blood vessel at a particular time.

Assuming negligible dispersion, the orientation of the grey level contours tracing the path of part of the bolus through time and space can be used to estimate the instantaneous velocity at a given position along the vessel, i.e. velocity is equal to $\tan\theta$ where θ is the orientation of the contour.

Colchester and Brunt (1983) used an interactive approach to analyse these images. Instantaneous blood flow velocities were estimated directly from the slope (distance/time) of iso-concentration contours on the concentration-distance-time surface. Each contour was divided into a series of segments, to each of which a straight line was fitted. This was performed interactively by the user. The slope of each segment of each contour provides an estimate of the mean velocity for that time period. To calculate the phasic flow, multiple estimations from different positions in the vessel at a particular time, and at different times for a particular position in the vessel, were generated using this principle. This technique was applied to 2D cineangiographic data, with the assumption that the vessel was straight and running perpendicular to the X-ray beam. However, this is not the case for most blood vessels in the body and to reduce this source of error Colchester et al (1986) described how a 3D reconstruction of the blood vessel centre line from biplane angiograms could be used to estimate path length (Mackay et al 1982; Hawkes et al 1987).

To validate their (Colchester et al 1986) technique a physical model of pulsatile blood flow was set up consisting of a pulsatile peristaltic pump, in series with a 4.2 mm diameter plastic tube and an EMF. However, interactive piecewise linear slope estimation on the parametric (concentration/distance/time) image was very time consuming and subjective. A more objective computer based method was

developed (du Boulay et al 1987) to estimate the grey level contours using a gradient vector operator. The gradient is defined as follows: given a scalar function $f(x,y)$ and a coordinate system with unit vectors **i** in the x-direction and **j** in the y-direction, the gradient is a vector function defined by:

$$\nabla f(x,y) = \mathbf{i}\frac{df(x,y)}{dx} + \mathbf{j}\frac{df(x,y)}{dy} \tag{4.9}$$

where ∇ indicates the vector gradient operator. The vector $\nabla f(x,y)$ defines the direction of maximum upward slope, and its length represents the magnitude of the slope. Important scalar functions are the gradient magnitude and direction given by:

$$|\nabla f(x,y)| = \sqrt{(\frac{df}{dx})^2 + (\frac{df}{dy})^2} \tag{4.10}$$

$$\mathrm{Arg}(\nabla f(x,y)) = \tan^{-1}(\frac{df}{dy}/\frac{df}{dx}) \tag{4.11}$$

The gradient magnitude takes on large values in areas of steep slope. From the above equations the blood velocity V can be calculated as:

$$V = R\tan(\arg(\nabla) + \frac{\pi}{2}) \tag{4.12}$$

where R is the calibration constant dependent on the frame rate, X-ray magnification and image scaling.

Using this principal of parametric images, du Boulay et al (1987) were able to detect the gradient direction and hence the velocity of the contrast material at each time interval. Using a similar phantom to Colchester et al (1986), the accuracy of the technique in comparison with measurements by an EMF was improved from discrepancies of 15% (Colchester et al 1986) to 10% against the EMF reading. However, neither of these techniques exert systematic control over

the extent of the integration of flow estimates in the spatial and temporal dimensions. Also, they can only be applied to a few regions of the contrast boluses, where the concentration gradient is highest. Therefore, it is unlikely that all flow information stored in the parametric image can be extracted.

Wicks (1989) tried to overcome these discrepancies by applying a digital circular gradient operator (Davies 1984). This operator was reported to increase the accuracy of blood flow estimations from the parametric images. The technique was applied to a range of parametric images generated by digitising cine-angiographic film from physical phantom experiments. In comparison with EMF readings, the results were disappointing. This inaccuracy was considered to be due to the limited contrast gradient in the parametric images rather than inaccuracies of the gradient technique. The technique is sensitive to artefacts caused by spatial and temporal variations, such as beam hardening effects and non-uniformities of X-ray exposure.

To overcome problems with current techniques, a novel technique was proposed (Seifalian et al 1988b; 1988c; 1989) to derive pulsatile blood flow by the analysis of time sequences of distance-density curves (profiles of contrast material concentration along the vessel). Full details of the technique are described in chapters 5 and 6.

4.3 METHODS TO MEASURE VESSEL CROSS-SECTIONAL AREA

The volume flow rate is the product of the velocity of blood in the direction of the vessel axis (averaged over the vessel cross-section) and the cross-sectional area of the blood vessel.

Over the past decade various techniques of and approaches to the quantitative analysis of cross-sectional area have been described in the literature. These methods may be divided into two categories. The first approach is geometrical estimation of cross-sectional area. This includes those techniques that compute absolute vessel diameter estimates from angiograms and then calculate cross-sectional area assuming either elliptical or circular cross-sections. The second approach is densitometric estimation of cross-section area, usually obtained by

integrating the image density distribution across the blood vessel.

For the majority of the techniques described here intra-arterial injection of contrast material is carried out through a catheter manually or with a power injector.

4.3.1 Geometric Approaches

Subjective visual estimates of vessel diameter from X-ray angiographic images have been shown to be associated with substantial inter- and intra-observer variability (Detre et al 1975; Zir et al 1976; Fisher et al 1982; see review in Colchester 1984).

Early attempts to assess blood vessel diameter objectively from X-ray films employed mechanical or electromechanical callipers to measure the vessel diameter (Rafflenbeul et al 1980; Chikos et al 1983). Isner and colleagues (1981) compared mechanical calliper measurements of per cent diameter stenosis from cine-film images of the left main coronary artery with post mortem histologic cross-sectional area measurements in 84 angiograms. They observed an under- or over-estimation in 71% of these cases.

Later Scoblionko et al (1984) developed an electronic hand-held calliper wired to a programmable calculator that could be applied directly to projected cine-film images.

Although calliper measurements of percent diameter stenosis improve accuracy and reproducibility relative to subjective interpretation, three important limitations still remain: first, relative narrowing depends on the subjective definition of the 'normal' diameter, which may be complicated by the presence of post-stenotic dilation and/or diffuse disease; secondly, the definition of vessel boundaries is subjective, and is influenced by display contrast and brightness, quantum and structural noise, and radiographic scatter; and finally, single view measurements of diameter, even if accurate, produce erroneous estimates of lumen area for eccentric stenoses. Since the human variability inherent in visual interpretation is unlikely to diminish, callipers have not achieved widespread clinical application.

The logical extension of calliper measurement was the derivation of the digital coordinates from hand tracings of vessel boundaries (Gensini et al 1971; Brown et al 1977). Since the film image is optically magnified prior to tracing, the precision of these techniques is limited only by the inherent resolution of the film and the visual determination of the vessel edges.
Although the accuracy and reproducibility of arterial quantification is improved by digital hand tracing, these measurements are limited by vessel foreshortening, due to non-orthogonal imaging, blood vessel curvature and overlapping blood vessels. These features prevent accurate estimation by these techniques of cross-sectional area from a single projection.

In addition, the projected angiograms of the vascular segment have to be traced manually, and thus the key input data to be analysed by a computer must still be based on a subjective visual interpretation.

To overcome the limitations of these manual procedures, a number of computer assisted arteriographic techniques have been developed to reduce the variability of manual tracing of vascular segments by using computer analysis to provide a more accurate measurement of blood vessel diameter (Brown et al 1986). Using automated edge detection would eliminate subjective bias. The Canny edge detection operator (Canny 1986) is considered to be a very accurate edge detection technique by most computer scientists. As the Canny edge detector is customised to give the highest sensitivity detecting true edges, the lowest sensitivity for detecting false edge and multiply defining a single edge, while monitoring the highest accuracy in edge location. Currently the Canny detector has not been optimised for the blurred semielliptical profiles of blood vessel of the X-ray angiogram. However, at present there is no widely agreed algorithm for finding the true vessel edges. Most computer edge detection programs consist of the following steps:

1) *Operator selection of the blood vessel segment.* This is accomplished by using a mouse controlled cursor to interactively identify the approximate centre line of the vessel segment of interest by defining points along the vessel segment.
2) *Computation of the true vessel centre line.* The majority of techniques

used for accurate definition of vessel diameter require the analysis of cross-sectional profiles of the contrast density obtained perpendicular to the blood vessel axis the transverse density profile (TDP). The TDP is defined as the plot of grey level intensity across the X-ray image in a direction perpendicular to the image of the blood vessel axis after logarithmic transformation of image intensity. Centre line definition permits the acquisition of these profiles for vessels which curve within the image plane.

The TDP of a vessel can be approximated by a Gaussian plot. A method of least squares can then be applied to the profile to estimate the Gaussian parameters. The median of the Gaussian spread could then be used as an estimation of the centre line (Fessler and Macovsky 1991).

Others compute the centre of gravity of the grey level distribution perpendicular to the operator definition centre line. The true position of the vessel centre line is estimated as the locus of this centre of gravity (Reiber et al 1984 and Hawkes et al 1988a).

3) *Automatic detection of the vessel edges*. Previous determination of the true centre line allows extraction and subsequent analysis of cross-sectional densitometric profiles perpendicular to the defined axis. Several empirical algorithms, which calculate the true blood vessel luminal boundaries from these densitometric profiles, have been investigated (Alderman et al 1981; Pfaff et al 1985; Reiber et al 1984; Fujita et al 1987; Hawkes et al 1988a).

The first and most common of these edge detection algorithms finds the peak of the first derivative; i.e. the TDP is differentiated and then used to identify the position of maximum slope identified as the 'edge'. This method assumes that the vessel edges coincide with the positions of greatest intensity change within the densitometric profile (Alderman et al 1981; O'Handley et al 1973). This technique works well for sharp images of larger vessels with circular cross-section, but is less applicable for smaller or diseased vessels because of image blurring which alters the position of the maximum edge gradient, resulting in an underestimation of the true vessel diameter (Pfaff et al 1985). As there is no reason why the actual vessel edge should correspond exactly to the point at the maximum of the first derivative, calibration curves have been employed, which can be obtained with

the help of phantom measurements (Wong et al 1986).

The position of distinct points such as the maximum and minimum second-derivatives has also been investigated (Doriot et al 1985). In this second derivative approach, the edge points tend to be too wide to fit the arterial segment and the inherent sensitivity of the second derivative to noise limits the accuracy and precision of these methods. The ability to reduce this sensitivity to noise by image smoothing is limited since the errors due to blurring will only be increased.

Reiber et al (1984) developed a combined first and second derivative technique to compensate empirically for the observed under- and overestimation of vessel diameter associated with each technique. This technique is empirical in the sense that the row measurements are appropriately weighted to obtain the best correlation between measured and true vessel dimensions. The alternative is to rigorously define the radiographic factors which produce inaccurate measurements and then develop techniques to compensate for these errors. They reported a precision of 120 μm in digitized film images of a phantom when identifying the edge as a weighted sum of the modules of the first and second derivatives.

As described above, methods for determination of cross-sectional area using computerised edge detection techniques require a criterion to define the vessel edge, which may be highly subject to interference by noise, and may depend upon iodine concentration.

4.3.2 Densitometric Approaches

Vessel cross-sectional area may be quantified from the density of contrast material within the vessel lumen. The technique is based on the Lambert-Beer principle, which states that for a homogeneous material, the logarithm of the transmitted radiation is inversely proportional to the thickness of the material. The Lambert-Beer principle is thus:

$$I = I_0 \exp(-\mu t) \tag{4.13}$$

where I is the number of transmitted photons, I_0 the number of incident photons, μ the attenuation coefficient of the material and t=thickness of the material. Assuming I_0 and μ to be constant, Ln(I) is thus proportional to $-t$.

In theory, it should be possible to produce an image proportional to the mass of injected contrast material per unit area by careful densitometric calibration and subtraction of a mask, which removes detail due to superimposed anatomical structures, or by interpolating background image grey values from regions adjacent to the blood vessel image. The integral of a TDP is assumed to be proportional to the true intra-luminal area, irrespective of the shape of the stenosis and independent of system resolution and blur. This assumes that the imaging system is linear, i.e. that after logarithmic transformation the image intensity is proportional to projected thickness of the vessel. Thus, the most important potential advantage of densitometric quantification is the determination of the cross-sectional area of stenoses with complex geometry from a single projection.

Initial studies evaluated vessel contrast obtained from densitometric profiles of cine-film images (Brown et al 1986; Reiber et al 1983). Not only were these techniques laborious from an analytical perspective, but accurate results were dependent upon densitometric calibration. Digital image acquisition and processing, with its inherent computational speed and direct access to digital image matrices, revived interest in densitometric analysis. In addition, plumbicon video tubes have a linear response over the entire dynamic range of image brightness. These characteristics reduced the errors involved in accurate definition of intra-luminal contrast thickness.

Kruger (1981b) and later Simons et al (1986) employed a densitometric technique to calculate the vessel diameter D using digital subtraction angiographic images. The following formula was used

where $S(x)$ is the TDP across the blood vessel and S_{max} is the maximum value

$$D = \frac{4\int S(x)\mathrm{d}x}{\pi(S_{max})} \tag{4.14}$$

along the TDP.

This method assumes a linear relationship between the iodine concentration in a blood vessel and the resulting densitometric value in the subtracted image. However, when this assumption is not satisfied, the measured cross-sectional area depends on the contrast of the vessel. This dependence on vessel contrast is not completely corrected even after empirically determined correction factors have been applied.

Although the densitometric technique is in principle superior to geometric techniques, conventional densitometric techniques have several limitations which have prevented total acceptance of the method. These have been summarised by Hawkes et al (1988a) as follows:

(1) the concentration of contrast material is assumed to be constant along each vessel yet no check is incorporated within the techniques;
(2) the relationship between the image grey level and contrast mass projected along the X-ray beam is assumed to be linear and spatially invariant, but this relationship usually is not checked;
(3) the whole length of the analysed blood vessel segment is assumed to have the same orientation relative to the X-ray beam, but this does not hold for most blood vessels in the body.

To overcome problems with conventional densitometric techniques, Colchester (1984) proposed and validated a novel technique to compute the absolute cross-sectional area (see appendix). In this method the background contribution was subtracted and the grey level in the image was related to the value of contrast material within the arterial lumen. It was shown that the densitometry constant relating the grey level in the image to the volume of contrast material within the arterial lumen could be derived from the data contained within the TDP when circular cross-section vessels were analysed. In vivo, it was assumed that healthy

vessels were circular. However, it has been postulated that if the densitometry constant is obtained from a region of normal vasculature, then this value can be extrapolated down the entire vessel.

Initially this technique was validated from a single projection X-ray angiogram using a baboon skull phantom containing dummy blood vessels with circular cross-section of known sizes ranging from 0.1 to 3.2 mm diameter which were filled with contrast material of known concentration. The estimated diameter (the width of the best-fit ellipse) correlated very well with the known diameter down to 0.50 mm (r=0.998) and the standard deviation of the estimates was 0.03 mm (Colchester 1984).

Further validation in diseased vessels was carried out by Hawkes et al (1988a) using digital cinefilm and conventional film-screen by comparing the method, using a single projection of an X-ray angiogram of the diseased coronary artery, with post mortem histologic cross-sectional area measurements. Similar results were demonstrated (with SEE=0.47 mm^2) by both recording media.

Implementation and further validation of this technique in 3D is described in chapter 5.

4.4 DISCUSSION

Methods to measure flow based solely on the washout portion of contrast densograms must use high frame acquisition rates and the implementation of mathematical corrections to avoid errors caused by (1) perturbation in the tail-ends of the curves, which can be caused by recirculation, and (2) the delaying effects of contrast material itself. In addition such methods require precise volumes of contrast material. As discussed above the main problem with these methods is the assumption of a constant flow rate, whereas the blood flow in arteries is pulsatile, and this introduces an error in the estimation of blood flow.

Several investigators have attempted to determine mean blood flow rates from time-density curves using transport time methods. For steady-flow conditions, accurate flow rates have been calculated by this technique.

However, for pulsatile-flow conditions, the methods based on finding distinct points on the density curve suffer from relatively high inaccuracy, due to both the inaccurate definition of these points and the fact that in pulsatile flow relative times of passage of contrast between two fixed points cannot be used to measure mean flow.

In both indicator dilution and transport time techniques, flow is assumed to be constant during the measurement period and mean flow is determined. However, arterial blood flow is not constant, and significant errors occur in the mean flow determination, by both techniques, when the flow is highly pulsatile.

To overcome this problem, a new strategy has recently arisen for the measurement of the mean and instantaneous pulsatile blood flow using distance-density curves, as opposed to time-density curves, obtained from digital X-ray angiograms.

In principle the new approach should improve the accuracy of the measurement of pulsatile blood flow waveforms. This is due to the fact that the shape of the distance-density curves appears to be relatively consistent over time, whereas there are much greater changes in the shape of the time-density curves as the bolus proceeds through the vessel under pulsatile flow conditions (see figs 4.2 and 4.3). However, the current techniques used to analyse the distance-density curves are prone to error and particularly sensitive to temporal and spatial variations in background densities.

We have proposed a new technique (Seifalian et al 1988b; 1988c; 1989) for deriving pulsatile blood flow by analysis of time sequences of profiles of contrast material concentration along the vessel. The development and validation of this technique and initial clinical application forms a major part of the work presented in this thesis.

Our X-ray angiographic technique estimates vascular blood flow at the time of injection as the contrast material passes through the vessel(s). Many factors affect blood flow readings in a single subject such as recent food uptake, exercise, anxiety, drug therapy, and many others. Without repeat studies,

therefore, our method provides no information on the variation of flow over a period of time. Subject to X-ray and contrast dose limitations our X-ray angiographic technique is repeatable within a single investigation, as long as further injection of the contrast material does not have effects on blood flow. Investigation at another time will require repeat catheterisation with all the risks that will entail.

Lumen cross sectional area measurements are required to convert velocity blood flow measurements to volume blood flow. Quantitative estimation of cross-sectional area commonly incorporates biplanar X-ray angiograms and assumes circular or elliptical cross-section for measurement of vessel cross-sectional area. As described, various investigators have pointed out that these algorithms may not evaluate adequately the severity of generally eccentric cross-sectional stenoses.

An alternative approach to geometric analysis is the densitometric technique which has usually been applied to the estimation of relative cross-sectional area. This technique uses image intensity information for cross-sectional area measurements. Quantification of the amount of contrast material within a lumen by densitometry provides a measure of cross-sectional area that is independent of lumen geometry. Although accurate relative measurements of vessel narrowing have been demonstrated, it appears that absolute measurements require rigorous validation and correction for the predominant sources of densitometric error (Hawkes et al 1988a). In addition spatial calibration, (i.e. estimation of magnification), is necessary to calculate absolute object dimensions from the radiographic image, and may also be subject to measurement error.

In order to overcome problems with conventional densitometric techniques of measurement of cross-sectional area, Colchester (1984) fitted a semi-ellipse model to the TDP and then computed the cross-sectional area as described above. Initial results assuming that the blood vessel lies parallel to the imaging plane were encouraging and our group later overcame the problem of analysing tortuous vessels using 3D reconstructions of the vascular tree from two X-ray views (Hawkes et al 1988a).

In conclusion, it is clear that the densitometric technique provides potentially more accurate results for measuring the cross-sectional area of normal blood vessels and the only possible solution for measuring blood vessels of eccentric or irregular cross-section in which no geometric assumption about the cross-sectional shape can be made.

In this thesis the technique described by Hawkes et al (1988a) has been used to compute cross-sectional area, which is used to convert flow velocity estimates into volume flow rates.

CHAPTER 5

THREE DIMENSIONAL RECONSTRUCTION OF VASCULAR STRUCTURES

5.1 INTRODUCTION

In the previous chapter, a review of techniques for the quantitative measurement of blood flow from X-ray angiographic data has been presented. The instantaneous blood flow rate is equal to the product of the flow velocity and the cross-sectional area of the vessel. The absolute volume flow rate in a vessel can be calculated from measurable parameters as shown in fig. 5.1.

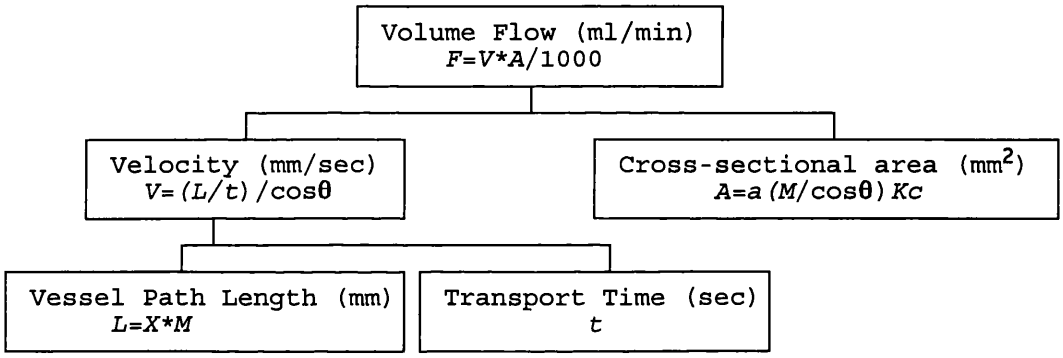

Fig. 5.1. Diagrammatic representation of the factors involved in calculating blood volume flow. *M* and θ are the vessel magnification factor and the orientation of the blood vessel to the X-ray beam axis respectively. *t* is the time taken for the contrast material bolus to move a distance *L* along the vessel. *X* is the apparent length of the vessel segment in pixels. The factor *Kc* is the product of the iodine concentration in the vessel *c* and a densimetric calibration constant *K* which relates the image grey value to the mass of iodine integrated along the X-ray path from X-ray focus to image. The integral of image intensity, *a*, is computed along the transverse density profile after subtraction of a background or mask to remove contributions from overlying and underlying tissues.

The apparent length of the vessel, i.e. as determined from a single X-ray projection, may be measured in terms of pixels, but calculation of the actual path length requires precise determination of the magnification factor M and orientation θ.

To measure true velocity along a tortuous vessel, or vessel that is not oriented parallel to the imaging plane, the angle of the vessel segment relative to the image plane is important, especially when the angle is large (and hence the $\cos\theta$ value is small).

In order to determine the X-ray magnification M and angle θ of the blood vessel to the imaging plane, one needs to deduce the 3D path of the blood vessel.

To reconstruct the 3D path of the blood vessel for this purpose, the possible choices are nuclear magnetic resonance (NMR), X-ray computer tomography (CT) or X-ray radiographic projections. At present NMR is expensive for use in 3D reconstruction purposes and images are not of a sufficiently reliable quality. There has been extensive work done on the reconstruction techniques of 3D paths with imaging modalities based on CT (for example: Pelc and Chester 1979; Ra et al 1982; Albright and Frame 1988) and X-ray projections (Vignaud et al 1979; Castleman 1979; Barnard et al 1980; Suetens et al 1983; Parker et al 1988; Mackay et al 1982; Mol 1984; Hawkes et al 1987; Guggenheim et al 1991).

Reconstruction of the vascular structure could, in principle, be accomplished using convolution back-projection techniques with CT data. Conventional image reconstruction from projections, as performed in standard CT scanners, uses knowledge of the orientation of each projection and the measured X-ray attenuation along each path. Errors in orientation result in significant artefacts such as streaking and blurring (Parker et al 1988). Inconsistencies in density measurements (polychromatic beam hardening, scatter, etc.) also lead to streaks between regions of highly different atomic number (bone, iodine, etc). In addition, as in other radiographic techniques, noise presents a problem in CT. The principal noise source is due to the random distribution of photons in the illuminating beam. This effect is called quantum mottle and arises as a result of the necessary low exposure dosage to the patient.

Finally, the ratio of vessel volume to reconstruction volume is typically very low. Thus, even if the reconstruction process were to be free from artefact, much effort would be wasted in reconstructing non-vascular information.

This chapter deals primarily with 3D reconstruction from X-ray angiographic projections. Initially an overview of the different reconstruction procedures is presented followed by a more detailed description of a technique using digital biplanar X-ray angiographic data. The technique uses computer-assisted analysis of angiographic images together with a knowledge of X-ray imaging geometry to achieve accurate quantitative measurements. The implementation and validation of the technique is described in detail.

Although unambiguous 3D reconstruction from 2D projection data, without prior geometric configuration of the X-ray equipment information, requires many projection images (Parker et al 1988), the 3D relationship of an object can be determined by only two projection images when a specific point on the object can be identified uniquely in both images. There are several methods used for 3D reconstruction of a vascular configuration from biplanar X-ray angiograms.

Stereometry is the technique of deriving a 'range image' from a stereoscopic pair of brightness images. A 'range image' is an image in which grey levels represent not brightness but rather the distance from the X-ray tube to the object points (Vignaud et al 1979; Castleman 1979; Barnard et al 1980; Suetens et al 1983). The key problem in the stereoscopic technique is that of finding the corresponding points between two views. Noise in the images tends to corrupt the correspondence measure.

Successful reconstruction from biplanar X-ray angiograms requires two things. The first is a knowledge of the geometric configuration of the X-ray equipment set-up. The second is the ability to identify the projection of a specific point on the blood vessel, in each of the X-ray biplanar images, in order to calculate the 3D coordinates of the vascular tree. In theory, the first condition can be satisfied if the geometrical relationship between the two views is calculated from the positioning of the X-ray set measured angle noted during the patient investigation. Then the 3D position of each object point that is identifiable in both

images can be determined by a process of 'triangulation', in which a ray is back-projected from the position in each image plane at which the point is found (Dodge et al 1960). The intersection of these two rays then specifies the 3D position of the object point.
However, because of the nature of the investigation, patient safety considerations, radiation exposure risk, and limited time, accuracy of measurements becomes less reliable (Smith and Starmer 1978; Mol 1984). In addition to these errors, when performing a patient study it is often difficult to perform the necessary pre-alignment of the imaging systems required by this technique.

To overcome the inflexibility imposed by pre-alignment requirements, a perspex calibration cube containing steel markers was imaged using the same positioning of the X-ray equipment as was used during acquisition of the angiograms in the patient (Mackay et al 1982; Mol 1984; Hawkes et al 1987; Guggenheim et al 1991). Each X-ray projection could then be fully determined by the relation between the known 3D positions of the markers in the cube, and the coordinates (of the projection of the markers) in the image. The cube calibration has fewer geometrical constraints than the previously described 'triangulation' system. All that is required is that the objects of interest appear in both biplanar projection views.

Some prior knowledge regarding the structure of the object of interest is required. In the case of the 3D reconstruction of the blood vessels, the object is sparse and anatomical knowledge allows for the identification of corresponding points between two projection views.

5.2 METHOD

The relative position of a point in space can be computed if two X-ray images of the point are taken from different views. The principal behind this is that the X-ray imaging can be thought of as a perspective projection and by use of knowledge of the X-ray imaging geometry and the mathematics of projective transformations, the 3D coordinates of points in space can be obtained.

5.2.1 The Transformation Matrix

The geometric mathematics for reconstructing the centreline of vessels from biplanar X-ray angiograms using a cube with steel markers has been presented by Kim et al (1982). This includes mathematical transformation from the object coordinated system to the two projected planes, as well as the principles of matching points in the two views. This technique has also been used by Mackay et al (1982) in the determination of 3D positions during heart motion analysis.

In general perspective projection of a 3D object can be fully described in homogenous coordinates by a 4*3 transformation matrix (Mackay et al 1982; Mol 1984; Hawkes et al 1987; Rogers and Adams 1990):

$$(x,y,z,1)*\mathbf{T}=S(u,v,1) \tag{5.1}$$

where:

x,y,z are the cartesian coordinates of a point in the object space,

u,v are the image coordinates on the projected digital image of the above point,

T is the (4*3) matrix describing the transformation from 3D space to 2D projections.

S is a scale factor depending on (*x,y,z*) and **T**,

The matrix **T** describes the complete transformation from actual 3D positions, imaged from any arbitrarily placed X-ray source, to an arbitrarily oriented image intensifier screen. The method will also correctly handle the subsequent photography of the image intensifier image and the digitisation (also with arbitrary scales and orientations).

The matrix, **T,** is a 4*3 matrix in order to describe the magnification effects of perspective projection (a 3*3 matrix would be adequate to describe orthogonal projection).

5.2.2 Determination of the Transformation Matrix

By eliminating S in matrix equation (5.1), we obtain the following two equations:

$$x(t_{11}-t_{13}u)+y(t_{21}-t_{23}u)+z(t_{31}-t_{33}u)+t_{41}-t_{43}u=0 \tag{5.2}$$

$$x(t_{12}-t_{13}v)+y(t_{22}-t_{23}v)+z(t_{32}-t_{33}v)+t_{42}-t_{43}v=0 \tag{5.3}$$

If the 3D coordinates of points and their corresponding 2D coordinates on the two different projection planes are known, the elements $t(i,j)$ of the transformation matrix can be obtained from equations (5.2) and (5.3). Since the transformation matrix contains 11 elements, six control points of known coordinates (x_i, y_i, z_i) (i=1, 2, 3, 4, 5, 6), and the 2D coordinates (u,v) of their projected points in two images are sufficient to establish the 12 simultaneous equation from (5.2) and (5.3), which are solved to obtain the transformation matrix. The obtained solutions, $t(i,j)$ values, are the characteristic parameters describing the projection of arbitrary points in 2D plane to the 3D space. Since, in practice, the available coordinates are never exact, the system of 12 equation may be solved by an approximation technique (such as least squares).

A perspex cube containing small steel balls at each corner and the centre of each face was constructed (Mackay et al 1982; Mol 1984; Hawkes et al 1987). The cube, has fourteen steel markers (0.2 mm cross-section) of known relative position embedded at each corner and the centre of each side of a 60 mm cube (fig. 5.2). The cube is imaged just after the patient is examined with exactly the same X-ray gantry positions as those used for the patient. From the measured 2D coordinates on these two images and the known 3D coordinates of each steel marker, the projective transformation matrices for the biplanar angiograms are obtained.

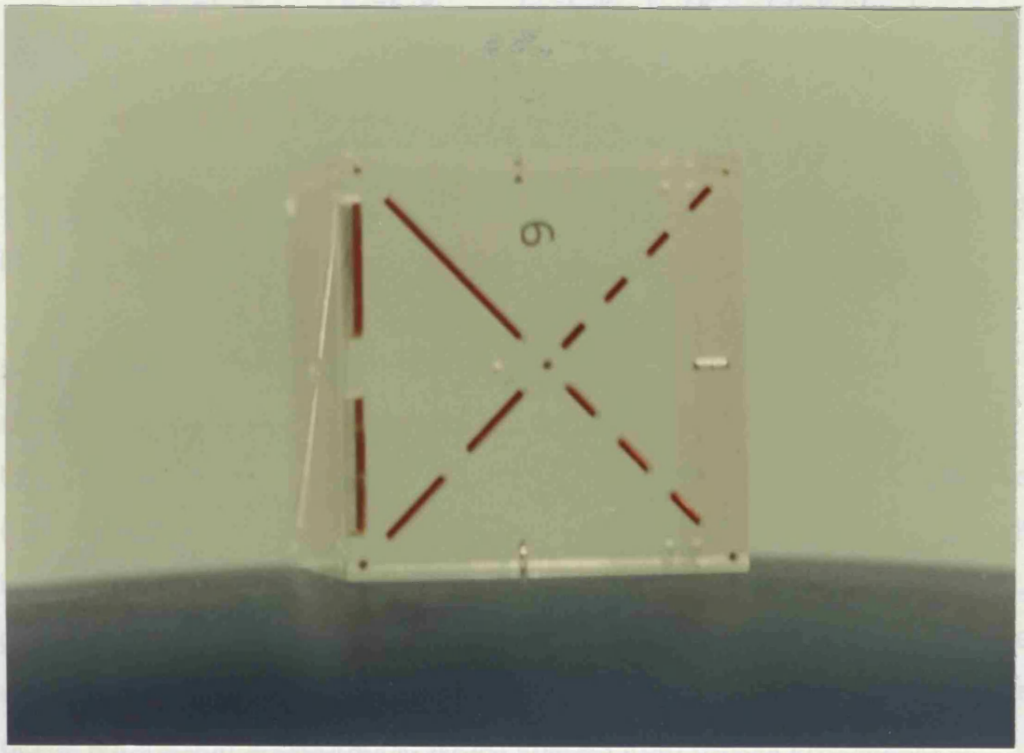

Fig. 5.2. The perspex calibration cube.

5.2.3 Reconstruction of 3D Skeleton

The relationship between a 3D point of interest and its projected 2D points in two views, (u_1,v_1) and (u_2,v_2) is given by the following equations (from equations (5.2) and (5.3)):

$$\begin{pmatrix} t_{11}-t_{13}u_1 & t_{21}-t_{23}u_1 & t_{31}-t_{33}u_1 \\ t_{12}-t_{13}v_1 & t_{22}-t_{23}v_1 & t_{32}-t_{33}v_1 \\ s_{11}-s_{13}u_2 & s_{21}-s_{23}u_2 & s_{31}-s_{33}u_2 \\ s_{12}-s_{13}v_2 & s_{22}-s_{23}v_2 & s_{32}-s_{33}v_2 \end{pmatrix} * \begin{pmatrix} x \\ y \\ z \end{pmatrix} = \begin{pmatrix} t_{43}u_1-t_{41} \\ t_{43}v_1-t_{42} \\ s_{43}u_2-s_{41} \\ s_{43}v_2-s_{42} \end{pmatrix} \quad (5.4)$$

This matrix of four equations contains only three unknowns, x, y and z, and the least squares solution is found.

5.3 IMPLEMENTATION OF THE TECHNIQUE

Using this principal, a system for angiographic reconstruction and analysis (SARA) was implemented (by C R Hardingham, Guy's Hospital) for digital biplanar X-ray angiographic images. SARA was programmed in 'C' on a SUN graphics workstation using the UNIX operating system, in the SUN View windowing environment, and applied to images of blood flow phantoms and digital subtraction angiographic (DSA) images from clinical investigations.

5.4 RADIOGRAPHY

All the 2D X-ray data was acquired on the Siemens Digitron II DSA system. Phantom images, used for validation and flow studies, were obtained with a tube voltage between 70 and 80 Kvp, with a small focal spot, in the pulsed X-ray exposure mode. The digital image grey values, proportional to the logarithm of the X-ray image brightness, were recorded. For the phantom experiments the X-ray beam was filtered by an additional 1 mm thickness of copper. The digital images were acquired at 512x512 pixels/frame, with 10 bits per pixel, and stored unsubtracted. A rate of 25 frames/second was used for the flow studies.

The phantom was positioned at the iso-centre of the 'C-arm' gantry of the unit, and the views obtained corresponded to the '45° left anterior oblique projection'

(LAO projection) and the '45° right anterior oblique projection' (RAO projection). Although the reconstruction method does not require that the two projections be orthogonally related, such projections are usually selected for simplicity. The transformation equations were again computed using the 60 mm perspex cube, with the 14 steel markers. Images were acquired with the X-ray equipment in the same positions, as during the study.

All these images were then transferred via the Ethernet Interface on the Digitron, to the VAX 11-750 attached to the NMR scanner (at Guy's Hospital) using the Decnet Ethernet protocol. They were subsequently transferred via the same Ethernet network to the SUN computers, using SUN software and the DecNet interface (DNI). All images were converted to a common image format, and corresponding cube and phantom images combined under one header to form a single image file.

5.5 3D RECONSTRUCTION OF THE ARTERIAL TREE USING A SYSTEM FOR ANGIOGRAPHIC RECONSTRUCTION AND ANALYSIS (SARA)

The initial stage of the reconstruction involved the estimation of the transformation matrices relating a point in the 2D image plane to a point in 3D space. A corresponding pair of cube images was displayed and six or more steel ball markers on the cube were manually identified by a mouse-controlled cursor on the screen (fig. 5.3). The program SARA computes the centre of gravity of the ball-bearing markers in order to determine these points accurately. The average square error of selected points is displayed to confirm the identification of the right points. To estimate the average square error, SARA first calculates the projection of a user defined point using a transformation matrix, then the sum of square errors is calculated as the sum square of (user defined point - actual value). From a knowledge of the dimensions of the cube, and a combination of the 2D coordinate information of each marker from the two biplanar views, the transformation matrices were computed.

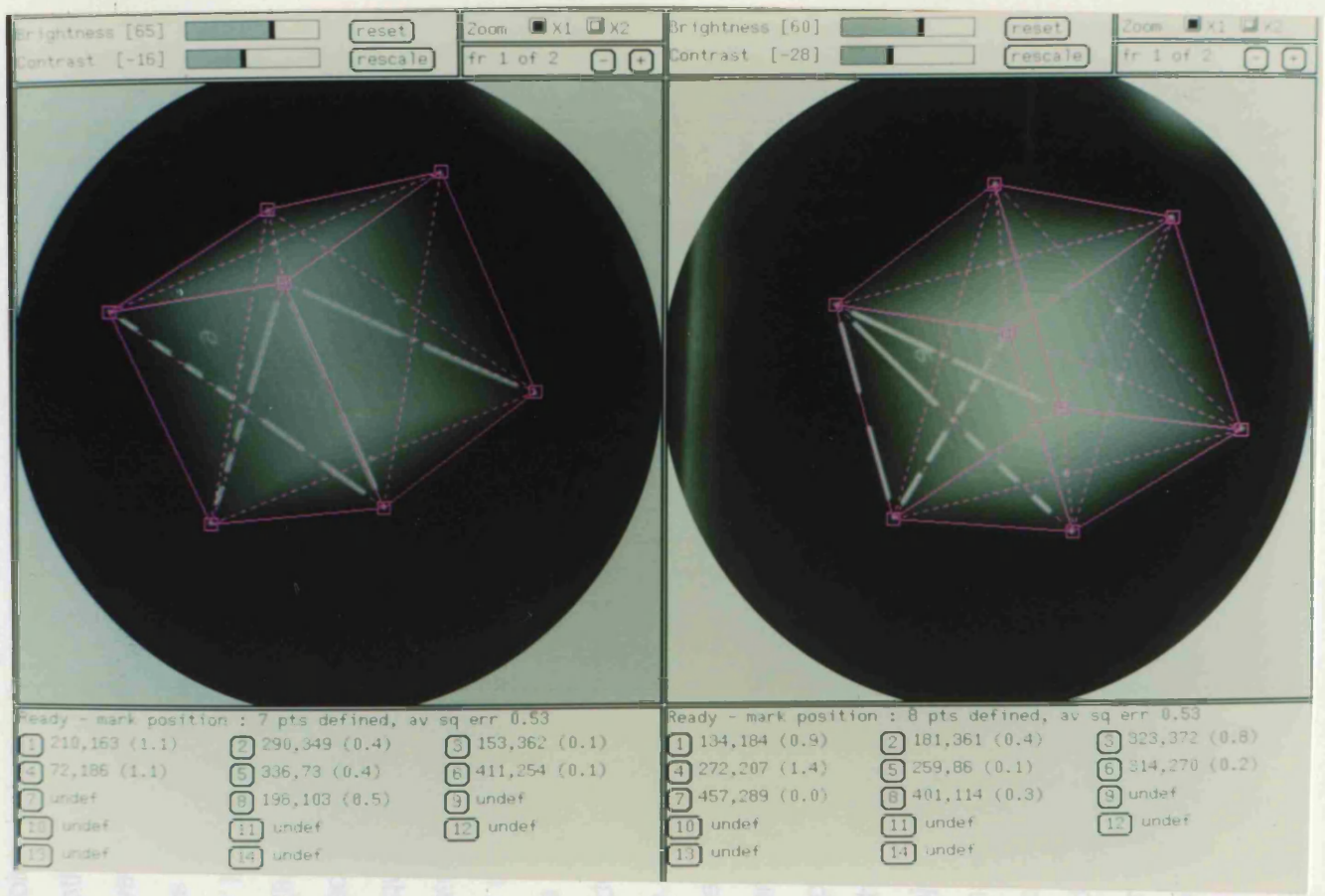

Fig. 5.3. A pair of X-ray images of the cube with graphical superimposition of the cube lines showing the generation of the transformation matrices.

5.5.1 Identification of Corresponding Points Between Two Projection Views

The 3D coordinates of a point can be found from two biplanar X-ray angiograms, after computation of the transformation matrices, by identifying the point on both views. A structure may be delineated by the identification of a set of corresponding points between the two projection views. If the structure under investigation is rather complex then this identification is not an easy task. The operator can however obtain some program assistance with this. As soon as the operator indicates the projection of a point in one view, the program is able to draw an 'epipolar' line in the second view on which the projection of the point has to be positioned (fig. 5.4). The existence of such a line and its actual location can be derived from equations (5.4). These equations represent an over determined system of four equations and three unknowns. If one of the rows of equation (5.4) was eliminated, it would still be possible to solve for (x,y,z). In the 3D reconstruction of the vascular tree, the centre-line is mapped out on a set of points: where the vessel centre line point $Q_1(u_1,v_1)$ in the one projected view image corresponds to the vessel centre line point $Q_2(u_2,v_2)$ in the other projected image. In practice, using the epipolar line for the identification of the blood vessel has proved to be an extremely useful aid. This feature was implemented in SARA; indication of the projection of a landmark by the operator in one view is followed immediately by a program-identified epipolar line in the second view, along which the projection of the same landmark must lie. The operator is required to identify and track the projection of a stretch of artery in each of the two biplanar views and, as the landmark here is a length of artery, the identification of the points on the epipolar line is a fairly simple task. In SARA, corresponding points in the two tracked lines are determined as follows. Starting from the first point of the first line (u_1,v_1) (fig. 5.5) an epipolar line in the second view is calculated. Subsequently, the intersection of this epipolar line with the drawn line in the second view is determined. This intersection is indicated by (u_2,v_2) in the second view. The matching 3D position of the point is then calculated according to equation (5.4) and the process is repeated for the second point in either the first or second view. This is continued until a complete series of 3D points is obtained, representing the structure of the identified artery.

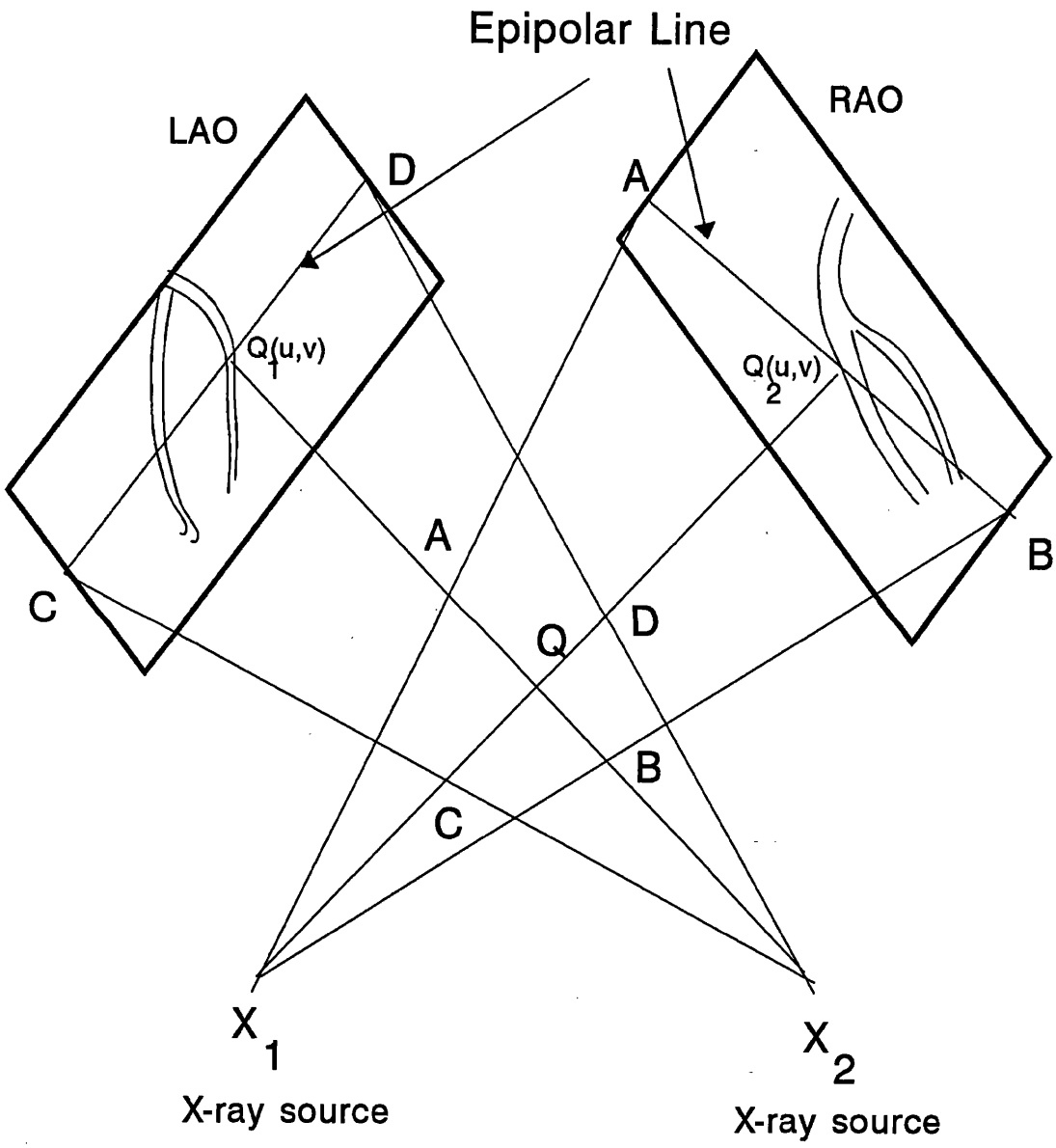

Fig. 5.4. Graphic explanation of the definition of the epipolar line.

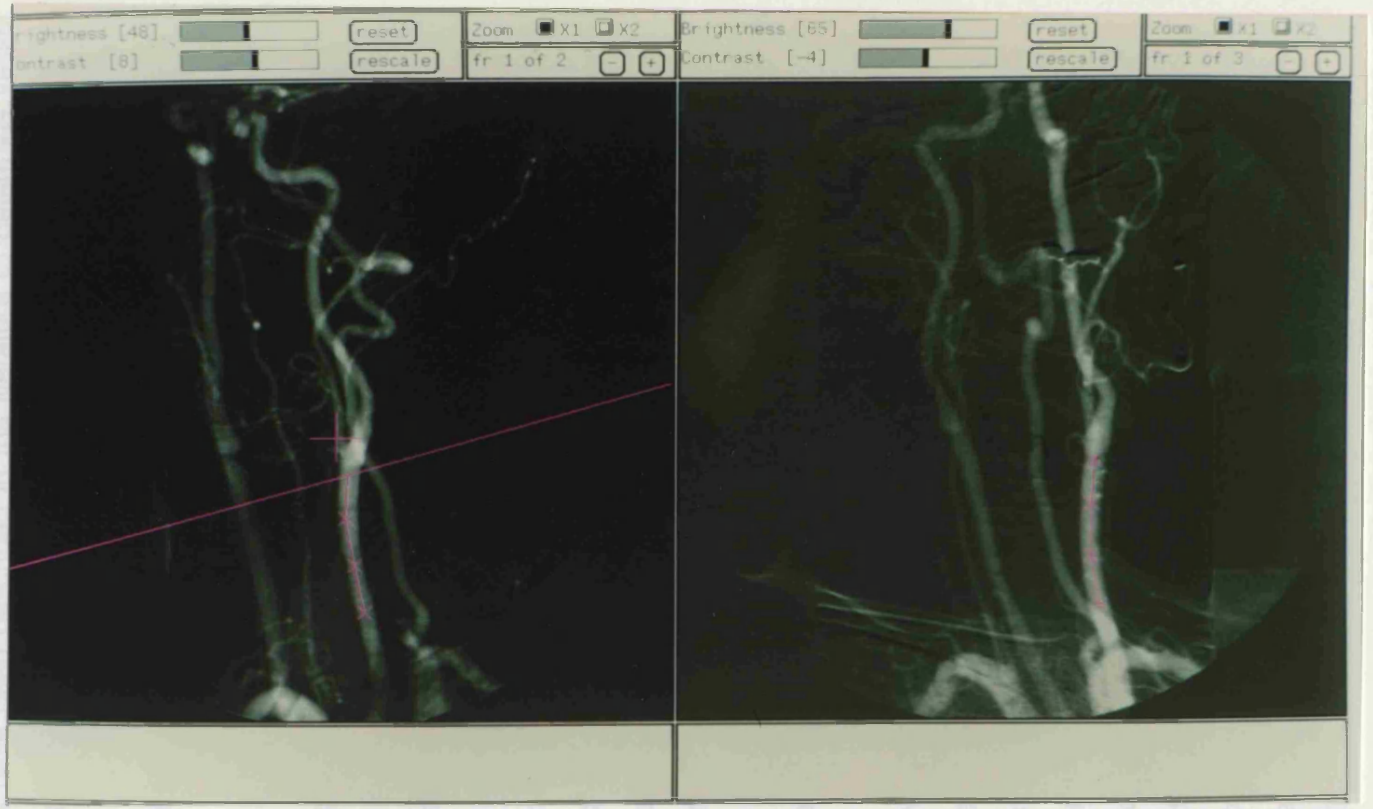

Fig. 5.5. Example of a landmark indicated in the right-hand view, plus the matching epipolar line in the left-hand view, on which the corresponding projection has to be located. The images represent the feeding vessel to the cerebral circulation of a patient in table 9.1 (MB).

From the 3D location of points on the vessel centre line, the precise geometric magnification factor relating the vessel of interest to the computer image, the angle between the vessel long axis and the imaging plane, and the vascular path length between selected points were calculated by SARA.

Various algorithms have been described in the literature to determine vessel edges from X-ray angiographic images (see chapter 4). In the previous chapter an edge detection technique was described for single X-ray projection (Reiber et al 1984). The same technique has been incorporated in SARA for use on biplanar data.

An interactive program was implemented by SARA to detect the edges of an identified segment of blood vessel. The program operated as follows. The sum of about 20 frames of mask subtracted images were calculated. A region was marked to include the blood vessel under consideration but to exclude artefact, crossing vessels, nearby vessels and bifurcating vessels. This ensures that the region used to calculate the residual background grey level contribution contains only valid data. The following procedures were used to outline the centre line and edges of the blood vessel.

5.5.2 Blood Vessel Centre Line Definition

As described above an observer uses a mouse cursor to identify interactively the approximate centre line of the vessel segment of interest by defining points along the vessel segment. As the centre line definition need only be approximate, this step may be performed rapidly. The system then joins successive points with a straight line. It also draws two lines parallel to this line that can be adjusted manually at the sides of the vessel to provide boundaries for calculation of the centre line and to search for the vessel edge. The system samples points perpendicular to each straight line and computes the centre of gravity of the grey level distribution. The updated position of the vessel centre line is taken as the locus of this centre of gravity. A smooth line is calculated to go through these centre line locations. The resulting centre line is displayed to the user and can be modified if necessary.

Although the centre line was only used as a guideline to generate the two boundaries parallel to the vessel, the exact location along the vessel is not critical. Tests performed on several types of vessel showed that the edge detection is not affected by the position of the centre line even if it does not follow the vessel exactly, as long as the boundaries generated parallel to this line are adequately spaced to include all of the segment of the vessel to be analysed. The number of points selected by the user along the vessel can be as few as two or three for relatively straight vessels (such as common femoral artery, see fig. 9.1) with many more for more tortuous vessels.

5.5.3 Calculation of the Edges of a Blood Vessel

The image was sampled along perpendiculars to the new centre line to yield the transverse density profile (TDP). The edges were computed by combining the results of two edge operators, the first and second derivative of the TDP. Since the first derivative operator tends to underestimate the actual edge position and the second derivative operator tends to overestimate the actual edge position (see fig. 5.6), it seems reasonable that a combination of the two operators would approximate the correct position. We chose the position where the sum of the moduli of the first and second derivatives of the TDP was a maximum. This was the same criterion as that made by Reiber et al (1984).

Temporal subtraction generally removes underlying and overlying unwanted structure (i.e. tissue, bone etc). In the physical flow phantom models, the residual background after subtraction is uniform and close to zero, and thus a simple average value for a representative region adjacent to the vessel is adequate for subtraction of any residual background. In clinical studies these residual background values are not uniform, due for example to patient movement during acquisition of the X-ray angiogram. This residual background was subtracted by linear interpolation of the average grey value of up to 4 pixels, starting 3 pixels outside the estimated edge point along the perpendicular to the vessel centre line. Invalid data were excluded from this calculation. If there were no background points of valid data then the previous background value was taken.

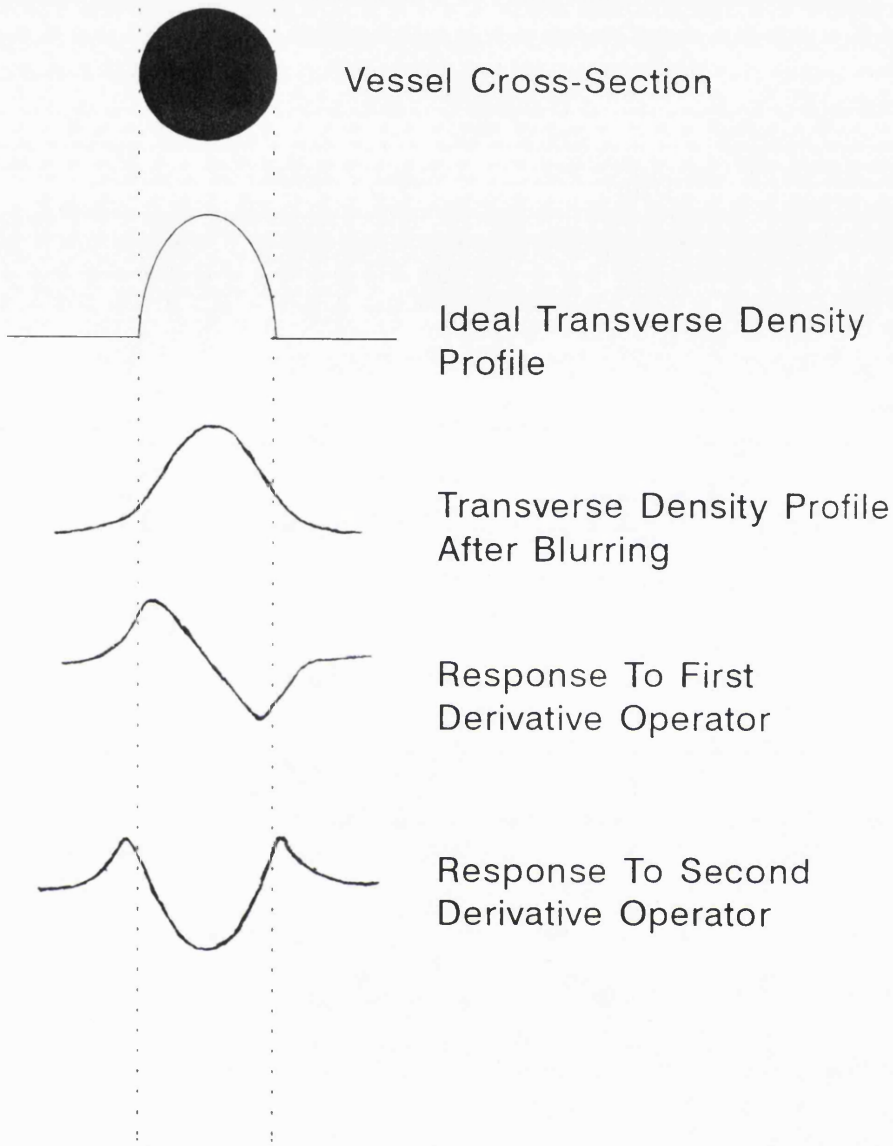

Fig. 5.6. Schematic drawing shows how image blur affects automatic vessel edge detection. The maximum responses of the first derivative operator underestimate the actual edge position while the maximum responses of the second derivative operator overestimate the actual edge position.

The edge points of the blood vessel were then calculated. A second order polynomial was fitted successively to 3, 5 or 7 points of the TDP and the first and second differentials of these fitted functions were computed for each point along the TDP. The edge was identified as the positions on each side of the centre line where the sum of the moduli of the first and second differentials was a maximum. Finally, the edge point locations were averaged by median filtering, which removes individually significant erroneous points (fig. 5.7).

5.6 CROSS-SECTIONAL AREA ESTIMATION

To compute volume flow from velocity the vessel cross-sectional area is required and to measure this we used a densitometric method, which we have described previously by Colchester 1984 and Hawkes et al 1988 (see appendix for details). In brief the technique is based on image densitometry in which the integral of image intensity *a* is computed along a profile perpendicular to the projection of the vessel axis. The true cross-section *A* is related to the densitometric measure *a* by (see fig. 5.8):

$$A=a\left(\frac{\cos\theta}{M}\right)\left(\frac{1}{Kc}\right) \tag{5.5}$$

The X-ray magnification factor *M* and angle θ between the vessel axis and the X-ray axis are computed from the 3D reconstruction of the vascular configuration from two views. The remaining term is the product of the iodine concentration in the vessel *c* and a densitometric calibration constant *K* which relates the image grey value to the mass of iodine integrated along the X-ray path from X-ray focus to image. These were obtained from data generated from 3D reconstructions of biplanar X-ray angiographic data.

5.7 VALIDATION OF SARA

With regards to the quantitative characterisation of the 3D reconstruction of the vascular structure using SARA, series of validation has been conducted.

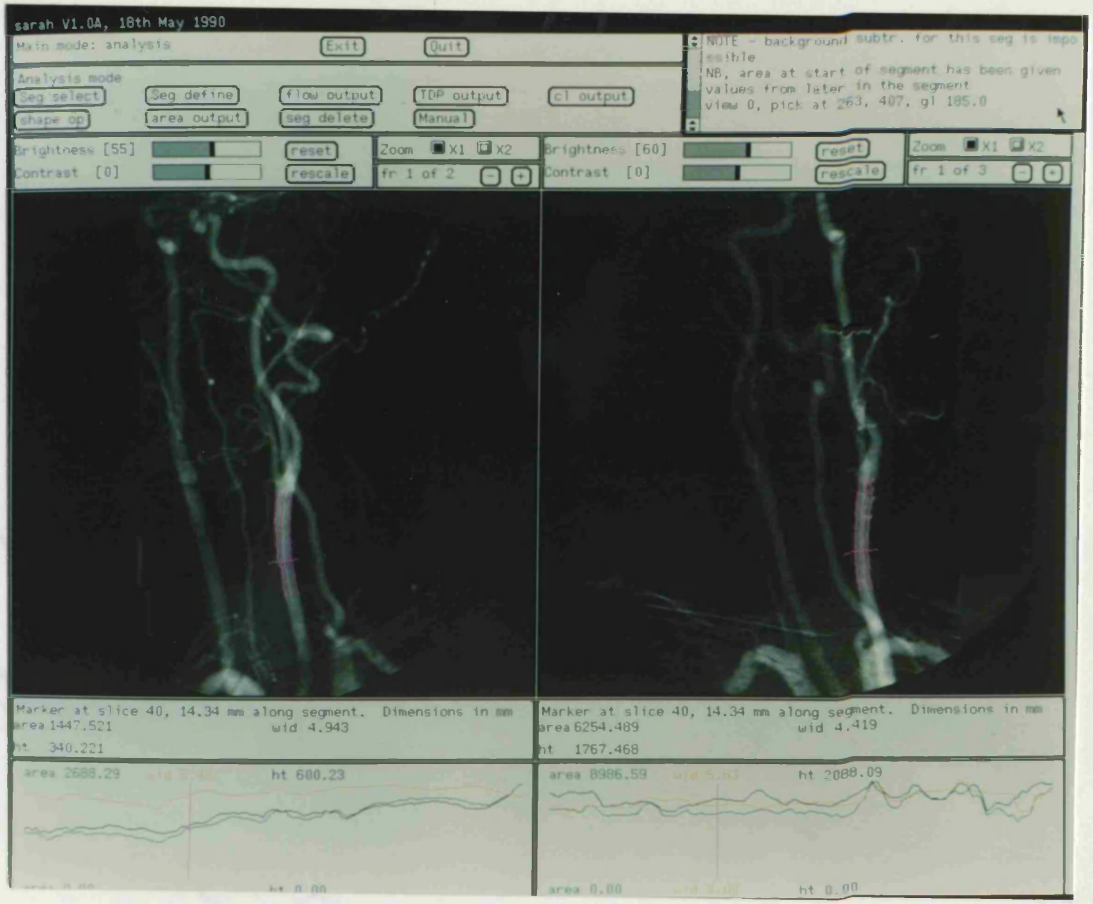

Fig. 5.7. A biplanar digital X-ray angiogram of the aortic arch and the major arteries leading towards the head, with the detected edges superimposed on the angiograms (see table 9.1, patient MB).

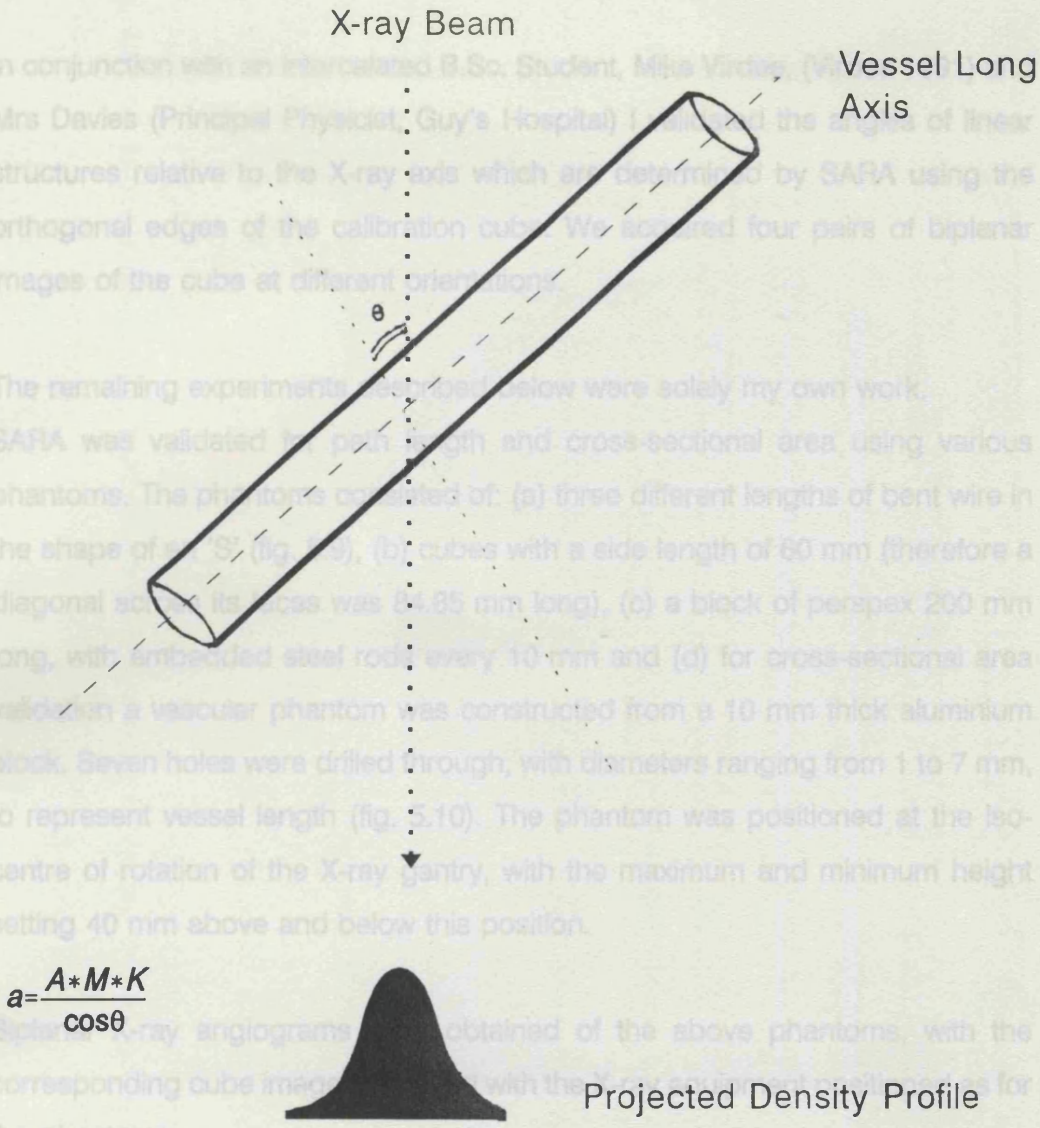

Fig. 5.8. The true cross-section *A* is related to the integral of image intensity *a* along a profile perpendicular to the projection of the vessel axis. The X-ray magnification factor *M*, angle θ between the vessel axis and the X-ray axis, and densimetric calibration constant *K* are computed from the 3D reconstruction of the vascular configuration.

5.7.1 Method and Materials

In conjunction with an intercalated B.Sc. Student, Mike Virdee, (Virdee 1991) and Mrs Davies (Principal Physicist, Guy's Hospital) I validated the angles of linear structures relative to the X-ray axis which are determined by SARA using the orthogonal edges of the calibration cube. We acquired four pairs of biplanar images of the cube at different orientations.

The remaining experiments described below were solely my own work.
SARA was validated for path length and cross-sectional area using various phantoms. The phantoms consisted of: (a) three different lengths of bent wire in the shape of an 'S' (fig. 5.9), (b) cubes with a side length of 60 mm (therefore a diagonal across its faces was 84.85 mm long), (c) a block of perspex 200 mm long, with embedded steel rods every 10 mm and (d) for cross-sectional area validation a vascular phantom was constructed from a 10 mm thick aluminium block. Seven holes were drilled through, with diameters ranging from 1 to 7 mm, to represent vessel length (fig. 5.10). The phantom was positioned at the iso-centre of rotation of the X-ray gantry, with the maximum and minimum height setting 40 mm above and below this position.

Biplanar X-ray angiograms were obtained of the above phantoms, with the corresponding cube images acquired with the X-ray equipment positioned as for the phantoms.

The effects of pincushion distortion were measured by imaging a metallic square grid and the typical pincushion distortion measured at the edge of a Siemens Digitron II digital subtraction angiographic 400 mm image intensifier was about 1%.

5.7.2 Analysis

The standard calibration procedure (as described above) was followed using a pair of cube images. It was ensured that the average squared error computed by SARA from the least squares solution of equations 5.2 and 5.3 was small when marking the steel points of the cube. Then the biplanar phantom images

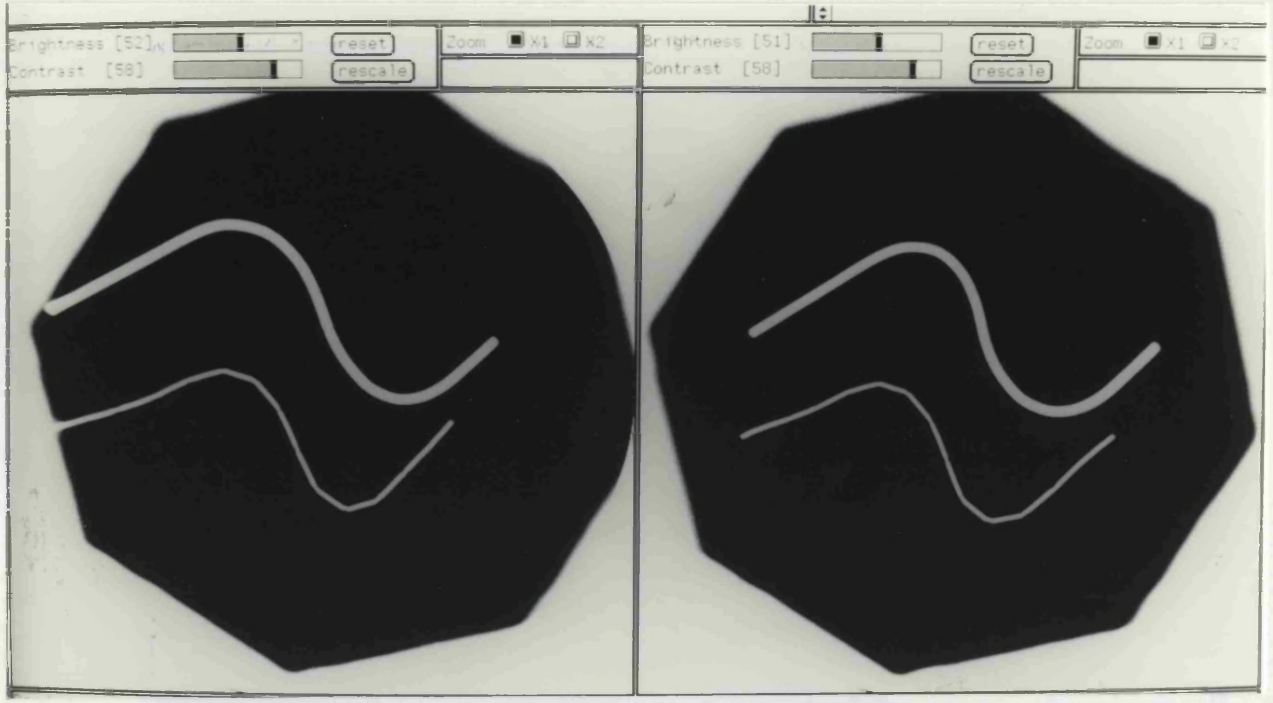

Fig. 5.9. Biplanar views of S' shape wire phantom used to assess the accuracy of path length.

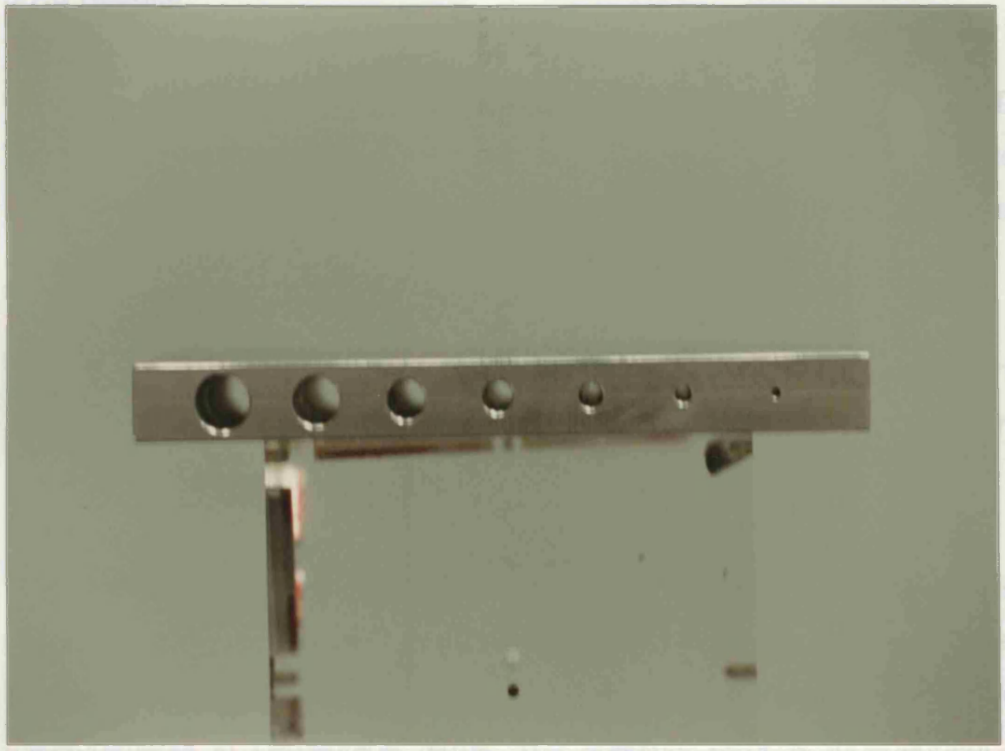

Fig. 5.10. Aluminium phantom used in the validation of the cross-sectional area study.

were displayed and the approximate centre line of the object to be reconstructed was identified interactively. As described above SARA then automatically computes the 3D path length. This was repeated up to seven times for each experiment. For each set of data, a mean, SD, standard error of the mean (SEM) (this is calculated as SD/square root of number of data points), and percentage error (i.e. 100*((actual value - measured value)/actual value)) were calculated.

5.7.3 Results

The mean angle between orthogonal sides was 90.08°±0.67° (mean ± 1 SD). The largest measured error was 1.6° and the mean error of -0.08° was calculated from 16 measurements. The mean percentage error in the angle measurement was -0.1%.

Table 5.1 shows the results of the path length experiments. They show that straight or curved path lengths can be measured with typically a 1.2% error ranging from -0.2 to -2.5 mm (-0.3 to 2.4%).

The absolute cross-sectional areas of the vessels are compared with the true cross-sectional areas in table 5.2, with ± 1 SD for each mean value. As expected, the bigger the diameter the more accurate are the cross-sectional area measurements in percentage terms. The absolute error is independent of diameter and lies within a range of 0 to 0.6 mm^2.

The results of this validation demonstrate that SARA can compute the angle, magnification, path length and cross-sectional area with sufficient accuracy to proceed with flow measurements calculated from data collected on a '3D' phantom (chapter 8) and clinical data (chapter 9).

5.8 DISCUSSION AND CONCLUSION

In order to deduce true velocities along a tortuous vessel, or vessel that is not oriented parallel to the imaging plane, a 3D reconstructed path length of identified blood vessel segments is required.

Table 5.1. Computation of path length measurements after 3D reconstruction.

Path Length Experiment	Actual Mean Length±SD (mm)	SEM (mm)	Measured Mean Length±SD (mm)	SEM (mm)	Number of Measurements	Actual Error (mm)	% Error
S shaped copper wire	140.1±0.2	0.1	142.3±0.7	0.3	7	-2.2	-1.6
S shaped copper wire	178.3±0.5	0.2	180.8±1.1	0.4	7	-2.5	-1.4
S shaped lead wire	159.8±0.7	0.3	161.9±1.4	0.5	7	-2.1	-1.3
Cube side (A)	60.0		61.0±0.8	0.3	6	-1.0	-1.7
Cube diagonal (A)	84.9		82.9±1.0	0.4	6	2.0	2.4
Cube side (B)	60.0		60.2±0.2	0.1	6	-0.2	-0.3
Cube diagonal (B)	84.9		85.2±0.7	-0.3	6	-0.3	-0.4
Perspex block	10-180		10.7-180.3		36	0.4	-0.9

Table 5.2. Table of the computation of the cross-sectional area *A* of holes drilled in aluminium block.

Diameter (mm)	Actual Cross-Sectional Area (mm^2)	Computed Cross-Sectional Area $A \pm SD$ (mm^2)			No. of Samples Along Image of Hole	Actual Error in A(mm^2)	% Error in A
		LAO View	RAO View	Average			
7	38.5	34.0±1.1	41.8±1.2	37.9±0.8	160	0.6	1.6
6	28.3	27.4±0.6	28.5±0.8	28.0±0.5	160	0.3	1.1
5	19.6	18.1±1.0	21.0±0.6	19.6±0.6	160	0.0	0.0
4	12.6	12.9±0.9	13.2±0.6	13.1±0.5	160	-0.5	-4.0
3	7.1	7.3±1.3	7.7±0.8	7.5±0.9	160	-0.4	-5.6
2	3.1	3.1±0.6	3.5±0.6	3.3±0.4	160	-0.2	-6.5
1	0.8	1.3±1.0	1.6±0.8	1.4±0.7	160	-0.6	-75.0

A 3D vascular tree reconstruction technique was implemented on a SUN Graphics workstation in SUN View. The use of the cube calibration method allowed satisfactory reconstruction of the 3D course of the vessel centre line 'in-vivo', and was validated in phantom studies. The 3D location of the blood vessel centre line permitted the computation of the radiographic magnification, the angle between the X-ray beams, and the true vessel path length.

The results from the validation of our program SARA showed that the error in the calculation of the path lengths (see table 5.1) was very small. There is a small systematic underestimation which was probably due to sampling effects along the tortuous wire. The accuracy is, nevertheless, more than adequate for our purposes.

The accuracy of the measurement of cross-sectional area "in-vivo" cannot be assessed, due to the lack of good independent standards that can be employed in humans. Error will be higher because of several further degrading factors involved. The imaging conditions are less favourable due to variable beam hardening effects caused by background tissues and bone, effects of patient movement, inadequate mixing of contrast material in the vessel of interest, and frame by frame variation in X-ray exposure.

These validation procedures provided sufficient evidence that SARA could accurately determine the 3D structure of objects recovered from biplanar images. Errors in calculating angles and path lengths were typically small and at a level of accuracy that would be sufficient in experimental and clinical applications of the study of blood flow.

In chapter 8, description given how SARA can be used to generate parametric images from biplanar dynamic X-ray angiographic data and to validate the volume blood flow measurement technique described in chapter 6. Examples of the clinical applications of SARA will be presented in chapter 9.

CHAPTER 6

A NEW TECHNIQUE FOR DERIVING PULSATILE BLOOD FLOW WAVEFORMS

6.1 INTRODUCTION

From the review of the literature outlined in chapter 4, it is apparent that there has been difficulty in determining accurately the rate of blood flow using X-ray angiographic data. Although numerous publications have shown their potential they have not been widely used, due in part, as discussed in the previous chapter, to the use of inappropriate algorithms to process the image data.

To overcome these problems, I pursued the development of a new digital X-ray angiographic technique (Seifalian et al 1988b; 1988c; 1989) for determining pulsatile flow waveform patterns from dynamic X-ray angiographic data, an example series of these 2D dynamic digital X-ray angiographic images is shown in fig. 6.1. These images were acquired using the physical flow phantom described in chapter 8. The tube calibre was 6.6 mm with a mean blood flow of 349 ml/min. The images show the leading edge of the bolus travelling upwards along the tube. Instantaneous blood velocities were estimated by generating a 'parametric image' from dynamic angiographic images in which the parametric image grey-level represented contrast material concentration as a function of time and distance along a vessel segment (Colchester and Brunt 1983; Colchester 1984; Seifalian et al 1989).

In this chapter the concept, and method of generation, of the parametric images will be described, and the novel method of extracting blood flow waveforms from these images will be presented.

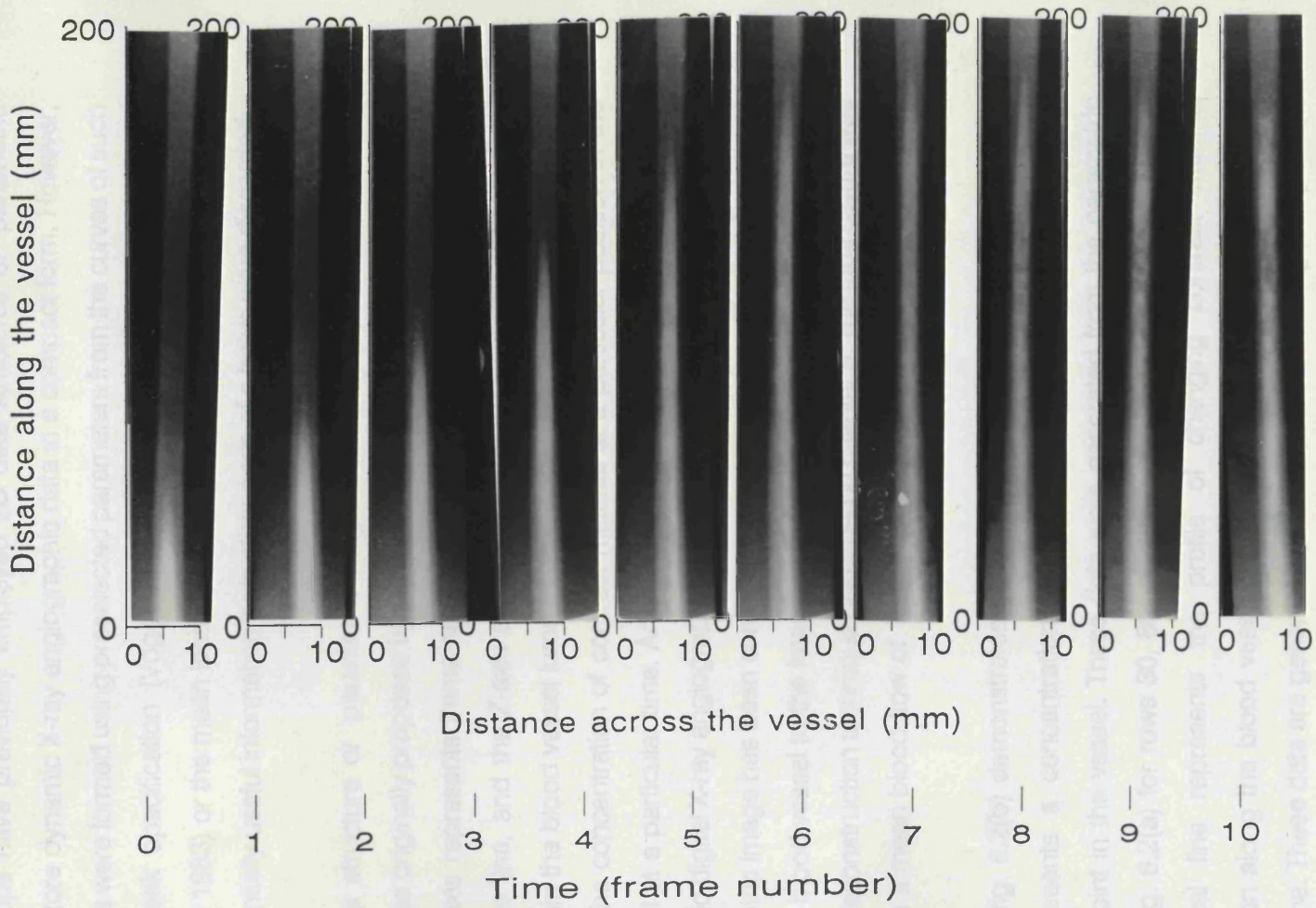

Fig. 6.1. Example of a series of 2D dynamic digital X-ray angiographic images. These images were acquired using the physical flow phantom described in chapter 8. The tube calibre was 6.6 mm with a mean blood flow of 349 ml/min. Images were acquired at a rate of 25 frames per second.

6.2 THEORY

6.2.1 Concept of Parametric Images

Several groups have previously employed 2D data structures or 'parametric images' to store dynamic X-ray angiographic data in a compact form. However, these images were formed using preselected parameters from the curves of such things as peak opacification (Vogel et al 1982), contrast peak arrival times (Kruger et al 1983) or the mean leading edge concentration (Höhne et al 1978). Hence, potentially useful information from other parts of a bolus were discarded.

The 2D data structure or 'parametric image' used to extract the blood flow waveform was originally proposed by Colchester and Brunt (1983). Viewed in this way, the *X*-axis represents frame number (time), the *Y*-axis distance along the vessel centre line, and the *Z*-axis or grey scale the concentration of contrast material within the blood vessel lumen. Thus, each pixel in the parametric image represents the concentration of contrast material at a particular position in the blood vessel at a particular time. An example of a parametric image generated from dynamic digital X-ray angiographic experimental data is shown in fig. 6.2(a). This parametric image has been corrected for the X-ray magnification factor and angle of the blood vessel to the imaging plane using biplanar X-ray angiograms and the 3D reconstruction technique described in chapter 5. The tube calibre was 4.0 mm with a mean blood flow of 176 ml/min.

The plot in fig. 6.2(b) demonstrates that each horizontal line of the parametric image represents a concentration-time (time-density) curve recorded at a particular point in the vessel. These data were generated from the parametric images in fig. 6.2(a) for rows 30, 80, and 150 mm. Fig. 6.3 demonstrates that each vertical line represents the profile of changing contrast material concentration along the blood vessel (distance-density curves) at a particular instant in time. These data are generated from the parametric image in fig. 6.2(a) for columns 25 and 26 (1 and 1.04 seconds).

The parametric image was adopted as a compact representation which contained the relevant information from the X-ray angiographic data.

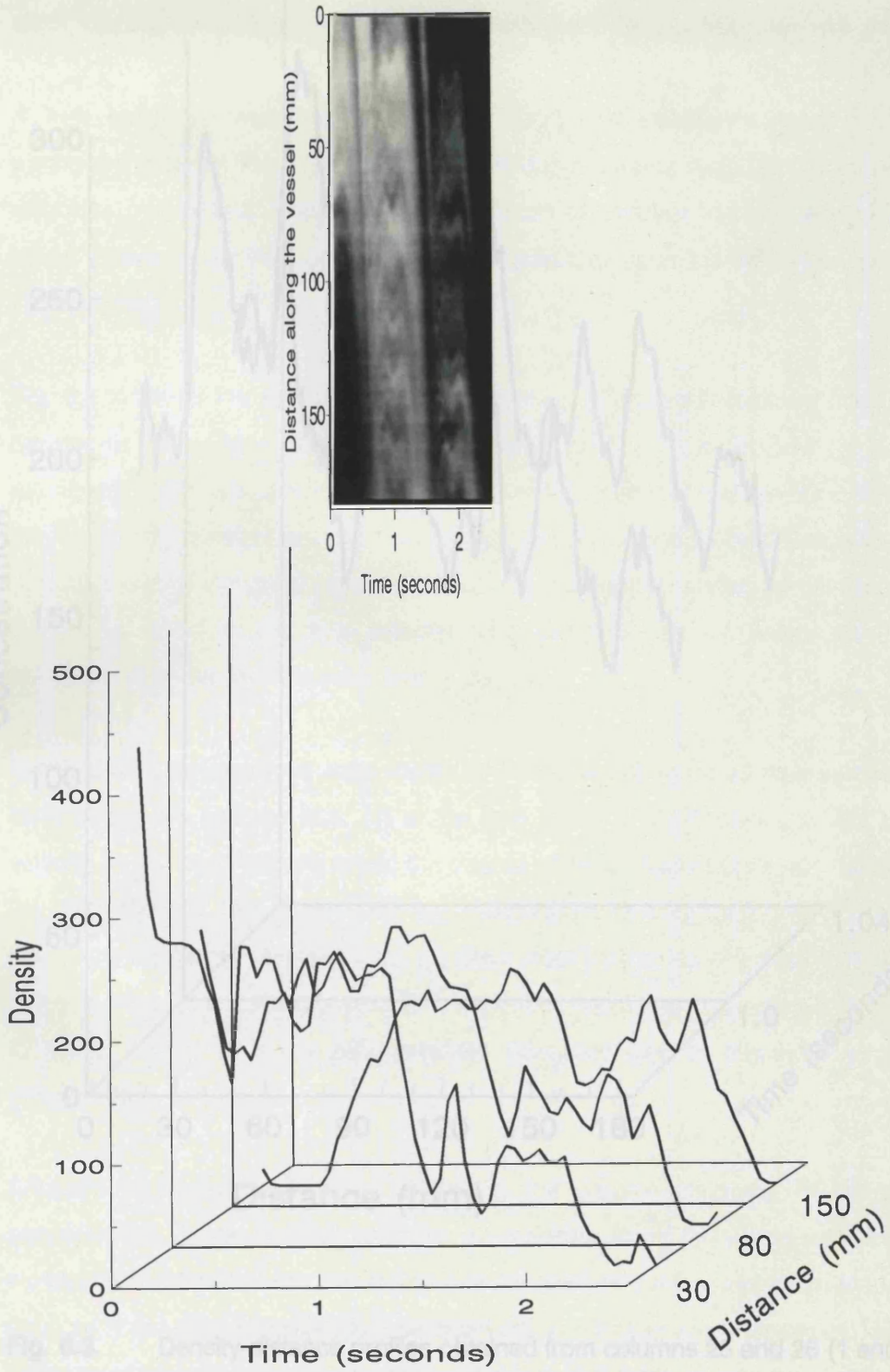

Fig. 6.2. (a) Parametric image showing contrast medium concentration (grey scale) at different positions along the blood vessel (vertical axis) at different times (horizontal axis), generated from 3D experimental data acquisition for a 4.0 mm calibre with mean blood flow of 176 ml/min. (b) Graphic presentation of above parametric image shown as three rows (30, 80, and 150 mm) of time-density curves.

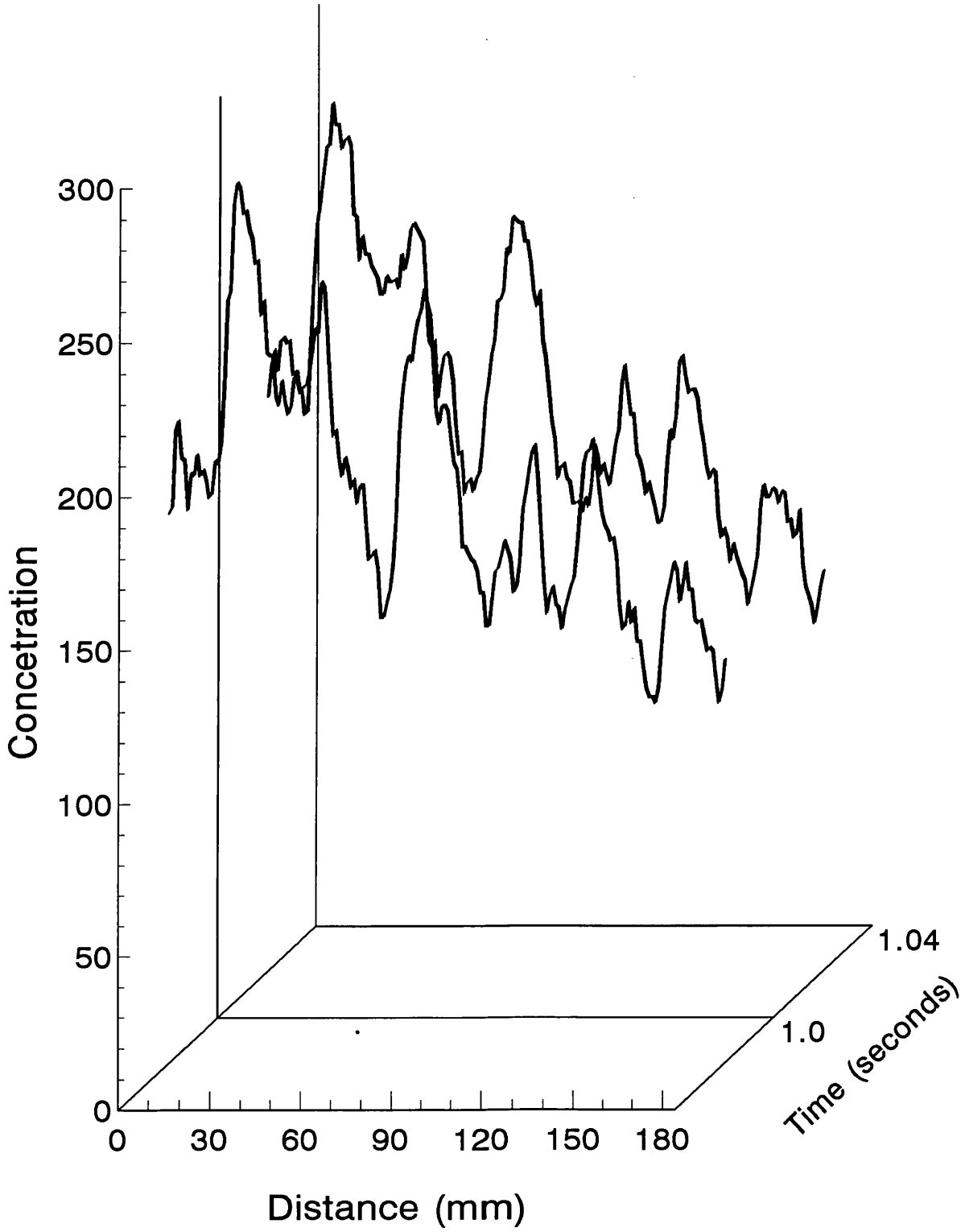

Fig. 6.3. Density-distance profiles obtained from columns 25 and 26 (1 and 1.04 seconds) of the parametric image in fig. 6.2(a).

6.2.2 Extraction of Blood Velocity Waveform from Parametric Images

A new technique was used to extract blood flow waveforms from these parametric images. The main principal of this technique is to measure blood flow velocities by tracking changes of concentration of contrast material along the blood vessel, rather than using predefined distances as in the bolus transport time method.

Fig. 6.3 presents the example of the distance-density curves obtained from a parametric image (fig. 6.2(a)) for two consecutive profiles. As is shown in fig. 6.3 the shape of the consecutive profiles appears to be very similar for short time intervals as the contrast material bolus travels along the vessel. The distance that the bolus moves along the vessel in two contiguous frames divided by the frame interval is equal to the flow velocity. This distance can be estimated by comparison of the two distance-density curves.

The following assumptions were made in the computation blood flow velocity information. We assume that: (1) in the time frame of each measurement of velocity (in our case 0.04 seconds) the degree of bolus dispersion is very small, (2) blood flow is time dependent but independent of position down a non-branching segment of blood vessel, (3) there must be overlap of portions of the bolus in adjacent frames. Our phantom work has shown that in practice, a frame to frame overlap of about 50% provides adequate data to match distance concentration functions.

Adjacent concentration-distance profiles in the parametric image of iodine concentration versus distance and time were shifted along the vessel axis until a match occurred. A match was defined as the point where the mean sum of the squares of the differences (MSSD) between the two profiles was a minimum. The distance of translation per frame interval is equal to the bolus velocity.

Matching (or re-registering) distance-density curves (or profiles of contrast concentration-distance) over time was performed in both directions (i.e. forward and reverse directions of blood flow along the vessel) and the disparity (or displacement) of matched curves was computed.

The matching criteria in the forward flow direction are satisfied when the function

$$MSSD=\frac{\sum_{K=n}^{K_{max}}[A(K)-B(K-n)]^2}{(K_{max}-n+1)} \tag{6.1}$$

is a minimum with respect to n (fig. 6.4). The integer n is the spatial shift (in pixels) along the vessel, A and B are consecutive profiles of contrast concentration along the blood vessel and K_{max} corresponds to the maximum length of the vessel used for flow analysis.

The dependence of the MSSD on the spatial shifts is demonstrated in fig. 6.5. This data is generated from columns 25-28 (1-1.12 seconds) of the parametric image in fig. 6.2(a). The data demonstrate a sharp minimum at a certain value of the shift. The shift that yields the minimum MSSD is taken to be the distance traversed by the contrast material between the two frames. We also generated a cost function image where the image grey level represents the MSSD as a function of time (horizontal axis) and shifts (vertical axis) along a vessel segment (fig. 6.6). Fig. 6.6 was generated by the application of our velocity algorithm, matching profiles of contrast concentration-distance over time, to the parametric image in fig. 6.2(a). In this thesis these images were used for display purposes to check the behaviour of the search algorithm (MSSD). The use of these images to improve the generation of blood flow velocity waveforms in clinical studies especially in noisy images will be discussed in chapter 10, "future work".

The maximum velocity, V_{max}, which can be detected using our velocity algorithm is given by:

$$V_{max}=RL \tag{6.2}$$

where L is the vessel path length over which the measurement is made and R is the X-ray image frame rate (25 frames/sec). If the peak blood flow velocity along the vessel is greater than the length of the vessel segment analysed per frame

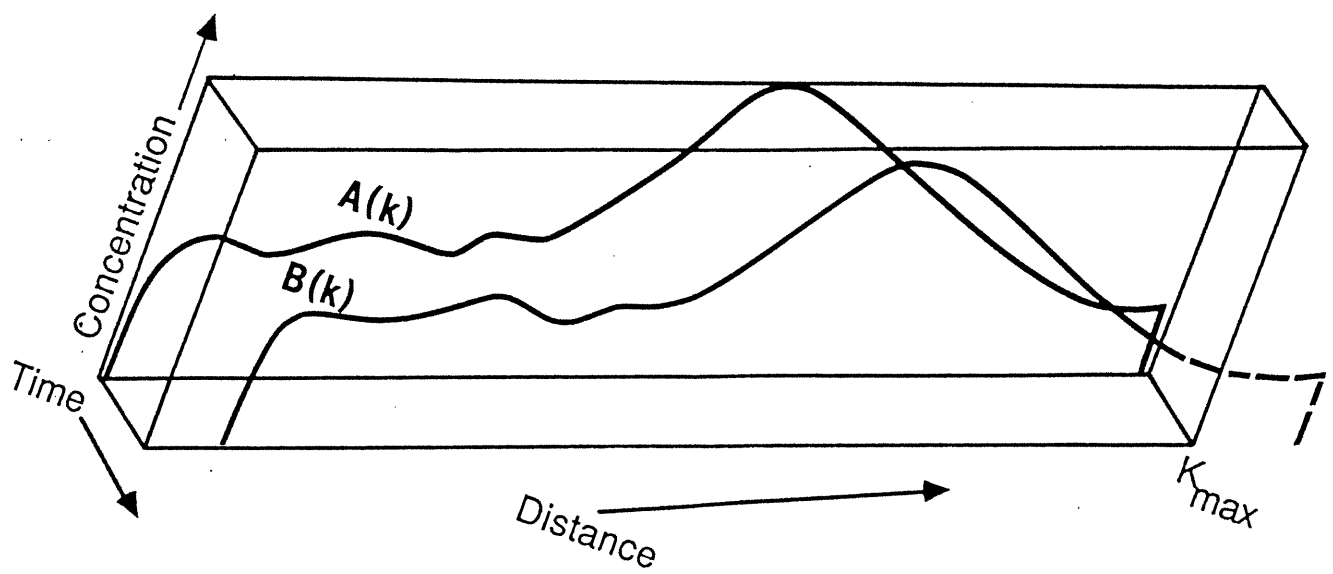

Fig. 6.4. Graphical representation of the method for matching density-distance profiles over time.

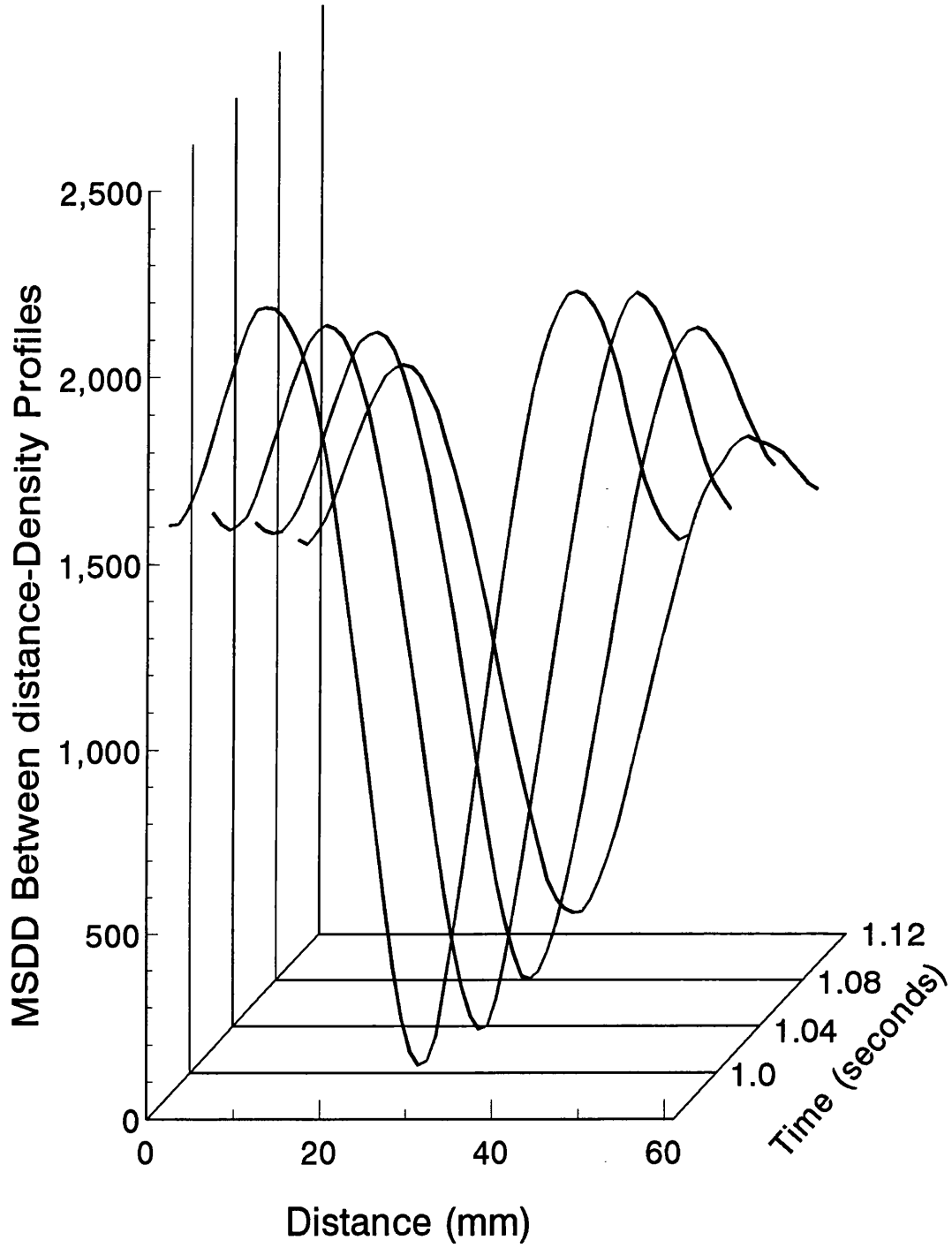

Fig. 6.5. A example of the dependence of the mean sum of the square differences (MSSD) on the spatial shifts. The data demonstrate a sharp minimum at a certain value of the shift. This value is taken to be the distance transversed by the contrast material between the two frames. Graphic presentation of the MSSDs are from the parametric image shown in fig. 6.2 in four consecutive columns 25-28 (1-1.12 seconds).

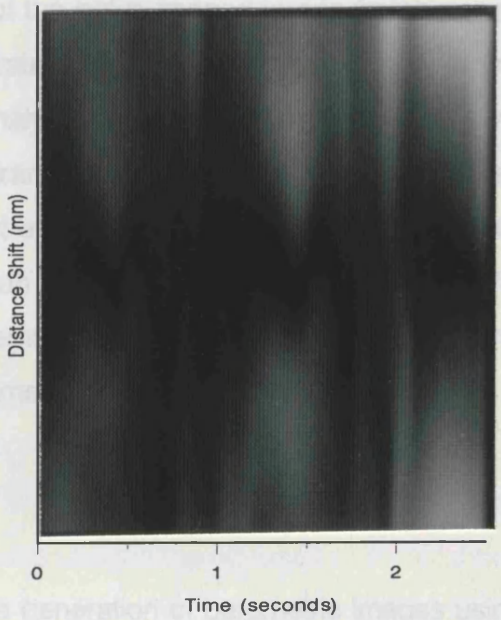

Fig. 6.6. A example of the cost function image, where the image grey level represents the mean sum of the square difference (MSSD) as a function of time (horizontal axis) and shift (vertical axis) along a vessel segment. The cost function image was generated by the application of our velocity algorithm to the parametric image in fig. 6.2(a).

interval, then the tracking algorithm will fail. In other words, in the comparison (using MSSD) of two distance-density curves, some of the same portions of the bolus must appear in the two profiles. This is entirely dependent on the frame rate acquisition and length of vessel imaged; the frame rate must be high enough so that a portion of the bolus imaged in one frame appears in the subsequent frame. The frame rate required can be estimated from the length of the vessel used in the flow analysis and the estimated peak velocity of the blood flow. For example with 25 frames per second and a 100 mm vessel length, the peak velocity should not exceed 2500 mm/second and this is adequate enough for most of the human vascular system (Caro et al 1974). Digital subtraction angiographic systems are sometimes capable of acquiring at a data rate of 50, 75 or even 100 frames per second.

6.3 METHOD

Here I describe the generation of parametric images using digital angiographic data and the extraction of blood velocity waveforms from these images.

6.3.1 Principle of the Technique

The digital X-ray angiographic image information was transferred to a SUN 4/260 Graphics workstation from a digital X-ray angiographic computer system. The first step was to subtract the 'background' from the images after the injection of a contrast material by subtracting an image obtained prior to the injection (mask mode imaging). The average of several images was used to obtain the mask: integrated mask mode imaging.

This process was performed on logarithmically transformed data which assumes that Lambert-Beer's law applies. Ideally this eliminates soft tissue and bone densities common to both the mask and contrast-containing images. Lambert-Beer's law only approximately applies because of radiographic scatter, light scatter within the image intensifier phosphors (veiling glare), and the nonlinearity of the radiographic and video transfer functions.

6.3.2 Generation of Parametric Images

In chapter 5 an edge detection technique that we have implemented was described for biplanar angiographic data. In brief, the implemented algorithm for measurement of vessel width analyses the grey scale values in the image along a line perpendicular to the tracked vessel centre line in one of the two views. First a 'background' value for every point along this line is estimated by linear interpolation between the background values found on either side, and well outside of the vessel. After subtraction of this background, the vessel edges are determined by calculating the maximum of the sum of the moduli of the first and second derivatives of the grey scale values along the TDP. The derivatives are computed by fitting a third-, fifth- or seventh-order polynomial spline function to the profile. The edge point locations were averaged by median filtering which removes individual erroneous points. Pairs of edge points which delineate either side of the vessel were used in the calculation of vessel width and as boundaries for the integration of image intensity used in densitometric area calculation and in the generation of the parametric images for the flow calculation. In addition the maximum intensity of the transverse density profile (TDP) and background values were computed.

A parametric image was generated using the detected edges and the masked dynamic angiographic data as follows. The area of each TDP between the edge points was calculated and used to construct a single vertical column of a parametric image. This calculation was repeated for each frame, producing a time-distance plot proportional to the mass of contrast material within the artery, assuming Lambert-Beer's law applies. Detailed discussion of the validity of the Lambert-Beer law is provided in chapter 3 and by Hawkes et al (1988). The grey values along each row corresponded to a plot of contrast material mass against time at a particular point along the vessel. In the 3D data processing technique the vertical axis (vessel length) of the parametric image was converted from pixel units to mm using the data from the 3D centre line path length (see chapter 5). Finally the grey values in each row were normalised by dividing by the maximum value in each row. This generated a parametric image with an intensity approximately proportional to the contrast material concentration allowing for variations in vessel cross-section along the vessel axis. This assumed that the

vessel cross-sectional area does not vary with time and that the peak concentration was not diluted along the sampled length of vessel as the bolus traversed it. An example of such a parametric image is shown in fig. 6.2.

6.3.3 Calculation of Instantaneous Blood Velocities

As described above, a novel technique was used to extract blood flow waveforms from these parametric images. The technique was based on finding the best match between two consecutive distance concentration profiles. The distance concentration profile from one X-ray image (one column of the parametric image) was compared with that from the next X-ray image (adjacent column of the parametric image) by computing the MSSD between the two profiles. One of the profiles was shifted spatially in units of one pixel until the minimum MSSD was formed. The spatial shift that yields the minimum MSSD is considered to be the distance that the bolus traversed in the time between the two frames. Thus, for high frame rate (25 frames/second) acquisition, 'instantaneous' blood flow velocity can be computed every 0.04 seconds.

6.3.4 Implementation of The Technique and Testing

The above algorithm for extracting blood flow waveforms from parametric images was implemented on a SUN graphics workstation and on a microcomputer (IBM PS/2) system. The goal of this second implementation was to demonstrate that the technique is effective and practical even on a modest system. Speed of execution and efficient use of memory were optimised.

6.3.5 Tuning The Velocity Algorithm

The following factors were provided to allow for fine tuning of the matching (re-registration) function:

(1) The first step in the algorithm was the computation of intensity along each column of the parametric images. Columns with no contrast (low magnitudes) were marked to be ignored in further processing.

(2) If any part of the blood vessel was overlapping with other vessels, that

part (on the vertical axis of the parametric image) was marked in the parametric image to be ignored for computation of the MSSD. This exclusion zone for overlapping vessels was found to be essential for blood vessels in the head and neck (see chapter 9). Data collected from within the exclusive zone were not considered when computing the match data on each side of the exclusion. The exclusion of overlapping vessels was done interactively by indicating the length of vessel overlap using a cursor and excluding this contrast concentration data from the calculation of the MSSD.

(3) Similar exclusion of data applied to other horizontal artefacts due, for example, to movement artefacts.

(4) A reverse time direction re-registration of the adjacent distance-density curves was performed similar to that for the forward time direction. This was done in an attempt to correct for any missing data in the blood velocity profile. In practice, however, data missing in the forward search was usually also missing in the reverse search.

(5) An optimal sampling search shift for forward and reverse direction of flow was selected.

6.3.6 Computation of Volume Blood Flow Waveforms and Estimation of The Mean Blood Flow

The blood velocity waveform estimate may be converted to a volume flow waveform by multiplying by the vessel cross-sectional area (as described in chapter 5).

The time-averaged volumetric flow F through a vessel is the product of average cross-sectional area of the vessel A_{av} (see chapter 5) and the mean velocity of flow within the vessel $v(t)$, and is computed as:

$$F=\frac{1}{TX}\int_{x=0}^{X}\int_{t=0}^{T}A(x)v(t,x)\,dt\,dx\approx\frac{A_{av}}{T}\int_{t=0}^{T}v(t)\,dt \qquad (6.3)$$

where $A(x)$ is assumed to be independent of x and equal to A_{av} hence we

assume that for an incompressible fluid $v(t,x)$ is independent of x and equal to $v_{av}(t)$, T is the averaging time which is taken over an integral number of cardiac cycles, and X is the length of blood vessel analysed. The average blood flow was calculated from blood flow waveforms by integrating over time for one or several cardiac cycles.

6.4 DISCUSSION

A novel digital X-ray angiographic technique has been developed to determine pulsatile flow waveform patterns from dynamic X-ray angiographic data. Instantaneous blood velocities were estimated by generating a 'parametric image' from dynamic angiographic images in which the image grey-level represents contrast material concentration as a function of time and distance along a vessel segment. Adjacent concentration-distance profiles in the parametric image were matched (or re-registered) along the vessel axis until a match occurred. A match was defined as the point where the mean sum of squares of the differences in the two profiles was a minimum. The distance translated per frame interval is equal to the bolus velocity.

Two procedures are described in chapters 7 and 8 respectively for the validation of this technique. The first method uses simulated X-ray angiographic data generated by computer models (details and results of the validation are described in chapter 7). Quantitative comparison with other algorithms is also made using computer generated images. The second method was a validation of the technique using an experimental model of blood circulation. The results obtained from this system are described in chapter 8.

In addition clinical data were used to confirm the feasibility and accuracy of using the technique 'in-vivo' (chapter 9).

CHAPTER 7

ASSESSMENT OF BLOOD FLOW MEASUREMENT TECHNIQUES USING SYNTHETIC DATA FROM A COMPUTER SIMULATED MODEL

7.1 INTRODUCTION

The objectives of this part of the work were:

(1) to demonstrate the errors inherent in conventional 'bolus-transport-time' angiographic techniques as described in chapter 4,

(2) to assess other strategies for deriving pulsatile blood flow by analysis of time sequences of profiles of contrast material concentration along the vessel,

(3) to assess the new algorithm for deriving pulsatile blood flow described in detail in chapter 6.

Initially these techniques were assessed using simulated angiographic data. These allowed greater flexibility in designing suitable experiments, more control of the experiments, and less cost in capital equipment and material. In addition, it was of interest to predict the X-ray quantum limited precision of the technique, for a wide range of blood vessel calibres and blood flow rates, with data that was free from non-random errors and artefacts.

To assist in the evaluation of these techniques parametric images were generated where the image grey level represented contrast material concentration as a function of time and distance along a vessel segment. Instantaneous blood velocity measurements were derived by analysis of this image.

The computer (numerical) model used to generate these images is described only briefly here as it has been described in full by Hawkes et al (1988b).

7.2 METHODS AND MATERIALS

7.2.1 Description of The Numerical Model

Numerical modelling involves the use of computers to generate an instance of a mathematical model by employing numerical methods. The mathematical model is an abstract representation of some real-world phenomenon. The predictions resulting from the solution are thus limited by the validity of the mathematical model. In general, blood flow and fluid flow phenomena can be modelled by the Navier-Stokes and conservation differential equations, which describe the conservation of mass, momentum, and energy.

The model used was developed at St George's Hospital by Hawkes et al (1988b) where the initial part of the work of this research was carried out. The model calculates the concentration of contrast material $C(X,t)$ at a point distance X along the vessel distal to the injection site at time t as:

$$C(X,t) = \frac{Q_I(t_i)C_I}{Q_T(t_i)} \tag{7.1}$$

where:

t_i	=	the time at which the portion of the bolus under consideration was injected
t	=	the time fluid arrived at point X
$Q_I(t_i)$	=	injection flow rate of contrast material at time t_i
$Q_T(t_i)$	=	total flow in the cylinder distal to the injection site at time t_i
C_I	=	concentration of contrast material in the injection

The concentration along the vessel at time interval δt was calculated recursively as follows. The concentration at X at time $(t+\delta t)$ was equal to the concentration at point $(X-\delta X)$ at time t, and the volume of fluid flowing distal to the site of injection in the time interval δt, $Q_T(t)\delta t$, was given by:

$$Q_T(t)\delta t = \int_{(X-\delta X)}^{X} A(x)dx \qquad (7.2)$$

The cross sectional area of the cylinder $A(x)$ was integrated from X back towards the site of injection until the distance δX was found which satisfies the above equation.

The graphical output of the computation is illustrated in fig. 7.1 (the generation of a parametric flow image). The partially formed parametric image is shown on the left, while on the right there is a graphical representation of contrast concentration across the diameter of the blood vessel lumen. The vessel was 5 mm in diameter and 100 mm long. The blood flow is from bottom to top and the injection site is shown by the lowest mark on the vessel outline (10 mm away from imaging site), while the other two marks indicate the length of the vessel used to generate the parametric image.

7.2.1.1 Accuracy of Modelling Techniques

The computer model described above used a substantial simplification of the true flow and transport of the contrast material in the artery. The major differences between the model and reality are:

(A) In the simulation, the walls of the vessel were assumed to be stiff (rigid walls) rather than compliant. This is not the case in actual blood vessels, which have visco-elastic properties which allow the diameter to vary during the cardiac cycle. The radius of arterial blood vessels tends to vary at the most by 5% (McDonald 1974). However, recently Eriksen (1992) report that 'The transient dilation (of the arterial wall) following systole is relatively small and its effect on the stability of flow is negligible'. Eriksen has studied the effect of pulsatile arterial diameter variations on blood flow using Doppler ultrasound. He found that the median of the peak-to-peak pulsatile diameter variations were 0.19 mm (2.8%) in the femoral artery and 0.49 mm (6.7%) in the common carotid artery. Flow values were calculated by Eriksen (1992) either by taking the time-averaged diameter as a

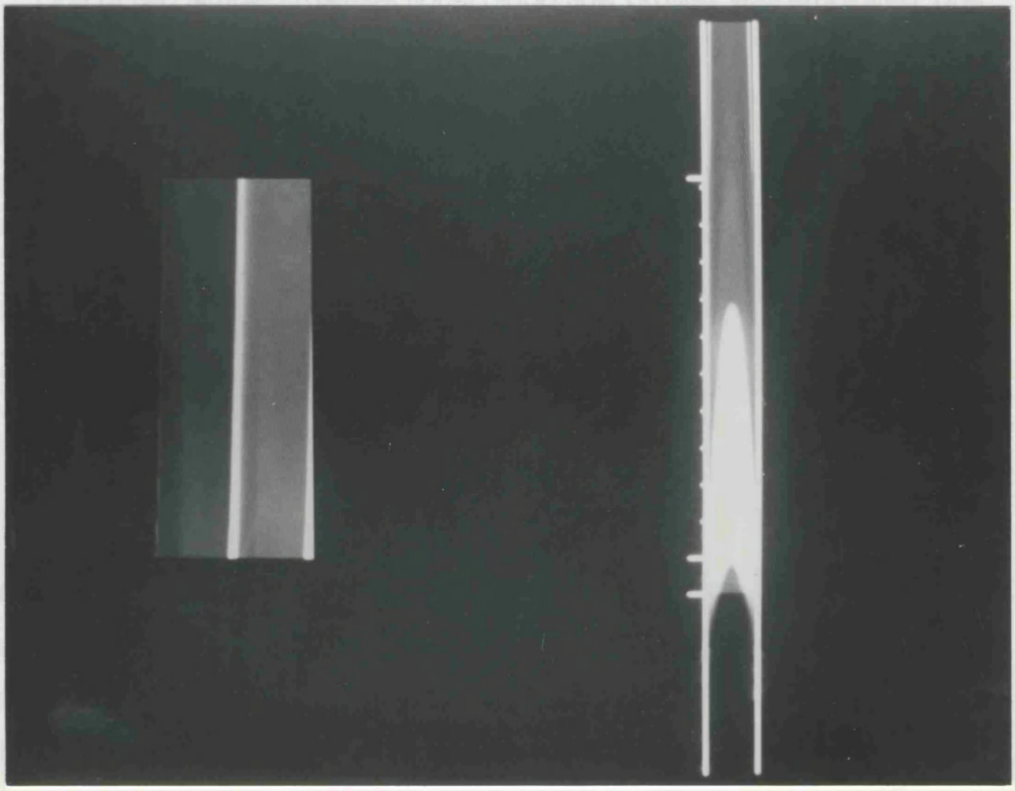

Fig. 7.1. Generation of a parametric flow image. The partially formed parametric image is shown on the left, while on the right there is a graphical representation of the contrast concentration across the diameter of the blood vessel lumen. The diameter of the vessel was 5 mm.

constant value, or by taking into account the dynamic variation in diameter. In comparing the two values, an error in the range 1.5-3.8% was found for the femoral artery, whereas the error in the common carotid artery was in the range 0.4-3.6% despite the large amplitude of the pulsations in this vessel.

(B) One of two simple cross-sectional blood flow profiles was employed, one representing laminar flow and the other 'plug' or constant axial flow over the vessel cross-section which was represented as 16 cylindrical laminae. In laminar flow the axial flow profile across the vessel is a parabolic. More accurate simulation of the flow patterns would have involved significant computation (Hawkes et al 1988b). The two flow patterns outlined above represent the extremes of expected flow.

(C) The vascular tree was assumed to be a very simplified arterial system (i.e. no branching).

(D) There is perfect mixing of contrast media at the injection site.

Because of these assumptions the results obtained from the model cannot be taken to be quantitatively accurate but should be considered merely as a step towards describing the flow of contrast material in vessels. The computational model was only intended to simulate a simplified physiological situation in order to validate the algorithms.

7.2.2 Description of The Vaiidation Experiment

7.2.2.1 Input parameters to the model

The computer model permits the interactive setting of 25 different parameters. Table 7.1 shows the input parameters to the model via the UNIX™ screen text editor 'vi' for laminar flow, and fig. 7.2 shows the graphical input of the blood flow waveform.

7.2.2.2 Injection strategy for contrast material

In order to study whether the injection technique was likely to have an effect on accuracy, four different injection techniques were examined and these are shown in fig. 7.3.

Table 7.1. Example of input parameters used in flow model for laminar blood flow pattern.

INTERACTIVE SETTING OF PARAMETERS FOR FLOW SIMULATION
* indicates variable set internally by program
& indicates variable checked for consistency
for boolean variables 1st or 2nd char t will identify true all else false
You are in vi if parameters are OK use ZZ to exit

0	*status (integer)
0.40	*pixel size in mm (real)
256	array size for vector image 256 or 512 (integer)
10.00	distance from catheter tip to image vessel (mm) (real)
102.40	length of vessel imaged (mm) real
256	&no of pixels in Y (distance) dirn. max 256 (integer)
1.00	X-ray magnification (real)
0	angle between imaging plane and vessel in degrees (integer)
5.12	*time of cine run (secs) (real)
50	frames per sec (integer)
256	&total no frames max 256 (integer)
true	vessel circular (boolean)
false	vessel constant width (boolean)
6.00	max width of vessel (mm) (real)
0.00	width increment (mm) (real)
1000.00	exposure to II in micro R/sec (real)
0.00	exposure increment (real)
12.25	mass attenuation coefficient of iodine cm^2/gm (real)
167.20	photons/square mm/mR (real)
9.33	*minimum value of noise added to vector image (real)
false	plug flow (boolean)
true	diffusion to be included (boolean)
false	turbulence to be included (boolean)
16	no of cyls in lam flow max 16 (integer)
0.0050	diffusion factor (real)
false	does vessel brach (boolean)
3200.00	peak blood flow (ml/min) (real)
0.00	peak blood flow increment (real)
2.00	peak contrast flow (ml/min) (real)
0.00	peak contrast flow increment (real)
300.00	contrast concentration mgms iodine/ml (real)
25.00	% of injection flow by which prox blood flow is reduced (real)
588.33	*mean blood flow (ml/min) (real)
1.37	*mean contrast flow rate (ml/sec) (real)
636.24	*mean total vessel flow (ml/min) (real)
2.11	*mass of iodine injected (gms) (real)
300.00	*scaling factor iodine conc/grey level (real)
622	*number of pixels in overflow region (integer)
655	*number of pixels in backflow region (integer)
0	*pixel offset to ensure vi in range (integer)

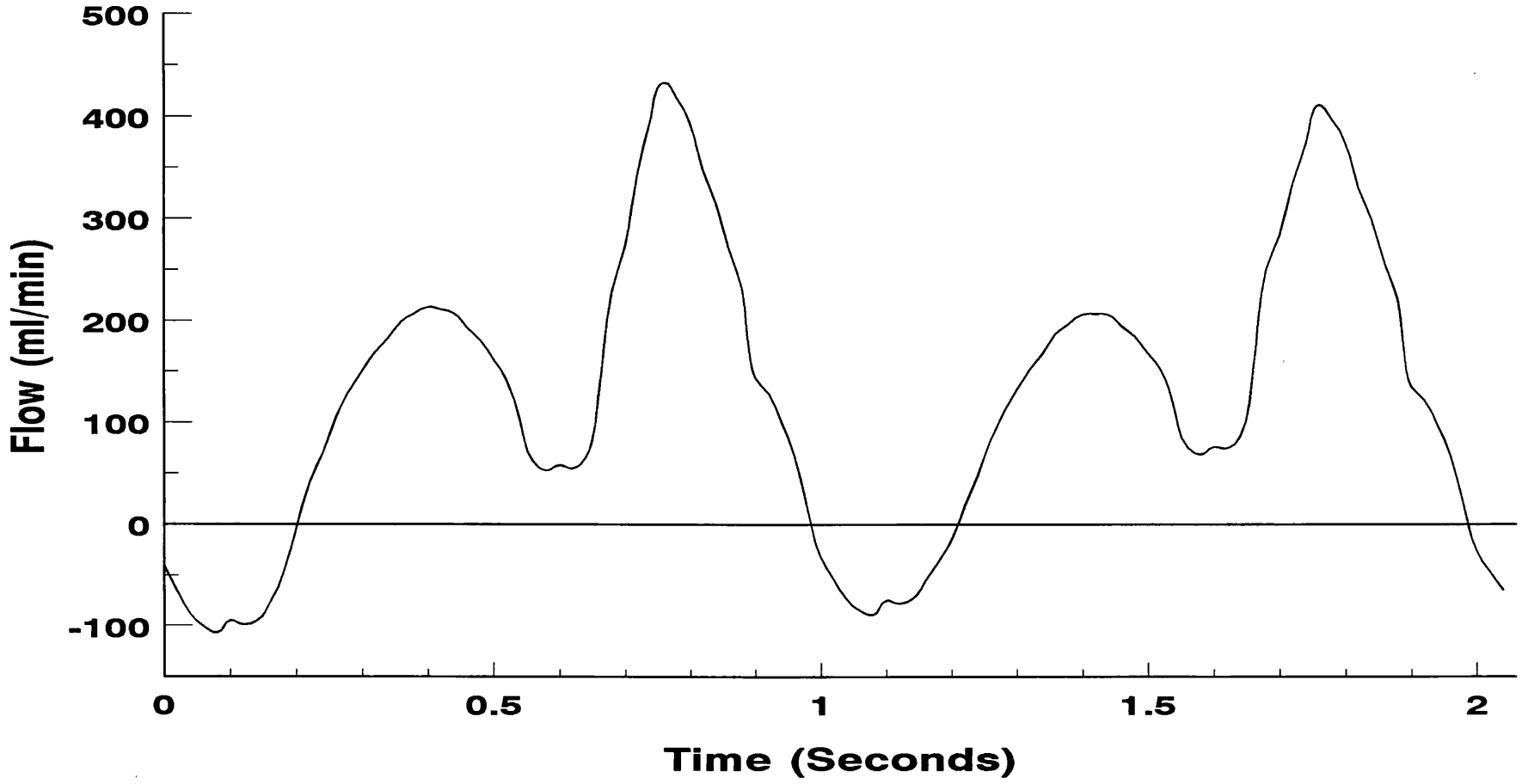

Fig. 7.2. Blood flow waveforms vs time used as input into the computer model.

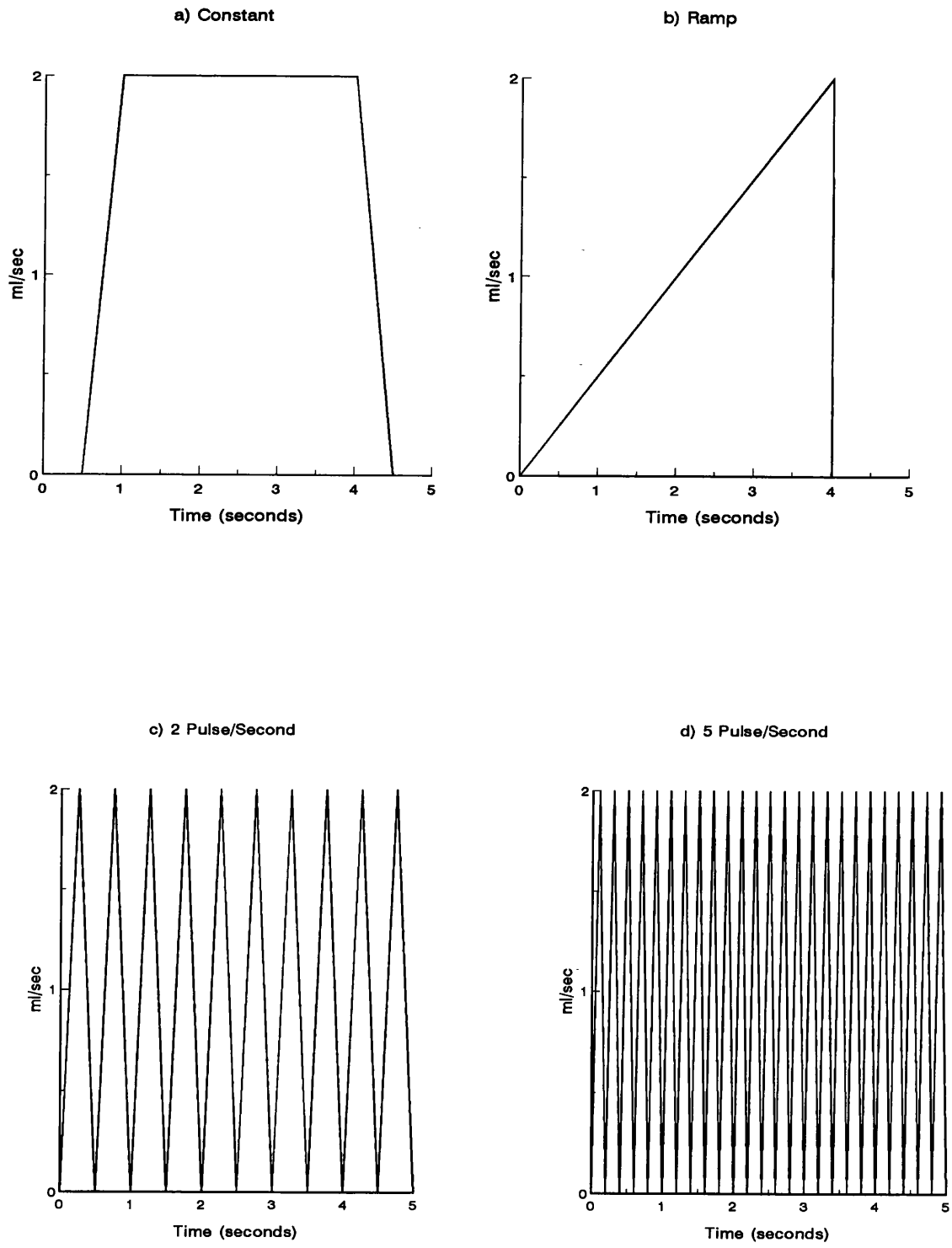

Fig. 7.3. Injection strategy for contrast medium in the simulation studies: (a) constant, (b) ramp, (c) 2 pulse/sec and (d) 5 pulse/sec.

The first mathematically determined injection technique consisted of a linear increase in flow over half a second, up to a constant rate of injection of contrast material, which continued for a period of three seconds and was followed by a linear decrease to zero flow (Link et al 1979). The second technique used a linear increase in the flow of contrast material injected over a period of four seconds. This was the injection strategy adopted by Swanson et al (1986). The third and fourth techniques consisted of two and five pulses per second. Five pulses per second is probably the highest that is achievable in practice, although it is unlikely that such sharp waveforms will be achievable. The total injected bolus volume was kept small (less than 2 ml) to minimise the disturbing effect on the blood flow.

7.2.2.3 Generation of dynamic angiographic data using the computer model

The computer model took as input data the function of blood velocity versus time, details of the injection, blood vessel dimensions and radiographic parameters. The output from the model is a parametric image of contrast material concentration versus time and distance. An example parametric image is shown in fig. 7.4, for a 6.0 mm diameter vessel a laminar flow pattern with 2 pulse/sec injection technique and a peak flow of 600 ml/min.

The model generates parametric images similar in appearance to those generated experimentally. The major limitation of the model is the assumption of an axial flow profile that is found for steady state laminar flow in an infinite, straight tube of uniform, circular cross-section. If the Womersley constant α (Womersley 1955) is less than 0.5, the blood vessel, by analogy with an electrical conductor, acts as a pure resistance to flow and flow would be described by Lamb's equations (Lamb 1932). If α is greater than about 10, the axial flow velocity is approximately constant across the vessel lumen ('plug flow'). For most arteries the value of α is intermediate between these two values. The parametric images were generated for both 'plug' flow and laminar flow using the model. Hence the effect and significance of either extreme of flow pattern in the artery can be investigated. As laminar flow patterns are likely to produce greater errors in flow estimation due to dispersion of the bolus, most results presented here have assumed this 'worst case' flow pattern.

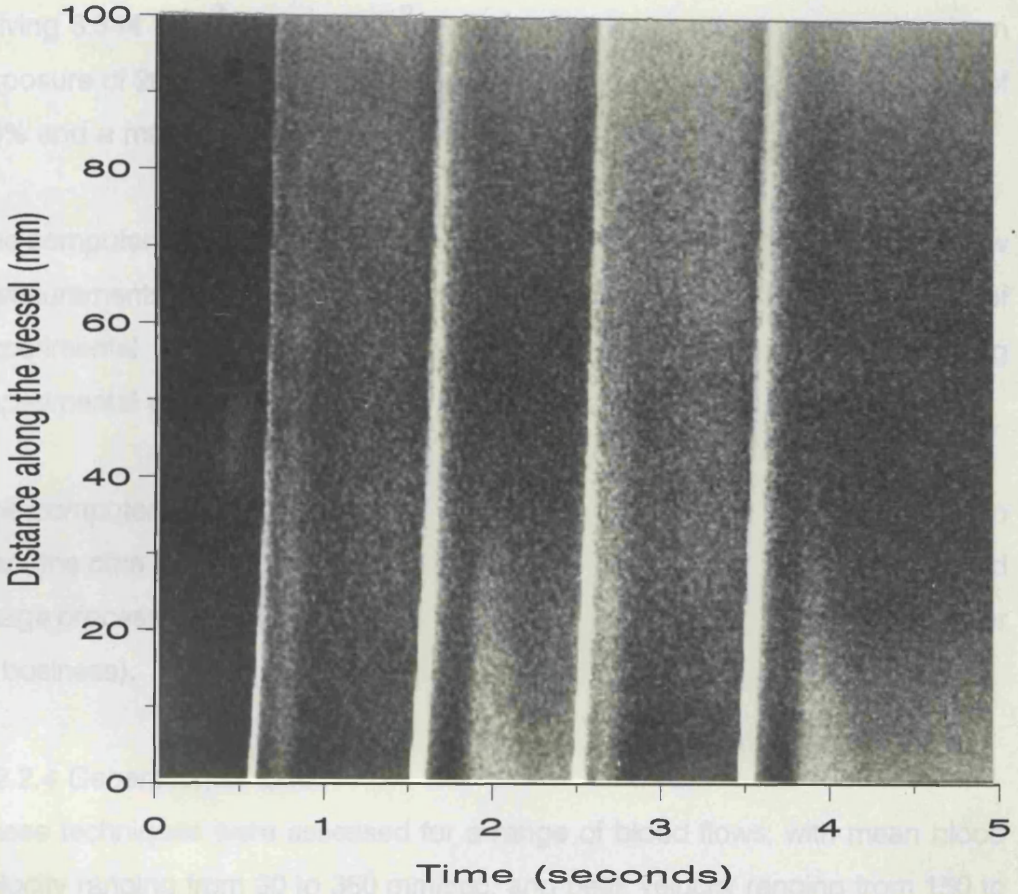

Fig. 7.4. Parametric image showing contrast medium concentration (grey scale) at different positions down the blood vessel (vertical axis) at different times (horizontal axis).

The model generates the parametric image of iodine versus time and distance along the vessel axis. X-ray quantum noise is added according to the radiographic parameters simulated. For the parametric images generated the following assumptions were made: a monoenergetic X-ray beam of 50 keV (giving 3.344 x 10^2 photons/mm^2/μR/frame incident on the imaging plane), an exposure of 20 μR/frame at the imaging plane, a quantum detection efficiency of 50% and a mass attenuation coefficient of iodine equal to 1.225 m^2/kg.

The computer modelling enables determination of the accuracy of the blood flow measurements for each algorithm investigated under a wide range of experimental conditions. It is possible to observe the effect of varying experimental parameters individually, and in combination with each other.

The computer model and the algorithms extracting the blood flow information from the data generated by the model were developed in Pascal on a dedicated image processing computer, a CVAS-3000 from Visual Machines (sadly no longer in business).

7.2.2.4 Generation of data

These techniques were assessed for a range of blood flows, with mean blood velocity ranging from 30 to 360 mm/sec, and peak velocity ranging from 150 to 1860 mm/sec, with different injection strategies and different sizes of vessels (2,4 and 6 mm diameter) for both laminar and 'plug' flow. The length of vessel segment analysed was always 100 mm. The injection point was 10 mm proximal to this segment. A total of 114 different experiments were simulated.

Figs 7.5 and 7.6 show plots of the blood flow waveform vs time (thin line) which were used in the simulation. The low blood flow waveform, fig. 7.5, had a mean flow of 139 ml/min and the high blood flow waveform, fig. 7.6, had a mean of 650 ml/min. For both, the vessel diameter was taken to be 6 mm. This flow waveform was used to generate the parametric images and is taken from the results of McDonald (1974). These were measured in a canine femoral artery.

Fig. 7.4 shows an example of the parametric images generated by the computer model, assuming laminar flow.

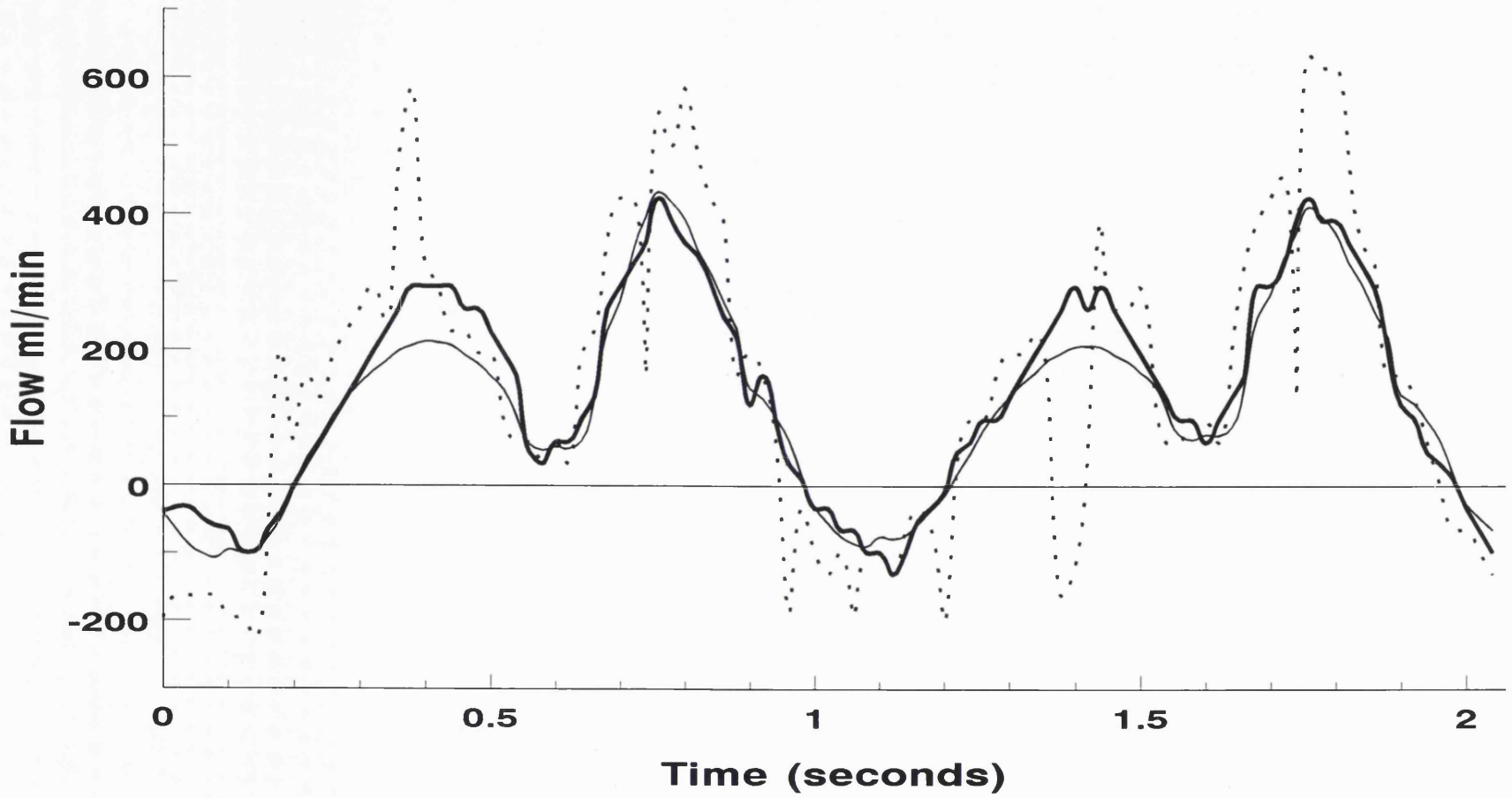

Fig. 7.5. True and estimated blood flow waveforms vs time for low blood flow (mean 139 ml/min) with vessel internal diameter of 6 mm. The thin lines inputs the true waveform, the dotted lines that from the bolus mass tracking algorithm (Swanson et al 1986) and the thick lines the results using our velocity algorithm computing.

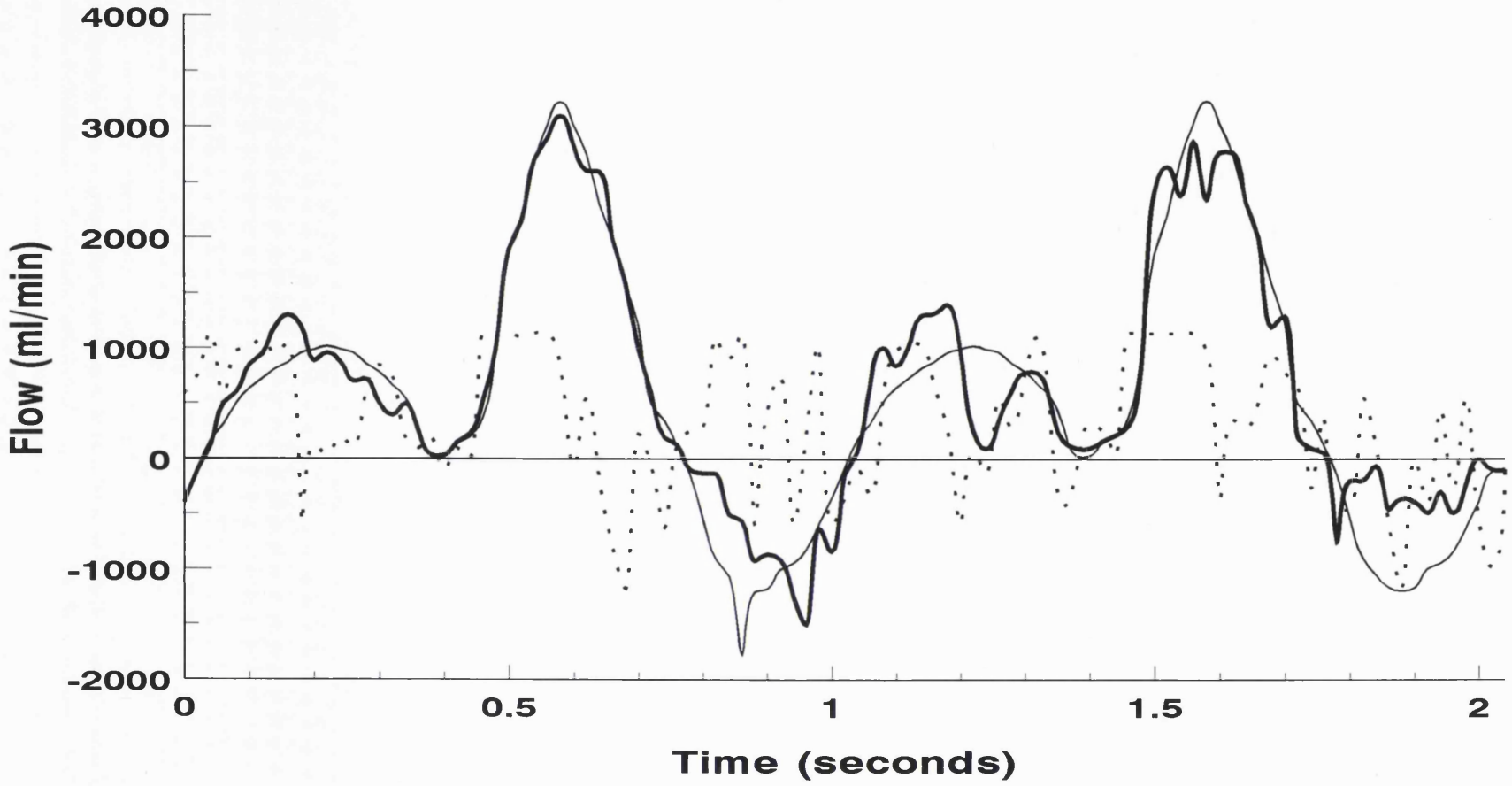

Fig. 7.6. True and estimated blood flow waveforms vs time for high blood flow (mean 650 ml/min) with vessel internal diameter of 6 mm. The thin lines inputs the true waveform, the dotted lines that from the bolus mass tracking algorithm (Swanson et al 1986) and the thick lines the results using our velocity algorithm computing.

All the data generated in this study were analysed using simple regression modelling with one predictor and one outcome variable. The degree of linearity between the two variables was expressed by the correlation coefficient, with a value of 1.00 being perfect linearity.

The mean error (ME) was calculated as the mean of 'input flow - measured flow' and is presented with ± 1 SD (Bland and Altman 1986). In addition the % error in the measurement of the flow was computed for each vessel size by:

$$\%error = 100*[(input\ flow - measured\ flow)/input\ flow]$$

and presented by ± 1 SD.

7.2.3 Blood Flow Measurement Algorithms

7.2.3.1 Bolus transport time

The following techniques were used to compute the mean velocity of the contrast material.

(a) Transport time = peak-to-peak time of time-density curves.
The time separation of the peak of the two curves is assumed to be the mean transport time of the dye.

(b) Transport time = difference in time of maximum gradient of leading edges of time-density curves.
The time density curves are differentiated before locating the peaks.

(c) Transport time = centre of gravity (cog).
The difference in time between the cogs of two curves is taken as the transport time.

The transport time measurements were made at low and high pulsatile flow from synthetic data. The mean flows were calculated using the above three techniques at two sites 100, 50 and 25 mm apart with a vessel of width 6 mm. The injection technique consisted of 2 pulses of contrast material per second.

7.2.3.2 Tracking of bolus mass

Swanson et al (1986) suggested a technique of determining the blood velocity by tracking the position of a fixed length of vessel which contains the same mass of contrast material in time sequences of radiographic images.

The following procedure was implemented. The integrated radiographic density was determined along a defined length (80 mm) of the total arterial segment imaged (100 mm) on the first angiographic image. The integrated radiographic densities of regions of the same length (80 mm) in the next frame were then calculated for all positions from the most proximal site to the most distal site in single pixel intervals. For each shift the density in the first frame was subtracted from the density at each position on the second frame. The shift for which the absolute difference in the integrated radiographic density was a minimum was then determined. The length between this point and the previous point provides a measure of the distance moved by the blood during one frame period.

7.2.3.3 Matching distance-density curves over time

The flow velocity waveform was calculated using the algorithm described in chapter 6.

7.3 RESULTS

7.3.1 Transport Time Calculated From Two Time-Density Curves

Fig. 7.7 shows a typical plot of contrast mass, for two windows 40 mm apart, plotted against time for four seconds (four cardiac cycles). Each window covered a 1.2 mm length of vessel and contrast mass was averaged within the window. The mean blood flow was 367 ml/min and the internal diameter of the blood vessel was 6 mm. A laminar flow profile was assumed. The flow rate of injected contrast material was uniform and equal to 1.10 ml/sec.

The features visible in these plots were generated entirely by the rapid changes in bolus velocity over the cardiac cycle. These features had different shapes as the bolus dispersed and it was very difficult to identify consistent corresponding points on the two plots, which would be needed in order to calculate the time of

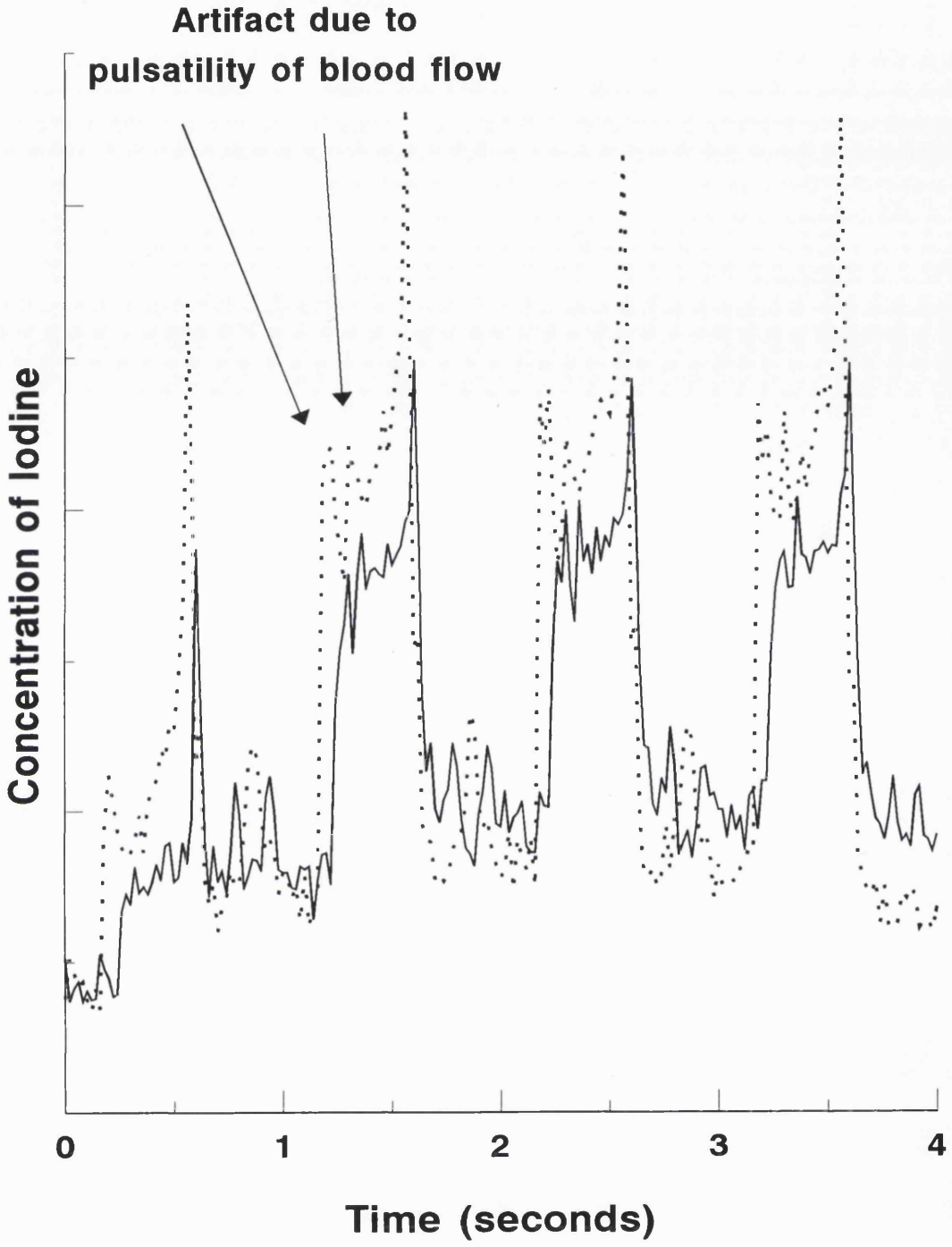

Fig. 7.7. Plots of typical contrast concentrations vs time generated from synthetic data at two sites A (dotted lines) and B (solid lines), 40 mm apart, along a blood vessel with an internal diameter of 6 mm and mean blood flow of 367 ml/min.

transport of the bolus.

Table 7.2 presents the measurements for the three different transport time methods of measuring mean blood flow at two sites, 100, 50, or 25 mm apart, (typical distances used in the transport time technique) with a vessel of width 6 mm using time-density curves. Note the large discrepancies and significant dependence on sampling site of the flow estimates.

7.3.2 Bolus Mass Tracking and Distance-Density Curve Matching

Flow was estimated using both the tracking of bolus mass, and the matching of distance-density curves over a period of time (0.05 second). Figs 7.5 and 7.6 show the superimposed estimated blood flow measurements on the simulated input flow waveform.

Scatter plots were generated relating mean calculated velocity against mean input velocity, averaged over two cardiac cycles, for a vessel of 6 mm diameter. The scatter plots generated using the bolus mass tracking technique are shown in fig. 7.8. The correlation coefficient of instantaneous blood flow input to the model and the measured blood flow was 0.735 (n=64, ME=5±7 mm/sec, with %$error$=22±30).

The scatter plots generated by matching distance-density curves over a period of time for a 6 mm diameter vessel, are shown in fig. 7.9. There was excellent correlation (r=0.994, n=64, ME=-0.2±0.1 mm/sec, with %$error$=-3±8) between input flow from the model and the measured blood flow. Results for all four injection techniques are shown on the scatter plots.

For the tracking of bolus mass technique, fig. 7.10 shows plots of mean estimated velocity against mean input velocity for vessels of 4 and 2 mm diameter (r=0.752, n=32, ME=7±7 mm/sec, with %$error$=31±28). Only results for the injection of 2 pulses of contrast material per second were calculated.

Fig. 7.11 shows plots of mean estimated velocity against mean input velocity for vessels of 4 and 2 mm diameter for the technique of matching distance-density

Table 7.2. Measurements for the three different transport time methods of measuring mean blood flow at two sites 100, 50, and 25 mm apart with a vessel of width 6 mm using time-density curves from synthetic data.

Distance between sites (mm) on blood vessel	MEAN	BLOOD	FLOW	(ml/min)
	Peak-to-Peak	Maximum Gradient of Leading Edges	Centre of Gravity (cog)	Actual Flow
100	395	425	921	240
50	228	404	472	
25	114	310	619	
100	691	921	1842	645
50	404	685	2741	
25	413	457	457	

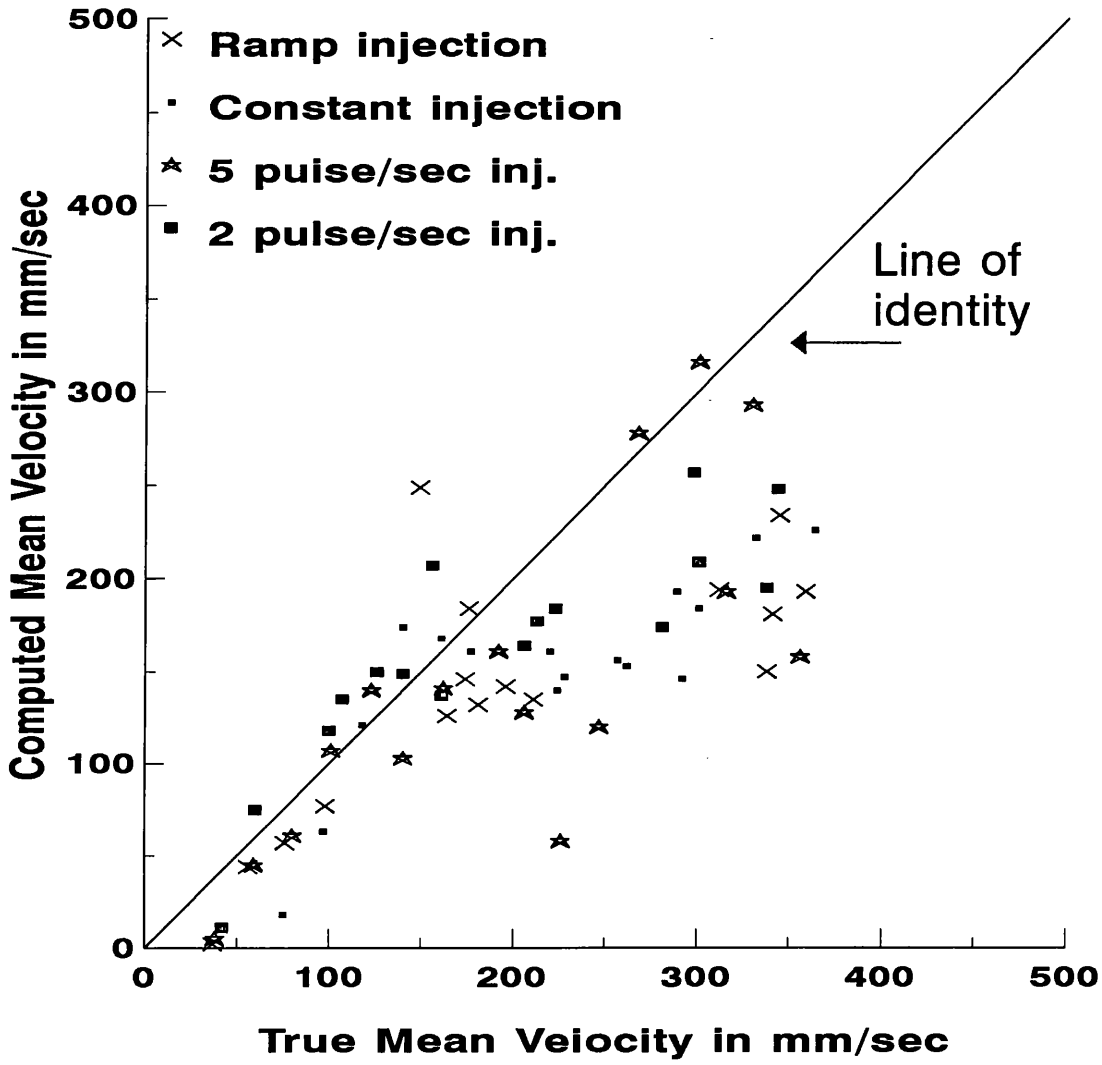

Fig. 7.8. Scatter plot showing the relationship between true mean velocity and mean velocity estimated by the tracking of bolus mass method (Swanson et al 1986) for a 6 mm diameter vessel and a laminar flow pattern. The results for ramp, constant, 2 and 5 pulse/sec injection techniques are plotted. The line represents the line of identity.

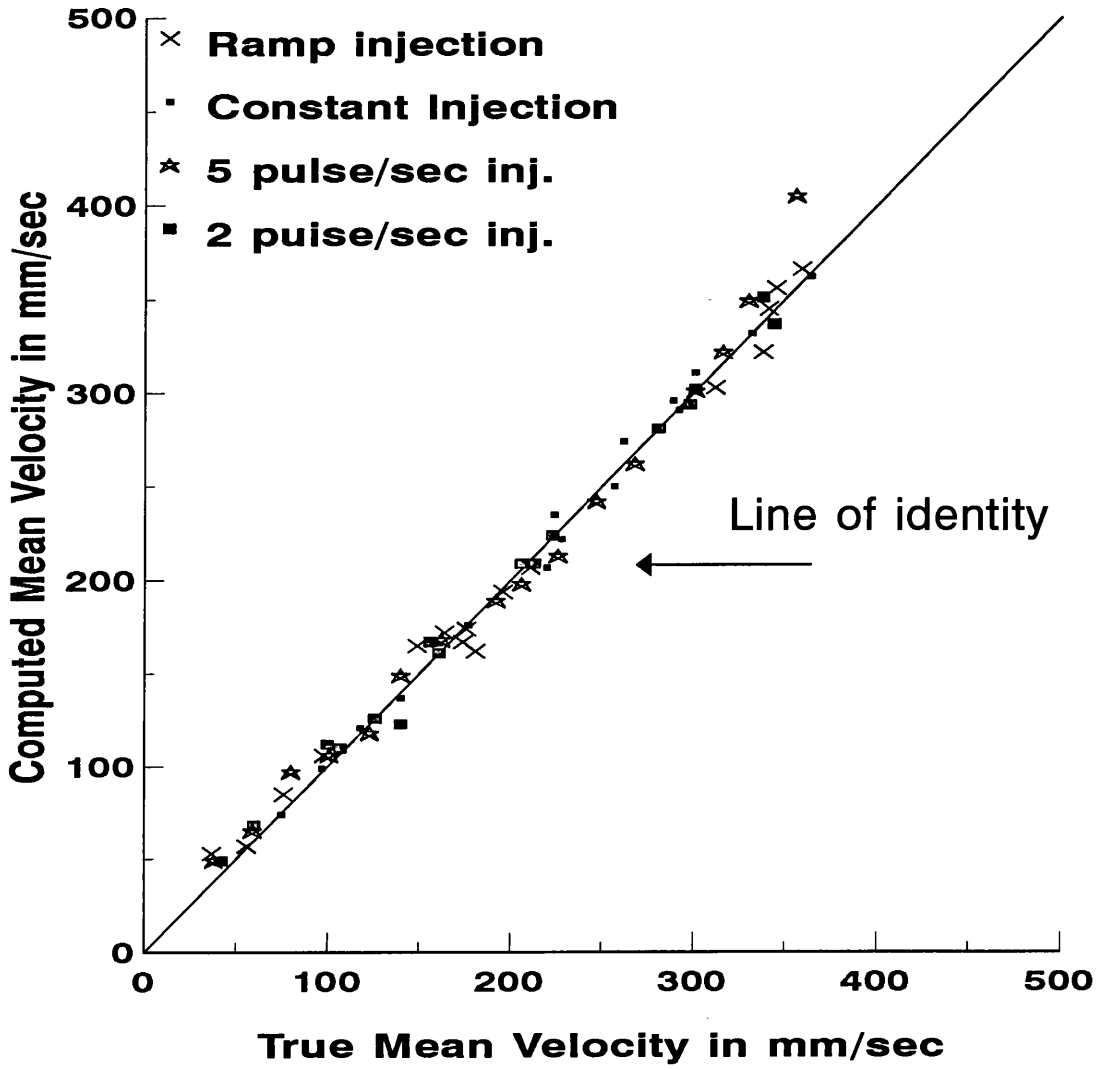

Fig. 7.9. Scatter plot showing the relationship between true mean velocity and mean velocity estimated by our velocity computing algorithm, for a 6 mm diameter vessel and a laminar flow pattern. The results for ramp, constant, 2 and 5 pulse/sec injection techniques are plotted. The line represents the line of identity.

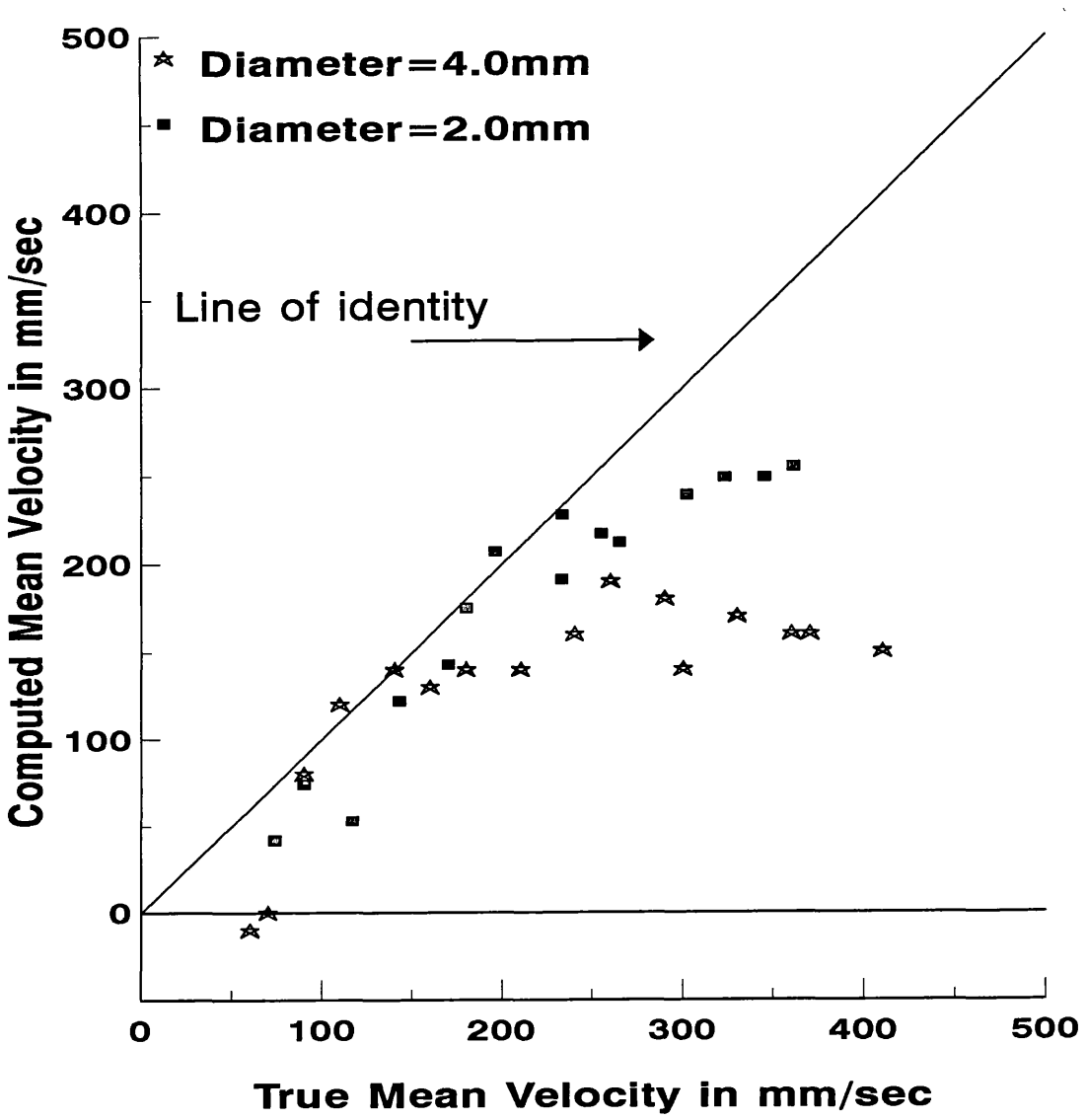

Fig. 7.10. Scatter plot showing the relationship between true mean velocity and the mean velocity estimated by the tracking of bolus mass (Swanson et al 1986) for 2 and 4 mm diameter vessels with a laminar flow pattern. The line represents the line of identity.

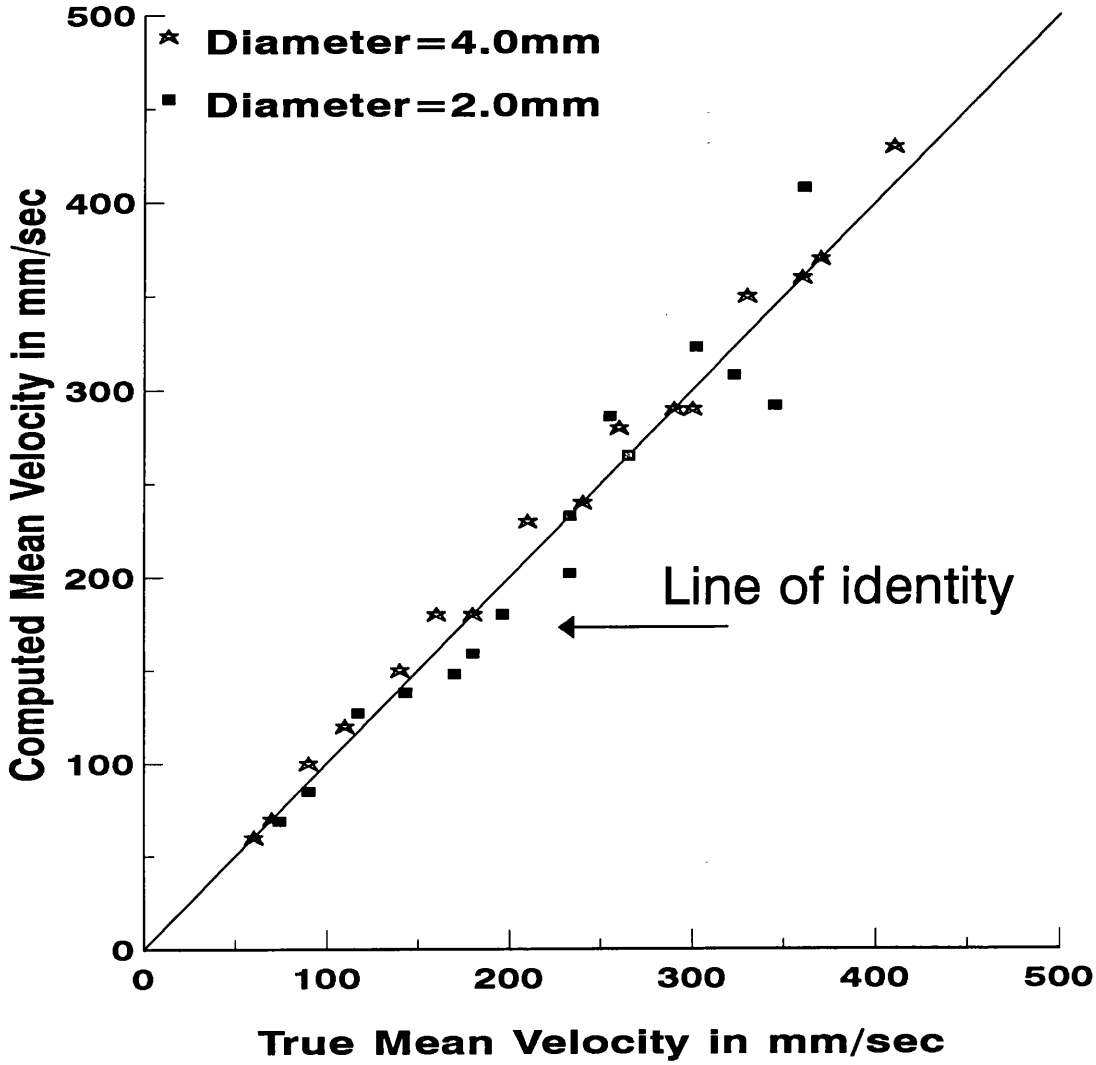

Fig. 7.11. Scatter plot showing the relationship between true mean velocity and the mean velocity estimated by our velocity computing algorithm (distance-density curve matching method), for 2 and 4 mm diameter vessels, for a laminar flow pattern. The line represents the line of identity.

curves over a period of time (r=0.983, n=32, ME=-0.2±2 mm/sec, with %*error*=-1±8). Only results for the injection of 2 pulses of contrast material per second were calculated.

For the tracking of bolus mass technique, with 'plug' flow fig. 7.12 shows plots of mean estimated velocity against mean input velocity for a vessel of 4 mm diameter (r=0.804, n=16, ME=98±72 mm/sec, with %*error*=45±29).

For the technique of matching distance-density curves over a period of time with 'plug' flow fig. 7.13 shows plots of mean estimated velocity against mean input velocity for a vessel of 4 mm diameter (r=0.996, n=16, ME=-7±13 mm/sec, with %*error*=-1±7).

7.4 DISCUSSION

Numerical modelling offers an alternative approach to the problem of algorithm validation, which can reduce the costs of phantom construction once a reliable model has been developed. In addition it is simple to control parameters which can be difficult or impossible to control in experimental work. The dependence of the accuracy on each parameter can be deduced quickly and effectively. Thus the aim of this study was to use a reliable mathematical model that would allow comparison and evaluation of the performance of blood flow measurement techniques. This study is concerned with the assessment of algorithms for calculating the pulsatile blood flow from dynamic angiographic images. The computer model was used to generate these images, and then several strategies were used to extract the blood flow rate from them.

The pulsatility of the blood flow waveform produces wide variations in contrast material concentration over time. These variations produce marked features in the time-density plots of fig. 7.7. As stated above, matching these features between different measurement sites was difficult. In addition the velocity estimates varied considerably with the timing of the appearance of features and the positions of regions of interest due to the pulsatile blood flow waveform. The results in table 7.2 confirm these observations. This finding has been demonstrated

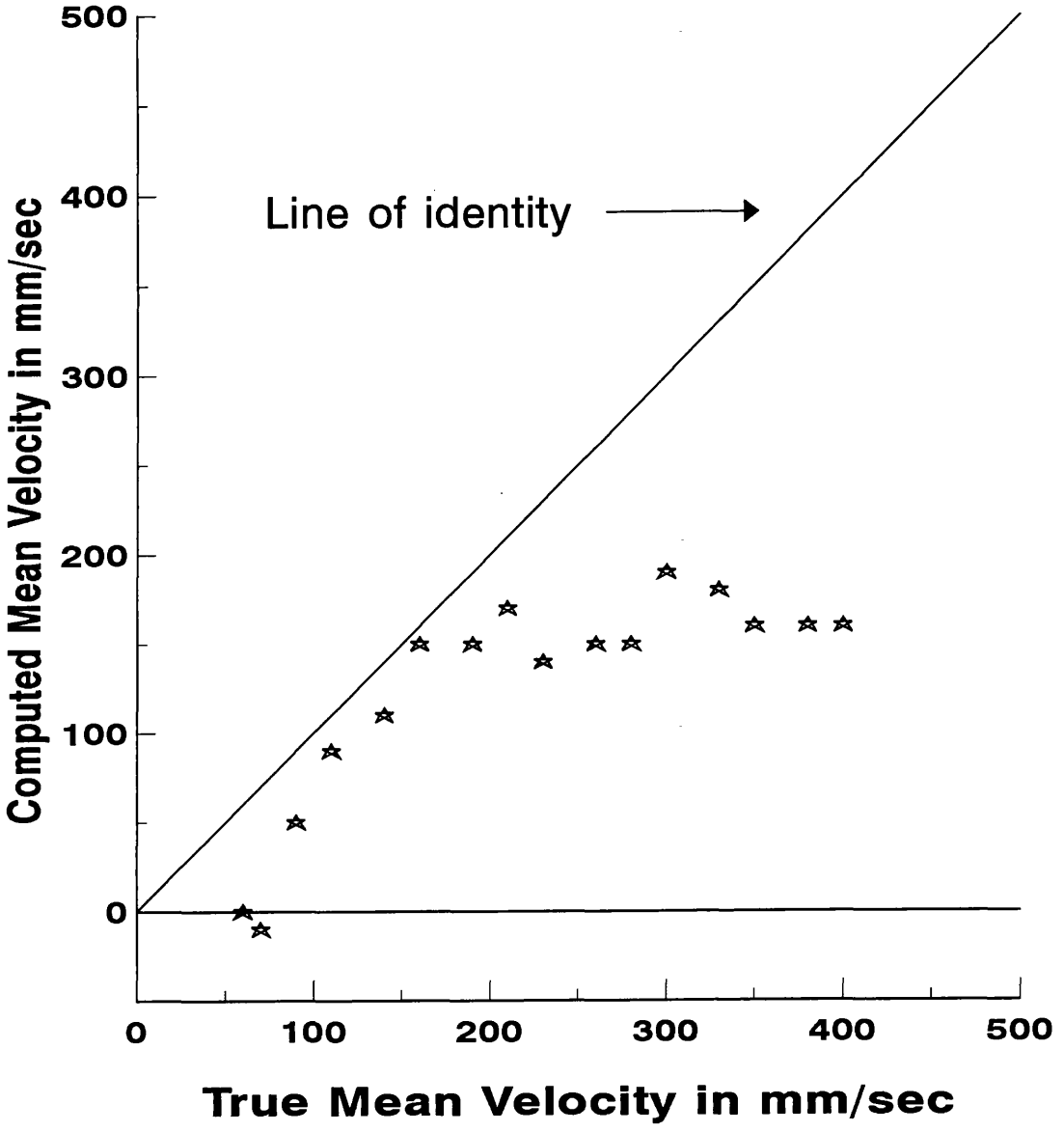

Fig. 7.12. Scatter plot showing the relationship between true mean velocity and the mean velocity estimated by the tracking of bolus mass (Swanson et al 1986) for a 4 mm diameter vessel for 'plug' or constant axial flow pattern. The line represents the line of identity.

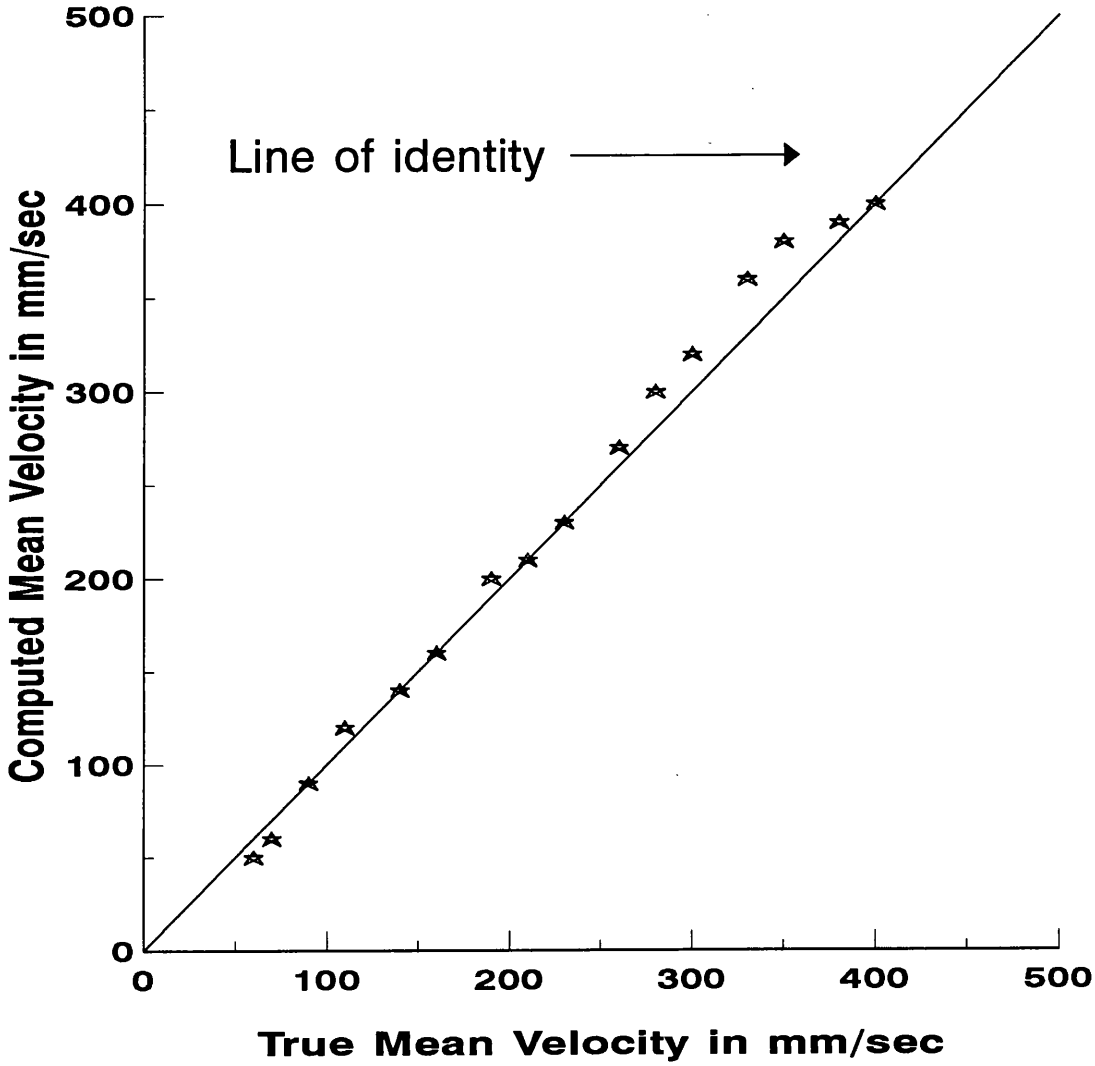

Fig. 7.13. Scatter plot showing the relationship between true mean velocity and the mean velocity estimated by our velocity computing algorithm, for a 4 mm diameter vessel, for a 'plug' or constant axial flow pattern. The line represents the line of identity.

experimentally by others (Colchester et al 1986; du Boulay et al 1987; Swanson et al 1986; Kruger et al 1983). Thus methods based on the comparison of two time-density curves are not suitable for measuring highly pulsatile blood flow.

The tracking of bolus mass method compares favourably with the input profile for low blood flow (fig. 7.5) but fails at high flow rates (fig. 7.6). Either no match is found or incorrect matches are made. Figs 7.8, 7.10 and 7.12 show that the tracking of bolus mass method is able to estimate the mean velocity at low flow rates (up to approximately 150 mm/sec, for a 100 mm length of vessel imaged at 25 frames/sec). However, it underestimates flow at high flow rates, for all four types of injection. These results are due to there being only a finite difference between (a) the total length of blood vessel which is visible within the image and (b) the length of blood vessel which is within the averaging window. This limits the maximum velocity, or distance travelled by the bolus, that can be measured in one frame time interval. When the window was reduced in size to detect higher velocities then the statistical error in the calculated velocities increased significantly. An experiment was performed at the time of the assessment of the technique which confirmed that the optimum sampling window was selected.

Figs 7.9, 7.11 and 7.13 demonstrate that the results obtained using the new technique, which matches distance-density curves over time, are in good agreement with the blood flow waveform over the whole range of blood flow rates investigated, for both laminar and 'plug' flow.

For a 6 mm diameter vessel (fig. 7.9) the matching of distance-density curves over time gave excellent results (r=0.994, n=64, ME=-0.2±0.1 mm/sec) over the entire range of flow rates, with mean blood velocities ranging from 30-360 mm/sec, and peak velocities ranging from 150 to 1860 mm/sec. Within the limits of the experiment, the accuracy of the technique is independent of the four injection strategies.

For laminar blood flow (fig. 7.11), good agreement (r=0.983, n=32, ME=-0.2±2 mm/sec) was obtained for the mean flow velocities of up to 410 mm/sec (mean volume flow rates of 307 ml/min) for 4 mm diameter vessels, and up to 360 mm/sec (mean volume flow rates of 68 ml/min) for 2 mm diameter vessels.

Fig. 7.13 confirms the excellent results obtained for 'plug' flow by matching distance-density curves over a period of time.

The effect of X-ray quantum noise was included in the parametric images generated for these experiments. The problems of the effects of X-ray scatter on image contrast, image artefacts due to misregistration resulting from patient motion, or beam hardening effects resulting from overlying dense structures, especially bone, on the image of the vessel of interest were not investigated at this stage, but will be discussed in a later chapter. These effects may require additional preprocessing steps before the application of a flow extraction algorithm to these images.

The effect of increasing distances between the site of injection and the imaging site was not investigated here but will be discussed in the next chapter. For the injection of contrast material at more remote sites a greater dispersion of the bolus is to be expected and hence some reduction in accuracy for both the bolus mass tracking method and our method for matching distance-density curves over a period of time.

The estimation of instantaneous and mean volume blood flow by matching distance-density curves over time is a robust technique when applied to synthetic data. It was considerably superior to other methods evaluated. In addition it is demonstrated that the method of matching distance-density curves over time is independent of the injection techniques used.

In the next chapter the technique of matching distance-density curves over time is validated using physical experimental data for the range of pulsatile flows expected in clinical practice in blood vessels.

CHAPTER 8

VALIDATION OF FLOW STUDIES IN PHYSICAL MODELS

8.1 INTRODUCTION

This chapter describes the validation of our flow technique (as described in chapters 5 and 6) 'in-vitro', using a physical flow circulation model.

The validation was performed initially using 2D representations of the blood vessel (2D data processing), where dynamic (25 frames/sec) single projection plane X-ray angiographic images were processed. This assumes that the blood vessel lies in a plane parallel to the imaging plane and that the X-ray magnification is known. I refer to this as '2D data processing'. Subsequently, in order to deduce true velocity along a tortuous vessel or vessel not oriented parallel to the imaging plane, the 3D path of the blood vessel relative to the imaging equipment was deduced using digital biplanar X-ray angiographic data. This I refer to as '3D data processing'.

The 3D location of the blood vessel centre line would permit the computation of the radiographic magnification, the angle between the X-ray beam and the vessel long axis, and the true vessel path length. In this chapter the measurement of pulsatile blood flow, in which blood was flowing in vessels which were tortuous in three dimensions, was also validated using a '3D' flow phantom.

8.2 METHODS AND MATERIALS

8.2.1 Construction of The Phantom

In order to assess the performance of the technique, a phantom was constructed to simulate pulsatile blood flow and hence to permit the correlation of flow velocities derived from X-ray angiography with independent flow measurements using an EMF.

The phantom consisted of a variable-speed pump (Bio Medicus, Bio-Medicus Inc., 15307 Industrial Road, Minnetonka, MN 55343, USA), 4-7 m length of flexible polythene tubing, a tubular probe of an EMF (Nycotron Blood Flow Meter 376, A/S Nycotron, PO Box 425-3001, Drammen, Norway) and a solenoid to simulate a pulsatile flow waveform, which included reverse flow (fig. 8.1). Normal saline solution (0.9% sodium chloride by weight) was used throughout the flow circuit. A catheter inserted upstream of the imaging site, by means of a Y-connector, was used to inject contrast material.

Instantaneous flow rates were measured with a 9.5 mm calibre tubular flow probe placed in series, downstream of the imaging site, and a Nycotron EMF connected to a strip chart recorder. An ion chamber was placed to one side of the tube, to record the X-ray exposure times in order to synchronise the EMF flow reading with the X-ray exposure. The ion chamber output was recorded on the same paper trace as the EMF reading. Synchronisation of the frame number of the angiographic run with the EMF trace was obtained by counting pulses derived from the ion chamber on the paper trace. This validation was therefore dependent on the accuracy of the timing of the pulsed exposure from the DSA system. The number of pulses recorded on the paper trace in a ten second sequence were counted and the timing was found to be accurate to within 1-2%. Although measurable, this error may be considered insignificant with respect to the error of the angiographic flow estimates. The distance between the end of the site of the X-ray measurements and the site of the EMF was about 10 mm. In the case of a rigid tube and incompressible fluid, there would not be any time delay, in blood flow waveforms at the two sites. We used polythene tubing, whose elastic properties will introduce a small time delay but this was ignored when comparing flow data.

The instantaneous blood flow was calculated at 0.04 second intervals, corresponding to the X-ray framing rate, and compared with the output of the EMF flowmeter. The flowmeter zero value and full scale deflection were checked before each experiment in order to compensate for DC drift. The probe was calibrated for zero flow by clamping the flexible plastic tube both up and down stream of the meter.

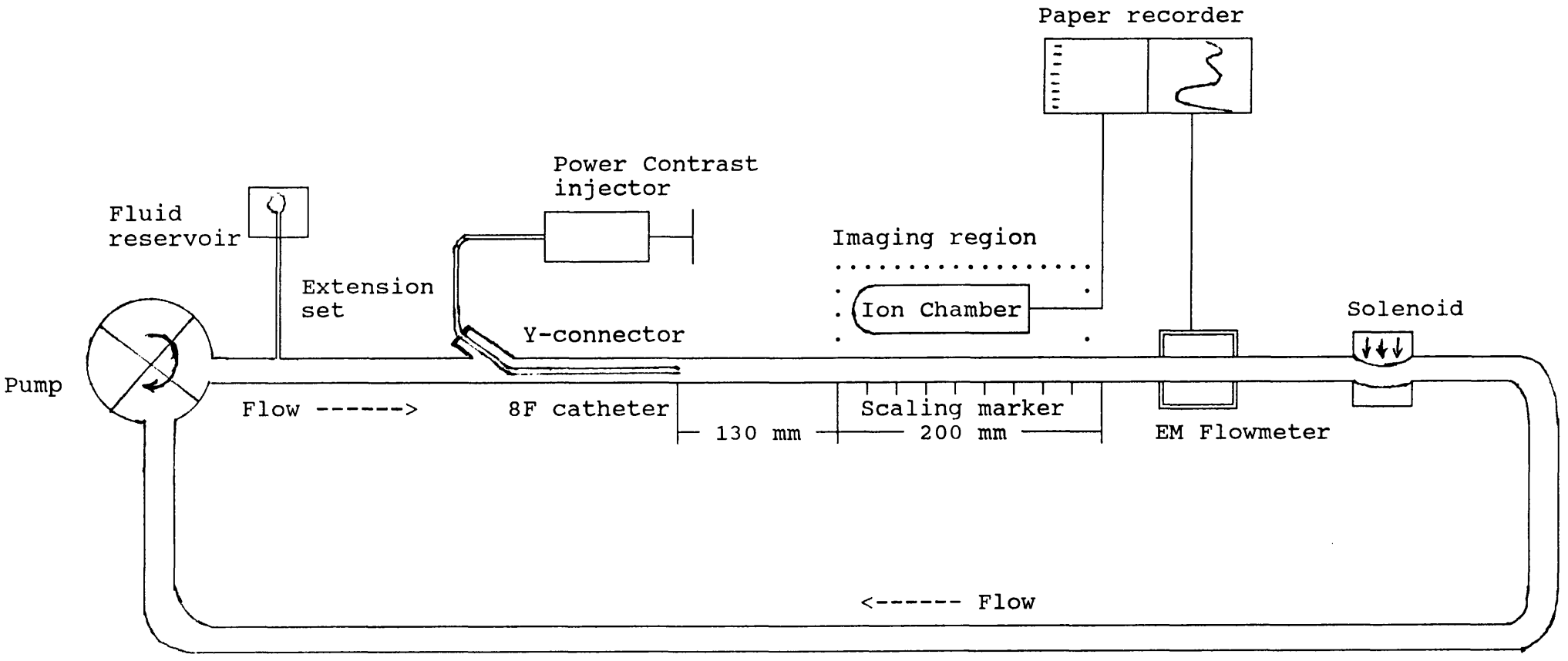

Fig. 8.1. Block diagram of flow phantom.

For phantom studies, Urografin 370 (370 mg of iodine/ml) was injected into the phantom via the catheter with a power injector (Simtrac C, Siemens, Siemens Aktiengesellschaft, Bereich Medizinische Technik, Erlangen, Germany). The injector delivered contrast material at a rate of 3 ml/sec for a 6.6 mm tube diameter (a total volume of 9 ml per injection) during the image acquisition. This was determined empirically to be the optimal injected flow rate. The point of injection was 130 mm upstream from the imaged section of tubing.

For 2D experiments, a 200 mm section of the flexible plastic tube was laid in the X-ray field of view on a perspex tray in an approximately straight line with its long axis parallel to the X-ray table. The flexible plastic tube was taped to the plastic tray to prevent movement caused by pulsatile flow. The X-ray magnification and image scaling were determined using a small metal disc and metal rods placed every 10 mm alongside the tube. The markers were visible on the X-ray image. The EMF measured flow rates are summarised in table 8.1.

In addition, data from two experiments (mean flow rates of 348 and 708 ml/min) were used to assess the effect of the distance between the catheter tip and the measurement site on the accuracy of the measurement. Data corresponding to a 100 mm section of the tube were analysed for distances ranging from 130 to 230 mm between the catheter tip and the start of the analysis site.

The same data sets were used to investigate the effect on the accuracy of the velocity measurements of reducing the vessel length analysed from 200 to 20 mm.

For analysis in 3D, six experiments were performed with the 3D phantom oriented at an angle of 15°, 33° and 35° (for tubes with internal diameters of 6.0, 4.0 and 3.0 mm respectively) to the imaging plane. The parameters of angle and calibre were purely arbitrary. The experimental details are summarised in table 8.1.

Table 8.1. Summary of phantom experiments for 2D and 3D data processing.

Experiment	Data Acquisition	Vessel Calibre (mm)	Vessel Angle to Imaging Plane (°)	Mean EMF Flow (ml/min)	Peak EMF Flow (ml/min)	Peak EMF Back Flow (ml/min)
I	2D	6.6	0	349	1232	-499
II	2D	6.6	0	708	2198	-699
III	2D	6.6	0	1705	4329	-999
IV	2D	4.0	0	339	900	-94
I	3D	6.0	15	586	1295	-70
II	3D	6.0	15	1157	2093	0
III	3D	4.0	33	176	488	-38
IV	3D	4.0	33	271	713	-75
V	3D	4.0	33	687	1763	-225
VI	3D	3.0	35	229	523	-21

8.2.2 Electromagnetic Flowmeter

The flow probe used in the experiments was originally calibrated by the manufacturer (Nycotron, Nycotron Blood Flow Meter 376, A/S Nycotron, PO Box 425-3001, Drammen, Norway). The accuracy of the instrument system was reported, in phantom experiments with blood and other electrolytic fluids, to be of the order of ±5% for mean blood flow. As Wyatt (1984) has reported that the errors of this calibration could be up to 15%. However, I decided to check the calibration of the probe prior to use.

In this thesis, the EMF readings were validated against fluid collection by using normal saline (0.9% sodium chloride by weight). With the available equipment, it was not possible to calibrate the instantaneous flow response of the EMF for pulsatile flow, although its mean flow response was calibrated at several steady flow rates up to 3270 ml/min, both before and after the radiographic experiments.

8.2.3 Radiography

All X-ray images were acquired on the Siemens Digitron II Digital Subtraction Angiographic (DSA) system at Guy's hospital. Images used for flow studies were obtained with a tube voltage between 70 and 80 kV, with a small focal spot in the pulsed X-ray exposure mode (giving an exposure time of 18 milliseconds and an exposure to the image intensifier of 100 μR/frame). Digital image grey values, proportional to the logarithm of the X-ray image brightness, were recorded. For the phantom experiments the X-ray beam was filtered by an additional 1 mm of copper. The digital images were acquired on a 512x512 pixels/frame matrix with 10 bits per pixel at a rate of 25 frames/sec. Up to 6 seconds of data were included in a single image series.

For 3D experiments, the phantom was positioned at the iso-centre of the 'C-arm' gantry of the unit, and the views obtained corresponded to the '45° left anterior oblique projection' (LAO projection) and the '45° right anterior oblique projection' (RAO projection). Although the two projections need not be orthogonal to each other, such projections are usually selected for simplicity. The transformation equations were again computed using a 60 mm perspex cube with 14 steel

markers at well known locations. Images of the cube were acquired with the X-ray equipment in the same positions as those used during the study (see chapter 5 for details).

8.2.4 Image Analysis

The SUN 4/260 Graphic workstation with a UNIX operating system was used for image analysis. The data were stored on an erasable optical disc.

All the image information from the DSA were transferred to the SUN Graphics workstation for further analysis. The following procedures were taken to set up images for flow analysis:

(1) all images were converted to a common format,
(2) an image 'mask' was generated by averaging four frames before the appearance of contrast material,
(3) this mask was subtracted from all subsequent images in the study,
(4) for vessel edge detection, an image was created by summing 20 frames of mask subtracted images,
(5) corresponding cube (in the case of 3D analysis) and phantom images were combined and appended with one header to form a single image file. The parametric images were generated using this image file as described in detail in chapters 5 and 6. In the 3D data processing technique the vertical axis (vessel length) of the parametric image was converted from pixel units to mm using the data from the 3D centre line path length and finally normalised (see chapters 5 and 6).

The flow velocity waveform was calculated using the algorithm described in chapter 6. The blood velocity estimates were converted to volume flow by multiplying by the actual vessel cross-sectional area, which was measured manually using a calliper. The estimated error in the area measurement was 1-1.5%, determined by six repeat measurements. To estimate the accuracy of our velocity algorithm for a different vessels diameters (3.0-6.6 mm) and different flow rate (with peak velocity ranging from 600 to 2337 mm/sec), the actual cross-sectional area were used for calculation of volume flow rate. This was because

I was interested in determing the accuracy of the velocity flow measurements. The cross-sectional area technique used in clinical study in chapter 9 has been extensively validated by others (see chapter 4) and in addition has been validated and accuracy has been determined by me (see chapter 5).

8.2.5 Statistical Methods

All the data generated in this study were analysed using simple regression modelling with one predictor and one outcome variable, where *Y* is the X-ray angiographic flow in ml/min and *X* is the EMF reading in ml/min. The degree of linearity between the two variables was expressed by the correlation coefficient, with 1.00 indicating perfect correlation.

The degree of agreement between the EMF reading and the angiographic technique was also analysed using the percentage mean error calculated as: ((EMF - Angiography)/EMF)x100.

8.3 RESULTS

8.3.1 Electromagnetic Flowmeter

Results of the calibration of the EMF, by comparison of the actual flow rates using fluid (normal saline solution) collection versus the EMF readings, are shown in fig. 8.2. This is the type of solution used in flow circulation. Flow rates computed from fluid collection ranged from 75 to 3270 ml/min, with corresponding EMF readings ranging from 68 to 2850 ml/min. Linear regression of the data yielded the best fit equation:

$$Y = -27.7 + 1.11X \qquad (8.1)$$

where *Y* is the fluid collection in ml/min and *X* is the EMF reading in ml/min. The standard deviation of the slope was 0.021 and of the Y-intercept: 30.21.

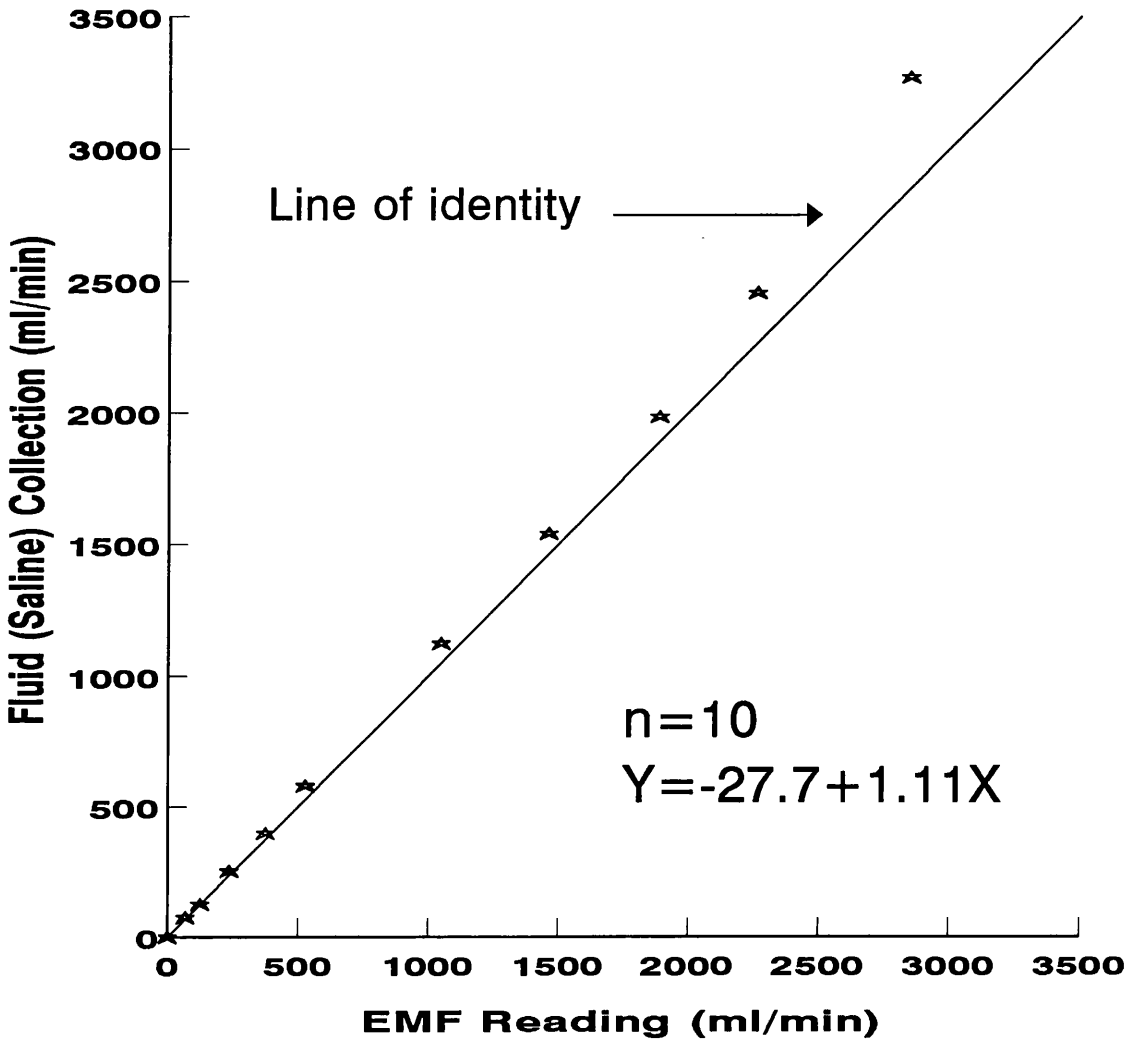

Fig. 8.2. Relationship between flow determined from timed fluid (saline) collection and the electromagnetic flowmeter (EMF) mean flow reading.

8.3.2 2D Data Processing

For the 6.6 mm calibre tube, figs 8.3, 8.4 and 8.5 show (a) the parametric images and (b) the flow waveforms extracted from the parametric images simultaneously with the reading of the EMF. A comparison of the radiographic and the corrected EMF estimates of mean, peak and back flow velocities with the statistical analysis of the results is shown in table 8.2.

These results demonstrate that our estimation of the velocity waveforms is in good agreement with the blood flow waveform measured by an independent method, the EMF, for mean flow rates of 349 and 708 ml/min with peak flow rates of 1232 and 2198 ml/min respectively, but failed at the very high flow rate of 1705 ml/min in which the peak flow rate reached 4329 ml/min. The shape of the blood flow waveform is faithfully reproduced, but there was an overestimation of peak flow rate by 17% at low flow rates (peak flow rate of 1232 ml/min), reducing to 8% at a 2198 ml/min peak flow rate with an underestimation of 29% at the peak flow rate of 4329 ml/min.

As in the two results at lower flow in the first experiments, again for a tube of diameter 4.0 mm, the correct shape of the blood flow waveform is reproduced for two cardiac cycles (fig. 8.6) but there is an overestimation by 10% for the peak flow rate of 1026 ml/min (table 8.2). Again lack of a contrast concentration gradient along the vessel during certain phases of the cycle resulted in no angiographic flow data, but in this case this corresponded to very low flow rates in the phantom.

Table 8.3 shows the effect that the distance between the injection site and imaging site had on the flow estimates. Data was analysed for a 100 mm length of tube beginning at a distance of between 130 and 230 mm from the injection site for a 6.6 mm calibre tube. The results showed that the effect of the injection site on our velocity algorithm was dependent on flow rate. The location of the injection site had less effect on the accuracy of the technique over the range of 130 to 230 mm between the injection and measurement sites at a mean flow rates of 349 ml/min. The mean flow estimates however showed a systematic fall at high flow rate (mean 708 ml/min) as the measurement site was moved away

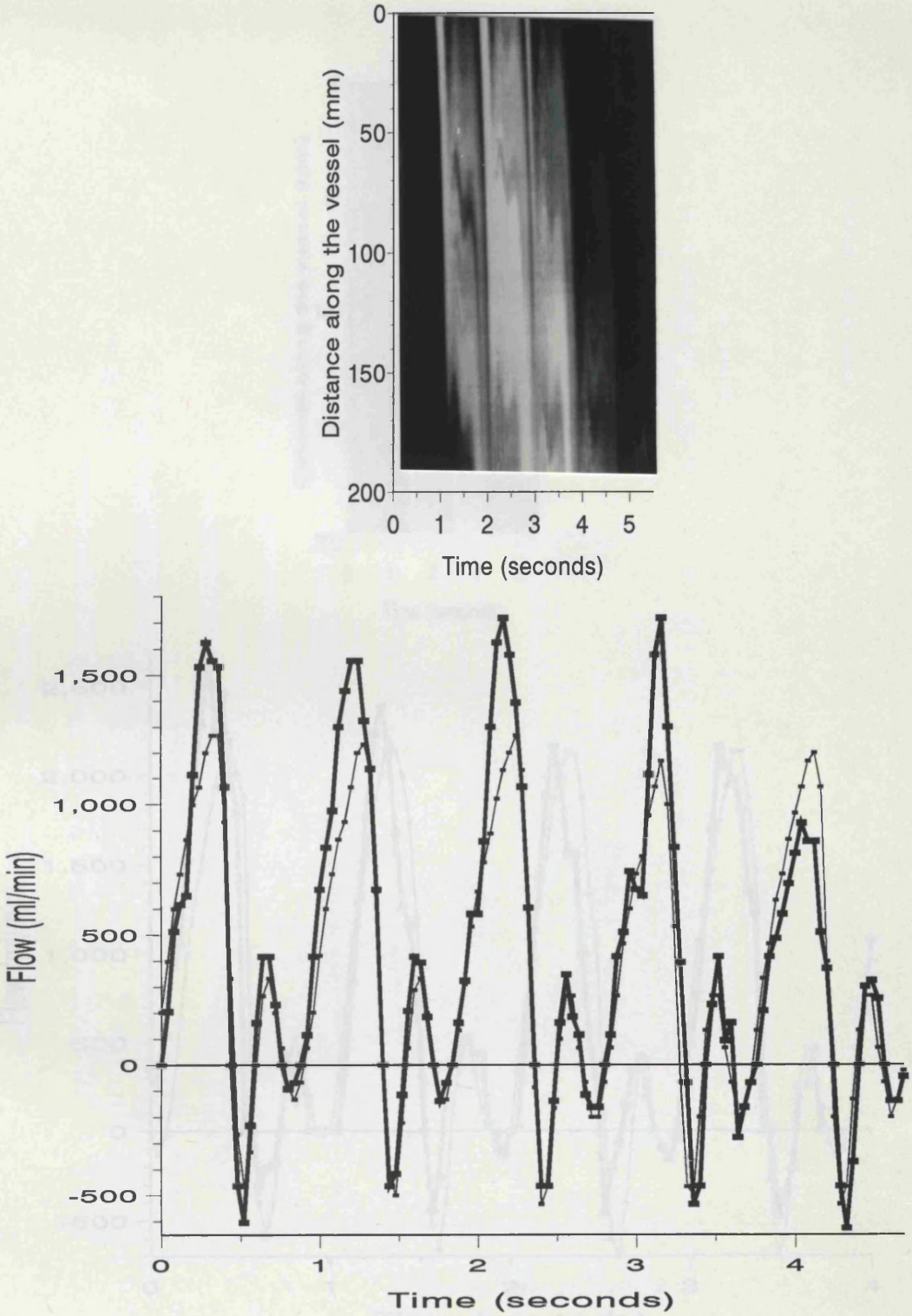

Fig. 8.3. (a) Parametric image generated by 2D data processing for a 6.6 mm calibre with a mean blood flow of 348 ml/min. (b) Direct comparison of volume flow waveforms measured synchronously using the standard EMF (thin lines) and from the parametric image using our velocity computing algorithm (thick lines).

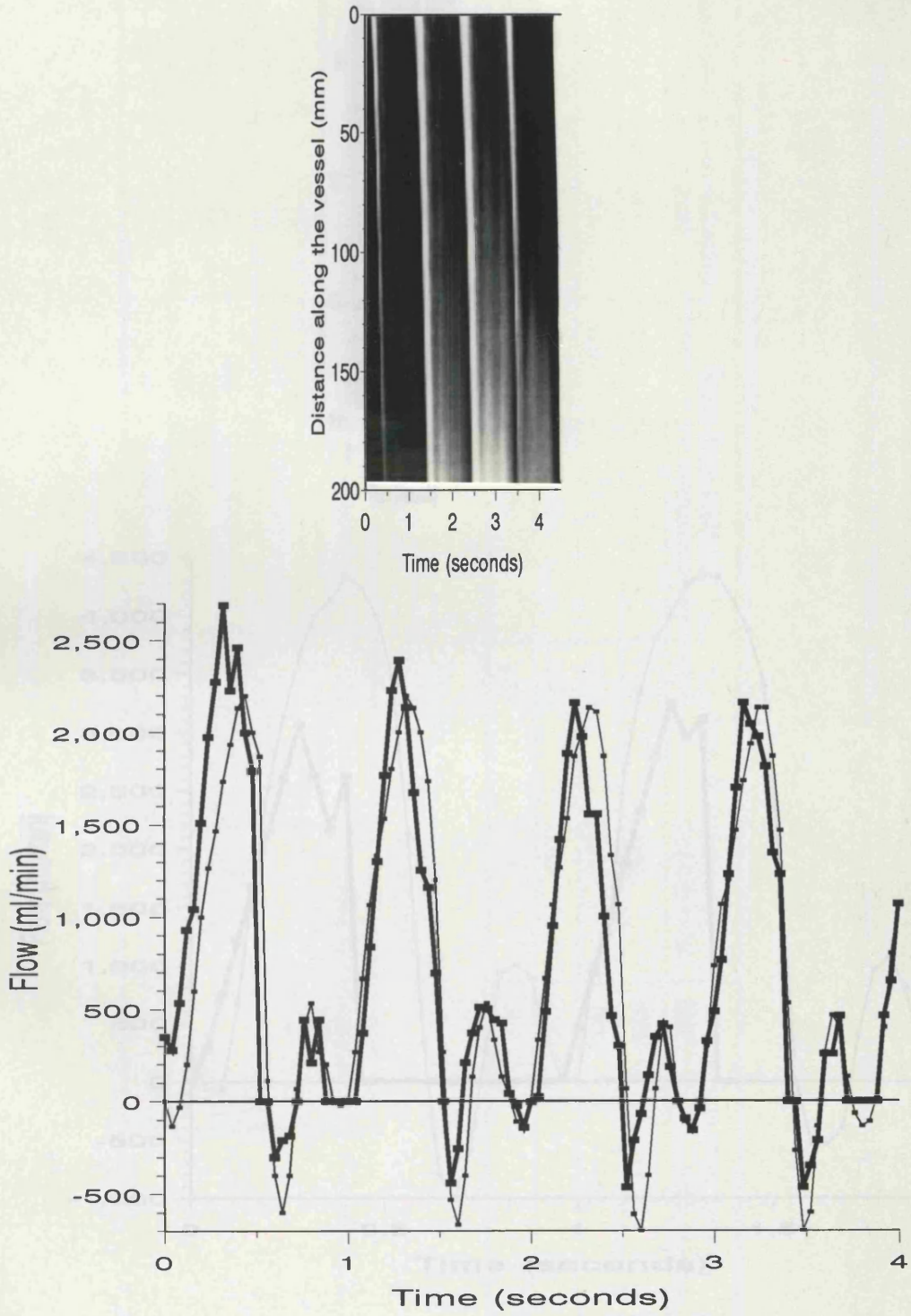

Fig. 8.4. (a) Parametric image generated by 2D data processing for a 6.6 mm calibre with a mean blood flow of 708 ml/min. (b) Direct comparison of volume flow waveforms measured synchronously using the standard EMF (thin lines) and from the parametric image using our velocity computing algorithm (thick lines).

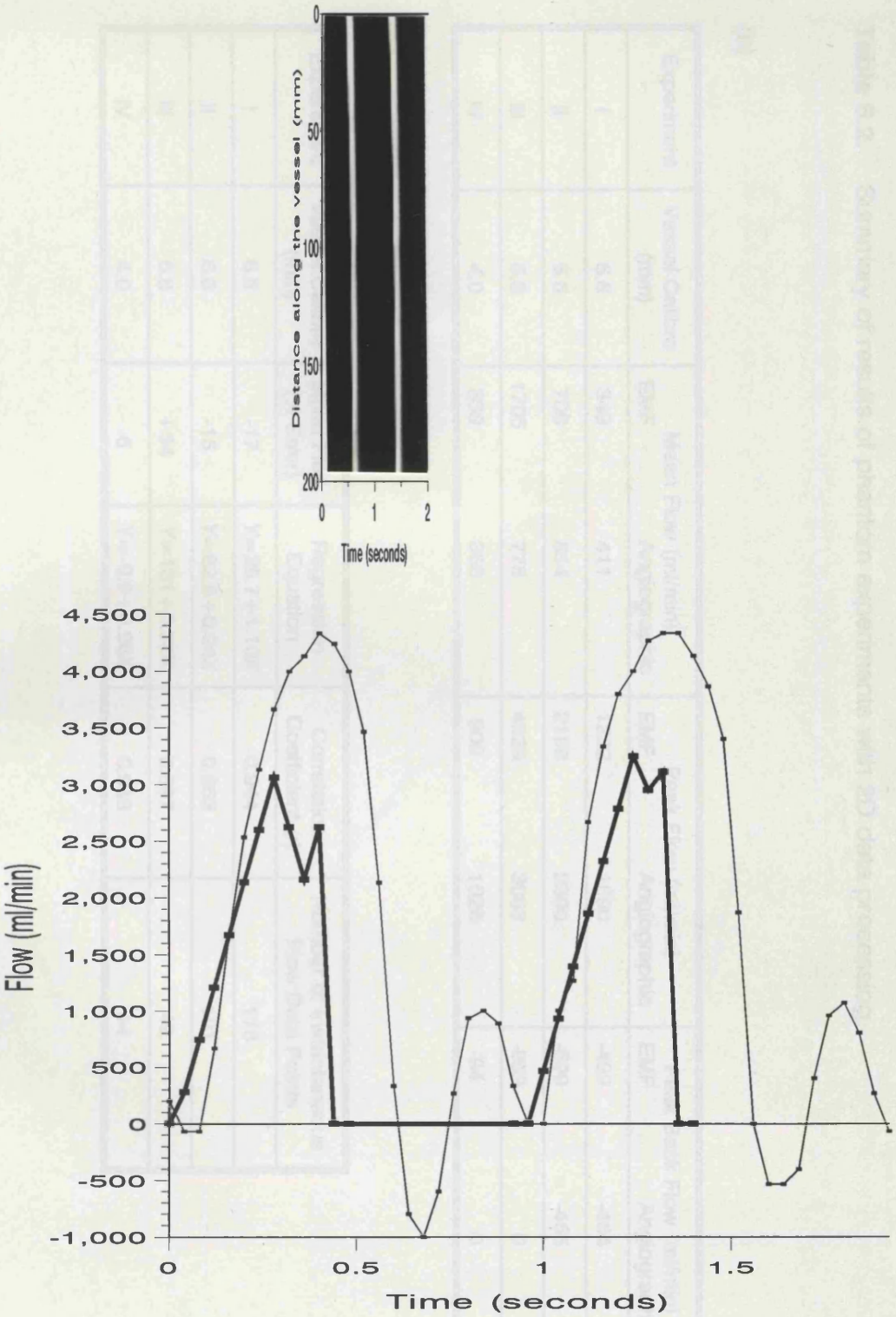

Fig. 8.5. (a) Parametric image generated by 2D data processing for a 6.6 mm calibre with a mean blood flow of 1705 ml/min. (b) Direct comparison of volume flow waveforms measured synchronously using the standard EMF (thin lines) and from the parametric image using our velocity computing algorithm (thick lines).

Table 8.2. Summary of results of phantom experiments with 2D data processing.

(a)

Experiment	Vessel Calibre (mm)	Mean Flow (ml/min)		Peak Flow (ml/min)		Peak Back Flow (ml/min)		Peak Velocity (mm/sec)	
		EMF	Angiographic	EMF	Angiographic	EMF	Angiographic	EMF	Angiography
I	6.6	349	411	1232	1690	-499	-464	600	823
II	6.6	708	814	2198	2390	-699	-465	1070	1164
III	6.6	1705	778	4329	3063	-999	0	2108	1492
IV	4.0	339	358	900	1026	-94	0	1193	1360

(b)

Experiment	Vessel Calibre (mm)	Mean Flow (% Error)	Regression Equation	Correlation Coefficient (r)	Number of Instantaneous Flow Data Points
I	6.6	-17	$Y=26.7+1.10X$	0.944	118
II	6.6	-15	$Y=82.6+0.94X$	0.863	101
III	6.6	+54	$Y=131+0.38X$	0.597	49
IV	4.0	-6	$Y=-0.9+0.96X$	0.948	44

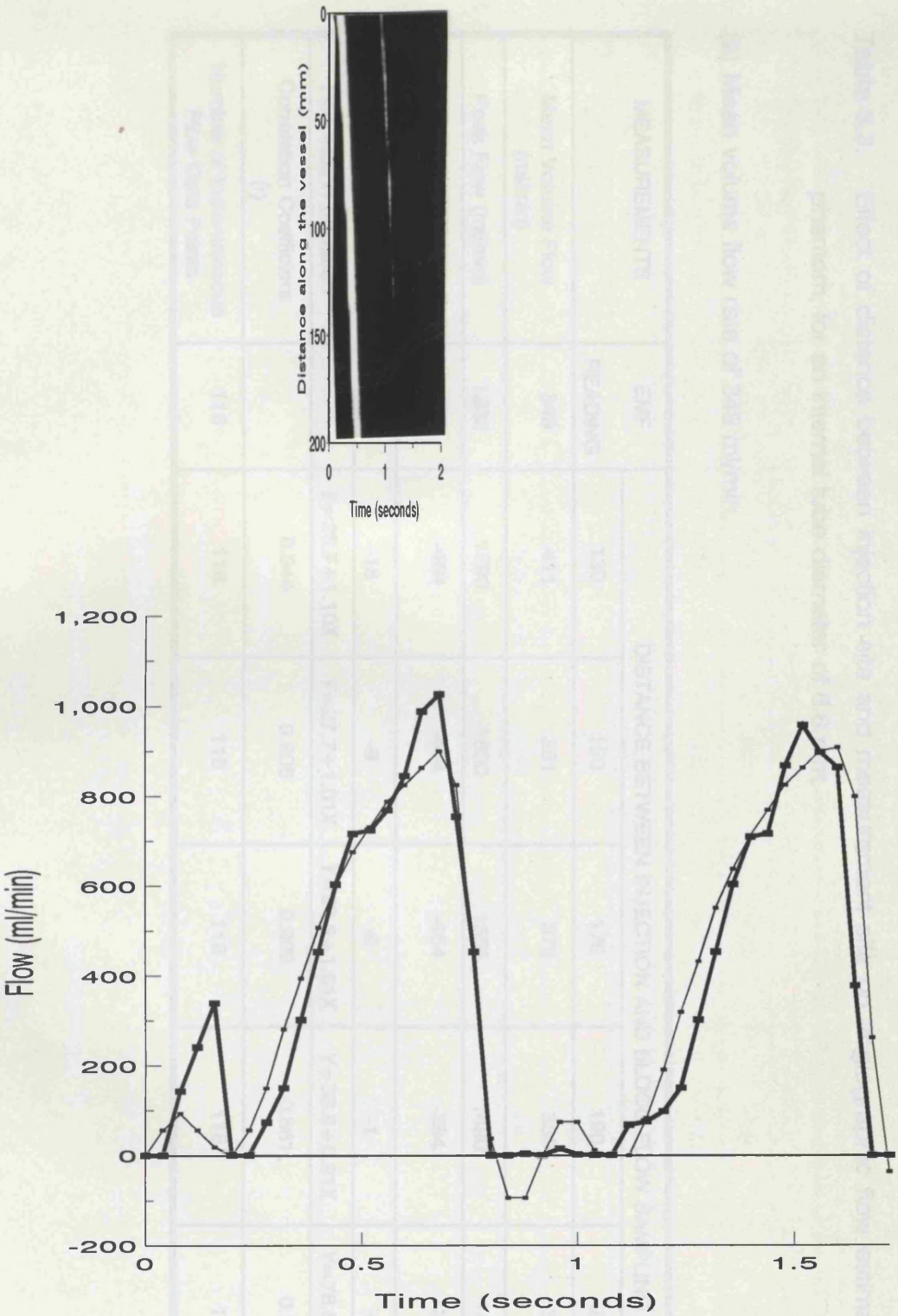

Fig. 8.6. (a) Parametric image generated by 2D data processing for a 4.0 mm calibre with a mean blood flow of 339 ml/min. (b) Direct comparison of volume flow waveforms measured synchronously using the standard EMF (thin lines) and from the parametric image using our velocity computing algorithm (thick lines).

Table 8.3. Effect of distance between injection site and measurement site on angiographic flow estimates using the experimental phantom, for an internal tube diameter of 6.6 mm.

(a) Mean volume flow rate of 349 ml/min.

MEASUREMENTS	EMF READING	DISTANCE BETWEEN INJECTION AND BLOOD FLOW SAMPLING SITES (mm)					
		130	150	170	190	210	230
Mean Volume Flow (ml/min)	349	411	381	379	350	340	339
Peak Flow (ml/min)	1232	1690	1600	1555	1490	1462	1460
Peak Back Flow (ml/min)	-499	-464	-464	-464	-394	-380	-380
Mean Flow (% Error)		-18	-9	-9	-1	+3	+3
Regression Equation		$Y=26.7+1.10X$	$Y=27.7+1.01X$	$Y=26.6+1.01X$	$Y=33.8+0.91X$	$Y=78.5+0.75X$	$Y=91.6+0.71X$
Correlation Coefficient (r)		0.944	0.905	0.909	0.861	0.790	0.763
Number of Instantaneous Flow Data Points	118	118	118	118	118	118	118

(b) Mean volume flow rate of 708 ml/min.

MEASUREMENTS	EMF READING	DISTANCE BETWEEN INJECTION AND BLOOD FLOW SAMPLING SITES (mm)					
		130	150	170	190	210	230
Mean Volume Flow (ml/min)	708	682	523	510	416	410	402
Peak Flow (ml/min)	2198	2390	1856	1856	1578	1578	1717
Peak Back Flow (ml/min)	-699	-465	-649	-696	-696	-696	-696
Mean Flow (% Error)		+4	+26	+28	+41	+42	+43
Regression Equation		$Y=82.6+0.94X$	$Y=44.2+0.77X$	$Y=5.3+0.61X$	$Y=52.6+0.58X$	$Y=-1.3+0.54X$	$Y=-8.1+0.66X$
Correlation Coefficient (r)		0.863	0.842	0.811	0.774	0.755	0.751
Number of Instantaneous Flow Data Points	101	101	101	101	101	101	101

from the catheter position over this range.

Table 8.4 shows the effect that reducing the length of the tube analysed had on the fluid velocity estimation. The length of vessel analysed ranged from 200 to 20 mm. The mean flow estimates showed a systematic fall as the length of tube analysed was reduced. For smaller tube lengths the velocity algorithm was more likely to fail, which may explain this result. This was due to the maximum velocity detectable by our velocity algorithm being about less than the length of the vessel segment analysed per frame interval, therefore as the length of the vessel reduced so did the maximum detectable velocity. In other words, in the comparison of two distance-density curves, some of the same portions of the bolus must appear in the two profiles. This is entirely dependent on the frame rate acquisition and length of vessel imaged; the frame rate must be high enough so that a portion of the bolus imaged in one frame appears in the subsequent frame. This was demonstrated by poor accuracy in the flow data for shorter vessels (see table 8.4).

8.3.3 3D Data Processing

Six experiments were performed with the 3D data structures in which flow was computed as a 3D vector after reconstruction in 3D of the course of the vessel containing the contrast material. These experiments were performed to study the effects of correction for vessel foreshortening on the accuracy of the flow measurements. These were performed for various flow settings and calibre sizes and the experimental details are summarised in table 8.1. The results for each experiment are presented and discussed in this subsection.

For the 6.00 mm calibre tube two different flow rates were used. Fig. 8.7 shows the flow waveforms produced from the parametric image in the experiments with a mean EMF flow rate of 586 ml/min. As is shown in the fig. 8.7 the flow waveform derived from the X-ray angiogram follows very closely that derived from the EMF with excellent correlation between the two instantaneous flow rates (table 8.5(b)). But, in the region of peak flows, the angiographic technique tends to overestimate by 4% (table 8.5(a)).

Table 8.4. The effect on angiographic flow estimates of reducing sampled length, for an internal tube diameter of 6.6 mm.

(a) Mean volume flow rate of 349 ml/min.

MEASUREMENTS	EMF READING	LENGTH OF VESSEL ANALYSED (mm)					
		200	150	100	50	40	20
Mean Volume Flow (ml/min)	349	413	367	345	218	234	159
Peak Flow (ml/min)	1232	1694	1680	1555	1550	1540	835
Peak Back Flow (ml/min)	-500	-464	-464	-464	-418	-418	-418
Peak Velocity (mm/sec)	600	825	818	757	754	750	407
Mean Flow (% Error)		-18	-5	1	38	33	54
Regression Equation		$Y=54.8+1.02X$	$Y=59.5+0.99X$	$Y=80.6+0.90X$	$Y=76.1+0.52X$	$Y=110.0+0.47X$	$Y=78.0+0.31X$
Correlation Coefficient (r)		0.954	0.917	0.901	0.618	0.583	0.455
Number of Instantaneous Flow Data Points	105	105	105	105	105	105	105

(b) Mean volume flow rate of 708 ml/min.

MEASUREMENTS	EMF READING	LENGTH OF VESSEL ANALYSED (mm)					
		200	150	100	50	40	20
Mean Volume Flow (ml/min)	708	814	568	403	312	299	244
Peak Flow (ml/min)	2198	2367	2134	1879	1810	1810	835
Peak Back Flow (ml/min)	-699	-696	-696	-441	-418	-418	-418
Peak Velocity (mm/sec)	1070	1153	1039	915	881	881	407
Mean Flow (% Error)		-15	20	43	56	58	65
Regression Equation		$Y=74.6+1.21X$	$Y=72.3+1.11X$	$Y=92.8+0.91X$	$Y=87.3+0.58X$	$Y=115.0+0.52X$	$Y=89.1+0.34X$
Correlation Coefficient (r)		0.954	0.916	0.831	0.608	0.577	0.445
Number of Instantaneous Flow Data Points	96	96	96	96	96	96	96

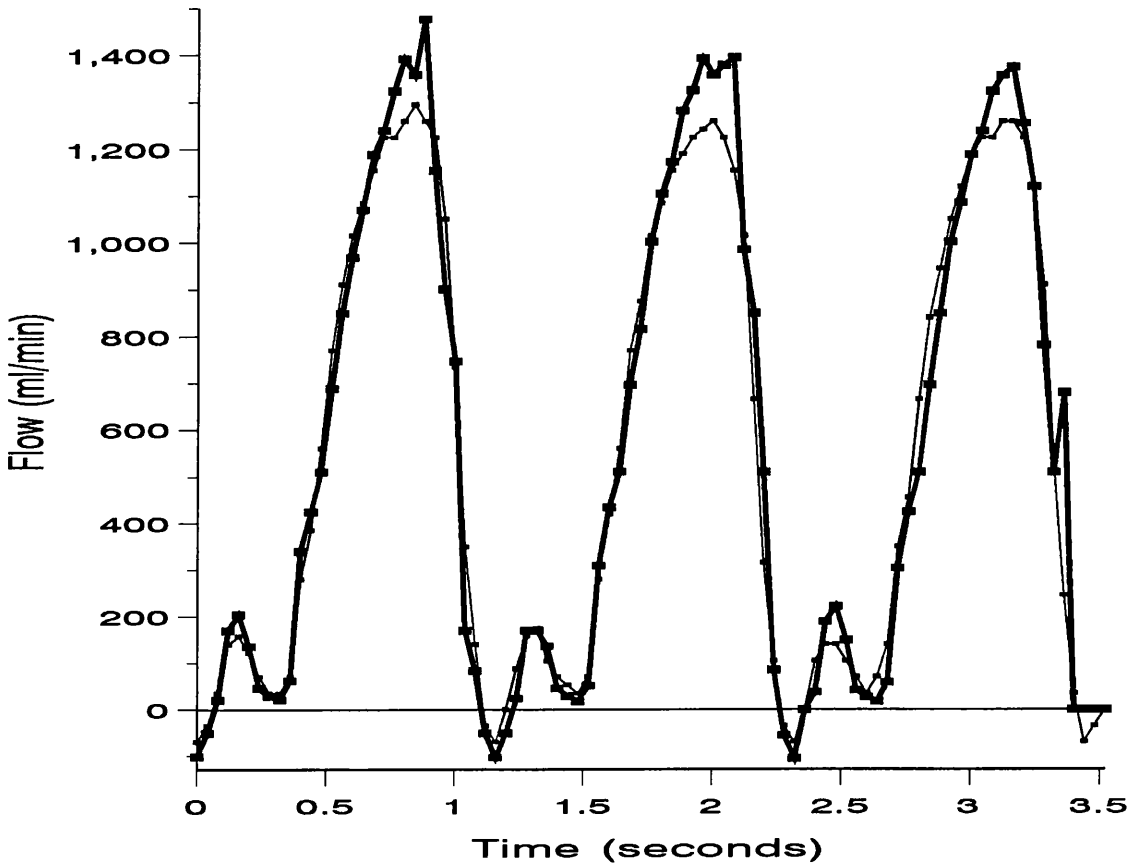

Fig. 8.7. Direct comparison of volume flow waveforms measured synchronously using the standard EMF (thin lines) and from the parametric image using our velocity computing algorithm (thick lines) for a tube of 6.0 mm lumen diameter with a mean fluid flow of 586 ml/min (parametric image generated by 3D data processing).

A much higher flow rate is shown in fig. 8.8; the parametric image and waveforms were produced from images acquired with a mean EMF flow rate of 1157 ml/min. The boluses produced several sharp edges with steep slopes in the parametric image (fig. 8.8(a)), which correspond closely to the peak flows. However, though the peak flow measured by EMF and angiography showed very close agreement, only the tailing edges of each pulse provided reasonable flow data which were detectable by the angiographic technique. The time of arrival of the bolus of contrast material was shortly after the beginning of systole and therefore the leading edge of the systolic waveform contained no flow data.

Using the 4.0 mm calibre tube, three experiments were performed with mean flow rates of 176, 271 and 689 ml/min, with corresponding peak velocities measured by the EMF of 647, 945 and 2337 mm/sec (table 8.5). Figs 8.9, 8.10 and 8.11 show parametric images from flow waveforms with characteristics which, including reverse flow (less evident in the higher flow rate of 689 ml/min), faithfully reproduced these reverse flows.

The last experiment was designed to test the angiographic technique of flow measurements in a smaller calibre (3.0 mm) vessel. Fig. 8.12 shows the flow waveforms obtained together with the EMF reading. The mean flow rate was 229 ml/min (with a peak EMF velocity of 1232 mm/sec). There was an overestimation by 19% of the flow when considering the first peak, which reduced to 11% for the second peak. The angiographic technique showed close agreement with the EMF and produced an accurate mean flow estimate (table 8.5).

8.4 DISCUSSION AND CONCLUSION

The purpose of this study was to evaluate the accuracy of an X-ray angiographic technique for the measurement of instantaneous pulsatile blood flow velocity. The technique was based on the matching of distance-density curves over time. A circulation phantom was constructed to simulate normal arterial blood flow in order to generate angiographic data. The experiments covered a wide range of flow rates, similar to physiological values found in the human circulation.

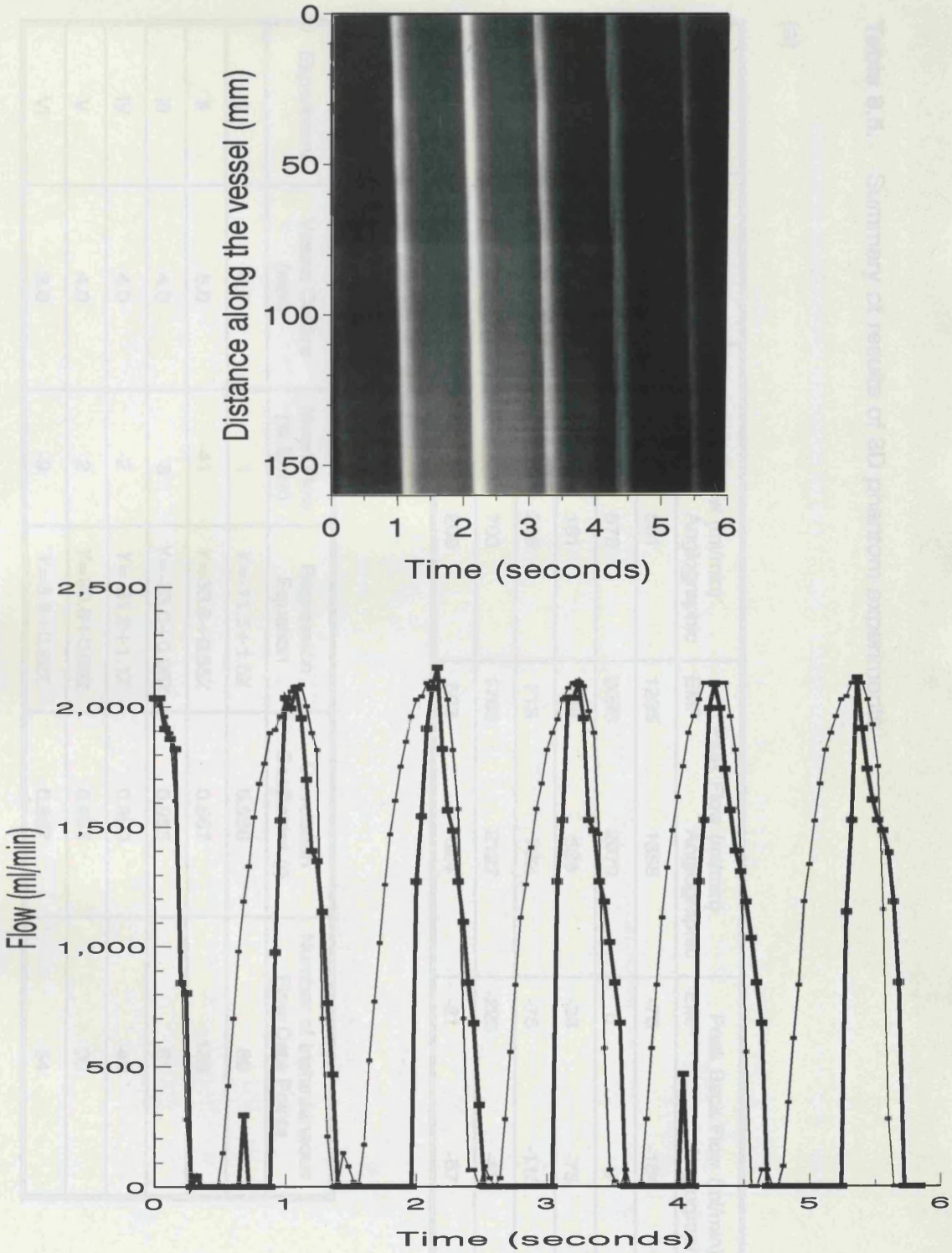

Fig. 8.8. (a) Parametric image generated by 3D data processing for a 6.0 mm calibre with a mean blood flow of 1157 ml/min. (b) Direct comparison of volume flow waveforms measured synchronously using the standard EMF (thin lines) and from the parametric image using our velocity computing algorithm (thick lines).

Table 8.5. Summary of results of 3D phantom experiments

(a)

Experiment	Vessel Calibre (mm)	Mean Flow (ml/min)		Peak Flow (ml/min)		Peak Back Flow (ml/min)		Peak Velocity (mm/sec)	
		EMF	Angiographic	EMF	Angiographic	EMF	Angiographic	EMF	Angiographic
I	6.0	586	591	1295	1358	-70	-104	763	800
II	6.0	1157	673	2093	2079	0	0	1233	1225
III	4.0	176	181	488	528	-38	-75	647	700
IV	4.0	271	266	713	792	-75	-113	945	1050
V	4.0	689	703	1763	2127	-225	-45	2337	2820
VI	3.0	229	209	523	624	-21	-67	1232	1471

(b)

Experiment	Vessel Calibre (mm)	Mean Flow (% Error)	Regression Equation	Correlation Coefficient (r)	Number of Instantaneous Flow Data Points
I	6.0	1	$Y=-11.5+1.0X$	0.986	89
II	6.0	-41	$Y=33.9+0.55X$	0.567	135
III	4.0	3	$Y=-23.0+0.96X$	0.955	61
IV	4.0	-2	$Y=-21.2+1.1X$	0.990	48
V	4.0	2	$Y=30.8+0.98X$	0.955	30
VI	3.0	-9	$Y=8.8+0.92X$	0.857	54

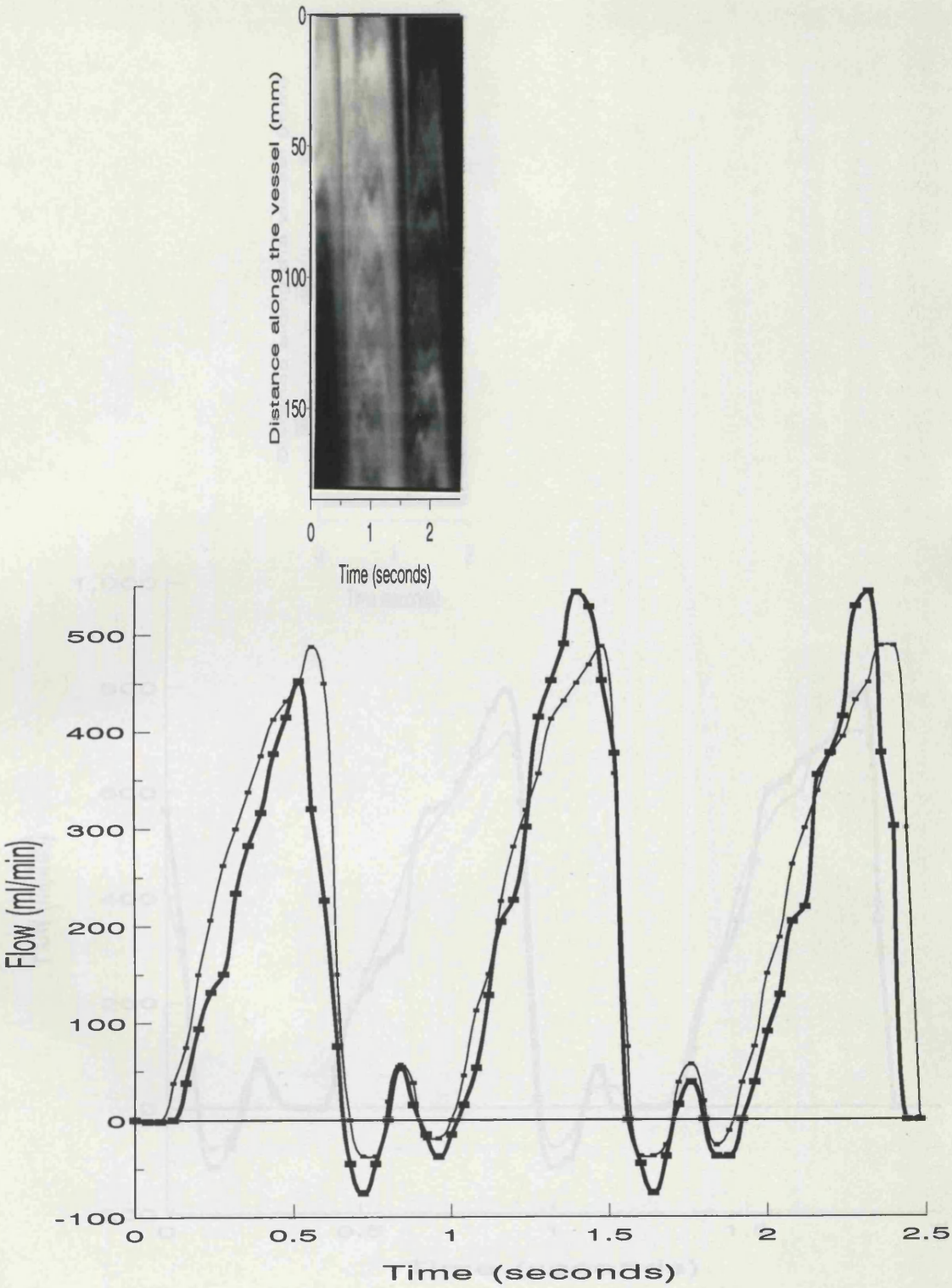

Fig. 8.9. (a) Parametric image generated by 3D data processing for a 4.0 mm calibre with a mean blood flow of 176 ml/min. (b) Direct comparison of volume flow waveforms measured synchronously using the standard EMF (thin lines) and from the parametric image using our velocity computing algorithm (thick lines).

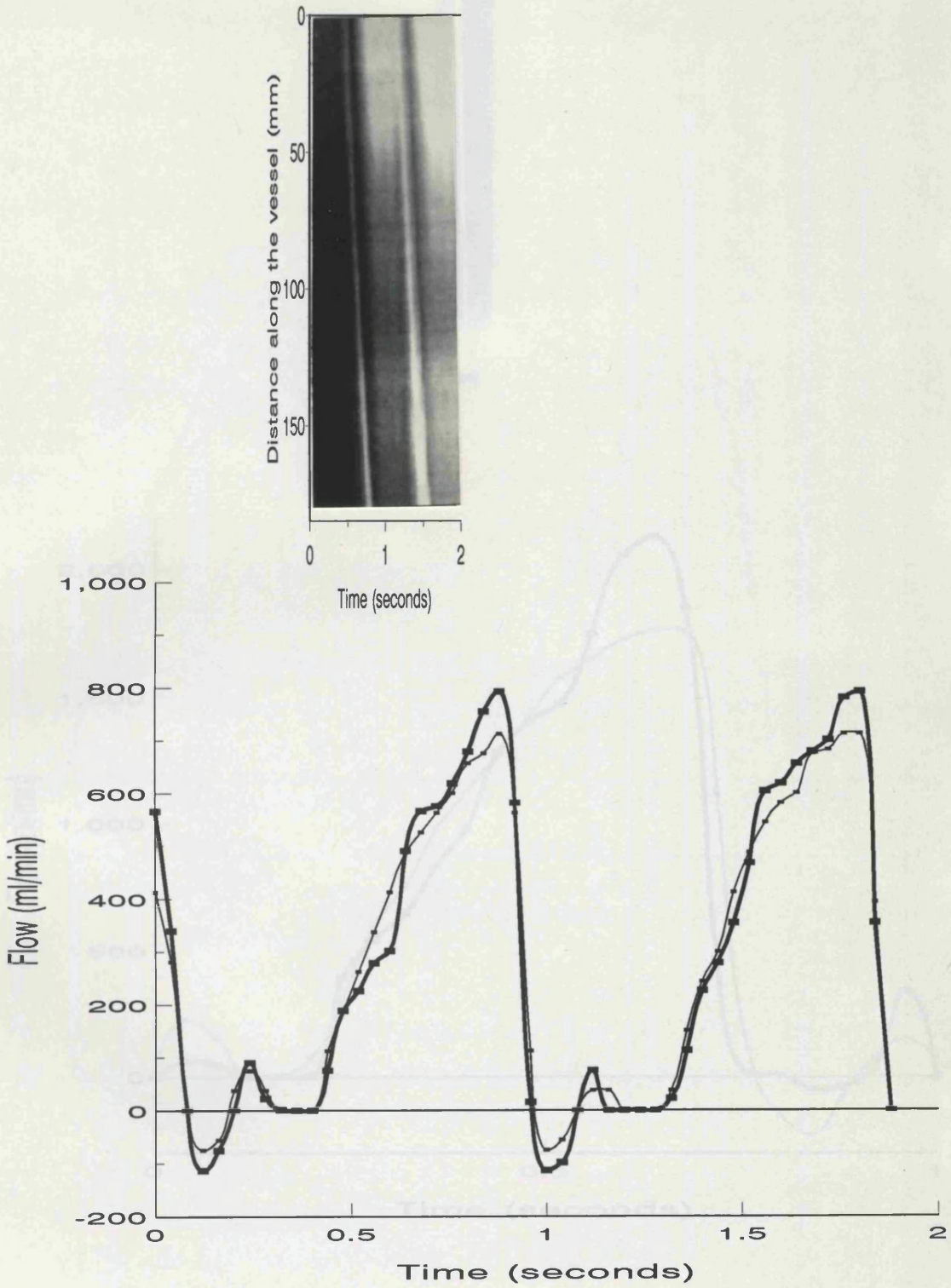

Fig. 8.10. (a) Parametric image generated by 3D data processing for a 4.0 mm calibre with a mean blood flow of 271 ml/min. (b) Direct comparison of volume flow waveforms measured synchronously using the standard EMF (thin lines) and from the parametric image using our velocity computing algorithm (thick lines).

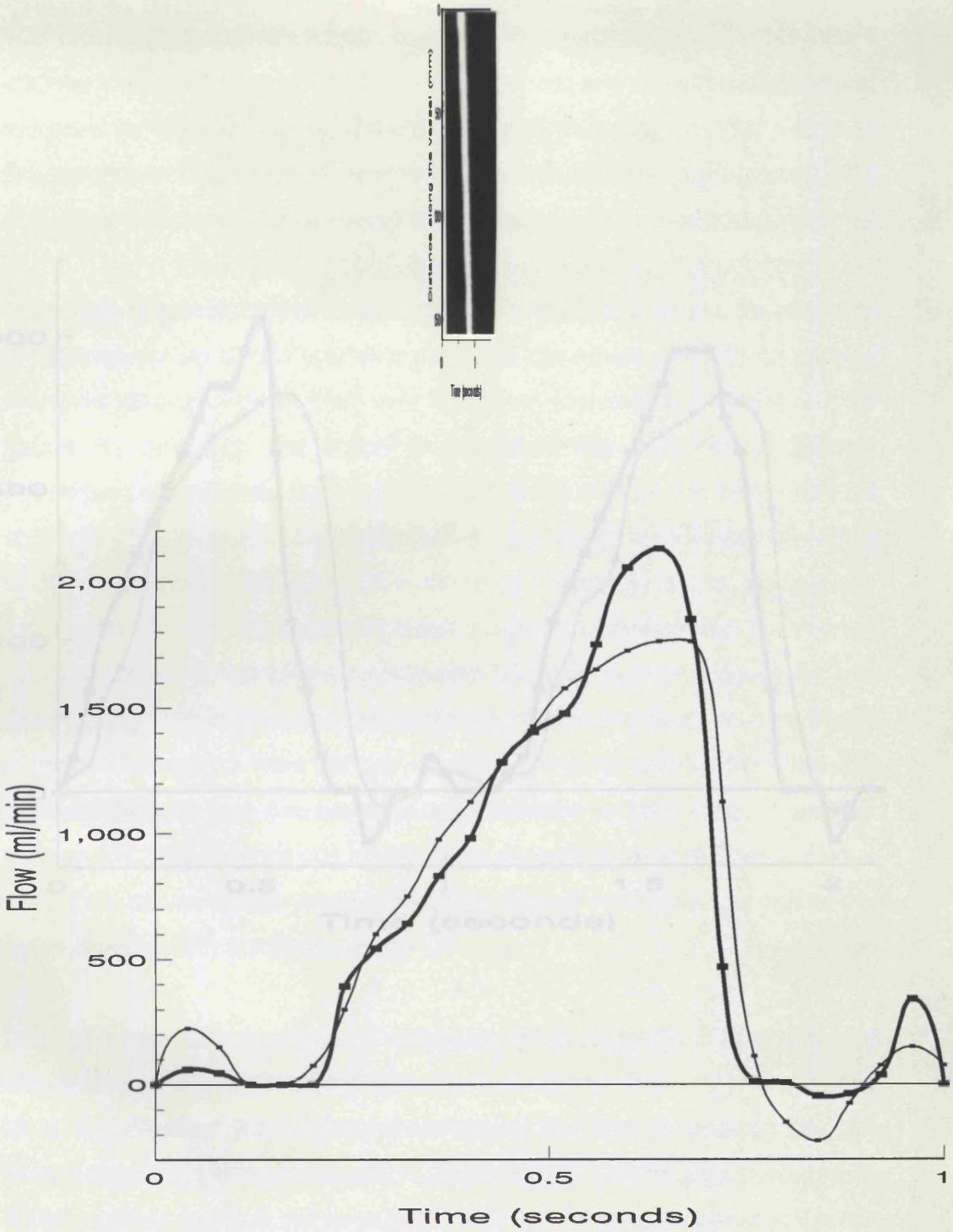

Fig. 8.11. (a) Parametric image generated by 3D data processing for a 4.0 mm calibre with a mean blood flow of 687 ml/min. (b) Direct comparison of volume flow waveforms measured synchronously using the standard EMF (thin lines) and from the parametric image using our velocity computing algorithm (thick lines).

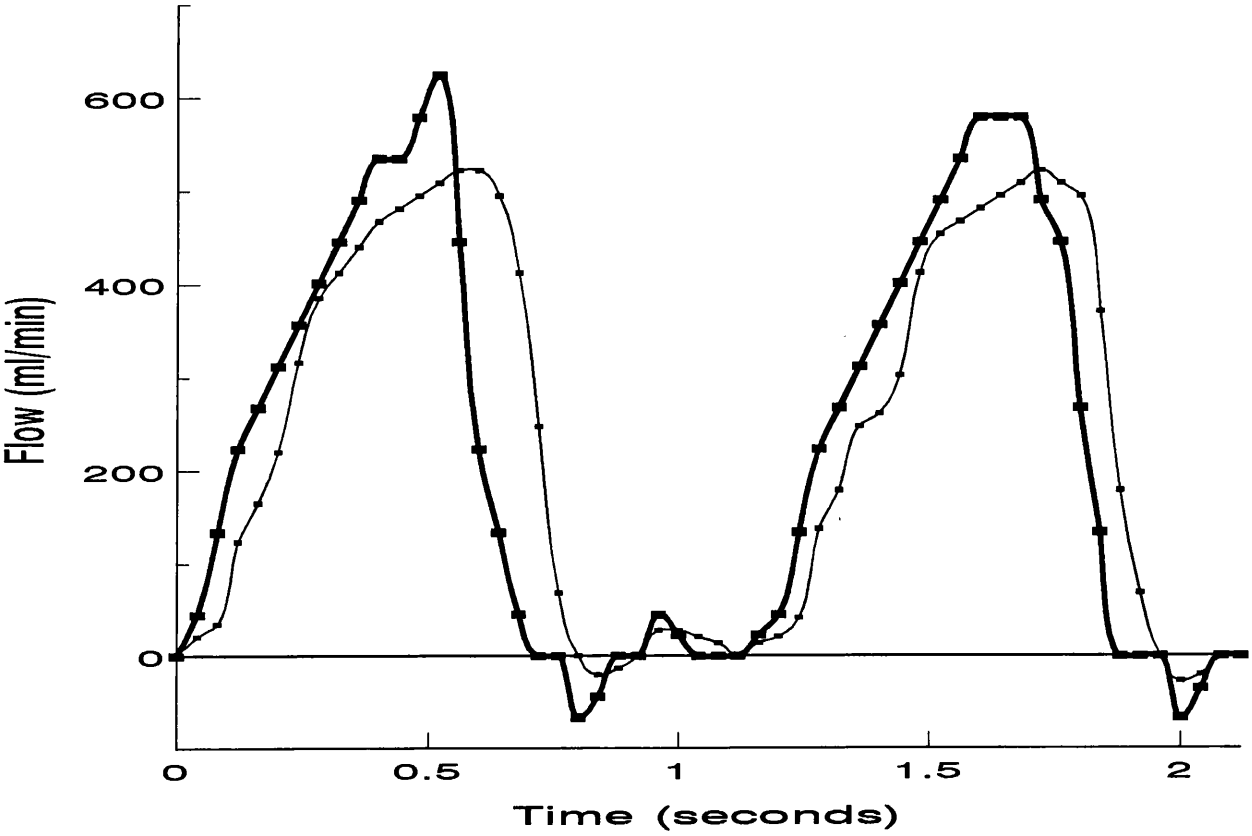

Fig. 8.12. Direct comparison of volume flow waveforms measured synchronously using the standard EMF (thin lines) and from the parametric image using our velocity computing algorithm (thick lines) for a tube of 3.0 mm lumen diameter with a mean fluid flow of 229 ml/min (parametric image generated by 3D data processing).

This results of validation of EMF against fluid collection shows a consistent underestimation of 11% by the EMF and the subsequent experimental data was corrected for this discrepancy. The estimated error in reading the EMF values off the paper chart from the chart recorder was estimated to be approximately ±2% and about ±3% error was estimated for fluid collection flow rate measurements.

The results demonstrate that using X-ray angiographic techniques, the matching of distance-density curves over time provide a close match with the blood flow waveform measured by an EMF, over a range of flow rates and vessel calibres (tables 8.2 and 8.5). The shape of the blood flow waveform is faithfully reproduced but generally there is an overestimation of peak flow rate. Table 8.3 shows that the distance between injection and measurement sites has little effect on the accuracy of the technique over the range 130 to 230 mm for low flow rate (with mean flow rate of 349 ml/min) but at a higher flow rates (mean 708 ml/min) the mean flow estimate shows a systematic fall when the flow analysis site was moved away from the injection catheter position. In both experiments the shape of the flow waveforms were faithfully reproduced but our velocity algorithm had a greater error for high flow and increasing distance between injection site and imaging site. This could be due to dispersion of contrast material. These findings were more visible on the velocity waveforms than from the comparison of the mean flow rate with the EMF reading.

The mean flow estimate showed a systematic fall as the length of tube analysed was reduced. For shorter tube lengths the tracking algorithm was more likely to fail at high velocities. The accuracy of our velocity algorithm depends on the peak blood flow velocity along the vessel. In the comparison of two adjacent distance-density profiles, some of the same portions of the bolus must overlap in the two profiles. In addition to the length of vessel imaged, this is dependent on the frame rate acquisition: the frame rate must be high enough such that a portion of the bolus imaged in one frame appears in the subsequent frame. The frame rate required can be estimated from the length of the vessel used in the flow analysis and the estimated peak velocity of the blood flow. Alternatively the minimum length of the vessel required in the analysis can be estimated from the maximum possible framing rate and the estimated peak velocity of the blood flow.

Overall agreement from 3D data processing was very good, (see table 8.5 for statistical details) except for experiment II which had a very high mean flow of 1157 ml/min. The poor accuracy of this experimental result was due to little or no change in the contrast concentration in the parametric image as described above. However, although the peak flow showed very close agreement between the EMF and angiography the beginning of each cycle provided poor flow data due to the absence of contrast material in the tube at this phase of the pump cycle.

Although the X-ray angiographic method for pulsatile flow measurements produced reasonable velocity waveforms for a wide range of flow velocities the results also demonstrated its limitations. Firstly the technique becomes inaccurate at very high velocities. If peak fluid flow along the vessel is greater than the length of the vessel segment analysed per frame interval, then the tracking algorithm will fail. Secondly a consistent overestimation of peak flow velocities at low flow rates was observed. This overestimation reduced as the flow increased.

Some of the discrepancies could be explained by:

(a) The estimated error in reading the EMF values off the paper chart from the chart recorder, this error was estimated to be approximately ±6% at peak deflection.

(b) A consistent underestimation by the EMF (Fig. 8.2). This error was estimated to be 11%, and the EMF data were corrected for this using the regression equation. But as this calibration was performed for constant flow, under pulsatile flow conditions the actual underestimation is not known and it may be even lower. This still leaves a consistent overestimation at lower flow rates. One possible explanation is that the contrast material was injected into the centre of the tube. At low flow rates there is little turbulence and near ideal laminar flow. Hence samples of fluid velocity in the centre of the tube will be higher than at the sides.

Our procedure for computing the shift, s, (see chapter 6) of the bolus along the axis of the vessel at each frame interval is simple but effective. However, it can fail in the presence of artefact or low contrast concentration gradient along the

vessel. Reliability would be improved by recording no value (rather than zero flow) when the distance-concentration gradient was lower than a threshold value. In figure 8.5 for example the zero flow values recorded from the angiographic data at the beginning of systole should not be treated as measurements at all and could have been identified as phases when no valid flow data were retrievable.

The error in blood flow measurements described in this chapter are due to computation of blood flow velocity using our algorithm described in chapter 6. The actual cross-sectional area was used in the calculation of volume blood flow. Therefore there will be additional error in computation of volume blood flow in clinical studies described in the next chapter. Our validation results using phantom vessels show that we can measure the cross-sectional area of a tube 5 mm diameter with a precision of about 5% at 0.5 mm intervals in the imaging plane and with negligible (<1%) systematic errors. Although as described in chapter 5 in clinical studies the error is expected to be higher.

One of the difficulties in developing techniques to measure blood flow is the difficulties in substantiating values, since a consistent, accurate, noninvasive method for measuring blood flow "in vivo" does not exist. The phantom for the physical flow model provided a known flow rate that was used as a standard for repeatable empirical evaluation of our X-ray angiographic flow determination. Our error in measuring flow in the phantom was consistently within about 10% of the EMF reading. Therefore I proceeded to clinical evaluation of the technique.

In conclusion, the physical flow model experiments have demonstrated that accurate instantaneous and mean volume blood flow, using the matching of distance-density curves was possible in phantoms that provide an approximation of the situation 'in-vivo'. In order to demonstrate the applicability of our flow technique in clinical practice, parametric images were generated from clinical dynamic X-ray angiographic data and flow waveforms were extracted in the femoral and cerebral arteries.

CHAPTER 9

APPLICATION TO CLINICAL DATA

9.1 INTRODUCTION

In order to demonstrate the applicability of the flow measurement technique in clinical practice, initial attempts were made to measure blood flow (using our X-ray angiographic technique) in the left femoral arteries of a 69-year-old male patient with severe superficial femoral artery stenosis, pre- and post-percutaneous transluminal angioplasty (PTA). The angiographic images were collected as part of the routine digital femoral arteriography for the PTA procedure. The analysis was performed using a 2D representation of the blood vessel in this case.

In order to deduce true volume blood flow along a tortuous vessel or vessel that is not oriented parallel to the imaging plane (such as a vessel in the head or neck), the 3D path length of the blood vessel relative to the imaging equipment was deduced. The 3D calibration method described in chapter 5 allows reconstruction of the 3D course of the vessel centre line with sufficient accuracy for these purposes. The reconstruction and flow measurements were validated in the phantom studies of chapters 5 and 8 respectively. The 3D location of the blood vessel centre line permits the computation of radiographic magnification, the angle between the X-ray beam and the vessel long axis, and the true vessel path length.

This method was applied to seven patients undergoing digital subtraction angiographs (DSAs) for the investigation of cerebrovascular disease. Blood flow waveforms of the carotid and vertebral arteries were produced and mean flow rate was calculated.

9.2 METHOD AND MATERIALS

9.2.1 Radiography

All X-ray images were acquired on a Siemens Digitron II DSA system. Images used for flow studies were obtained with a tube voltage between 70 and 80 kV, with a small focal spot in the pulsed X-ray exposure mode. The digital image grey values, which are proportional to the logarithm of the X-ray image brightness, were recorded. The digital images for flow analysis were acquired at 512x512 pixels/frame, 10 bits per pixel, at a rate of 25 frames/sec.

9.2.2 Femoral Artery

To assess the clinical applicability of the technique, initial attempts were made to measure blood velocity in the femoral artery of one patient before and after percutaneous transluminal angioplasty (PTA). PTA for the treatment of obliterating atherosclerosis was first described by Dotter and Judkins in 1964. In the late 1970s, the technique was refined by the introduction of an inflatable polyvinyl double-lumen balloon catheter by Gruentzig (Gruentzig et al 1976; Gruentzig 1977 and 1978). One of the main indications for this procedure has been localised stenosis of the femoral artery. In such cases the early evaluation of the procedure has been largely based on the angiographic appearances immediately following PTA (Arfvidsson et al 1983; Bergqvist et al 1984; Rösch et al 1974; Van Andel 1980). There might be considerable clinical benefit in measuring blood flow before and after PTA to plan the procedure and assess outcome using angiographic data derived as part of the standard PTA procedure.

For this study, contrast material was injected (Urografin 370, 370 mg of iodine/ml) at a rate of 3 ml/sec for a total of 9 ml into the left common femoral artery via a 5 French catheter positioned approximately 10 mm above the imaging site.

One patient who had a localised stenosis of the left superficial femoral artery was studied. Blood flow was measured using the X-ray angiographic technique before and immediately after PTA. Blood flow measurements were obtained in the left common femoral artery, left superficial femoral artery and left profunda femoris

artery. The arterial segments analysed had lengths of approximately 53, 57 and 112 mm respectively (fig. 9.1). The patient was positioned such that the analysed segments of the arteries lay approximately parallel to the imaging plane. The X-ray magnification and image scaling were determined using a small metallic disc of 23.5 mm diameter (an old 5 pence coin) which was attached to the skin surface of the inner thigh at a position estimated to be the same distance from the image intensifier as the femoral arteries. The circular disc was used so that longest distance across the 2D projection image through centre point is the diameter of the disc. In fact after 4 measurement the results showed that the diameters were the same and this ensured us the coin was parallel to the imaging plane. The catheter tip was placed approximately 73 mm proximal to the bifurcation of the superficial femoral artery and profunda femoris. After injection of contrast material, X-ray images were taken using the DSA system.

9.2.3 Head and Neck

The aims of the flow study in the head and neck were of interest to Dr Colchester and Dr Bladin (Department of Neurology, Guy's Hospital) who wished to assess the haemodynamic status of patients with carotid stenosis and symptoms consistent with transient cerebral ischaemic. Quantitative X-ray angiography was the choice of image modality to quantify appropriate haemodynamic parameters to determine the pressure drop along the afferent vessels to the circle of Willis (cow), i.e. the two vertebral and internal carotid arteries along with the common carotid arteries.

By combining these data acquired from quantitative DSA techniques with T1 weighted NMR images that show the features of the cow, and SPECT data regarding regional perfusion of cerebral hemispheres, it was hoped that an overall picture of the cerebral region would help in assessing the likelihood of haemodynamic stroke due to extracranial stenosis. Further data produced would be input into a haemodynamic model constructed for each patient to aid in the prediction of reduced risk following carotid artery endarterectomy (CAE).

One of the difficulties in deciding on the indications for CAE is uncertainty over the mechanism of cerebral ischaemia in patients with extracranial vascular

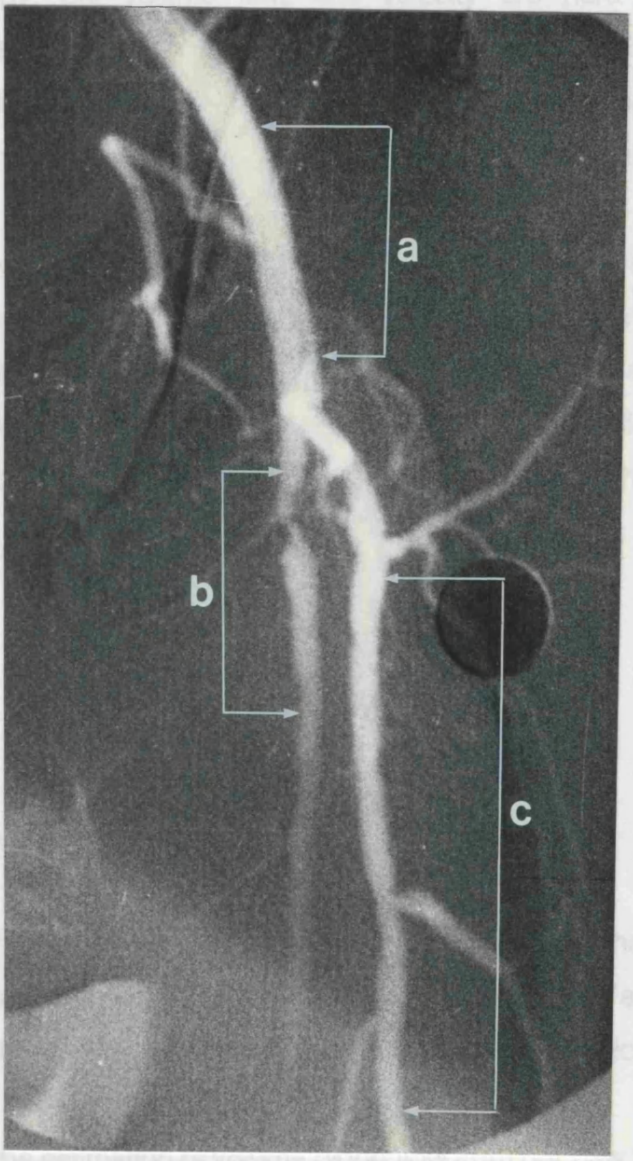

Fig. 9.1. X-ray angiogram showing the left femoral arteries. The arrows indicate the positions of the selected arterial segments for generation of the parametric images. a=left common femoral; b=left superficial femoral; and c=left profunda femoris arteries.

disease. The commonest cause is microembolism from atheroma, but haemodynamic factors are likely to be responsible in a significant number of patients, especially those with widespread disease (Bladin et al 1992). Methods of quantifying the haemodynamic parameters of the extra-cranial vessels are limited. Duplex Doppler ultrasound can provide estimates of per cent stenosis or plaque morphology, but volume flow and velocity are hard to estimate quantitatively. These parameters are important (in conjunction with length, width, and cross-sectional area measurements) if one is to estimate the pressure drop and resistance (and hence haemodynamic effects) of a vessel or stenosis.

Digital X-ray angiography is used to compute the precise length, cross-sectional area and flow measurements of the main supply vessels (and stenoses) to the cow, and then this information is used to calculate the resistance and pressure drop of each vessel from the aortic arch to the cow using Poiseuille's equation. Poiseuille's equation for the pressure drop ΔP in a vessel of length L is defined as:

$$\Delta P = 8\frac{LF}{\Pi R^4} \qquad (9.1)$$

where F is the volume flow rate and R is the vessel radius.

The parameter ΔP is used to predict the critical drop in pressure that would lead to the risk of haemodynamic stroke due to vascular stenoses and hence to predict the reduction in risk after the removal of a specific stenotic lesion.

In this thesis only the estimation of volume blood flow from our new technique for the quantitative estimation of volume flow using digital X-ray angiographic data (see chapter 6) is discussed.

Seven patients (one male and six females), with an age range from 57 to 74, were selected who were undergoing routine angiographic procedures for the investigation of cerebrovascular disease (table 9.1). All these patients had

Table 9.1. Summary of patient data of patients who have undergone head and neck DSA examination.

Patient	Age (years)	Sex	Angiographic Results
MB	62	F	Minor right internal carotid stenosis; aberrant left brachiocephalic artery.
JA	68	M	Completely occluded left internal carotid and severe stenosis of the right internal carotid.
PT	66	F	Left subclavian stenosis and minor bifurcation disease.
KC	57	F	Complete occlusion of right common carotid and internal carotid and vertebral arteries.
BN	70	F	Severe right internal carotid and moderate left internal carotid arteries stenosis.
SC	64	F	Bilateral subclavian stenosis and mild left external carotid stenosis.
FM	74	F	Right internal carotid stenosis, narrowing left common carotid artery.

suffered a transient ischaemic attack (TIA). Symptoms of residual neurological damage were minimal, but a Doppler investigation, subsequent to hospital admission, had documented evidence of an extra-cranial vascular stenosis (<50% diameter reduction). These patients had been recommended for a routine DSA investigation to determine suitability for CAE. To allow for the quantification of the DSA run, slight modification of the usual DSA procedure was required with one of the runs (neck) acquired at a rate of 25 frames/sec. Ethical committee approval for the study protocol was obtained and all patients gave informed consent to the study.

For each patient three biplanar pairs of images were obtained at the level of the head, neck and arch in that order (i.e. head first). For each pair of data acquisitions or runs the patient was aligned at the iso-centre of the X-ray gantry and care was taken not to move the patient between each run. Each pair of runs consisted of biplanar X-ray angiography (LAO and RAO views at 45°). Each run was performed at 2 frames/sec apart from one of the neck views which was performed at 25 frames/sec for the flow analysis. The timing between each run was about five minutes, and the small amount of the contrast material (9 ml in total) injected for each run will be uniformly diluted throughout the cardiovascular system and therefore there was not expected to be any problem of recirculation of contrast material between injections. There will however be a pharmacological effect of vasoconstriction which will effect the repeatability of the measurements.

To prevent patient movement during biplanar views, the patient's head was strapped to the table. The positions of the X-ray table and gantry, and the image intensifier height were recorded for each of the runs.

The magnification factor and the 3D orientation of a selected vessel were obtained after calibration of each X-ray view with a cube of known dimensions (see chapter 5).

9.3 RESULTS

9.3.1 Femoral Artery

In the clinical study, the blood flow velocity measurements showed a change of flow waveform after PTA of the stenosis in the superficial femoral artery. Changes between pre- and post-PTA are apparent in the parametric images (figs 9.2 and 9.3 respectively), derived from (a) approximately 53 mm of the left common femoral artery; (b) approximately 57 mm of the left superficial femoral artery; and (c) approximately 112 mm of the left profunda femoris artery (fig. 9.1).

Figs 9.4 and 9.5 show plots of the flow velocity waveforms vs time. The waveforms were extracted from the parametric images shown in figs 9.2 and 9.3. The plot in fig. 9.4 demonstrates that there was negligible flow through the superficial femoral artery pre-PTA due to severe stenosis. The stenosis is also apparent in parametric image (fig. 9.2 (b)). Flow in this artery was restored post-PTA as shown in fig. 9.5.

9.3.2 Head and Neck

Fig. 9.6 shows examples of the parametric images generated for the carotid and vertebral arteries of a 62-year-old female (patient MB, in table 9.1) with minor right internal carotid stenosis and an aberrant left brachiocephalic artery (fig. 9.7). The left vertebral artery arises from the left brachiocephalic artery in front of the origin of the left common carotid artery (LCC). There were overlap and horizontal artefacts in all the parametric images and these were ignored during flow analysis (see table 9.2 for the region of exclusion). Fig. 9.8 shows plots of the flow waveforms vs time. The waveforms were extracted from the parametric images shown in fig. 9.6. The plots in fig. 9.8 demonstrate that flow in the internal carotids are of the order of 70% of that in the common carotids as expected. Also, in Doppler studies, it generally has been shown that the carotid arteries there is normally significant forward flow but this is not the case with the angiographic data, which show that between each cardiac cycle the flow has fallen to zero, this could be due to lack of contrast material.

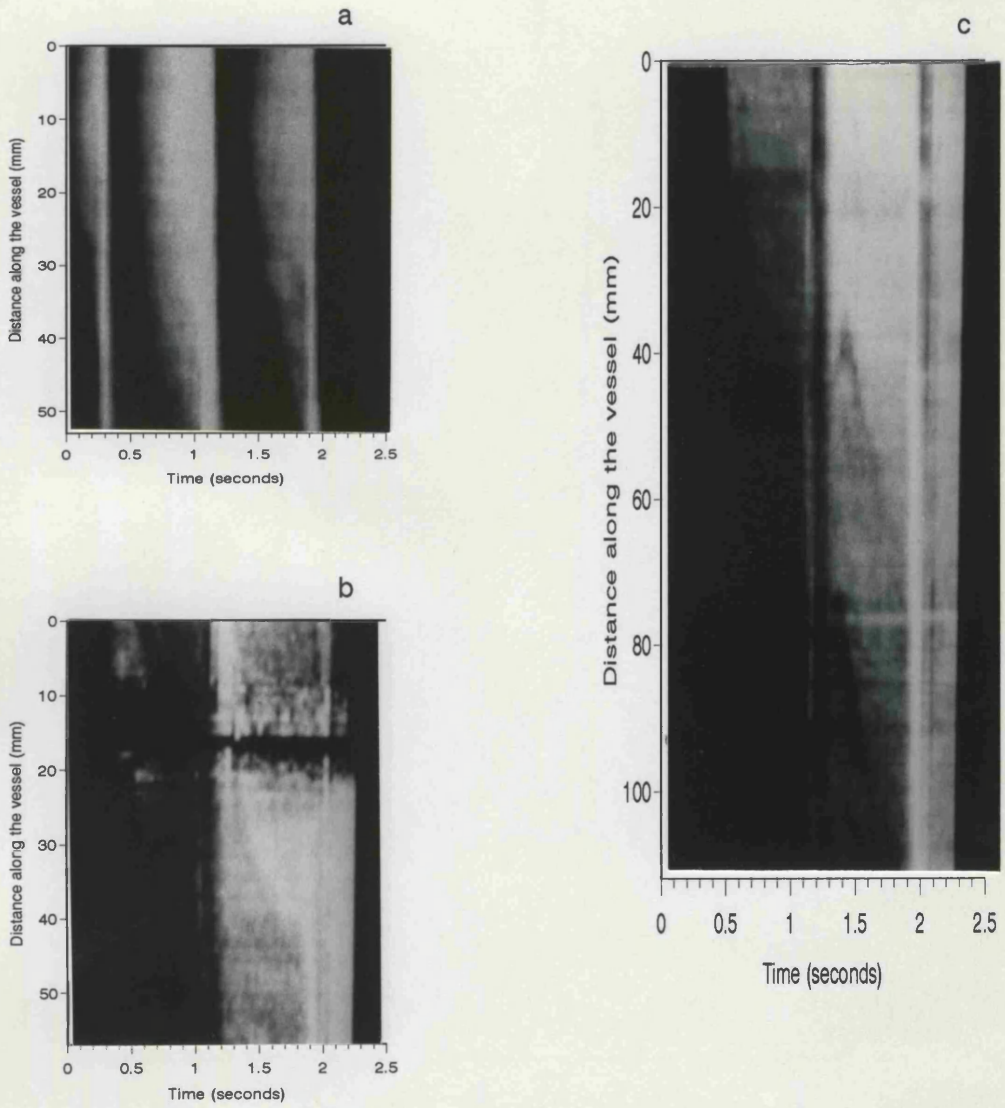

Fig. 9.2. Parametric image showing contrast medium concentration (grey scale) at different positions down the blood vessel (the vertical axis) and at different times (the horizontal axis) pre-angioplasty for: (a) the left common femoral, (b) the left superficial femoral with severe stenosis and (c) the left profunda femoris arteries.

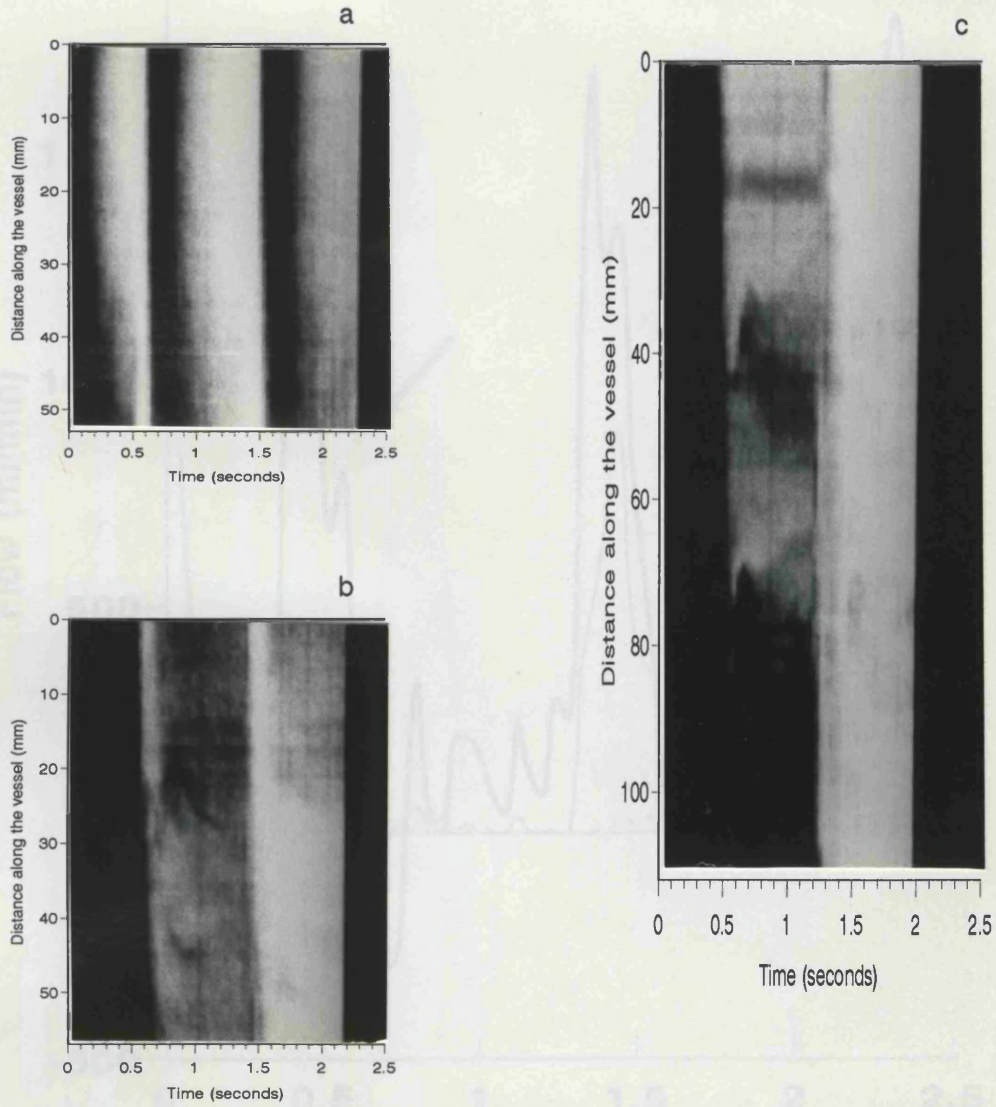

Fig. 9.3. As in fig. 9.2 but post-angioplasty.

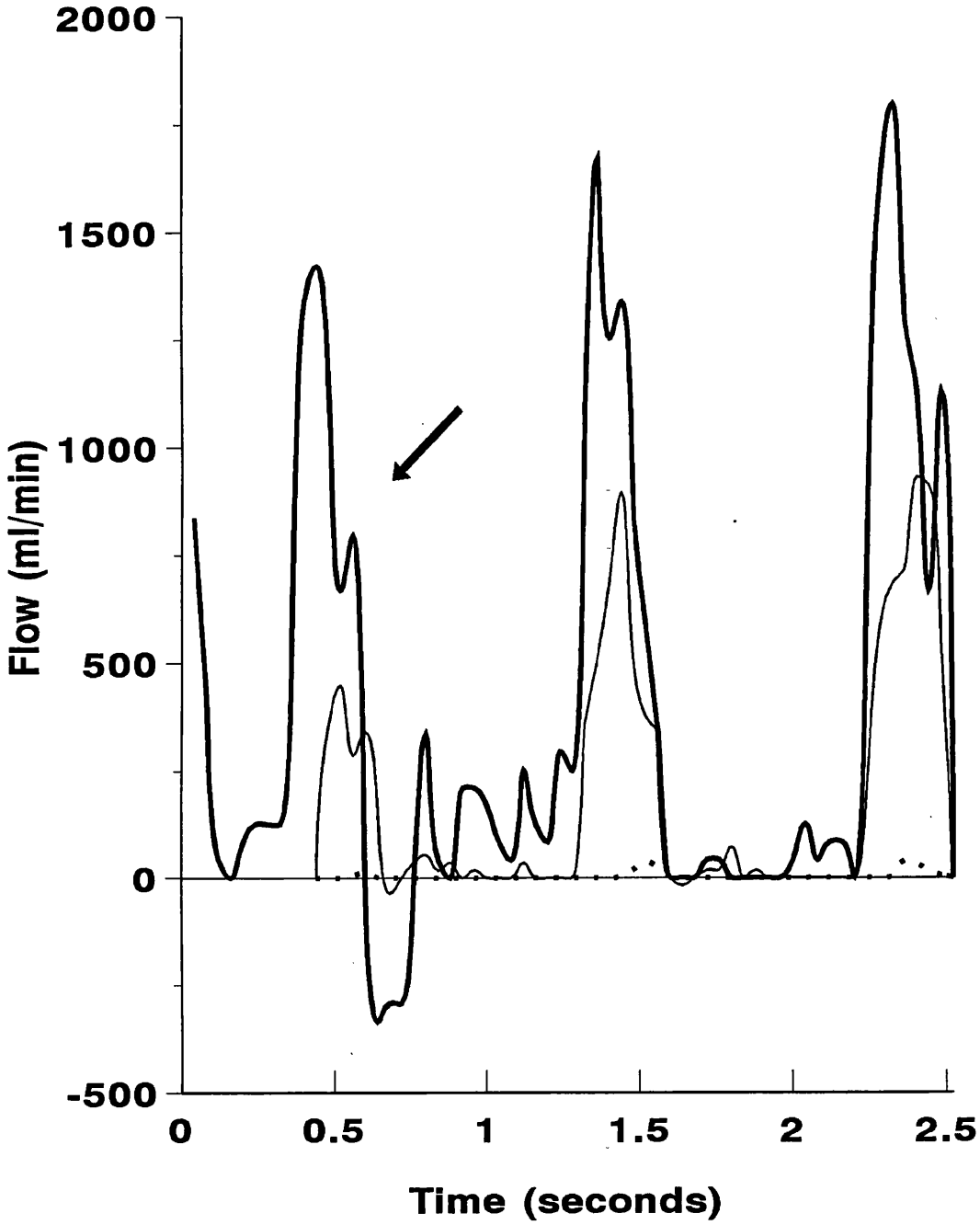

Fig. 9.4. Plots of the flow velocity waveforms pre-angioplasty derived from the parametric images shown in fig. 9.2. The waveforms were extracted from the parametric images constructed for the left common femoral artery (thick solid lines), the left superficial femoral artery (dotted lines) and the profunda femoris artery (thin solid lines).

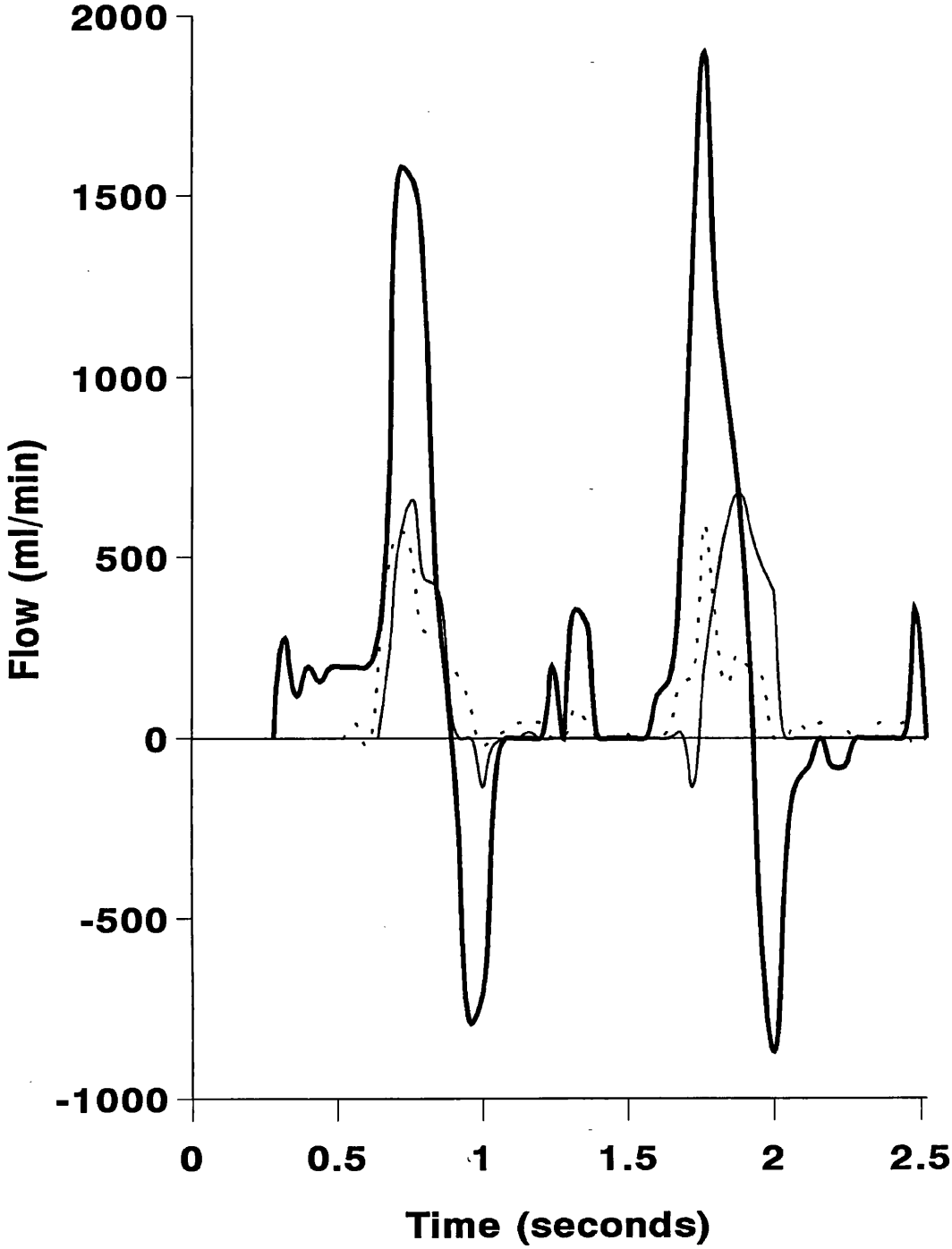

Fig. 9.5. Plots of the flow velocity waveforms post-angioplasty. The waveforms were extracted from the parametric images shown in fig. 9.3 for the left common femoral artery (thick solid lines), the left superficial femoral artery (dotted lines) and the profunda femoris artery (thin solid lines).

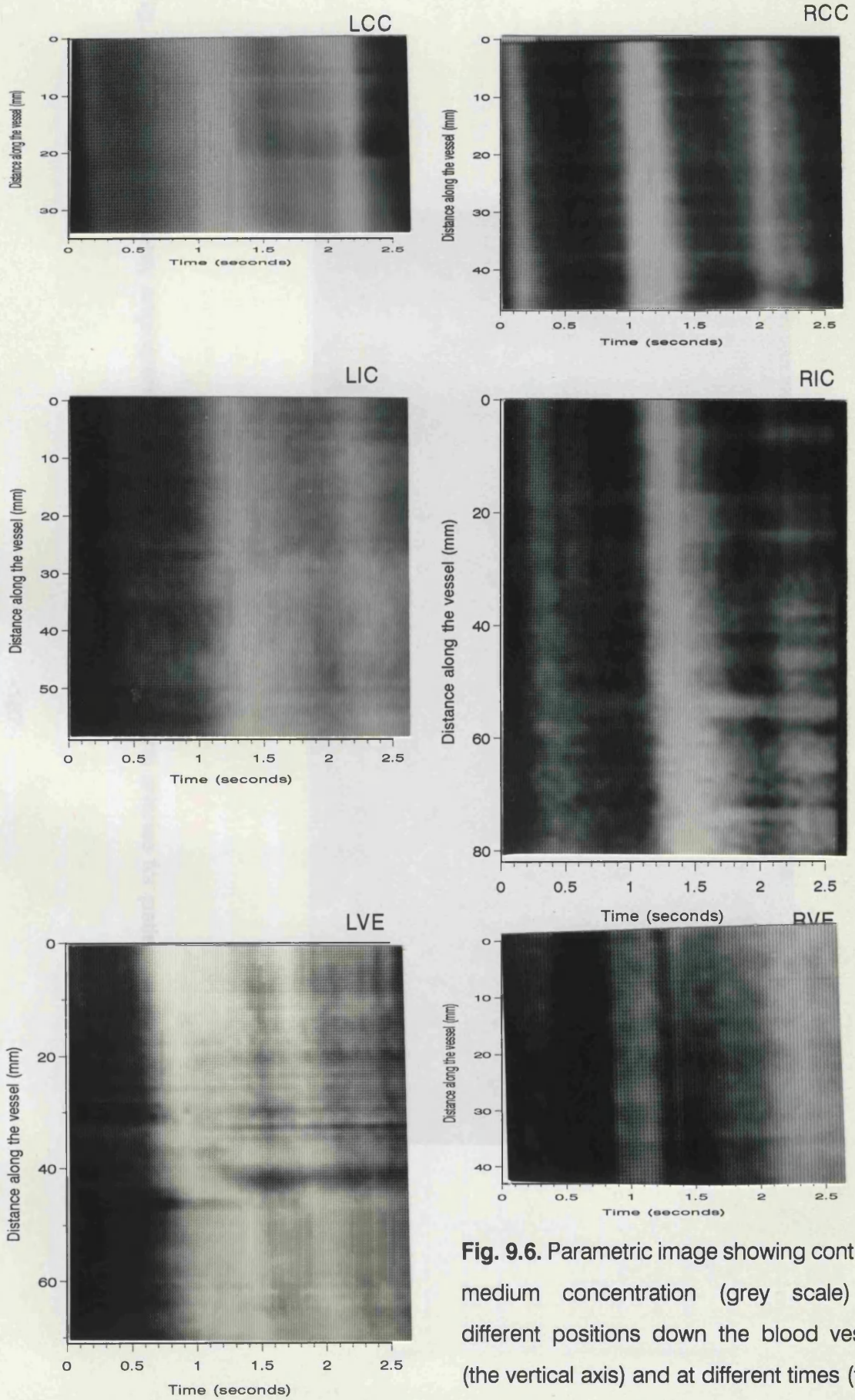

Fig. 9.6. Parametric image showing contrast medium concentration (grey scale) at different positions down the blood vessel (the vertical axis) and at different times (the horizontal axis), the left and right common carotid (LCC, RCC), internal carotid (LIC,RIC) and vertebral (LVE,RVE) arteries for patient MB (see table 9.3).

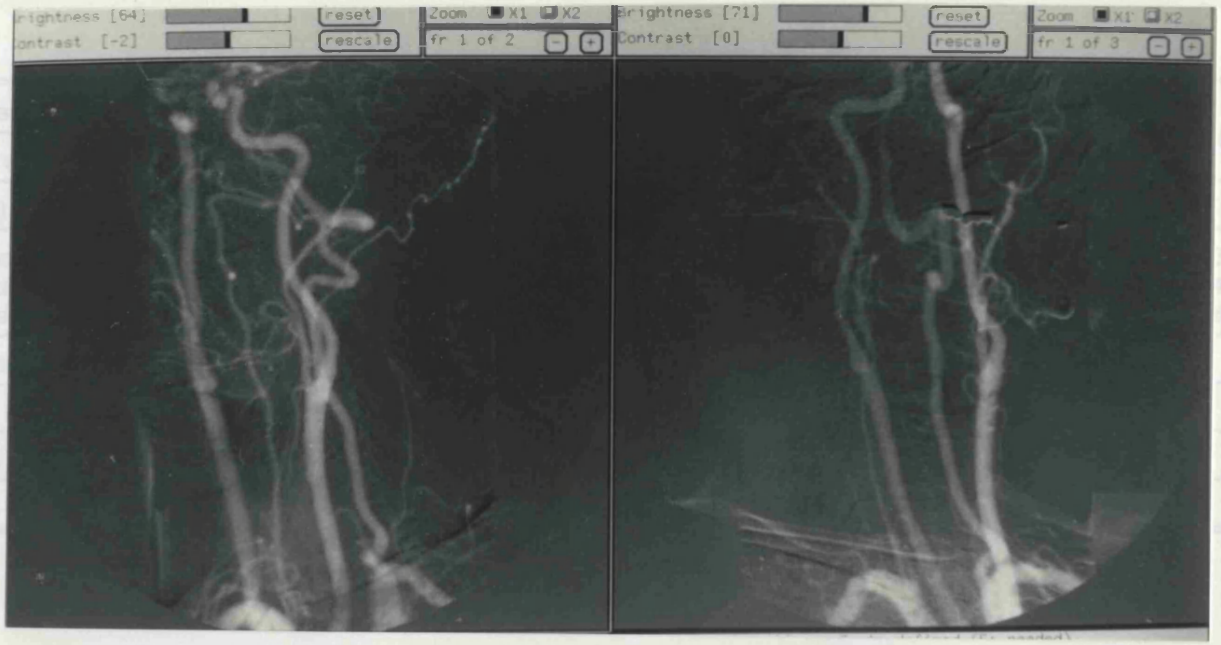

Fig. 9.7. Biplanar X-ray angiogram showing the carotid and vertebral arteries for patient MB (see table 9.3).

Table 9.2. Flow analysis from a 62-year-old female with minor right internal carotid artery stenosis.

Selected Artery Segment -> / Parameter Calculated ↓	Left Common Carotid	Right Common Carotid	Left Internal Carotid	Right Internal Carotid	Left Vertebral	Right Vertebral
Total Vessel Size (mm)	36	47	59	82	71	42
Following segment(s) of vessel have been excluded, due to overlap of other vessel: distances are shown in mm.	5 - 7 27 - 32	31 - 44	26 - 54	6 - 15 46 - 56 66 - 79	12 - 34 38 - 48 58 - 66	14 - 21 25 - 38
Mean Velocity Calculated (mm/sec)	359	453	480	415	590	504
Mean Cross Sectional Area (mm^2)	19.7	18.2	10.2	13.3	10.6	4.5
Mean Flow Calculated (ml/min)	425	494	293	331	376	136
Time Interval Between Cardiac Cycle (sec)	0.84	0.84	0.84	0.84	0.84	0.84

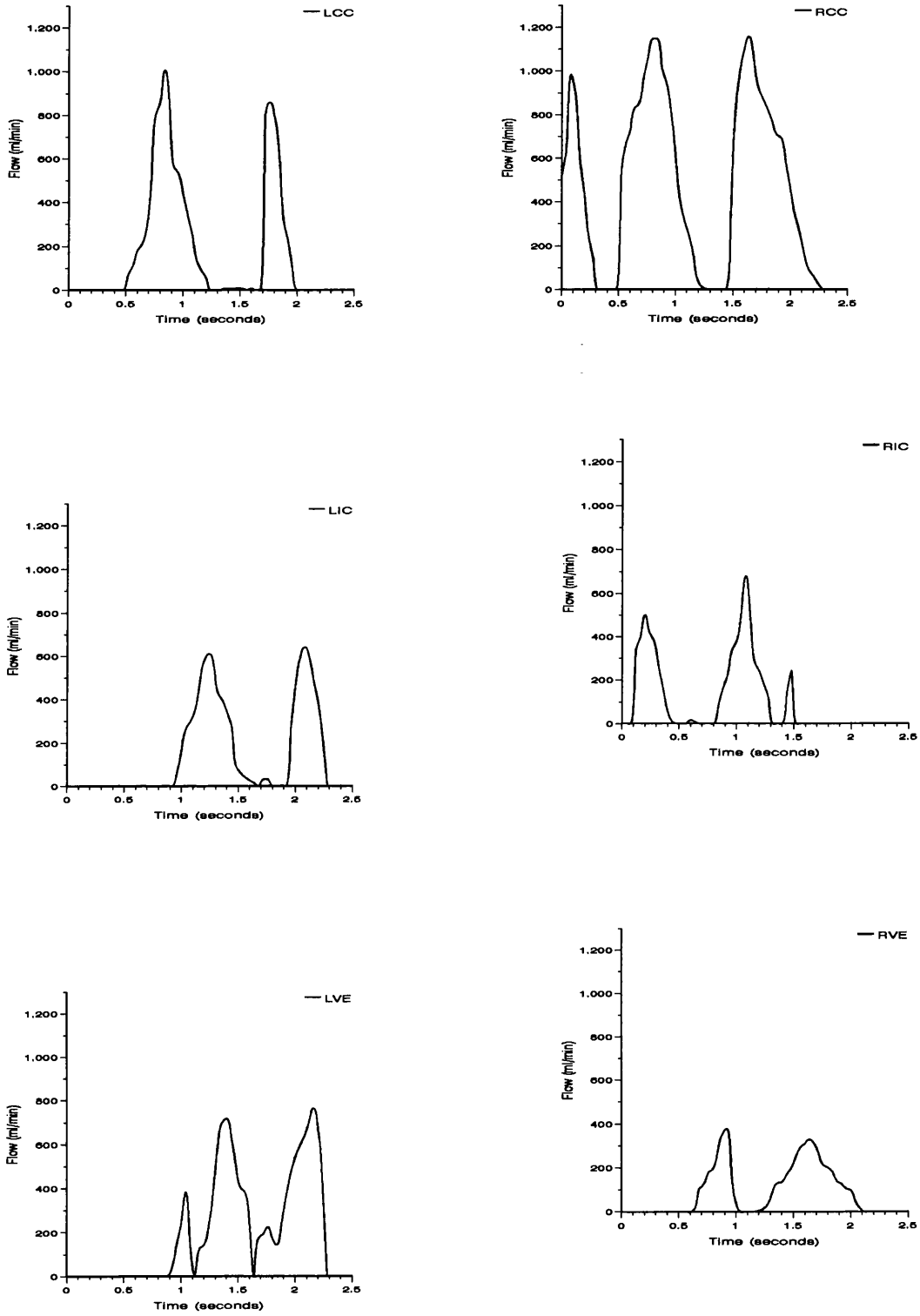

Fig. 9.8. Plots of the volume flow velocity waveforms. The waveforms were extracted from the parametric images shown in fig. 9.6 for the left common carotid (LCC), right common carotid (RCC), left internal carotid (LIC), right internal carotid (RIC), left vertebral (LVE) and right vertebral (RVE) arteries.

Table 9.3 presents a summary of the results obtained for the seven patients. As can be seen from table 9.3 some data are missing. This was due to either that vessel being absent on the angiograms or the length of vessel being too short to analyse, and these are indicated by '#' in the table. In addition some vessels were not visible or were totally occluded and some data were too noisy to analyse due to miregistration artefacts resulting from movement.

9.4 DISCUSSION

The method of estimation of flow waveform and mean blood flow using our angiographic technique, has been validated using synthetic data from a computer simulated model (chapter 7) as well as in a physical model (chapter 8). We have not yet fully evaluated the technique "in-vivo". In particular we have not compared our results with Doppler ultrasound or MR flow measurements. But we feel that we have demonstrated significant advances in the accurate measurement of cross-sectional area, vessel path length, and blood flow velocity which are the factors necessary for improved accuracy of volume blood flow measurement. The results of validations in chapters 7 and 8 have confirmed the precision and accuracy of the technique under conditions approximating "in-vivo" blood flow. Initial clinical results have confirmed the practicality of the technique.

9.4.1 Femoral Artery Study

Initially the femoral artery was chosen for clinical validation of our velocity computing algorithm because the femoral artery remains relatively stationary during angiography, has few branches, and is straight. It is relatively straight-forward to ensure that the vessel is parallel to the imaging plane.

The normal common femoral artery velocity waveform is triphasic with maximal forward flow occurring in systole, followed by reverse flow during the first half of diastole, and concluding with forward flow again in the latter half of diastole. With a haemodynamically significant stenosis proximal to the site of evaluation, the velocity waveform loses its reverse component and thereby becomes monophasic (Breslau et al 1985) (fig. 9.4).

Table 9.3. Summary of results from quantitative digital X-ray angiographic studies in patients who have undergone head and neck DSA examinations. The table shows mean velocity V in mm/sec, cross-sectional area A in mm^2 and flow F in ml/min. # indicates that vessel segments were too short to analyse. The results have been computed for the left common carotid (LCC), right common carotid (RCC), left internal carotid (LIC), right internal carotid (RIC), left vertebral (LVE) and right vertebral (RVE) arteries.

Patient ->	MB			JA			PT			KC			BN			SC			FM		
Artery	V	A	F	V	A	F	V	A	F	V	A	F	V	A	F	V	A	F	V	A	F
LCC	359	19.7	425	259	24.4	380	374	24.9	558	350	19.2	403	302	23.2	421	213	23.0	294	443	16.8	446
RCC	453	18.2	494	412	25.2	623	301	26.5	478.6	Occluded			#			200	19.8	237	494	22.3	660
LIC	480	10.2	293	Occluded			Not visible			520	10.5	327	183	8.5	93.8	240	15.4	222	417	8.8	220
RIC	415	13.3	331	396	18.3	435	Not visible			Occluded			187	12.6	142	Noisy			#		
LVE	590	10.6	376	442	3.7	98	Not visible			470	11.3	319	Occluded			Noisy			Not visible		
RVE	504	4.5	136	287	22.5	387	Not visible			Occluded			225	11.8	159	Noisy			381	11.9	272

In clinical practice, angiography is very commonly carried out on occlusive disease in many parts of the vascular system. Often it can be difficult to determine whether a stenosis is haemodynamically significant especially when the diameter (often on a single view) is in the region of 50% of the 'normal' arterial lumen. Furthermore PTA is now frequently the treatment of choice for stenotic disease where angiography is again used to assess whether an improvement has been effected. In clinical studies, flow waveforms of the left common femoral, left superficial femoral and left profunda femoris arteries were estimated for pre-PTA (fig. 9.4) and post-PTA (fig. 9.5). Fig. 9.4 shows that there was flow through the left common femoral artery and very high blood flow velocity through the left profunda femoris artery which presumably compensated for the left superficial femoral artery occlusion. There was a very small amount of flow through the left superficial femoral artery (fig. 9.4), this is apparent in the contrast enhancement seen in the summation of 20 frames of the pre-PTA images. It should be noted that even a very small flow of contrast material would be sufficient to opacify a blood vessel distal to a stenosis. The common femoral artery waveform shows a small kink which could correspond to the reflected pressure wave from the occluded superficial femoral artery (arrow).

Immediately after the completion of superficial femoral artery transluminal angioplasty, our angiographic flow measurements showed that flow through the occluded vessel had been re-established together with a normal bi-phasic blood velocity waveform for the common femoral artery (Okadome 1989) (fig. 9.5).

9.4.2 Vessels in The Head and Neck

The human brain receives its vascular supply from four main arteries, the carotids and the vertebrals. In most studies dealing with cerebral ischaemia, quantitative information about the state of these arterial systems is lacking, especially for the vertebral arteries. The reason for this is that the lack of any adequate technique that works adequently enough to estimate vertebral artery blood flow. This is due to cope with the relatively deep course of the vessels which are often overlaid by other arteries or bone.

Gold standards are unavailable in the clinical setting which made the accuracy

of the results difficult to gauge, but assessment of the results with regard to patient history and radiological interpretation of the X-ray images showed good correlation in most cases. Normal velocities obtained using duplex Doppler ultrasound in the carotid arteries are usually between 600 and 1000 mm/sec, however, they can range from less than 300 to 1200 mm/sec (Robinson 1992). There is normally no significant increase in velocity as one progresses from the common carotid artery into the internal carotid artery, but there may be a slight decrease in peak systolic velocity. The values obtained using the angiographic method (table 9.3) are consistent with these values.

One of the problems of our technique is the presence of stenosis along the blood vessel imaged. When matching contrast concentration profiles, we assume that axial flow velocity is independent of position along the vessel. By normalising each row of the parametric image to peak opacification we, in effect, convert parametric images to concentration rather than mass. This will partially compensate for any effect that small stenoses might have on the matching technique, but in long or more severe stenoses, this region will have to be excluded from the matching procedure.

In conclusion angiography remains an important and frequently used clinical procedure, despite improvement in other less invasive techniques such as ultrasound and MRI, which underlines the value of the structural information it provides even without quantitative processing. Considering the risk of angiography, every effort should be made to extract all the potentially useful quantitative information from the procedure, especially if further investigations might thereby be avoided.

CHAPTER 10

SUMMARY AND CONCLUSIONS

10.1 INTRODUCTION

Blood flow measurements in individual vessels have a number of important clinical and research applications but previous techniques have serious clinical limitations or inaccuracies.

X-ray angiography remains the vascular imaging modality which gives the highest spatial and temporal resolution and is widely used in clinical practice to obtain high-quality vessel images. The ability to derive quantitative flow data from this procedure would be a useful clinical tool.

A novel technique has been developed for the quantitative measurement of pulsatile blood flow waveforms and mean blood flow rates using digital X-ray angiographic data.

Blood flow waveforms were determined following an intra-arterial injection of contrast material. The first stage in data reduction was to generate a 'parametric image' from dynamic X-ray angiographic images in which the image grey-level represented contrast material concentration as a function of time and distance along a vessel segment.

Adjacent concentration-distance profiles in the parametric image of iodine concentration versus distance and time were shifted along the vessel axis until a match occurred. A match was defined as the point where the mean sum of the squares of the differences between the two profiles was a minimum. The distance translated per frame interval gave the instantaneous contrast material bolus velocity.

A 3D reconstruction technique for locating the 3D path length of a blood vessel from biplanar angiograms that had been implemented by our group was validated. The use of a perspex calibration cube for the geometric calibration of

the X-ray gantry orientation allows satisfactory reconstruction of the 3D course of the vessel centre line 'in-vivo', and has been validated in phantom studies. The 3D location of the blood vessel centre line permits the computation of the radiographic magnification, the angle between vessel axis and the X-ray beam, and the true vessel path length.

For measurements of vessel cross-sectional area a densitometric method was used. The technique is based on image densitometry in which the integral of the image intensity is computed along a profile perpendicular to the projection of the vessel axis. The true cross-section is related to the densitometric measure. The X-ray magnification factor and angle between the vessel axis and the X-ray axis were used in the calculation. This technique was validated using 3D reconstruction of a phantom simulating vascular structures. The blood velocity waveform estimates were converted into volume flow waveforms by multiplying by this computed vessel cross sectional area.

Initially our algorithm for computing velocity was assessed using simulated angiographic data as this allowed greater flexibility in designing suitable experiments, more control of experiments, and less cost in capital equipment and material. In addition, it was of interest to predict the X-ray quantum limited precision of the technique, for a wide range of blood vessel calibres and blood flows, with data that was free from non-random errors and artefacts. Quantitative comparison with other algorithms was also made using these computer generated images. A total of 114 different experiments were simulated for a range of calibres and flow rates using a computer model. When used to measure the blood flow waveform using our velocity algorithm, there was excellent agreement between the input flow waveforms and those determined by our radiographic technique, with both laminar flow and constant axial flow ('plug' flow) patterns. In addition our algorithm for computing velocity produced results which were independent of the injection techniques used.

Further validation of our technique computing pulsatile flow was carried out using an experimental model of blood circulation. A phantom haemodynamic circulation was designed and constructed, it consisted of a pump, flexible plastic tubing, the tubular probe of an EMF and a solenoid valve to allow simulation of pulsatile flow

waveforms including reverse flow. Small boluses of contrast material were injected at various positions in the circuit. Phantom studies were used to compare simultaneous measurements of blood flow using X-ray angiographic data with measurements using an EMF. A range of blood flow rates and plastic tube diameters was used. The validation of our technique was performed on 2D digital X-ray projections and also using 3D reconstruction from biplanar X-ray projections. The validation was repeated (1) for a range of distances between the injection and flow analysis measurement sites and (2) for various lengths of vessel analysed.

The results from physical flow model experiments have demonstrated that accurate instantaneous and mean volume blood flow is possible in phantoms that provide an approximation of the situation 'in-vivo'.

In order to demonstrate the applicability of the flow technique in clinical practice, parametric images were generated from clinical dynamic X-ray angiographic data and flows were computed in the femoral and cerebral arteries. Although satisfactory results were obtained from clinical data several problems were encountered:

(1) Artefact due to overlapping blood vessels. This was dealt with by modification of our algorithm for computation of velocity to exclude regions containing data from overlapping blood vessels (see chapter 6).
(2) Patient motion. This could cause severe artefacts in the parametric images which in turn led to inaccuracies in the computed flow.

10.2 ADVANTAGES OF OUR ANGIOGRAPHIC FLOW TECHNIQUE

The main advantages of our flow technique are that:

(1) Accurate instantaneous flow information is provided.
(2) It permits the determination of average flow under highly pulsatile conditions.
(3) The method is relatively insensitive to slow blood vessel motion during the imaging procedure (as the analysis is performed on two consecutive

frames, any vessel motion that is slow relative to one frame duration (0.04 sec)) can, in principle, be accounted for.

(4) The method will provide useful flow data with comparatively small amounts of contrast medium.

(5) It is insensitive to the precise injection technique.

(6) It appears to be relatively insensitive to the distance between the injection site and blood flow measurement site.

(7) This technique is no more invasive or inconvenient than the standard DSA procedure. The high framing rate used in this study can easily be reformatted to give the framing rate of about 2 frames/sec used in routine angiography and as such would deliver no extra total radiation dose to the patient or total contrast load.

10.3 LIMITATIONS OF OUR ANGIOGRAPHIC FLOW TECHNIQUE

Although the proposed digital X-ray angiographic technique for pulsatile flow measurements can compute accurate velocity waveforms from distance-density curves for a wide range of flow velocities, there are limitations to this technique.

(1) *High blood velocities.* The technique becomes inaccurate at very high velocities. This is due to the limited length of artery that can be analysed. This limits the maximum velocity that can be detected by our algorithm. In the comparison of two distance-density curves, some of the same portions of the bolus must appear in the two profiles. This is entirely dependent on the frame rate acquisition and length of vessel imaged; the frame rate must be high enough so that a portion of the bolus imaged in one frame appears in the subsequent frame.

(2) *Misregistration artefacts.* One of the inherent limitations of temporal subtraction DSA is the susceptibility of this technique to misregistration artefacts resulting from either voluntary movement (breathing and displacement of the extremities), or involuntary movement (peristalsis, cardiac motion, swallowing, and arterial pulsations). The misregistration artefacts result in an artefactual signal that cannot be separated from the true iodine signal. This could be overcome by using unsubtracted X-ray angiographic images for the quantification of volume blood flow. The

primary disadvantage of the unsubtracted images is the presence of overlying tissue signals, which will vary unpredictably along the vessel profile. Therefore our initial clinical efforts have been concentrated on parts of the body which are less prone to patient movement and hence, the technique has been applied to the femoral arteries and the vessels of the head and neck.

(3) *Scattered radiation*. The contribution of scattered X-ray radiation is difficult to correct because the distribution and quantity of scattering is not expected to be uniform. The light intensity at each location of the intensifier output image is made up of two components. One is dependent on the degree of X-ray absorption while the other is an additional quantity dependent on scattering from other parts of the body. The latter portion is not only dependent on the site of sampling (centre or border of the image) and the distribution of brightness across the image, but may change with temporal variations in brightness (e.g., the presence of contrast material in vascular structures adjacent to the site of measurement). Inaccuracies of this kind may be overcome in the future by the application of algorithms that provide simulation of scattering for each individual angiographic image.

(4) *Injection of Contrast Material.* In order that the velocity information may be extracted from the movement of a contrast bolus, there must be a contrast material concentration gradient along the vessel. Also we have shown that our velocity algorithm is independent of injection technique (see chapter 7) but injection of a large volume can perturb the flow substantially. We used an automatic injector for extremely precise control over the volume and flow rate of injection.

In addition, the effects of the process of introducing a catheter into a blood vessel, the continuing presence of the catheter, the disturbing influence of the injection, the volumetric, viscous and inertial consequences of having introduced a foreign fluid, and the pharmacological effects of contrast material must all be considered as possible sources of error in flow estimates.

10.4 FUTURE DIRECTIONS

There are numerous areas for application and future development of the technique of quantitative measurement of pulsatile blood flow using our algorithm for computing velocity. These range from the simple application of the technique in peripheral arteries to its application in tortuous overlapping vessels in abdominal blood flow studies in, for example, the hepatic and renal arteries, which are difficult to study by Doppler ultrasound (Seifalian et al 1991a). Efforts are currently underway (in collaboration with Brompton Hospital, Dr N Buller and DR R Underwood) to develop a reliable assessment of the extent and severity of coronary artery disease by measurement of flow. In brief, prognosis in patients with coronary artery disease is determined primarily by two factors: (1) the severity and extent of atheromatous obstruction in the coronary arterial circulation, and 2) the degree of left ventricular impairment. To obtain information regarding these two factors, different clinical procedures are involved: for assessment of the extent and severity of atheromatous obstruction, the "gold standard" remains coronary angiography (Gould 1986), whereas for assessment of the extent and severity of myocardial ischemia and infarction, the "gold standard" remains myocardial perfusion tomography (Wackers et al 1976; Pamelia et al 1981), employing techniques such as SPECT imaging with thallium-201 (^{201}Tl) or PET with $^{13}NH_3$ and ^{18}FDG. In essence, dynamic coronary angiography yields vascular blood flow and anatomical information, while myocardial perfusion tomography yields tissue perfusion. Hence, an accurate assessment of the extent and severity of CAD ideally requires the integration of these two types of information obtained independently from these two imaging modalities. At Guy's hospital the image processing group have a strong interest and expertise in image registration (Hill et al 1991 and 1993). We are trying to combine these two types of information, using biplane X-ray angiograms as described in this thesis and myocardium perfusion using ^{201}Tl or $^{13}NH_3$ and ^{18}FDG.

Measurement of coronary blood flow is still difficult. To our knowledge, none of the previously reported approaches have yet achieved satisfactory accuracy. Intra-arterial Doppler ultrasound is still subject to important limitations. Thus, the direct way of measuring flow by determing the volume of blood passing through

a particular artery in a given time interval remains an interesting alternative. Using our 3D angiographic technique, we can measure arterial lengths and diameters reasonably accurately, but it is difficult to measure coronary artery blood flow velocity due to the movement of the arteries over the cardiac cycle. Work is in progress to overcome this problem by tracking the coronary arteries over the cardiac cycle, reconstructing their 3D path and hence generating plots of contrast concentration versus distance over the complete cardiac cycle.

The main unsolved problem with applying the technique to the coronary arteries arises from the movement of the blood vessels over the cardiac cycle. The flow program that has been developed by us is equally well suited to subtracted or unsubtracted coronary imaging. When coronary structures or lesions are obscured by the attenuation caused by superimposed non-vascular structures, mask subtraction techniques reduce error in the quantitative flow measurements. There are several image processing schemes that have been applied to coronary angiography to remove the interfering effects of over or underlying tissues. The simplest mode is the mask mode, in which a single pre-injection image (mask) is used to subtract backgrounds automatically from subsequent contrast images. This model has the disadvantage that even in the absence of respiration the motion of the heart causes distracting soft-tissue misregistration artefacts. Another related mode is the blurred mask mode, in which the mask is integrated over one heart cycle. This has the effect of blurring the mask image so that misregistration artefacts are somewhat decreased.

A more accurate masking technique may be obtained by separate recording of an entire cycle of pre-injection masks. These masks are then subtracted from corresponding iodine images to form a phase-matched mask. Phase matching can usually be done automatically if ECG information is recorded along with image data, provided that the cardiac rhythm is regular.

The cost function described in chapter 6 was used to give a visual indication of confidence in the flow estimates described in this thesis. This function could be used to further improve our estimates of velocity. This might be achieved by generating a parametric model of the flow waveform and fitting it to the cost function using an optimisation procedure to minimise cost. The blood flow

waveforms in each artery have certain characteristics which can be generalised such as height, width, etc. This might enable us to predict the blood velocity waveform, in regions where the data is corrupted by artefact or where little information on flow is presented.

In conclusion I believe that this technique has great potential for the measurement of blood flow in arteries 'in vivo'. Computer simulation and experimental validation have confirmed the precision and accuracy of the technique under conditions approximating blood flow 'in-vivo'. Initial clinical results have confirmed the practicality of the technique.

APPENDIX

THEORY OF ABSOLUTE CROSS-SECTIONAL AREA

This theory was proposed and initially validated by Colchester et al (1984) and was further validated in samples of artery obtained 'post-mortem' by Hawkes et al (1988a).

To a good approximation, the mask subtracted image grey value G_i^s at pixel i is given by:

$$G_i^s = K_i c Z_i \tag{A.1}$$

where c is the concentration of iodine in the blood vessel, K_i is densitometric calibration constant and Z_i is the thickness of the vessel. In an angiogram we generally do not know the factor $K_i c$ and therefore cannot retrieve Z_i directly.

For a blood vessel whose axis is orientated at an angle θ to the x-ray beam, summation of the function G_i^s, the transverse density profile (TDP) perpendicular to the vessel axis, yields the TDP area, '*a*'. The true cross-section, '*A*', is related to the densitometric measure, '*a*', by:-

$$A = a\left(\frac{\cos\theta}{M}\right)\left(\frac{1}{K_i c}\right) \tag{A.2}$$

The x-ray magnification factor, M, and angle (θ) between the vessel axis and the x- ray axis are computed from the 3D reconstruction of the vascular configuration from two views as described in chapter 5. The remaining term is the product of the iodine concentration in the vessel, c, and a densitometric calibration constant, K_i, which relates the image grey value to the mass of iodine projected from the x-ray focus to the imaging plane. The factor $K_i c$ is computed by assuming circularity of an identified segment of vessel. For a straight segment of blood vessel of circular cross-section the maximum value of the TDP, h, can be

expressed in terms of the diameter D of the vessel:-

$$h=\frac{K_f cD}{\cos\theta} \tag{A.3}$$

As the true cross-section A is $= (\pi/4)D^2$, the calibration factor $K_f c$ is given by

$$K_f c=(\frac{\pi}{4})(\frac{h^2}{a})M\cos\theta \tag{A.4}$$

Extrapolation of $K_f c$ from regions of circular cross-section and substitution into equation (A.1) permits computation of absolute cross-sectional area, A, in regions of non-circular section (e.g. across stenoses, at bifurcations etc.).

Similar algebraic steps lead to the following interrelated expressions for the factor $K_i c$:

$$K_i c=(\frac{4}{\pi})(\frac{a}{W^2})M\cos\theta \tag{A.5}$$

and

$$K_i c=(\frac{h}{W})M\cos\theta \tag{A.6}$$

where W is the width of the artery in pixels. The constant $K_i c$ is referred to in this project as the densitometry constant and is symbolised by K.

Each of these expressions could be used to derive the absolute cross-sectional area. Equation (A.4) was selected in this thesis: previous validation has shown it to be the most accurate method for estimation of cross-sectional area, as it is independent of the vessel width (Virdee 1991; Iqbal 1992).

REFERENCES

Albright RE, Frame EK. Microcomputer-based technique for 3-d reconstruction and volume measurement of computer tomographic images. Part 1: Phantom studies. Invest Radiol 1988; 23:881-885.

Alderman EL, Berte LE, Harrison DC, Sanders W. Quantitation of coronary artery dimensions using digital image processing. Proc SPIE 1981; 314:273.

Arfvidsson B, Davidsen JP, Persson B, Spangen L. Percutaneous transluminal angioplasty (PTA) for lower extremity arterial insufficiency. Acta Chir Scand 1983; 149:43-47.

Arnold MT, Hawkes DJ. Quantification of iodine mass in digital subtraction angiography. BJR 1989; 62[congress supplement]:S83.

Baily NA, Rimkus D, Nalcioglu O. Normalization (division) versus subtraction of digitized images. Medical Physics 1983; 10:25-28.

Barnard ST, Thompson WB. Disparity analysis of images. IEEE Trans on Pattern Analysis and Machine Intelli 1980; PAMI-2(4):333-340.

Bateman W, Kruger R. Blood flow measurement using digital angiography and parametric imaging. Med Phys 1984; 11(2):153-157.

Bergqvist D, Takolander R, Jonsson K, Karlsson S, Hellekant C. Percutaneous transluminal angioplasty of arteriosclerotic lesions in the pelvis and lower extremities. Acta Chir Scand 1984; 150:445-449.

Bladin CF, Seifalian AM, Iqbal N, Colchester ACF, Hawkes DJ. Haemodynamic assessment of extracranial vascular stenoses using quantitative angiography. Second European Stroke Conference 1992; (Abs).

Bland JM, Altman D. Statistical methods for assessing agreement between two methods of clinical measurement. Lancet 1986; 307-310.

Bradley SE, Inglefinger FJ, Bradley GP, Curry JJ. The estimation of hepatic blood flow in man. J Clin Incest 1945; 24:890.

Bradley WG, Waluch V. Blood flow: Magnetic resonance imaging. Radiology 1985; 154:443-450.

Breslau PJ. Ultrasonic duplex scanning in the evaluation of carotid artery disease. Thesis, University of Limburg, Masstricht, Netherlands. 1982.

Breslau PJ, Jorning PJG, Greep JM. Assessment of aortoiliac disease using hemodynamic measures. Arch Surg 1985; 120:1050-2.

Brody WR. Hybrid subtraction for improved arteriography. Radiology 1981;

141:828-831.

Brown BG, Bolson EL, Frimer M, Dodge HT. Quantitative coronary arteriography. Estimation of dimensions, hemodynamic resistance, and atheroma mass of coronary artery lesions using the arteriogram and digital computation. Circulation 1977; 55(2):329-337.

Brown BG, Bolson EL, Dodge HT. Quantitative computer techniques for analyzing coronary arteriograms. Progress in Cardiovascular Diseases 1986; XXVIII:403-418.

Burns PN. The physical principles of doppler and spectral analysis. J clin Ultrasound 1987; 15:567-590.

Bürsch JH, Hahne HJ, Brennecke R, Hetzer R, Heintzen PH. Functional-angiograms derived from densitometric analysis of digitized x-ray picture series. Biomedical Engineering (Berlin) 1979; 24(Suppl):189-90.

Bürsch JH, Hahne HJ, Brennecke R, Gronemeier D, Heintzen PH. Assessment of arterial blood flow measurements by digital angiography. Radiology 1981; 141:39-47.

Canny J. A computational approach to edge detection. IEEE PAMI 1986; 8(6):679-698.

Caro CG, Pedley TJ, Seed WA. Mechanics of the circulation. In: Cardiovascular physiology. Edited by AC Guyton. Ch 1. Medical and Technical publishers, London, 1974.

Castleman KR. Three-dimensional image processing. In: Digital image processing. Published by Prentice-Hall. 1979; 347-383.

Chakraborty DP. Image intensifier distortion correction. Med Phys 1987; 14:249-252.

Chikos PM, Fisher LD, Hirsch JH, Harley JD, Thiele BL, Strandness DE. Observer variability in evaluating extracranial carotid artery stenosis. Stroke 1983; 14(6):885-92.

Colchester ACF, Brunt JNH. Measurement of vessel calibre and volume blood flow by dynamic qualitative digital angiography: An initial application showing variation of cerebral artery diameter with $PaCO_2$. Cereb B Flow Metabol 1983; 3:S640-641.

Colchester ACF. The effect of changing paCo2 on cerebral artery calibre estimated by a new technique of dynamic quantitative digital angiography.

Ph.D. Thesis, University of London 1984.

Colchester ACF, Hawkes DJ, Brunt JNH, du Boulay GH, Wallis A. Pulsatile blood flow measurements with the aid of 3-d reconstruction from dynamic angiographic recordings. In: Information Processing in Medical Imaging. Edited by SL Bacharach. Martinus Nijhoff Publishers 1986; 247-265.

Crummy AB, Strother CM, Sackett JF, Ergun DL, Shaw CG, Kruger RA. Computerised fluoroscopy: digital subtraction for intravenous angiocardiography and arteriography. AJR 1980; 135:1131-1140.

Davies ER. Circularity: a new principle underlying the design of accurate edge orientation operators. Image & Vision Computing 1984; 2(3):134-142.

Detre KM, Wright E, Murphy ML, Takaro T. Observer agreement in evaluating coronary angiograms. Circulation 1975; 52:979-986.

Dodge HT, Sandler H, Ballew DW, Lord JD, Wash S. The use of biplane angiocardiography for the measurement of left ventricular volume in man. Am Heart J 1960; 60(5):762-776.

Doriot PA, Pochon Y, Rasoamanambelo L. Densitometry of coronary arteries-an improved physical model. Comput Cariol 1985; 91.

Dotter CT, Judkins MP. Transluminal treatment of arteriosclerotic obstruction. Circulation 1964; 30:654-670.

Drapanas T, Kluge DN, Schenk WG. Measurement of hepatic blood flow by bromsulphalein and by the electromagnetic flowmeter. Surgery 1960; 48:1017-1021.

du Boulay GH, Brunt JBH, Colchester ACF, Hawkes DJ, Wallis A, Wicks D. Volume flow measurement of pulsatile flow by digitised cine angiography. Acta Radiologica 1987; Suppl(13):59-62.

Enzmann DR, Djang WR, Riederer SJ, Collins WF, Hall A, Keyes GS, Brody WR. Low-dose, high-frame-rate versus regular-dose, low-frame-rate digital subtraction angiography. Radiology 1983; 146:669-676.

Eriksen M. Effect of pulsatile arterial diameter variations on blood flow estimated by Doppler ultrasound. Med & Biol Eng & Comput 1992; 30:46-50.

Evans DH. Some aspects of the relationship between instantaneous volumetric blood flow and continuous wave Doppler ultrasound recording. Ultrasound Med Biol 1982; 8:606-609.

Evans DH. Can ultrasonic duplex scanners really measure volumetric flow ? Physics in Medical Ultrasound, Ed J A Evans, York; IPSM 1986:600-4.

Fabre P. Utilisation des forces electromotrices d'enrigistrement des variations de vitesse des liquids conducteurs: un nouvel hemodromograph sans palette dans le sang. C. R. Acad. Sci. Paris 1932; 194:1097-1098.

Fegler G. Measurement of cardiac output in anaesthetised animals by a thermodilution method. Q.Jl exp Physiol 1954; 39:153.

Fessler JA, Macovsky A. Object-based 3-D reconstruction of arterial trees from magnetic resonance angiograms. IEEE Trans on Medical Imaging 1991; 10(1):25-39.

Fisher LD, Judkins MP, Lespearance J, Cameron A, Swaye P, Ryan T, Maynard C, Bourassa M, Kennedy JW, Gosselin A, Kemp H, Faxon D, Wexler L. Reproducibility of coronary arteriographic reading in the coronary artery surgery study (CASS). Cathet Cardiovas Diagn 1982; 8:865-875.

Forbes G. Quantitative blood flow analysis with digital techniques. In: Digital Radiology, Physical and Clinical Aspects. Edited by: RM Harrison and I Isherwood. The Institute of Physical Sciences in Medicine 1984; 137-145.

Fujita H, Doi K, Giger M L, Chan H P. Characteristic curves of II-TV systems. Med Phys 1985; 13:13-18.

Fujita H, Doi K, Fencil L. Image feature analysis and computer-aided diagnosis in digital radiography. 2. Computerized determination of vessel sizes in digital subtraction angiography. Med Phys 1987; 14(4):549-556.

Garroway AN. Velocity measurements in flowing fluids by NMR. J Phys D: Appl Phys 1974; 7:L159-63.

Gensini GG, Kelly AE, Da Costa BCB, Huntington PP. Quantitative angiography: The measurement of coronary vasomobility in the intact animal and man. Chest 1971; 60(6):522-30.

Gill RW. Measurement of blood flow by ultrasound: accuracy and sources of error. Ultraosund Med Biol 1985;11:625-41.

Gould KL. Assessing coronary atenosis severity: A recurrent clinical need. JACC 1986;8:91-94.

Gruentiz AR, Turina MI, Schneider JA. Experimental percutaneous dilatation of coronary artery stenosis. Circulation 1976; 54:81.

Gruentzig AR, Myler RK, Hanna EH et al. Coronary transluminal angioplasty. Circulation 1977; 56:84 (Abs).

Gruentzig AR. Transluminal dilatation of coronary artery stenosis. Lancet 1978; 1:263.

Guggenheim N, Doriot PA, Dorsaz PA, Descouts P, Rutishauser W. Spatial reconstruction of coronary arteries from angiographic images. Phys Med Biol 1991; 36(1):99-110.

Hahn EL. Detection of sea water motion by nuclear procession. J Geophys Res 1960; 65:776-777.

Hamilton WF, Moore JW, Kinsman JM, Spurling RG. Studies on the circulation. IV. Further analysis of the injection method, and of changes in hemodynamics under physiological and pathological conditions. Am J Physiol 1932; 99:534-51.

Harper AM, Lorimer AR, Thomas DL. Methods of measuring blood flow. In: Scientific Foundation of Anaesthesia. Edited by C Scurr and S Feldman. London: Heinemann. 1974; pp. 28-44.

Hawkes DJ, Mol CB, Colchester ACF. The accurate 3-D reconstruction of the geometric configuration of vascular trees from x-ray recordings. In: Physics and engineering of medical imaging. NATO ASI. Edited by R Guzzardi. Martinus Nijhoff publications, Holland 1987; 250-258.

Hawkes DJ, Colchester ACF, de Belder MA, Norbury RN, Camm AJ, Davies MJ. The measurement of absolute lumen cross sectional area and lumen geometry in quantitative angiography. In: The Formation, Handling and Evaluation of Medical Images. Edited by A. Todd-Pokropek. Proc NATO ASI (Portugal), September. 1988a.

Hawkes DJ, Colchester ACF, Brunt JNH, Wicks DAG, du Boulay GH, Wallis A. Development of a model to predict the potential accuracy of vessel blood flow measurements from dynamic angiographic recordings. In: Physics and Engineering of Medical Imaging. Edited by Guzzardi R. Nijhoff M. The Hague Publication 1988b.

Hawkes RC, Holland GN, Moore WS, Worthington BS. Nuclear magnetic resonance (NMR) tomography of the brain: a preliminary clinical assessment with demonstration of pathology. J Comput Assist Tomogr 1980; 4:577-586.

Hilal SK. Determination of the blood flow by a radiographic technique. Am J Roentgenol 1966; 96(4):896-906.

Hill DLG, Hawkes DJ, Crossman JE, Gleeson MJ, Cox TCS, Bracey EE, Strong AJ, Graves P. Registration of MR and CT images for skull base surgery using point-like anatomical features. Bri J Radiol 1991;64(767):1030-1035.

Hill DLG, Hawkes DJ, Harrison N, Ruff CF. A strategy for automated multimodality image registration incorporating anatomical knowledge and imager characteristics. In: Bannett HH and Gmitro AF, eds. Information processing in Medical Imaging. Springer Verlg Pub., Berlin 1993 (in press).

Holcroft JW, Lantz BMT, Foerster JM, Link DP. Vido dilution technique. An Accurate measure of blood flow during routine arteriography. Arch Surg 1980; 115:1299-1303.

Höhne KH, Bohm M, Erbe W, Nicolae GC, Pfeidder G, Sonne B. Computer angiography: A new tool for X-ray functional diagnostics. Medical Progress through Technology 1978; 6:23-28.

Iqbal N. 3D angiography. Determining in vivo measures of lengths, calibres and velocities. BSc Project Report, UMDS, Guy's Hospital 1992.

Isner JM, Kishel J, Kent KM, Ronan JA, Ross AM, Roberts WC. Accuracy of angiographic determination of left main coronary arterial narrowing. Circulation 1981; 63(5):1056-64.

Jaffe CC. Doppler applications and limits of the method. Clin Diag Ultrasound 1984; 13:1-10.

Johnson EL, Yock PG, Hargrave VK, Srebro JP, Manubens SM, Seitz W, Ports TA. assessment of severity of coronary stenoses using a Doppler catheter. Validation of a method based on the continuity equation. Circulation 1989; 80:625-35.

Keyes GS, Pelc NJ, Riederer SJ, Sieb LE. Digital fluorography. General Electric Technology Update 1981; 29-31.

Khouri EM, Gregg DE. Miniature electromagnetic flow meter applicable to coronary arteries. J Appl Physiol 1963; 18:224.

Kim HC, Min BG, Lee TS, Lee SJ, Lee CW, Park JH, Han MC. Three-dimensional digital subtraction angiography. IEEE Trans on Med Imaging 1982; MI-1(2):152-158.

Korbuly DE. Determination of the pulsatile blood flow by a radiographic method. Invest Radiol 1973; 8:255-258.

Kruger RA, Mistretta CA, Riederer SJ. Physical and technical considerations of computerized fluoroscopy difference imaging. IEEE Transactions on Nuclear Scince 1981a; 28(1):205-212.

Kruger RA. Estimation of the diameter of and iodine concentration within blood vessels using digital radiography devices. Med Phys 1981b; 8(5):652-8.

Kruger RA, Anderson RE, Koehler PR, Nelson JA, Sorenson JA, Morgan T. Method for the noninvasive evaluation of cardiovascular dynamics using a digital radiographic device. Radiology 1981c; 139:301-305.

Kruger RA, Miller FJ, Nelson JA, Liu PY, Bateman W. Digital subtraction angiography using a temporal bandpass filter: Associated patient motion properties. Radiology 1982; 145:315-320.

Kruger RA, Bateman W, Liu PY, Nelson JA. Blood flow determination using recursive processing: a digital radiographic method. Radiology 1983; 149:293-298.

Kruger RA, Rieder SJ. Basic concepts of digital subtraction angiography. GK Hall Medical Publishers. Boston. 1984.

Lamb H. Hydrodynamics, 5th edition (reprinted 1953). University Press, Cambridge 1932.

Langlois YE, Greene FM, Roederer GO, Jager KA, Philips DJ, Beach KW, Stranness DE. Computer based pattern recognition of carotid artery Doppler signals for disease classification: Prospective validation. Ultrasound Med Biol 1984; 10:851-595.

Lantz B, Strid KG. Contrast formation in fluoroscopic videodensitometry. II. A comparison between theoretically computed and experimentally measured contrast. Acta Radiol Diagn 1973; 14:625-637.

Leeuw P. Quality considerations on cine-imaging and PTCA-fluoroscopy anticipating a digital future. In: State of the art in quantitative coronary arteriography, edited by JHC Reiber and PW Serruys. Martinus Nijhoff, Dordrecht 1986; 3-16.

Link DP, Lantz BMT, Foerster JM, Holcroft JW, Reid MH. New Videodensitometric method for measuring renal artery blood flow at routine arteriography: Validation in the canine model. Invest Radiol 1979; 14:465-470.

Mackay SA, Potel MJ, Rubin JM. Graphics methods for tracking three-dimensional heart wall motion. Comput Biomed Res 1982; 15:455-473.

Maher KP, O'Connor MK, Malone JF. Experimental examination of videodensitometry of large opacifications in digital subtraction angiography. Phy Med Biol 1982; 32:1273-1282.

McCormick PA, Seifalian AM, Stansby G, McGann G, Collins P, Chin J, McIntyre

N, Dick R, Burroughs AK. Superior mesenteric artery blood flow in man measured with intra-arterial Doppler catheters: Effect of Octreotide. Hepatology 1993; 17:20-27.

McDonald DA. Blood flow in arteries. 2nd edition, Edward Arnold, London 1974.

Meaney TF, Weinstein MA, et al. Digital subtraction angiography of the human cardiovascular system. AJR 1980; 135:1153-1160.

Meisner H, Messmer K. Significance and limitations of electromagnetic blood flowmetry, experimental and clinical results. Progr Surg 1970; 8:124-144.

Merritt CRB. Doppler blood flow imaging. J Clin Ultrasound 1987; 15:591-597.

Mistretta CA. Current practice and future directions in digital subtraction angiography. SPIE 1981; 314:18-23.

Miyatake K, Okamoto M, Kinoshita N, Izumi S, Owa M, Takao S, Sakakibara H, Nimura Y. Clinical applications of a new type of real-time two-dimensional doppler flow imaging system. Am J Cardiol 1984; 54:857-868.

Modic MT, Meredith AW. Intravenous digital angiography of the head and neck: a clinical update. SPIE 1981; 314:244-247.

Mol CR. 3D reconstruction from biplane x-ray angiography. Tech. Rep. IBM UK Scientific Centre 1984; Sept:1-44.

Nadel SN, Greene AS, White RI, Anderson JH. Measurement of peripheral blood flow by thermodilution techniques. Invest Radiol 1986; 21:631-636.

Nalcioglu O, Roeck WW, Siebert JA, Lando AV, Tobis JM, Henry WL. quantitative aspects of image intensifier-television based digital x-ray imaging. In: Digital Radiography, edited by JG Kereiake, SR Thomas and CG Orton. Plenum Press, New York 1986; 13-33.

Nelson JA, Miller FJ, et al. Digital subtraction angiography using a temporal bandpass filter: Initial clinical results. Radiology 1982; 145:309-313.

Nelson TR, Pretorius DH. The Doppler signal: where does it come from and what does it mean?. AJR 1988; 151:439-447.

Nissen SE, Booth DC, Smith M, DeMaria AN. Sources of error in videodensitometric calculation of ejected fraction. Circulation 1983; 68(suppl.II):II-350.

Nordenström B, Grim S. A method for determination of blood flow with use of roentgen contrast medium. Radiology 1965; 84:644-655.

O'Handley DA, Beckenbach ES, Castleman KR, Selzer RH, Wall RJ. Picture analysis applied to biomedicine. Comput Graphics and Image Processing

1973; 2:417-432.

O'Leary DH. Vascular ultrasonography. Eadiol Clin North Am 1985; 23:39-56.

Okadome K, Eguchi H, Yukizane T, Mii S, Muto Y, Sugimachi K. Doppler flow waveform analysis aids in early detection of late graft failure in cases of lower extrmity arterial reconstruction; case studies. Vascular Surgery 1989; 23(2):519-527.

Pamelia FX, Graddock GG, Watson DD, Gibson RS, Sirowatka J, Beller GG. Outcome and prognosis of patients with chest pain and normal thallium-201 exercise scans. Circulation 1981;64:34.

Parker DL, Wu J, Pope DL, Van Bree R, Caputo GR, Marshall HW. Three-dimensional reconstruction and flow measurements of coronary arteries using multi-view digital angiography. In New developments in quantitative coronary arteriography. ed. by: JHC Reiber and PW Serruys. Kluwer Acad Pub 1988; 225-247.

Pelc NJ, Chesler DA. Utilization of cross-plane rays for three-dimensional reconstruction by filter back-projection. JCAT 1979; 3(3):385-395.

Pfaff JM, Whiting J, Vas R, Eigler N, Weiss M, Nivatpumin T, Forrester JS. Automated geometric/densitometric coronary analysis: Comparison of accuracy and reproducibility. J Am Coll Cardiol 1985; 5:501.

Pfaff JM, Whiting JS, Eigler NE. Accurate densitometric quantification requires strict attention to the physical characteristics of X-ray imaging. In: New developments in quantitative coronary arteriography. Edited by JHC Reiber, and PW Serruys. Kuwer Academic Publishers 1988; 22-23.

Powis RL. Color flow imaging: Understanding its science and technology. J Diagn Med Sonogr 1988; 4:236-245.

Price JB, Britton RC, Peterson LM, Reilly JW, Voorhees AR. The validity of chronic hepatic blood flow measurements obtained by the electromagnetic flow meter. JSR 1965; V(7):313-317.

Ra JB,Lim CB, Cho ZH, Hilal SK, Correll J. A true three-dimensioanl reconstruction algorithm for the sperial positron emission tomograph. Phys Med Biol 1982; 27(1):37-50.

Rafflenbeul W, Urthaler F, Lichtlen P, James TN. Quantitative differences in 'critical' stenosis between right and left coronary artery in man. Circulation 1980; 62(6):1188-96.

Reiber JHC, Gerbrands JJ, Troost GJ, Kooijman CJ, Slump CH. 3-D

reconstruction of coronary arterial segments from two projections. In: Digital Cardiovascular radiology. Edited by PH Heintzen and R Brennecke. Thieme-Stratton (New York) Publication 1983; 151-163.

Reiber JHC, Kooijman CJ, Slager CJ. Computer assisted analysis of the severity of obstructions from coronary cineangiograms: A methodological review. Automedica 1984; 5:219-238.

Ridgway JP, Turnbull LW, Smith MA. Demonstration of pulsatile cerebrospinal-fluid flow using magnetic resonance phase imaging. Bri J Radiology 1987; 60:423-427.

Riederer SJ, Kruger RA, Mistretta CA. Limitations to iodine isolation using a dual beam non-edge apprach. Med Phys 1981; 8:54.

Rittgers SE, Fei D. Flow dynamics in a stenosed carotid bifurcation model - part II: Derived indices. Ultrasound in Med & Biol 1988; 14:33-44.

Robinson ML. Duplex sonography of the carotid arteries. Seminars in Roentgenology 1992; XXVII(1):17-27.

Roehring H, Nudelman S, Fisher HD, Frost MM, Capp MP. Photoelectronic Imaging for Radiology. IEEE NS 28 1981; 1:190-204.

Rogers DF, Adams JA. Mathematical elements for computer graphics. McGraw-Hill Pub. 1990:101-133.

Rosen L, Silverman NR. Videodensitometric measurements of blood flow using cross-correlation techniques. Radiology 1973; 109(2):305-10.

Rutishauser W, Simon H, Stucky JP, Schad N, Noseda G, Wellauer J. Evaluation of roentgen cinedensitometry for flow measurement in models and in the intact circulation. Circulation 1967; XXXVI:951-63.

Rösch J, Anderson JM, Antonovic R, Robinson M. Transluminal iliac artery dilatation. Nonsurgical catheter treatment of atheromatous narrowing. J Amer Med Ass 1974; 230:117-124.

Sakurai T., Yamada I, Ohta T. Flow velocity measurement using digital subtraction angiography for hemodynamic evaluation in arterial occlusive disease. Angiology 1986; 37(11):846-54.

Sandrik JM. The video camera for medical imaging. In: Electronic imaging in Medicine. AAPM Monograph No 11. American Institute of Physics, New York. 1984.

Schmiel FK, Huber H, Neuhaus KL, Spiller P. Densitometric measurements of coronary blood flow: methodological improvements. In: Roentgen video

techniques for dynamic studies of structure and function of the heart and circulation. Edited by PH Heintzen and JHB Büersch. Stuttgart, Germany: George Thieme Publishers 1978; 49-55.

Schmiel FK, Block M, Jehle J, Pölitz B, Spiller P. Densitometric measurement of phasic blood flow in the coronary artery system. In: Angio-cardiography Edited by H. Just, PH Heintzen. 1986; 389-399.

Scoblionko DP, Brown BG, Mitten S, Caldwell JH, Kennedy JW, Bolson EL, Dodge HT. A new digital electronic caliper measurement of coronary arterial stenosis: Comparison with visual estimates and computer-assisted measurements. Am J Cardiol 1984; 689-93.

Seibert JA, Nalcioglu O, Roeck WW. Removal of image intensifier veiling glare by mathematical deconvolution techniques. Med Phys 1985; 12:281-288.

Seifalian AM, Young JM, Hobbs KEF. Quantitative assessment of portal vein blood flow by duplex ultrasound scanning. Clin Radiol 1988a; 39:681.

Seifalian AM, Hawkes DJ, Colchester ACF, Hobbs KEF. New algorithm for deriving pulsatile blood flow waveforms tested with simulated dynamic angiographic data. Radiology 1988b; 169(P):324.

Seifalian AM, Hawkes DJ, Colchester ACF, Hobbs KEF. Comparison of processing techniques for measurement of intravascular blood flow from simulated dynamic angiographic images. Bri J Radiol 1988c; 61:721.

Seifalian AM, Hawkes DJ, Colchester ACF, Hobbs KEF. A new algorithm for deriving pulsatile blood flow waveforms tested using simulated dynamic angiographic data. Neuroradiology 1989; 31:263-269.

Seifalian AM, Stansby GP, Hawkes DJ, Colchester ACF, Hobbs KEF. Measurement of liver blood flow: A review. HPB Surgery 1991a; 4:171-186.

Seifalian AM, McCormick A, Stansby G, Burrough A, Hamilton G, McIntyre N, Hobbs K. Validation of an intravascular Doppler ultrasound flowmeter for measurement of pulsatile blood flow in vitro and in vivo. Med Biol Eng & Comput 1991b; 29:482.

Shaw CG, Ergum DL, Myerowitz PD, Van Lysel MS, Mistretta CA, Zarnstorff WC, Crummy AB. technique of scatter and glare correction for videodensitometric studies in digital subtraction videoangiography. Rad Phy 1982; 142:209-213.

Shaw CG, Plewes DB. Pulsed - injection method for blood flow velocity measurement in intraarterial digital subtraction angiography. Radiology

1986; 160:556-559.

Shimizu K, Matsuda T, Sakurai T, Fujita A, Ohara H, Okamura S, Hashimoto S, Mano H, Kawai C, Kiri M. Visualization of moving fluid: Quantitative analysis of blood flow velocity using mr imaging. Radiology 1986; 159:195-199.

Shroy RE. Dependence of noise on array width and depth in digital radiography. Med Phys 1988; 15(1):64-6.

Sibley DH, Millar HD, Hartley CJ, Whitlow PL. Subselective measurement of coronary blood flow velocity using a steerable Doppler catheter. JACC 1986; 8(6):1332-40.

Silverman NR, Rosen L. Arterial blood flow measurement: Assessment of velocity estimation methods. Invest Radiol 1977; 12(4):319-324.

Simons MA, Kruger RA, Power RL. Cross-Sectional area measurements by Digital Subtraction Videodensitometry. Invest Radiol 1986; 21:637-644.

Sinclair JD, Sutterer WF, Wolford JL, Armelin E, Wood EH. Problems in comparison of dye-dilution curves with densitometric variations at the same site in the circulation measured from simultaneous cineangiograms. Staff Meeting of the Mayo Clinic 1960; 7:764-73.

Smith MA. The measurement and visualisation of vessel blood flow by magnetic resonance imaging. Clin Phys Physiol Meas 1990; 11(2):101-123.

Smith WM, Starmer CF. Error propagation in quantitative biplane cineroentgenography. Phys Med Biol 1978; 23(4):677-685.

Sovak M, Ziskin M C, Oigaard A, Mygind T. Lipiodol droplets in cineradiographic quantitation of pulsatile and non-pulsatile blood flow, Model Experiments. Invest Radiol 1971; 6:141-145.

Spiller P, Schmiel FK, Politz B, Block M, Fermor U, Hackbarth W, Jehle J, Korfer R, Pannek H. Measurement of systolic and diastolic flow rates in the coronary artery system by x-ray densitometry. Circulation 1983; 68(2):337-347.

Stacey-Clear A, Fish PJ. Repeatibility of blood flow measurement using multichannel pulsed Doppler ultrasound. Bri J Radiol 1984; 57:419-420.

Starmer CF, Clark DO. Computer computations of cardiac output using the gamma function. J Appl Physiol 1970; 28:219-220.

Stewart GN. Studies on the circulation in man. 1. The measurement of blood flow in the hands. Heart 1912; 3:33.

Suetens P, Jansen P, Haegemans A, Oosterlinck A, Gybels J. 3D reconstruction of the blood vessels of the brain from a stereoscopic pair of subtraction angiograms. Image and vision computing 1983; 1(1):43-51.

Suryan G. Nuclear resonance in flowing liquids. Proc Ind Acad Sci 1951; 33:107-11.

Swanson DK, Myerowitz PD, Hegge JO, Watson KM. Arterial blood-flow waveform measurement in intact animals: New digital radiographic technique. Radiology 1986; 161:323-328.

Swanson DK, Kress DC, Pasaoglu I, Hegge JO, Kroncke GM. Quantitation of absolute flow in coronary artery bypass grafts using digital subtraction angiography. J Surg Res 1988; 44:326-335.

Switzer DF, Nanda NC. Doppler color flow mapping. Ultrasound Med Biol 1985; 11:403-416.

Thompson HK, Starmer F, Whalen RE, McIntosh HD. Indicator transit time considered as a gamma variate. Circ Res 1964; 14:502-515.

Van Andel GJ. Transluminal iliac angioplasty, long-term results. Radiology 1980; 135:607-611.

Vignaud J, Rabischong P, Yver JP, Pardo P, Thurel C. Multidirectional reconstruction of angiograms by stereogrammetry and computer. Application to computed tomography. Euroradiology 1979; 18(1):1-7.

Virdee MS. Angiographic quantification of lumen shape and absolute cross sectional area by 3-dimensional videodensitometry. BSc Project Report, UMDS, Guy's Hospital 1991.

Vogel R, LeFree M, Bates E, O'Neill W, Foster R, Kirlin P, Smith D, Pitt B. Application of digital techniques to selective coronary arteriography: Use of myocardial contrast appearance time to measure coronary flow reserve. Am Heart J 1982; 107(1):153-163.

Wackers FG, Sokole EB, Samson G et al. Value and limitation of thallium-201 scintigraphy in the accute phase of myocardia infarction. New Eng J Med 1976;295:1.

Waluch V, Bradley WG. NMR even echo rephasing in slow laminar flow. J Comput Assist Tomogr 1984; 4:594-598.

Webster JG. Measurement of flow and volume of blood. In: Medical instrumentation: Application and Design. Edited by JG Webster. Boston, Houghton Mifflin 1978; ch. 8.

West DJ, Tarnawski M, Graves MJ, Taylor MG, Padayachee TS, Ayton VT, Smith MA. Blood flow imaging by magnetic resonance. Medicamundi 1988; 33(3):101-111.

Wicks DAG. Intravascular blood flow measurement by quantitative cineangiographic image analysis. Ph.D. Thesis, Manchester University 1989.

Wilson RF, Laughlin DE, Ackell PH, Chilian WM, Holida MD, Hartley CJ, Armstrong ML, Marcus ML, White CW. Transluminal, subselective measurement of coronary artery blood flow velocity and vasodilator reserve in man. Circulation 1985; 72:82-92.

Womersley JR. Method for the calculation of velocity rate of flow and viscous drag in arteries when the pressure gradient is known. J Physiol 1955; 127:553-563.

Wong WH, Kirkeede RL, Gould KL. Computer applications in angiography. In: cardiac imaging and image processing. Edited by SM Collins and DJ Skorton. McGraw-Hill, New York 1986; 206-238.

Wyatt DG. Blood flow and blood velocity measurement in vivo by electromagnetic induction. Med Biol Eng & Comput 1984; 22:193-211.

Zierler KL. Theoretical basis of indicator-dilution methods for measuring blood flow and volume circulation. Circulation 1962; 10:393-407.

Zir LM, Miller SW, Dinsmore RE, Gilbert JP, Harthorne JW. Interobserver variability in coronary angiography. Circulation 1976; 53:627-632.

Ziskin MC, Revesz G, Kundel HL, Shea FJ. Spatial frequency spectra of radiographic images. Radiology 1971; 98(3):507-517.

Zoli M, Marchesini G, Brunori A, Cordiani MR, Pisi E. Portal venous flow in response to acute beta blocker and vasodilatatory treatment in patients with liver cirrhosis. Hepatology 1986; 6:1248-1251.

Zwiebel WJ. Color Duplex imaging and Doppler spectrum analysis: Principle capabilities, and limitations. Seminars in Ultrasound, CT, and MR 1990; 11(2):84-96.

RELEVANT PUBLICATIONS AND CONFERENCE PRESENTATIONS

PUBLICATIONS

Seifalian AM, Hawkes DJ, Colchester AC, Hobbs KEF. New Algorithm for Deriving Pulsatile Blood Flow Waveform Tested With Simulated Dynamic Angiographic Data. Radiology 1988; 169(P):324 [Abstract].

Seifalian AM, Hawkes DJ, Colchester AC, Hobbs KEF. Comparison of processing techniques for measurement of intravascular blood flow from simulated dynamic angiographic images. Bri J Radiol 1988; 61:721 [Abstract].

Seifalian AM, Hawkes DJ, Colchester AC, Hobbs KEF. A new algorithm for deriving pulsatile blood flow waveform tested using simulated dynamic angiographic data. Neuroradiology 1989; 31:263-269.

Piasecki C, Seifalian AM. Continuous monitoring of hepatic blood perfusion using a noninvasive surface electrode. Digestive Diseases and Sciences 1990; 35(3):399-405.

Seifalian AM, Hawkes DJ, Hardringham CR, Colchester ACF, Reidy JF. Validation of a quantitative radiographic technique to estimate pulsatile blood flow waveforms using digital subtraction angiographic data. J. Biomed. Eng. 1991; 13:225-233.

Seifalian AM, Stansby G, Hawkes DJ, Colchester ACF, Hobbs KEF. Measurement of liver blood flow: A review. HPB Surgery 1991; 4:171-186.

Hawkes DJ, Hardingham CR, Seifalian AM, Virdee M, Colchester ACF. Recent advances in extracting quantitative information from x-ray angiographic data. Innov Tech Biol Med 1992;13(1):99-107.

McCormick PA, Seifalian AM, Stansby GP, McGann G, Collins P, Chin J, McIntyre N, Dick R, Burroughs AK. Superior mesenteric artery blood flow in man measured with intra-arterial Doppler catheters: effect of octreotide. J

Hepatology 1993;17:20-27.

Brunt JN, Wicks DA, Hawkes DJ, Seifalian AM, du Boulay GH, Colchester AC, Wallis A. The measurement of blood flow waveforms from X-ray angiography Part 1: Principles of the method and preliminary validation. J Eng in Med 1992; 206(Part H): 73-85.

Colchester ACF, Seifalian AM, Hawkes DJ, Brunt JN, Wicks D, du Boulay G, Hobbs KEF. "Determination of instantaneous and average blood flow rates from digital angiograms of vessel phantoms using distance-density curves." Invest Radiol 1992; 27(3):274 [letter].

Bladin CF, Seifalian AM, Iqbal N, Colchester ACF, Hawkes DJ. Haemodynamic assessment of extracranial vascular stenoses using quantitative angiography. 2nd European Stroke Conference 1992 [Abstract].

Seifalian AM, Hawkes DJ, Bladin CF, Hardingham CR, Iqbal N, Colchester ACF, Hobbs KEF. Volume blood flow waveforms measurements from quantitative X-ray angiographic data with aid of 3D reconstructions. Proceedings IEEE EMB 1992;14(5):1946-7.

Seifalian AM, Davidson BR, Rolles K. Laser Doppler Imaging for the assessment of liver perfusion during transplantation. Eur J Gastroenterology & Hepatology 1993;5:479-482.

Seifalian AM, Jackson A, Howell K, Stansby G, Hamilton G. Assessment of laser Doppler perfusion imaging with laser Doppler flowmetery, and thermographic imaging for investigating blood flow in human skin. [Submitted to the Eur J Vascular Surgery].

Seifalian, Howell K, Stansby G, Jackson AE, Hamilton G, Black CM. Laser Doppler perfusion imaging: a new technique for measuring skin blood flow in Rheumatology. [Submitted to Bri J Rheumatology].

Hawkes DJ, Seifalian AM, Colchester ACF, Iqbal N, Hardingham CR, Bladin C,

Hobbs KEF. Validation of Volume Blood Flow Measurements using 3D Distance-Concentration Functions derived from Digital X-ray Angiograms [submitted to Invest Radiol].

CONFERENCE PRESENTATIONS

Seifalian AM, Young JM, Hobbs KEF. Quantitative assessment of portal vein blood flow by duplex ultrasound scanning. The Royal College of Radiologists, Annual Scientific Meeting 1988.

Seifalian, AM. Critical review of image processing strategies for the angiographic measurement of blood flow. Seminar at Image Analysis, Division of Radiological Sciences, Guy's Hospital, London, May 1988.

Seifalian AM, Hawkes DJ, Colchester AC, Hobbs KEF. Comparison of processing techniques for measurement of intravascular blood flow from simulated dynamic angiographic images. British Radiology Conference 1988.

Seifalian AM, Hawkes DJ, Colchester AC, Hobbs KEF. New Algorithm for Deriving Pulsatile Blood Flow Waveform Tested With Simulated Dynamic Angiographic Data. 74th Scientific Assembly and Annual Meeting of Radiological Society of North America (RSNA), USA 1988.

Seifalian AM, Piasecki C, Hobbs KEF. A new non-invasive oxygen surface electrode for the continuous measurement of liver blood flow. European Society for Surgical Research, 24th Congress, Brussels 1989.

Seifalian AM, Hawkes DJ, Hardingham CR, Reidy JF, Colchester ACF. Quantitation of absolute flow velocity from the femoral arteriogram: pre and post angioplasty. Presented Euro-Sigma'90 (poster), Guy's Hospital, London, 6-7 September, 1990.

Seifalian AM, Hawkes DJ, Hardringham CR, Colchester ACF, Reidy JF. Validation of a quantitative radiographic technique to estimate pulsatile blood flow

waveforms using digital subtraction angiographic data. 30th Biological Engineering Society Annual Scientific Meeting 1990.

Seifalian AM, McCormick A, Stansby GP, Burroughs A, Hamilton G, McIntyre N, Hobbs KEF. Validation of an intravascular Doppler ultrasound flowmeter for measurement of pulsatile blood flow in vitro and in vivo. World Congress on Medical Physics and Biomedical Engineering, Japan, July, 1991.

McGann G, McCormick A, Harwood A, Seifalian A, Burroughs A, Dick R. Intra-arterial Doppler validation of splenic blood flow measurements obtained by percutaneous colour duplex Doppler studies. Irish and British Radiology Conference, Dublin 91.

Bladin CF, Seifalian AM, Iqbal N, Colchester ACF, Hawkes DJ. Haemodynamic assessment of extracranial vascular stenoses using quantitative angiography. 2nd European Stroke Conference, Lausanne, Switzerland, 25-27 June, 1992.

Seifalian AM, Hawkes DJ, Bladin CF, Hardingham CR, Iqbal N, Colchester ACF, Hobbs KEF. Volume blood flow waveforms measurements from quantitative X-ray angiographic data with aid of 3D reconstructions. 14th Annual IEEE-EMBS Conference, Paris, France, October, 1992.

Davies MT, Morrison GD, Seifalian AM, Hawkes DJ. Specifications for digital angiography equipment to perform three dimensional reconstruction of blood vessels. BIR (Images Quality in the Selection of Equipment), London, February 1993.

Seifalian AM, Davidson BR, Rolles K. Laser Doppler perfusion imaging in liver transplantation. Bri Microcirculation Society, London, March 1993.

Jackson AE, Seifalian AM, Howell K, Stansby GP, Hamilton G, MaClean AB. A comparison of laser Doppler flowmetry, with the laser Doppler perfusion imager and thermographic imaging of the skin. Biol Eng Society (Forum

on Angiology), Dundee, April 1993.

Seifalian AM. Validation of Volume Blood Flow Measurements Using 3D Distance-Concentration Functions Derived from Digital X-ray Angiograms. Cologne University, Germany, May 1993.

Seifalian AM, Stansby G, Jackson AE, Howell K, Hamilton G. Laser doppler perfusion imaging and skin blood flow. European Laser Doppler User Meeting on laser Doppler assessment of microvascular perfusion in clinical research. Oslo June 3-5, 1993.

Seifalian AM, Davidson BR, Stansby G, Hamilton G, Kurzawinski T, Rolles K. A continuous hepatic tissue blood flow monitoring during liver transplantation by laser Doppler flowmeter. European Laser Doppler User Meeting on laser Doppler assessment of microvascular perfusion in clinical research. Oslo June 3-5, 1993.

HPB Surgery, 1991, Vol. 4, pp. 171–186
Reprints available directly from the publisher
Photocopying permitted by license only

REVIEW ARTICLE

MEASUREMENT OF LIVER BLOOD FLOW: A REVIEW

A.M. SEIFALIAN, G.P. STANSBY and K.E.F. HOBBS
Department of Hepatobiliary Surgery and Liver Transplantation, Royal Free Hospital School of Medicine, London NW3 2QG, UK

D.J. HAWKES
Division of Radiological Sciences, United Medical and Dental School, Guy's Hospital Campus, London SE1 9RT, UK

A.C.F. COLCHESTER
Department of Neurology, United Medical and Dental School, Guy's Hospital Campus, London SE1 9RT, UK

(Received 7 February 1991)

The study of hepatic haemodynamics is of importance in understanding both hepatic physiology and disease processes as well as assessing the effects of portosystemic shunting and liver transplantation. The liver has the most complicated circulation of any organ and many physiological and pathological processes can affect it[1,2]. This review surveys the methods available for assessing liver blood flow, examines the different parameters being measured and outlines problems of applicability and interpretation for each technique.

The classification of these techniques is to some extent arbitrary and several so called "different" methods may share certain common principles. The methods reviewed have been classified into two groups (Table 1): those primarily reflecting flow through discrete vessels or to the whole organ and those used to assess local microcirculatory blood flow. All techniques have their advantages and disadvantages and in some situations a combination may provide the most information. In addition, because of the many factors affecting liver blood flow and sinusoidal perfusion, readings in a single subject may vary depending on positioning, recent food intake, anxiety, anaesthesia and drug therapy. This must be borne in mind if different studies are to be meaningfully compared.

KEY WORDS: Blood flow, tissue perfusion, portal blood flow, hepatic blood flow, Doppler ultrasound, Doppler laser, x-ray angiography

Address correspondence to: Mr. Alexander M. Seifalian, Department of Hepatobiliary Surgery and Liver Transplantation, Royal Free Hospital School of Medicine, Pond Street, London, NW3 2QG, UK.

Table 1 Hepatic blood flow measurement techniques.

METHODS MEASURING BLOOD FLOW
Velocity or Transit Time Methods
Electromagnetic Flowmeter
Dopler Ultrasound
X-Ray Angiography
Nuclear Magnetic Resonance
Dye Dilution Techniques
Plasma Disappearance Method
Radioisotope techniques
METHODS MEASURING TISSUE PERFUSION
Radiolabelled Microspheres
Heat Exchange
Hydrogen Electrode
Oxygen Electrode
Laser Doppler

METHODS MEASURING BLOOD FLOW

Velocity or Transit Time Methods

Electromagnetic flowmeter

The measurement of blood flow by electromagnetic induction was first suggested by Fabre[3] and the principle of the technique is based on Faraday's law of electromagnetic induction. If a magnetic field is applied across a vessel in which blood is flowing then an electric field is induced at right angles both to the induced magnetic field and the flow vector[4,5]. The electrical field is detected along its axis from the potential difference across the outside of the vessel. This potential is primarily determined by the velocity of the flowing blood within the vessel. Accuracy demands attention to detail and proper calibration[6,7] using a pump and saline solution. There is no way of checking calibration *in vivo* except vessel clamping for zero flow. Interference from other electrical instruments also minimise the accuracy of the technique[8].

In practice the method involves the placement of the device around the vessel to be assessed. For a good signal, close contact is essential. Drapanas, *et al*[9] and Price *et al.*[10] compared electromagnetic flowmetry with the bromsulphalein clearance method[11] for measuring hepatic arterial and portal vein flow in the dog and found a good correlation between the two methods. Because of the invasive nature of the technique, it is more applicable to animal studies and on patients at the time of surgery. These devices are, however, still regarded as the "gold standard" against which all other methods of measuring flow must be compared. They are able to measure instantaneous and mean blood flow in an exposed vessel. They can detect forward and reverse flow and the temporal resolution is fast enough for flow to be

studied during the cardiac cycle. Other advantages of the method are its insensitivity to changes in blood temperature and viscosity.

Doppler ultrasound

The first attempted use of Doppler ultrasound for the measurement of blood flow from the surface of the body was reported by Satomura in 1959[12] but compared to ultrasound imaging the role of Doppler ultrasound has evolved slowly and has largely been restricted to a relatively few well-defined indications in cardiac diagnosis, evaluation of carotid and peripheral vascular disease, and more recently in obstetrics and the abdomen[13,14]. The combination of real time B-mode ultrasound imaging and a pulsed Doppler flowmeter is referred to as a duplex scanner[15]. Using these machines the diameter of the vessel, peak velocity, mean velocity, volume flow rate, and pulsatility of blood flow waveforms can be measured[16]. A recent refinement is the development of colour flow mapping where the image provides flow information concerning all structures in the image field rather than just at one selected site.

Duplex ultrasound offers the best non-invasive way of assessing portal vein patency[17] and can demonstrate cavernous transformation and whether portal flow is hepatopetal or hepatofugal. Doppler has also been used in quantitative measurement of portal blood flow. Ohnishi *et al.*[18] compared a pulsed Doppler flowmeter with cineangiography[19] for calculating portal vein velocity in normal volunteers and patients with liver disease. Doppler and cineangiographic measurements exhibited significant correlation ($r=0.960$; $n=31$; $p<0.001$) for velocities from 2.4 to 12.2 cm/sec, but Doppler values were consistently about twice that of the cineangiographic values, underlying the need for calibration against a flow model. They suggested that Doppler might be of more use for assessing relative changes in portal flow rather than for giving absolute flow values. Ackroyd *et al.*[20] stated that raw flow values vary from person to person according to body weight, state of fasting, and position, as well as anxiety level and exercise and suggested that the use of standardised conditions could improve accuracy. One further reason for not relying on portal velocity measurements in studying cirrhotic patients is that portal flow is well maintained by portal vein dilatation until portal hypertension is severe[21]. For this reason a portal congestion index, which is the cross sectional area divided by the mean velocity, has been suggested by Moriyasu *et al.*[22] as being more useful than absolute flow values.

The Duplex scanner can also be a useful non-invasive tool for assessing patients with portosystemic shunts. Nelson *et al.*[23] studied patients before and after portosystemic shunting with both duplex scanning and angiography. They concluded Duplex was accurate in determining the direction of flow if an adequate tracing was obtained. Preoperatively it allows the determination of portal vein patency and direction of flow. Postoperatively most porto-caval and mesocaval shunts can be visualised as well as some Warren type shunts. As with many ultrasound applications success is largely dependent on operator skill and experience. Patency is directly demonstrated by flow in the correct direction and a confirmatory sign is the demonstration of corresponding phasic patterns of blood flow in the portal vein and inferior vena cava. Other confirmatory signs are dilatation of the inferior vena cava proximal to portocaval and mesocaval shunts and dilatation of the superior mesenteric vein above a mesocaval shunt[17].

Duplex is less useful in the assessment of hepatic and splanchnic arterial flow[24]. The vessels are relatively short, tortuous and deeply situated, making them difficult to image and the hepatic arterial supply is frequently multiple. Post liver transplantation the anatomy may be even harder to demonstrate and scanning of the hepatic artery is currently too time consuming and inaccurate to make it clinically useful in detecting hepatic arterial thrombosis. Intra-arterial Doppler flow probes are now being developed and combined with angiography may ultimately provide the best way to quantitatively measure hepatic and splanchnic arterial flow[24].

In summary, Duplex scanning potentially provides a non-invasive way of assessing liver blood flow in many clinical situations including the assessment of portal vein patency, direction of flow, surgical porto-systemic shunting and liver transplantation. Its accuracy has been validated *in vitro* and in experimental animals[25,26], but problems do exist in using this technique in clinical practice (see appendix A). Improvements both in hardware and software as well as the development of colour flow mapping are likely to be reflected in a greater use of Duplex ultrasound in liver blood flow studies in the future. It offers one of the best approaches to the non-invasive assessment of portal flow but is not yet capable of reliably assessing hepatic arterial flow.

X-Ray angiography

Angiography, or radiographic imaging of blood vessels, has a well established role in the diagnosis of liver disease and portal hypertension and is widely used in clinical practice for obtaining high quality vessel images[27]. As well as anatomical information, however, information on blood flow is also potentially available.

The techniques available for measuring flow using angiography are based on one of two principles. The first approach uses the principle that when an indicator is injected at constant rate into a blood vessel, the degree of dilution is proportional to blood flow, and the concentration in blood after mixing will be lower with higher flow and vice versa[28]. The main problem with this technique is accurate densitometric calibration. The second technique involves the measurement of the time taken for the passage of a bolus of contrast material between two sites but unfortunately precise timing of the passage of a dispersing bolus is often difficult to achieve[29]. In a new approach to this problem flow is determined by computer analysis of contrast concentration profiles as a function of time and distance along a vessel segment[29,30]. Another solution has been to assess relative flow by using two injections and measuring superior mesenteric, hepatic and splenic arterial flow relative to cardiac output[31,32].

The measurement of liver blood flow by angiographic techniques has largely been limited to hepatic arterial studies because catheter access to the portal system is not a routine procedure. Indirect portography, where contrast is injected into either the superior mesenteric artery or coeliac artery and imaged as it passes out into the portal system results in generally poor images unsuitable for flow analysis. Following direct insertion of a catheter into the portal system, Sovak *et al.*[33] used a computer to calculate the displacement of lipoidal droplets per frame. The average velocity ranged from 15.5 to 24.4 cm/sec in 6 normal patients and decreased during inspiration. Recently Iwanaga *et al.*[34] used this method[35] as a "gold standard" to test the validity of a Doppler duplex system for measuring portal blood flow in 10 patients with liver disease and found a significant correlation ($r = 0.970$) between

the maximum portal blood flow velocity by duplex ultrasound and the mean velocity calculated from cineangiographic methods.

Although it requires vascular catheterisation X-ray angiography is still the modality of choice for critical morphological vascular studies. That X-ray angiography has not been widely used for measuring blood flow is due in part, we believe, to the use of inappropriate algorithms for processing the image data[29,36]. The method does, however, have great potential especially when combined with lower dose Digital Subtraction Angiography and new low osmolarity non-ionic contrast agents[37]. Minipuncture needles and catheters[38] have led to increased safety of the technique and the equipment and expertise is potentially available in many centres.

Nuclear magnetic resonance

Nuclear Magnetic Resonance (NMR) imaging is a noninvasive imaging modality that is rapidly gaining clinical acceptance, although widespread introduction has been delayed by expense. Flow detection with NMR spectroscopy has been explored for more than 30 years[39–41]. When NMR imaging was first performed in the late 1970s signal loss was noted within arteries and attributed to high flow rates[42]. In the early 1980s, several causes of increased signal intensity were described, generally associated with slow flow in veins and dural sinuses[43,44]. Understanding these flow phenomena has provided the basis for the development of specialized NMR imaging sequences intended to quantitate blood flow measurements. Several methods have been proposed to quantify blood flow[45–47] but at this stage their relative merits in terms of spatial and velocity resolution and image acquisition times have not been completely evaluated, nor has liver blood flow measurement been considered specifically. We suspect, however, that this will be an area of great development in the future.

Dye Dilution Techniques

Plasma disappearance methods

Attempts have been made since the middle of this century to measure liver blood flow by dye infusion methods[48]. Certain organic dyes are extracted by the hepatocytes and if the rate of extraction is measured, liver blood flow can be calculated using Fick's Principle[49]. The liver plasma flow (LPF) is defined as:

$$LPF = \Pi/[C_a(t)-C_v(t)]$$

where, Π is rate of removal of the dye from the circulation by the liver in mg/min, $C_a(t)$ and $C_v(t)$ are the dye concentrations in mg/ml of the blood entering and leaving the liver respectively, leading to LPF measured in ml/min. LPF can be converted into liver blood flow if the value for the haematocrit is known.

The first dye used was bromsulphalein[50] but indocyanine green is now used more commonly as it is more specifically extracted by the liver[51]. The first measurements made using this substance employed the constant infusion method but Caesar *et al.*[51] have shown that analysis of plasma disappearance curves after a bolus injection gives nearly identical results. Hepatic extraction is usually measured by hepatic vein sampling, however, a method requiring only peripheral vein sampling and

utilising pharmacokinetic modelling has been described and validated in normal subjects[52]. This method has, however, been criticised when applied to patients after liver transplantation[53] and it may be unreliable in patients with liver disease[54].

Pirttiaho *et al.*[55] estimated liver blood flow by fast intravenous injection of indocyanine green (0.5 mg/kg body weight). They found that the liver blood flow in 5 normal patients was 1258 ± 119 ml/min and that there was a close correlation ($r = 0.88$) with dynamic ^{99m}Tc-sulphur colloid imaging but not with values obtained using the ^{133}Xe clearance technique.

The advantage of dye clearance techniques is that they are relatively simple. Inaccuracies arise, however, when extrahepatic removal of the dye occurs[50] or when it is used in patients with liver disease[54]. These inaccuracies, combined with the development of other, more accurate methods, for measuring liver blood flow, have resulted in dye clearance methods being used less commonly. For many years, however, they were the best technique available and much pioneering work was done using them.

Radioisotopic methods

The concept of using radioactive tracers to help in the assessment of liver blood flow and perfusion is attractive. Three basic groups of techniques have been described.

A. Diffusible Gas Tracers

Kety[56] introduced the principle of "local tissue clearance" or "washout" of rapidly diffusing isotopes as a way of measuring blood flow. Initially small amount of radioactive ^{24}Na was used but later inert and lipid-soluble gases such as ^{85}Kr and ^{133}Xe[57] were found to be more valuable with the cellular membrane not constituting a barrier to diffusion[58].

Following injection of an arterial or portal venous bolus of gas dissolved in saline the elimination of these elements is in most situations only limited by the rate of capillary blood flow. Such an isotope will be eliminated in the form of a monoexponential function (giving a straight line when plotted on a logarithmic scale) if the tissue is uniformly perfused. Externally placed scintillation detectors are used to record the clearance curve. Fick's principle is then used in the analysis of the data and from a series of washout curves liver blood flow can be calculated.

B. Radio-labelled Colloids

In this technique colloid-bound radionuclides are administered intravenously and the rate constant of liver uptake is measured either by multiple blood sampling or external scintillation counting. The Fick principle is then applied to calculate blood flow, with the assumption that extraction efficiency is 100%.

Various colloids have been used with different radionuclides. The first work was with ^{32}P labelled chromic phosphate which is a pure β-particle emitter and cannot be detected by external counting[59,60]. It does, however, have a relatively high extraction efficiency at 95%. Colloidal ^{198}Au has been used for external counting[61,62] but has a lower extraction efficiency (80% or less). Now ^{99m}Tc-labelled sulphur colloid is most frequently used as it has a high extraction efficiency and can be counted externally. Dynamic images are acquired via a gamma camera and an on-line computer system and the assumption is made that the liver and spleen have an

equal extraction efficiency for colloidal particles[63] and that this is close to 100%. Unfortunately, although these assumptions are probably valid in normal subjects, they may not be true in patients with liver disease[64]. Analysis of the time variation in liver activity is performed following bolus intravenous injection. The arterial and portal components are separated by their times of arrival at the liver. Several different methods have been described to estimate fractional hepatic arterial flow using hepatic artery, portal vein, and reference organ time activity curves[63–67].

C. Hepatosplenic Radionuclide Angiography

This technique is based on the use of ^{99m}Tc-pertechnetate which is not extracted by the liver. A bolus injection is given intravenously and dynamic images are acquired during its first pass phase[68]. The original technique[69] has been modified[70] and is now reported to be more reproducible[68]. Sarper *et al.*[68] generated first-pass radioactivity versus time curves by following a rapid intravenous injection of 740 MBq of ^{99m}Tc-pertechnetate. For analysis, two time points were identified: the arrival time of activity in the liver, t_o, and the time of maximum activity of the abdominal organs, t_c. The former was estimated from the liver time-activity curve; the latter from the kidney time-activity curve and the accuracy of the method depends on there being normal perfusion of the kidneys which act as a reference organ. The gradients of the liver curve from $t_o + 7$ seconds and from t_c to $t_c + 7$ seconds, calculated by linear least-squares regression analysis, are G_o and G_c respectively. A hepatic perfusion index (HPI) is then defined as:

$$HPI = G_c/(G_o + G_c).$$

This method was applied to 7 normal volunteers and 57 patients with biopsy proven cirrhosis. The HPI was $66 \pm 7\%$ for the normals and ranged from 8–59 for patients with liver cirrhosis[68].

Advantages and limitations of radioisotope methods

The use of radio-labelled diffusible gas tracers has gained acceptance and popularity for measuring cerebral blood flow, where an inhalation technique can be used successfully. Unfortunately the technique is not as accurate for measuring liver blood flow and the washout curves are frequently not monoexponential[71], perhaps due to recirculation of the tracer, the fact that liver tissue may not be homogenously perfused or because there is incomplete clearance of tracer during its first passage[72]. In addition, the need to catheterise either the hepatic portal or arterial system is a major disadvantage and one of the reasons why the technique has failed to gain widespred popularity in hepatic studies.

Colloid bound tracers and radionuclide angiography can not provide absolute values for flow but they can provide valuable information about the relative contribution of the hepatic arterial and portal systems. Such an index may be of more interest than absolute flow values in certain disease states such as cirrhosis. However, the background scatter of tracer and the affinity to fat which many tracers have, makes the measurements difficult to evaluate. Colloids also have a range of particle sizes and hence a range of values of extraction efficiency.

METHODS MEASURING TISSUE PERFUSION

Radioactive Microspheres

If a bolus of tracer is well mixed in the afferent blood supplying an organ, then it will be distributed to different parts of the organ in exactly the same way as the blood which is transporting it. This is called the indicator fractionation principle. This principle has been used to quantify regional blood flow distribution using radio-labelled particles, diffusible indicators and autoradiography[73,74]. Microspheres are chosen to be of a size (10 – 15μm) which will just lodge in the capillary circulation. The injection can be given some time before local distribution of the trapped spheres is measured, a procedure usually carried out post-mortem by taking biopsies of the tissue being studied and measuring radioactivity in a well counter.

Using this technique Greenway *et al.*[75] studied the regional distribution of portal and hepatic blood flow in the liver by injecting ^{14}C amd ^{51}Cr-microspheres into the portal vein and hepatic artery of 12 cats and 15 dogs. They found the liver homogeneously perfused from both systems in contrast to other work using different techniques[76,77]. The technique has also been used to study the vascularity of experimental liver tumours and in particular the relative role of portal and arterial blood supply to these tumours[78-81].

The microsphere method is useful for providing values of blood flow in animal studies where sacrifice of the animal occurs. Impaction of microspheres must, however, affect local flow and with multiple injections before sacrifice this may become a significant source of artefact. To minimize this problem, injection quantities are made as small as possible, but this militates against accurate measurement of regional flow, especially in regions with low volume flow. Its major disadvantage is, however, that it cannot be used clinically.

Heat Exchange Methods

The concept of measuring tissue blood flow using heat clearance techniques was first suggested by Gibbs[82]. This method requires a heated thermocouple, maintained at a certain temperature (2–4°C) above that of the surrounding tissue, to be either placed onto the liver surface or inserted into the liver tissue. The temperature of the needle is dependent on local blood flow – increased perfusion tends to cool the needle, whereas reduced perfusion allows it to heat up. Measurement of the energy required to maintain the temperature increment constant therefore can be regarded as giving an indirect measurement of flow[82-85]. However, values will depend on the exact position of the probe and the metabolic state of the liver[86]. The method is, therefore, only a semiquantitative approach to flow and because of its invasiveness has not yet found widespread favour for liver studies.

Hydrogen Electrode

This method was introduced by Auckland and Bower[87] and further developed by Fieschi *et al.*[88,89] and by Bozzao *et al.*[90]. Molecular hydrogen is administered with the respiration gas until the tissue reaches saturation. The hydrogen supply is then turned off and its clearance rate is determined polarographically through platinum

electrodes placed on, or into, the liver. A current is generated at the electrode surface by oxidation of molecular hydrogen to hydrogen ions. This current declines as hydrogen is removed and the steepness of the clearance curve correlates directly with the magnitude of the total liver blood flow and reflects perfusion within a radius of approximately 5 mm of the electrode. The calculation of tissue blood flow from hydrogen clearance curves is based on the theory developed by Kety,[91] and the method has been reviewed and simplified by Young[92].

Gouma *et al.*[77], using a hydrogen electrode applied to the surface of porcine liver, found that calculated liver blood flow measurements using this method gave much lower values than those obtained using the indocyanine green clearance method and in addition flow fell by over 90% if the hepatic artery was ligated. They concluded from these experiments that the surface of the liver is mainly supplied from the arterial system. Nishiwaki *et al.*[93] used the hydrogen clearance method and transit-time ultrasonic blood flowmetry to investigate blood flow after liver transplantation in 40 mongrel dogs and found reductions in both hepatic arterial and portal venous flow after transplantation.

The advantages of this method are that it can provide unlimited measurements of liver blood flow without significant alteration in physiological variables. There is no evidence that the administration of the hydrogen itself significantly alters flow. Despite this, most investigators have not used the technique, mainly due to concern over the inflammability and explosiveness of pure hydrogen gas. In addition the method is not continuous, cannot handle rapit changes of flow and may reflect arterial rather than venous inflow[77]. It may also be inaccurate if the liver is not homogenously perfused.

Oxygen Electrode

An oxygen electrode consists of a noble metal cathode maintained at a negative potential with respect to a reference electrode. It is placed on the surface of the organ to be studied and oxygen diffusing from the tissue to the cathode surface is reduced when the potential is applied, giving rise to a current[94]. A naked electrode is subject to "poisoning" by electrophoretic deposition of tissue protein on its surface but this can be prevented by covering the electrode with a gas-permeable membrane[95]. When the oxygen consumption of the electrode is low, tissue oxygen is not disturbed and so a direct measurement of the partial pressure (pO_2) is obtained[96]. However, if the oxygen consumption of the electrode is high the electrode will measure the rate of supply of oxygen to the tissue and this is dependent on local blood flow[97,98].

Ji *et al.*[99] applied a microneedle electrode to rat liver and found that tissue pO_2 values were different at periportal and perihepatic sites. Kram and Shoemaker[100] applied a "miniature" oxygen electrode in a single illustrative case to human cirrhotic liver to measure tissue pO_2 and their instrument responded to both changes in local organ blood flow and arterial pO_2. In these two studies electrode readings were not related to portal venous flow. We compared readings from a membrane covered (Clark type) flow dependent oxygen electrode applied to the surface of rabbit liver, with those from an electromagnetic flowmeter on the portal vein. We found that under operative conditions, changes in oxygen electrode

readings correlated well with portal blood flow as measured by an electromagnetic flowmeter over a range of flow rates[101].

This technique can give a continuous and instantaneous measurement of portal venous inflow when hepatic arterial inflow is undisturbed. However, it is invasive as the electrode must be applied directly onto the liver surface. In addition it only gives a measure of flow in the tissue immediately below the electrode and no absolute value for flow can be calculated. Potentially, however, it can be used on human liver either at laparotomy or laparoscopy.

Laser Doppler

Laser Doppler is a relatively new technique (1972)[102] for measuring local blood flow. The device consists of a helium-neon laser and an optic fibre which transmits this light to the surface of the tissue to be studied. Light that is scattered by red blood cells undergoes a frequency shift and a portion of this spectrally-broadened light is transmitted back by a fibre light-guide to two photodetectors. This signal is analyzed and the relative portion of light which has undergone Doppler shift is proportional to velocity of blood flow. The microvascular bed consists of an intricate network of small blood vessels and hence the angle between the red cell velocity vectors and the beam propagation vectors of the scattered light can be regarded as random[103].

This technique gives a continuous measure of red cell motion in the outermost layer of the tissue under study with little or no influence on blood flow. The depth to which the beam penetrates varies with the tissue being studied[103,104,76] and flow is likely to be measured in a volume of approximately 0.6–1.3 mm^3 when the probe is applied to the liver surface.

Laser Doppler has been studied *in vitro* by measurement of liquid flow through small-bore tubes and a coefficient of variation for readings of 6%[105] confirmed its accuracy. *In vivo* it has been used extensively to measure skin blood flow[106] but less has been written on its use and limitations for estimating liver blood flow[76,107].

Arvidsson *et al.*[76], using Laser Doppler flowmetry in pigs, investigated liver blood flow and confirmed previous work[77] with hydrogen clearance methods that the liver surface is mainly supplied from the arterial system. Laser doppler has also been used to study blood flow to experimental liver metastases[108].

The advantages of the method are that it can provide an instantaneous and continuous measurement of microcirculatory flow in a way that does not alter flow. Its disadvantages are that the probe must be applied directly onto the liver, flow can not be measured in absolute units, the absolute volume of tissue measured is not known and only surface flow is assessed (needle probes have not been used in the liver as haematoma formation around the probe tip would make readings unreliable).

CONCLUSION

Currently the measurement of hepatic blood flow and perfusion is fraught with difficulties. There are often large variations in both flow and perfusion measurements, not only between techniques but also between different groups using the same technique. Some of these differences may be due to the methods and

conditions used and others are undoubtedly caused by complexities of the liver circulation which we do not yet understand.

Most importantly, we are still looking for a reliable method of non-invasively assessing liver blood flow in the clinical context. Duplex Doppler Ultrasound offers a good way of assessing portal vein flow but its many inaccuracies should be borne in mind. Clinical measurement of hepatic and splanchnic arterial flow is more difficult and duplex does not yet have the accuracy to perform this function reliably. Intraarterial Doppler flow probes, flow analysis of digital x-ray angiograms and NMR may have a role in the future. Radiolabelled colloids or hepatosplenic radionuclide angiography can provide valuable information about the relative contribution of the portal and arterial system but are still largely research tools and are less accurate in the presence of pathology. Currently, investigators are best advised to familiarise themselves with a range of techniques as it is apparent that no single method is able to fulfil all the requirements of either basic research or routine clinical practice.

APPENDIX A

DOPPLER'S LIMITATIONS AND SOURCES OF ERRORS

Although duplex instrumentation is now widely accepted as valid for most vascular applications, there are several disadvantages which have prevented total acceptance of the method[109]. These have been well documented and summarised by Burns[16] and Merritt[110]. Briefly, they are as follows:

(a) When used to measure laminar flow in a vessel and the beam width is less than the diameter of the vessel, only the central portion of the vessel lumen will be insonated[111] leading to an error in estimating velocity and hence flow.

(b) Errors can arise in estimating blood vessel diameter due to: (1) Imaging not being perpendicular to the longitudinal axis of the vessel. (2) Poor resolution of the imaging transducer. (3) Pulsatility of blood flow, causing variation in vessel diameter with time. (4) Observer variability[112]. (5) Only a short length of vessel being available for imaging such as occurs with the portal vein[13,25].

(c) Sampling problems: Nearly all current pulse mode Doppler machines are based on centre-line measurements of peak velocity and spectral broadening[113]. Abnormalities may be missed due to failure to sample nearer the wall where flow disturbances are most likely to occur[114,115].

(d) Errors due to beam angle: the magnitude of velocity is the function of the cosine of the intercept angle between beam direction and the blood vessel. The flow-volume rate calculation equation is a trigonometrical function of the angle between the beam direction and the blood flow. Errors vary considerably with that angle, being minimal in the angle range 55–76°[116].

Acknowledgements

We thank Dr. S. Padayachee, Division of Radiological Sciences, Guy's Hospital School of Medicine, London, for valuable discussion on application of Doppler ultrasound to measure liver blood flow and also we thank Dr. C. Piasecki for valuable discussions on application of oxygen electrode to measure liver blood flow. D.J.H. is grateful for the support of the Leverhulme Trust.

References

1. Richardson, P.D.I. and Withrington, P.G. (1981) Liver blood flow I.Intrinsic and nervous control of liver blood flow. *Gastroenterology*, **81**, 159–173
2. Richardson, P.D.I. and Withrington, P.G. (1981) Liver blood flow: II. Effects of drugs and hormones on liver blood flow. *Gastroenterology*, **81**, 356–375
3. Fabre, P. (1932) Utilisation des forces electromotrices d'enrigistrement des variations de vitesse des liquids conducteurs: un nouvel hemodromograph sans palette dans le sang. *C. R. Acad. Sci. Paris*, **194**, 1097–1098
4. Webster, J.G. (1978) Measurement of flow and volume of blood. In: Medical instrumentation: Application and Design. Ed. Webster J G. Boston: Houghton Mifflin, ch. 8
5. Harper, A.M., Lorimer, A.R. and Thomas, D.L. (1974) Methods of measuring blood flow. In: Scientific Foundation of Anaesthesia, Ed. Scurr C, Feldman, S. London: Heinemann, pp. 28–44
6. Khouri, E.M. and Gregg, D.E. (1963) Miniature electromagnetic flow meter applicable to coronary arteries. *J. Appl. Physiol.*, **18**, 224
7. Wyatt, D.G. (1984) Blood flow and blood velocity measurement in vivo by electromagnetic induction. *Med. Biol. Eng. Comput.*, **22**, 193–211
8. Meisner, H. and Messmer, K. (1970) Significance and limitations of electromagnetic blood flowmetry, Experimental and Clinical results. *Progr. Surg.*, **8**, 124–144
9. Drapanas, T., Kluge, D.N. and Schenk, W.G. (1960) Measurement of hepatic blood flow by bromsulphalein and by the electromagnetic flowmeter. *Surgery*, **48**, 1017–1021
10. Price, J.B., Britton, R.C., Peterson, L.M., Reilly, J.W. and Voorhees, A.R. (1965) The validity of chronic hepatic blood flow measurements obtained by the electromagnetic flow meter. *J. Surg. Res.*, **V(7)**, 313–317
11. Bradley, S.E., Inglefinger, F.J., Bradley, G.P. and Curry, J.J. (1945) The estimation of hepatic blood flow in man. *J. Clin.Invest.*, **24**, 890
12. Satomura, S. (1959) Study of the flow pattern in peripheral arteries by ultrasonics. *Nihon Onkyo-gakkai, Shi*, **15**, 151
13. Taylor, K.J.W. and Burns, P.N. (1985) Duplex Doppler scanning in the pelvis and abdomen. *Ultrasound Med. Biol*, **11**, 643–658
14. Okazaki, K., Miyazki, S. and Onishi, S. (1987) Noninvasive measurements of portal blood flow. *Gastroenterology*, **93**, 656–657
15. Baker, D.W. (1970) Pulsed ultrasonic Doppler blood-flow sensing. *IEEE Trans. Sonics Ultrasonic*, **17(3)**, 170
16. Burns, P.N. (1987) The physical principles of doppler and spectral analysis. *J. Clin. Ultrasound*, **15**, 567–590
17. Koslin, D.B. and Berland, L.L. (1987) Duplex Doppler examination of the liver and portal venous system. *J. Clin. Ultrasound*, **15**, 675–686
18. Ohnishe, K., Saito, M., Koen, H., Nakayama, T., Normura, F. and Okuda, K. (1985) Pulsed Doppler flow as a criterion of portal venous velocity : Comparison with cineangiographic measurements. *Radiology*, **154**, 495–498
19. Sovak, M., Soulen, R.L. and Reichle, F.A. (1971) Blood flow in the human portal vein. A cineradiographic method using particulate contrast medium. *Radiology*, **99**, 531–536
20. Ackroyd, N., Lane, R. and Dart, L., *et al.* (1984) Colour-coded carotid Doppler imaging: An angiographic comparison of 324 bifurcation. *Aust. NZ. J. Surg.*, **54**, 509–517
21. Okazaki, K., Miyazaki, M., Onishi, S. and Ito, K. (1986) Effect of food intake and various extrinsic hormones on portal blood flow in patients with liver cirrhosis demonstrated by pulsed doppler with the octoson. *Scand. J. Gastroenterol.*, **21**, 1029–1038
22. Moriyasu, F., Nishida, O. and Ban, N., *et al.* (1986) Congestion index off the portal vein. *AJR*, **146**, 735–739

23. Nelson, R.C., Lovett, K.E., Chezmar, J.L., Moyers, J.H., Torres, W.E., Murphy, F.B. and Bermardino, M.E. (1987) Comparison of pulse Doppler sonography and angiography in patients with portal hypertension. *AJR*, **149**, 77–81
24. Barbara, L., Bolondi, L. and Bosch, J., *et al.* (1990) The value of Doppler US in the study of hepatic hemodynamics. *J. Hepatol.*, **10**, 353–355
25. Miyatake, K., Okamoto, M., Kinoshita, N., Izumi, S., Owa, M., Takao, S., Sakakibara, H. and Nimura, Y. (1984) Clinical applications of a new type of real-time two-dimensional doppler flow imaging system. *Am. J. Cardiol.*, **54**, 857–868
26. Seifalian, A.M., Young, J.M. and Hobbs, K.E.F. (1988) Quantitative assessment of portal vein blood flow by duplex ultrasound scanning. *Clin. Radiol.*, **39**, 681
27. Dick, R. (1983) Portal and hepatic venous system. In: Techniques in diagnostic radiology. Eds, G.H.Whitehouse and B.S.Worthington. Blackwell Scientific Publications, 165–182
28. Hillal, S.K. (1966) The determination of the blood flow by a radiographic technique. *Am. J. Roentgenol.*, **96**, 896–906
29. Seifalian, A.M., Hawkes, D.J., Colchester, A.C.F. and Hobbs, K.E.F. (1989) A new algorithm for deriving pulsatile blood flow waveforms tested using simulated dynamic angiographic data. *Neuroradiology*, **31**, 263–269
30. Colchester, A.C.F. (1985) The effect of changing PaCo2 on cerebral artery calibre estimated by a new technique of dynamic quantitative digital angiography. Phd Thesis, University of London
31. Lantz, B.M.T., Link, D.P., Foerster, J.M. and Holcroft, J.W. (1980) Angiographic determination of splanchnic blood flow. *Acta Radiologica Diagnosis*, **21**, 3–10
32. Kedem, D., Kedem, D., Smith, D.W., Dean, R.H. and Brill, A.B. (1978) Veocity distribution and blood flow measurements using videodensitometric methods. *Invest. Radiol.*, **13(1)**, 46–56
33. Sovak, M., Soulen, R.L. and Reichle, F.A. (1971) Blood flow in the human portal vein. A cineradiographic method using particulate contrast medium.*Radiology*, **99**, 531–536
34. Iwanaga, T., Koyannagi, N. and Sugimachi, K. (1987) Validity of ultrasonic duplex system for measurement of the portal blood flow in patients with liver disease. *Japanese J. Surgery*, **17(1)**, 58–59
35. Reichle, F.A., Sovak, M., Soulen, R.L. and Rosemond, G.P. (1972) Portal vein blood flow determination in the unanesthetized human by umbilicoportal cannulation. *J. Surg. Res.*, **12**, 146–150
36. Du Boulay, G.H., Brunt, J., Colchester, A., Hawkes, D., Wallis, A. and Wicks, D. (1987) Volume flow measurement of pulsatile flow by digitised cine angiography. *Acta Radiologica*, **Suppl(13)**, 59–62
37. Bettman, M.A. and Morris, T.W. (1986) Recent advances in contrast agents. *RCNA*, **24(3)**, 347–357
38. Cope, C. (1986) Minipuncture angiography. *RCNA*, **24(3)**, 359–367
39. Carr, H.Y. and Purcell, E.M. (1950). *Phys. Rev.*, **94**, 630
40. Garroway, A.N. (1974) Velocity measurements in flowing fluids by NMR. *J.Phys. D: Appl. Phys.*, **7**, 159–163
41. Hahn, E.L. (1960) Detection of sea water motion by nuclear procession. *J. Geophys. Res.*, **65**, 776–777
42. Hawkes, R.C., Holland, G.N., Moore, W.S. and Worthington, B.S. (1980) Nuclear magnetic resonance (NMR) tomography of the brain: a preliminary clinical assessment with demonstration of pathology. *J.Comput. Assist. Tomogr.*, **4**, 577–586
43. Waluch, V. and Bradley, W.G. (1984) NMR even echo rephasing in slow laminar flow. *J. Comput. Assist. Tomogr.*, **4**, 594–598
44. Bradley, W.G. and Waluch, V. (1985) Blood flow: Magnetic resonance imaging. *Radiology*, **154**, 443–450
45. Ridgway, J.P., Turnbull, L.W. and Smith, M.A. (1987) Demonstration of pulsatile cerebrospinal-fluid flow using magnetic resonance phase imaging. *Bri. J. Radiology*, **60**, 423–427
46. Shimizu, K., Matsuda, T., Sakurai, T., Fujita, A., Ohara, H., Okamura, S., Hashimoto, S., Mano, H., Kawai, C. and Kiri, M. (1986) Visualization of moving fluid: Quantitative analysis of blood flow velocity using mr imaging. *Radiology*, **159**, 195–199
47. West, D.J., Tarnawski, M., Graves, M.J., Taylor, M.G., Padayachee, T.S., Ayton, V.T. and Smith, M.A. (1988) Blood flow imaging by magnetic resonance. *Medicamundi*, **33(3)**, 101–111
48. Bradley, S.E. and Curry, J.J. (1945) The estimation of hepatic blood flow in man. *J. Clin. Invest.*, **24**, 890–987
49. Fick, A. (1870) Uber die Messung des Blutquantums in den Herzventrikeln. *S. B. Phys-med. Ges. Wurzb.*, **21**, 171–180

50. Brauer, R.W., Pessotti, R.L. and Krebs, J.S. (1955) The distribution and excretion of 35S-labeled Sulfobromophthalein-sodium administered to dogs by continuous infusion. *J. Clin. Invest.*, **34**, 35–40
51. Caesar, J., Shaldon, S., Chiandussi, L. and Sherlock, S. (1961) The use of indocyanine green in the measurement of hepatic blood flow and as a test of hepatic function. *Clin. Sci.*, **21**, 43–57
52. Grainger, S.L., Keeling, P.W.N., Brown, I.M.H., Marigold, J.H. and Thompson, R.P.H. (1983) Clearance and non-invasive determination of the hepatic extraction of indocyanine green baboons and men. *Clin. Sci.*, **64**, 307–412
53. Clements, D., West, R. and Elias, E. (1986) Comparison of two methods of estimating liver blood flow in patients with liver disease using indocyanine green. *Gut*, **27**, A613-4
54. Combes, B. (1960) Estimation of hepatic blood flow in man and dogs by ^{131}I-labelled Rose Benfal:Simultaneous comparison with sulfabromophthalein sodium. *J. Lab. Clin. Med.*, **56**, 537–543
55. Pirttiaho, H., Pitkanen, U., Rajasalmi, M. and Ahonen, A. (1980) Comparison of three methods of measuring liver blood flow. *Acta Radiological Diagnosis*, **21**, 535-539.
56. Kety, S.S. (1949) Measurement of regional circulation by the local clearance of radioactive sodium. *Am. Heart. J.*, **38**, 321--328
57. Lassen, N.A. and Munck. (1955) Cerebral blood flow in man determined by the use of radioactive Krypton. *Acta. Physiol. Scand.*, **33**, 30–49
58. Lassen, N.A. (1964) Muscle blood flow in normal man and in patients with intermittent claudication evaluated by simultaneous ^{133}Xe and ^{24}Na clearances. *J. Clin. Invest.*, **43**, 1805–1812
59. Dobson, E.L. and Jones, H.B. (1952) The behaviour of intravenously injected particulate material. Its rate of disappearance from the blood stream as a measure of liver blood flow. *Acta. Med. Scand.*. **144**, 71–85
60. Dobson, E.L., Warner, G.F., Finney, C.R. and Johnston, M.E. (1953) The measurement of liver circulation by means of the colloid disappearance rate. I. Liver blood flow in normal young men. *Circulation*, **7**, 690–695
61. Riddell, A.G., Griffiths, D.B., McAlister, J.M. and Osborn, S.B. (1957) The measurement of liver blood flow with colloidal radiogold (^{198}Au). *Clin. Sci.*, **16**, 315–324
62. Fauvert, R., Benhamou, J., Nicollo, S. and Loverdo, A. (1958) La clearance de l'or colloidal radio-actif (198-Au). I. Valeurs normales et valeurs pathologiques. *Rev. Franc. Etud. Clin. Biol.*, **3**, 762–766
63. Fleming, J.S., Humphries, N.L.M., Karran, S.J., Goddard, B.A. and Ackery, D.M. (1981) In vivo assessment of hepatic-arterial and portal-venous components of liver perfusion:Concise communication. *J. Nucl. Med.*, **22(1)**, 18–21
64. Wright, E.P., Barber, R.W. and Ritson, A. (1982) Relative hepatic arterial and portal flow in liver scintigraphy. *Nucl. Med. Commun.*, **3**, 273–279
65. Fleming, J.S., Ackery, D.M., Walmsley, B.H. and Karran, S.J. (1983) Scintigraphic estimation of arterial and portal blood supplies to the liver. *J. Nucl. Med.*, **24**, 1108–1113
66. Parkin, A.C., Robinson, P.J., Baxter, P., Leveson, S.H., Wiggin, P.A. and Giles, G.R. (1983) Liver perfusion scintigraphy – Method, Normal range and laparotomy correlation in 100 patients. *Nucl. Med. Commun.*, **4**, 395–402
67. Britten, A.J., Fleming, J.S., Flowerdew, A.D.S., Hunt, T.M., Taylor, I., Karran, S.J. and Ackery, D.M. (1990) A comparison of three indices of relative hepatic perfusion derived from dynamic liver scintigraphy. *Clin.Phys. Physiol. Meas.*, **11**, 45–51
68. Sarper,R., Fajman, W.A., Rypins, E.B., Henderson, J.M., Tarcan, T.A., Galambos, J.T. and Warren, W.D. (1981) A noninvasive method for measuring portal venous/total hepatic blood flow by hepatosplenic radionuclide angiography. *Radiology*, **141**, 179–184
69. Biersack, H.J., Thelen, M. and Schulz, D. (1977) Die sequentielle hepatospleno szintigraphie zur quantitiven beurteilung der leberdurchblutung. *Fortschre, Roentgenstr*, **126**, 47–52
70. Rypins, E.B., Fajman, W. and Sarper, R. (1981) Radionuclide angiography of the liver and spleen. A non-invasive method of assessing portal venous/total hepatic blood flow ratio and portasystemic shunt patency. *Am. J. Surg.*, **142**, 574–579
71. Birtch, A.G., Casey, B.H. and Zakheim, R.M. (1967) Hepatic blood flow measured by the ^{85}Kr clearance technique. *Surgery*, **62**, 174–180
72. Mackenzie, R.J., Leiberman, D.P., Mathie, R.T. (1976) Liver blood flow measurement. The interpretation of ^{133}Xe clearance curves. *Acta Chir.Scand*, **142**, 519–525
73. Heymann, M.A., Payne, B.D., Hoffman, J.I.E. and Rudolph, A.M. (1977) Blood flow measurements with radionuclide labelled particles. *Prog. Cardivas. Dis.*, **20**, 55–79

74. Romeo, J.M., Lopez-Farre, A., Martin-Paredero, V. and Lopez-Novoa, J.M. (1990) Hepatic haemodynamic changes after portacaval anastomosis in normal, cirrhotic and chronic prehepatic portally hypertensive rats. *Br. J. Surg.*, **77**, 335–338
75. Greenway, C.V. and Oshiro, G. (1972) Intrahepatic distribution of portal and hepatic arterial blood flows in anaesthetized cats and dogs and the effects of portal occlusion, raised venous pressure and histamine. *J. Physiol.*, **227**, 473–485
76. Arvidsson, D., Svensson, H. and Haglung, U. (1988) Laser Doppler flowmetry for estimating liver blood flow. *Am. J. Physiol.*, **254**, G471–6
77. Gouma, D.J., Coelho, J.C., Schlegel, J., Fisher, J.D., Li, Y.G. and Moody, F.G. (1986) Estimation of hepatic blood flow by hydrogen gas clearance. *Surgery*, **99(4)**, 439–444
78. Ackerman, N.B., Lien, W.N., Kondi, E.S. and Silverman, N.A. (1969) The blood supply of experimental liver metastases. *Surgery*, **66**, 1067–1072
79. Archer, S.G., Gray, B.N. (1989) Vascularization of small liver metastases. *Br. J. Surg.*, **76**, 545–548
80. Nott, D.M., Grime, S.J., Yates, J., Day, D.W., Baxter, J.N., Jenkins and Cooke, T.G. (1989) Changes in the hepatic perfusion index during the development of experimental hepatic tumours. *Br. J. Surg.*, **76**, 259–263
81. Romeo, J.M., Lopez-Farre, A., Martin-Paradero, V. and Lopez-Novoa. (1990) Hepatic haemodynamic changes after portacaval anastomosis in normal, cirrhotic and chronic prehepatic portally hypertensive rats. *Br. J. Surg.*, **77**, 335–338
82. Gibbs, F.A. (1933) A thermoelectric blood flow recorder in form of a needle. *Proc. Soc. Exp. Biol. Med.*, **31**, 141–146
83. Grabner, G. and Neumayer (1958) A continuous recording method for the estimation of liver blood flow in man. In: Proceedings Harey Tercentenary Congress. Ed. J. McMichael. pp386–392
84. Grayson, J. and Kinnear, T. (1962) Observations on temperature, blood flow and heat production in the human liver in relation to environment and to glucose and insulin administration. *Clin. Sci.*, **22**, 125–140
85. Newman, W.H., Curley, M.G., Summit, S.C., Bowman, H.F., DelHomme, G. and Dittmar, A. (1990) Simultaneous, continuous measurements of tissue perfusion and oxygenation. *Annual International Conf.IEEE Eng. Med. Biol. Soci.*,**12(3)**, 1036–1037
86. Grayson, J. and Johnson, D.H. (1953) The effect of adrenalin and noradrealin of the liver blood flow. *J. Physiol.*, **120**, 73--94
87. Aukland, K., Bower, B.F. and Berliner, R.W. (1964) Measurement of local blood flow with hydrogen gas. *Circulation Research*, **XIV**, 164–187
88. Fieschi, C., Bozzao, L. and Agnoli, A. (1965) Regional clearance of hydrogen as a measure of cerebral blood flow. *Acta Neurol. Scand*, **14(Supl)**, 46–52
89. Fieschi, C., Bozzao, L., Agnoli, A., Nardini, M. and Bartolini, A. (1969) The hydrogen method of measuring local blood flow in subcortical structures of the brain: Including a comparative study with the 14-C antipyrine method. *Exp. Brain Res.*, **7**, 111–119
90. Bozzao, L., Agnoli, A., Bartolini, A. and Fieschi, C. (1969) Local cerebral blood flow measured by clearance curves of hydrogen gas. In: Research of the cerebral circulation. Eds, J.S. Meyer, H. Lechner and O. Eichorn. Third International Salzburg Conference, 86-96, Ch C. Thomas Springfield/111., USA
91. Kety, S.S. (1951) The theory and applications of the exchange of inert gas at the lungs and tissue. *Pharmacol. Rev.*, **3**, 1–41
92. Young, W. (1980) ^{2}H-clearance measurement of blood flow: A review of techniques and polarographic principles. *Stroke*, **11**, 552–564
93. Nishiwaki, H., Ohira, M., Boku, T., Ishikawa, T., Nakagawa, H., Yata, K. and Umeyama, K. (1989) The measurement of hepatic circulation before and after orthotopic liver transplantation in dog by using transit time blood flow meter and H-2 clearance method. *Nippon-Geka-Gekkai-Zasshi*, **90(2)**, 243–9
94. Baumberger, J.P. and Goodfriend, R.B. (1951) Determination of arterial oxygen tension in man by equilibration through intact skin. *Federation Proc.*, **10**, 10–11
95. Clark, L.C. (1956) Monitor and control of blood and tissue oxygen tension. *Tran. Am. Soc. Artif. Intern. Organ.*, **2**, 41–48
96. Hunt, T.K., Rabkin, J., Jensen, J.A., Jonsson, K., Smitten, K.V. and Goodson, W.H. (1987) Tissue oximetry: An interim report. *World J. Surg.*, **11**, 126–132
97. Piasecki, C. (1985) First experimental results with the oxygen electrode as a local blood flow sensor in canine colon. *Br. J. Surg.*, **72**, 452–453

98. Piasecki, C. (1981) A new method for the assessment of gut viability. *Br. J. Surg.*, **68**, 319–322
99. Ji, S., Lemasters, J.J., Christenson, V. and Thurman, R.G. (1983) Selective increase in pericentral oxygen gradient in perfused rat liver following ethanol treatment. *Pharmacology Biochemistry and Behaviour*, **19**, 439–442
100. Kram, H.B. and Shoemaker, W.C. (1984) Method for intraoperative assessment of organ perfusion and viability using a miniature oxygen sensor. *Am. J. Surg.*, **148**, 404–7
101. Piasecki, C. and Seifalian, A.M. (1990) Continuous intraoperative monitoring of hepatic blood perfusion using a noninvasive surface electrode. *Dig. Dis. Sci.*, **35(3)**, 399–405
102. Riva, C., Ross, B. and Benedek, G. (1972) Laser Doppler measurements of blood flow in capillary tubes and retinal arteries. *Invest. Opthalmol.*, **11**, 936–944
103. Nilson, G.E., Tenland, T. and Obser, P.A. (1980) Evaluating of a laser Doppler flowmeter for measurement of tissue blood flow. *IEEE Trans. Biomed. Eng*, **27**, 597–604
104. Bonner, R. and Nossal, R. (1981) Model for laser Doppler measurements of blood flow in tissue.*Applied Optics*, **20**, 2097--2107
105. Damber, J.E., Lindahl, O., Selstan, G. and Tenland, T. (1982) Testicular blood flow measured with a laser Doppler flowmeter: acute effects of catecholamines. *Acta Physiol.Scand*, **115(2)**, 209–15
106. Swain, I.D. and Grant, L.J. (1989) Methods of measuring skin blood flow. *Phys. Med. Biol.*, **34**, 151–175
107. Shepheard, A.P., Riedel, G.L. and Ward, W.F. (1983) Laser Doppler measurements of blood flow within the intestinal wall and on the surface of the liver. In: Microcirculation of the alimentary tract, Ed. by A.Koo, R.F.Lam, L.M.Swaje. Singapore: World Scientific, pp115–129
108. Bloom, N.D., Kroop, E., Sadjadi, M., Jacobs, R., Ramaswamy, G. and Akerman, N.B. (1987) Enhancement of tumour blood flow and tumoricidal effect of Doxorubicin by intraportal epinephrine in experimental liver metastases. *Arch. Surg.*, **122**, 1269–1272
109. Jaffe, C.C. (1984) Doppler applications and limits of the method. *Clin. Diag. Ultrasound*, **13**, 1–10
110. Merritt, C.R.B. (1987) Doppler color flow imaging. *J. Clin. Ultrasound*, **15**, 591–597
111. Evans, D.H. (1982) Some aspects of the relationship between instantaneous volumetric blood flow and continuous wave Doppler ultrasound recording - 1. *Ultrasound Med.Biol.*, **8**, 606–609
112. Zoli, M., Marchesini, G., Brunori, A., Cordiani, M.R. and Pisi, E. (1986) Portal venous flow in response to acute beta blocker and vasodilatatory treatment in patients with liver cirrhosis. *Hepatology*, **6**, 1248–1251
113. Langlois, Y.E., Greene, F.M., Roederer, G.O., Jager, K.A., Phillips, D.J., Beach, K.W. and Strandness, D.E. (1984) Computer based pattern recognition of carotid artery Doppler signals for disease classification: Prospective validation. *Ultrasound Med.Biol.*, **10**, 581–595
114. Switzer, D.F. and Nanda, N.C. (1985) Doppler color flow mapping. *Ultrasound Med.Biol.*, **11**, 403–416
115. Rittgers, S.E. and Fei, D. (1988) Flow dynamics in a stenosed carotid bifurcation model - part II: Derived indices. *Ultrasound Med. Biol.*, **14**, 33–44
116. Stacey-Clear, A., Fish, P.J. (1984) Repeatibility of blood flow measurement using multichannel pulsed Doppler ultrasound. *Bri. J. Radiol.*, **57**, 419–420

(Accepted by S. Bengmark 7 February 1991)

Electro-rheological fluids: an introduction for biomedical applications

W.A. Bullough

Department of Mechanical and Process Engineering, The University, PO Box 600, Sheffield S1 4DU, UK

ABSTRACT

The subject of electro-rheology is introduced to biological engineers in a concise manner to allow presentation of a procedure for effective quantitative evaluation of possible medical applications of this new technology. More detailed phenomena are included in the references. Characteristics of the current best available fluid are given in brief.

Keywords: Electro-rheology, biological engineering

INTRODUCTION

Not all machine power transmission requirements can be met by existing electromagnetic or mechanical means. This has led to the development of a new electron-hydraulic concept: a hydraulic semi-conductor that can be controlled with solid-state derived signals, yet be employed in conventional hydraulic devices. By doing this the position, speed, force and displacement transmitted by a moving or stationary element, whether it be a pressure driven piston or shear loaded friction plate, can be regulated rapidly by a computer. In turn, this allows the output of a transmission to be adjusted proportionally and operated flexibly, because the same system can be electronically governed to perform on a range of job sizes and different functions. Such a machine is capable of relatively high forces and speeds.

If hydraulic machines are not manually or electro-magnetically managed, they must be controlled via an electrostatic interface. This limits the specific force per unit control excitation and requires good dielectric properties and the use of high electric fields. The resulting circuit benefits from the absence of slow inductive influences and the associated tendency to disruptive current and voltage surges. The speed of response of the composite electron-mechanical system is thus enhanced. The absence of large amounts of heavy moving materials is also an advantage.

In order to perform hold and run duties the generalized characteristic of the system fluid needs to be both elastic and/or plastic, at the dictate of the electric field. Ideally it should have the Bingham plastic form of *Figure 1*. The shear mode clutch of *Figure 2* could then easily be manipulated by the conditioning of the electric field, e.g. by the resistance–capacitance (RC) control of electrode voltage with time. If a particular duty is better accommodated by the control of flow, then the passive controller of *Figure 3* may well apply.

These arrangements may find application in the robotic transmission of surgeons' instructions, exercise or therapeutic machines and exploratory devices. The latter constitute a class of controllable shape and stiffness structures which are the present subject of a great deal of attention in their own right[1–4].

ELECTRO-RHEOLOGICAL FLUIDS

One fluid type which has matched many of the above requirements is based on the Winslow effect[5]. These electro-rheological fluids (ERFs) are dense mixtures of micron-sized solids and liquids and approximate well to the ideal characteristic without leading to any excessive electrical or mechanical time constant. Currently the yield stress available approaches that of a conventional magnetic shear or tangential transmission stress. They are resistive enough to limit steady current demand and charging currents are manageable.

When activated between electrodes, the particles seem to polarize and come together in a chain-like mesh (see *Figure 4*)[6]. The precise mechanisms involved are not fully understood but the indications are that they seem to be overwhelmingly capacitive, in an external sense. The primary effects are very fast and occur in approximately 1–2 ms. The overall result seems to be that a field–induced matrix resists the flow thus forcing up the apparent shear stress on the electrodes.

The phenomena can be highly repeatable. However, a type of pseudo hysteresis has been observed at zero flow (the voltage can be reduced over a period of time to give the same effect as the higher voltage needed to arrest the flow) and a time dependence on exposure to shear work and electric field can lead to the impression that they are not repeatable[7]. Because of potentially lucrative patent and intellectual property rights, work in the field is often unpublished and until recently it has proved difficult even to purchase fluids, at any price.

In one sense the technological state of the problem can be thought of as an advanced state of time

0141–5425/91/030234–05

5. Taylor KJW, Holland S. Doppler US: Part 1. Basic principles, instrumentation, and pitfalls. *Radiology* 1990; **174:** 297–307.
6. Scoutt LM, Zawin ML, Taylor KJW. Doppler US: Part II. Clinical applications. *Radiology* 1990; **174:** 309–19.
7. Ridgway JP, Smith MA. A technique for velocity imaging using MR imaging. *Br J Radiol* 1986; **57:** 1145–8.
8. Shimizu K, Matsuda T, Sakurai T. *et al.* Visualization of moving fluid: Quantitative analysis of blood flow velocity using MR imaging. *Radiology* 1986; **159:** 195–9.
9. Ridgway JP, Turnbull LW, Smith MA. Demonstration of pulsatile cerebrospinal-fluid flow using magnetic resonance phase imaging. *Br J Radiol* 1987; **60:** 423–7.
10. West DJ, Tarnawski M, Graves MJ *et al.* Blood flow imaging by magnetic resonance. *Medicamundi* 1988; **33:** 101–11.
11. Pond GD, Osborne RW, Capp MP *et al.* Digital subtraction angiography of peripheral vascular bypass procedures. *AJR* 1982; **138:** 279–81.
12. Guthaner DF, Wexler L, Enzmann DR *et al.* Evaluation of vascular disease using digital subtraction angiography. *Radiology* 1983; **147:** 393–8.
13. Brown BG, Bolson EL, Dodge HT. Quantitative computer techniques for analysing coronary arteriograms. *Prog Cardiovasc Dis* 1986; **6:** 403–18.
14. Reiber JHC, Serruys PW. *State of the Art in Quantitative Coronary Angiography.* The Hague: Martinus Nijhoff, 1986.
15. Mancini GBJ (ed.). *Clinical Cardiac Applications of Digital Angiography.* New York: Raven Press, 1987.
16. Nordenstrom B, Grim S. A method for determination of blood flow with use of roentgen contrast medium. *Radiology* 1985; **84:** 644–55.
17. Rutishauser W, Simon H, Stucky JP, Schad N, Noseda G, Wellauer J. Evaluation of roentgen cinedensitometry for flow measurement in models and in the intact circulation. *Circulation* 1967; **36:** 951–8.
18. Silverman NR, Rosen L. Arterial blood flow measurement: Assessment of velocity estimate methods. *Invest Radiol* 1977; **12:** 319–24.
19. Heintzen PH. Review of research into and some aspects of the modern development of densitometry, particularly roentgen-video-computer techniques. *Ann Radiol (Paris)* 1978; **21:** 343–8.
20. Kedem D, Kedem D, Smith CW, Dean RH, Brill AB. Velocity distribution and blood flow measurements using videodensitometric methods. *Invest Radiol* 1978; **13:** 46–56.
21. Bürsch J, Hahne HJ, Brennecke R, Grönemeier D, Heintzen PH. Assessment of arterial blood flow measurements by digital angiography. *Radiology* 1981; **141:** 39–47.
22. Forbes G. Quantitative blood flow analysis with digital technique. In: Harrison RM, Isherwood I, eds, *Digital Radiology — Physical and Clinical Aspects.* IPSM, 1984; pp. 137–45.
23. Colchester ACF. The effect of changing $PaCO_2$ on cerebral artery calibre estimated by a new technique of dynamic quantitative digital angiography. *PhD Thesis,* University of London, 1985; pp. 136–42.
24. Hawkes DJ, Colchester ACF, Brunt JNH, Wicks DAG, du Boulay GH, Wallis A. In: Viergever MA, Todd-Pokropek A. *Development of a Model to Predict the Potential Accuracy of Vessel Blood Flow Measurements from Dynamic Angiographic Recordings.* Berlin: Springer-Verlag, 1988; pp. 469–78.
25. du Boulay GH, Brunt J, Colchester A, Hawkes D, Wallis A, Wicks D. Volume flow measurement of pulsatile flow by digitised cine angiography. *Acta Radiol* 1987; **13** (Suppl): 59–62.
26. Colchester ACF, Hawkes DJ, Brunt JNH, du Boulay GH, Wallis A. Pulsatile blood flow measurements with the aid of 3-D reconstruction from dynamic angiographic records. In: Bacharach SL, ed., *Information Processing in Medical Imaging* Dordrecht: Martinus Nijhoff 1986; 247–65.
27. Seifalian AM, Hawkes DJ, Colchester ACF, Hobbs KEF. A new algorithm for deriving pulsatile blood flow waveforms tested using simulated dynamic angiographic data. *Neuroradiology* 1989; **31:** 263–9.
28. Hawkes DJ, Colchester ACF, de Belder MA, Norbury RN, Camm AJ, Davies MJ. The measurement of absolute lumen cross sectional area and lumen geometry in quantitiative angiography. In: Todd-Pokropek A, ed., *The Formation, Handling and Evaluation of Medical Images, Proc NATO ASI* (Portugal), September 1988.
29. Dotter CT, Judkins MP. Transluminal treatment of arteriosclerotic obstruction. *Circulation* 1964; **30:** 654–70.
30. Gruentzig AR. Transluminal dilatation of coronary artery stenosis. *Lancet* 1978; *i:* 263.
31. Gruentzig AR, Turina MI, Schneider JA. Experimental percutaneous dilatation of coronary artery stenosis. *Circulation* 1976; **54:** 81.
32. Gruentzig AR, Myler RK, Hanna EH *et al.* Coronary transluminal angioplasty. *Circulation* 1977; **56:** (Suppl. III): 84 (Abstract).
33. Arfvidsson B, Davidsen JP, Persson B, Spangen L. Percutaneous transluminal angioplasty (PTA) for lower extremity arterial insufficiency. *Acta Chir Scand* 1983; **149:** 43–7.
34. Bergqvist D, Takolander R, Jonsson K, Karsson S, Hellekant C. Percutaneous transluminal angioplasty of arteriosclerotic lesions in the pelvis and lower extremities. *Acta Chir Scand* 1984; **150:** 445–9.
35. Rösch J, Anderson JM, Antonovic R, Robinson M. Transluminal iliac artery dilatation. Nonsurgical catheter treatment of atheromatous narrowing. *JAMA* 1974; **230:** 117–24.
36. Van Andel GJ. Transluminal iliac angioplasty, long-term results. *Radiology* 1980; **135:** 607–11.
37. Okadome K, Eguchi H, Yukizane T, Mii S, Muto Y, Sugimachi K. Doppler flow waveform analysis aids in early detection of late graft failure in cases of lower extremity arterial reconstruction: Case studies. *Vasc Surg* 1989; **23:** 519–27.
38. Johnston KW. Peripheral arterial Doppler blood flow–velocity waveform analysis. In: Kempczinski RF, Yao JST, eds, *Practical Noninvasive Vascular Diagnosis* 2nd edn. Chicago: Year Book Medical Publishers, 1987; pp. 154–77.
39. Skimore R, Woodcock JP. Physiological significance of arterial models derived using transcutaneous ultrasound flowmeters. *J Physiol* 1978; **277:** 29–30.
40. Johston KW, Maruzzo BC, Cobbold RSC. Doppler methods for quantitative measurement and localization of peripheral arterial occlusive disease by analysis of the blood flow velocity waveform. *Ultrasound Med Biol* 1978; **4:** 209.
41. Humpheries KN, Hames TK, Smith SWJ *et al.* Quantitative assessment of the common femoral to popliteal arterial segment using continuous wave Doppler ultrasound. *Ultrasound Med Biol* 1980; **6:** 99–105.
42. Mackay SA, Potel MJ, Rubin JM. Graphics methods for tracking three-dimensional heart wall motion. *Comput Biomed Res* 1982; **15:** 455–73.
43. Hawkes DJ, Colchester ACF, Mol C. The accurate 3-D reconstruction of the geometric configuration of vascular trees from X-ray recordings. In: Guzzardi R, ed., *Physics and Engineering of Medical Imaging.* The Hague: Martinus Nijhoff, 1985.
44. Smith WM, Starmer CF. Computer representation of coronary arterial trees. *Comput Biomed Res* 1976; **9:** 187–201.
45. Wicks DA, Brunt JN, Colchester ACF, du Boulay GH, Hawkes DJ, Wallis A. A quantitative cine-angiographic technique to estimate blood flow in identified vessels. *Biological Engineering Society 26th Ann Conf* 1986: Abstract p. 60.

- The estimated error reading the EMF values on the paper chart from the chart recorder; we estimated this to be approximately ±6% at peak deflection.
- A consistent underestimate by the EMF (*Figure 5*). This estimated error was 13% at high flow rates, reducing to 9% at low flow rates.

This still leaves a consistent overestimate at lower flow rates. One possible explanation is that the contrast material was injected into the centre of the tube lumen. At low flow rates there is little turbulence and near ideal laminar flow. Hence samples of fluid velocity in the centre of the tube will be higher than at the sides. This problem could be alleviated by ensuring adequate mixing of the contrast material at the injection site via a multi-side holed catheter.

In clinical practice angiography is very commonly carried out in occlusive disease in many parts of the vascular system. Often it can be difficult to determine whether a stenosis is haemodynamically significant, especially when the diameter (often on a single view) is in the region of 50% of the 'normal' arterial lumen. Furthermore, PTA is now frequently the choice of treatment for stenotic disease when again angiography is used to assess whether an improvement has been effected. It is of course well accepted that the post-PTA angiographic appearance may underscore the haemodynamic improvement resulting, and in some situations the pre- and post-PTA pressure gradient has been used as a guide to determine a satisfactory 'end result'. In clinical studies, flow waveforms of the left common femoral, left superficial femoral and left profunda femoris arteries were estimated for pre-PTA (*Figure 8*) and post-PTA (*Figure 9*). *Figure 8* shows that there was flow through the left common femoral artery and very high blood flow velocity through the left profunda femoris artery, which presumably compensated for the left superficial femoral artery occlusion. The common femoral artery waveform shows a small kink, which could correspond to the reflected pressure wave from the occluded superficial femoral artery (arrow).

Immediately after the completion of superficial femoral artery transluminal angioplasty, our angiographic flow measurements showed that flow through the occluded vessel had been re-established together with a normal biphasic blood velocity waveform for the common femoral artery[37] (*Figure 9*).

This technique is no more invasive or inconvenient than the standard DSA procedure. The high framing rate used in this study can easily be reformatted to give the framing rate of 2 frames s^{-1} used in routine angiography and delivers no extra total radiation dose to the patient.

Doppler ultrasound[38–41] is already well established in this application and we do not claim any specific advantage over it except in so far as the angiographic technique as described involves no extra intervention with the patient. We emphasize that the main purpose of this clinical study was to test the feasibility of the angiographic analysis on a clinical angiographic procedure.

The blood velocity estimate may be converted to volume flow by multiplying by the vessel cross-sectional area. This can be computed conventionally from the X-ray data and we have implemented a system to do this which is described elsewhere[28].

The technique will be sensitive to densitometric calibration errors. In our laboratory we have devised a technique for densitometric calibration using a pair of scanning slits. The technique is designed to remove the effects of X-ray scatter, beam hardening, veiling glare and vignetting (Davies and Hawkes, unpublished observations).

To deduce true velocity along a tortuous vessel or a vessel that is not oriented parallel to the imaging plane we need to deduce the three-dimensional (3-D) path of the blood vessel relative to the imaging equipment. We have completed implementation of a 3-D vascular tree reconstruction technique on a Sun 4/260 Graphics workstation. Our implementation of the 3-D calibration method[42,43] allows satisfactory reconstruction of the 3-D course of the vessel centre line '*in vivo*' and is being validated in phantom studies. The 3-D location of the blood vessel centre line will permit the computation of radiographic magnification, the angle between the X-ray beam and the vessel long axis, and the true vessel path length.

Patient movement, both voluntary and involuntary, may lead to significant error, especially when subtraction of a mask is used prior to analysis. Therefore, we are carefully concentrating our efforts on parts of the body that are less prone to patient movement and a study of flow in the vessels of the head and neck is under way. Derivation of flow estimates in carotid and intra-cranial vessels would be a very useful application of this technique. Significant work is still required to track the moving artery in 3-D. Promising techniques have, however, been implemented. Smith and Starmer[44] and ourselves are investigating incorporating these techniques into our program in order to assess the feasibility of measuring coronary artery flow.

ACKNOWLEDGEMENTS

We acknowledge fruitful collaboration with Dr J.N.H. Brunt of the Department of Medical Biophysics at Manchester University and Dr D.A. Wicks and Professor G.H. du Boulay of the Institute of Neurology, Queen Square, London (who are investigating the use of gradient operators[45] to derive blood flow from the parametric image). We are grateful to radiography staff at Guy's Hospital for their assistance in collecting technical data, to the Leverhulme Trust, Siemens plc and Guy's Hospital Special Trustees who have all contributed to this work.

REFERENCES

1. Gill RW. Measurement of blood flow by ultrasound: Acuracy and sources of error. *Ultrasound Med Biol* 1985; **11:** 625–41.
2. Kontis SK. Application of micro-processors in Doppler ultrasound. *PhD Thesis*, University of London, 1985.
3. Burns PN. The physical principles of Doppler and spectral analysis. *J Clin Ultrasound* 1987; **15:** 567–90.
4. Grigg MJ, Nicolaides AN, Wolfe JHN. Detection and grading of femorodistal vein graft stenoses: Duplex velocity measurements compared with angiography. *J Vasc Surg* 1988; **8:** 661–6.

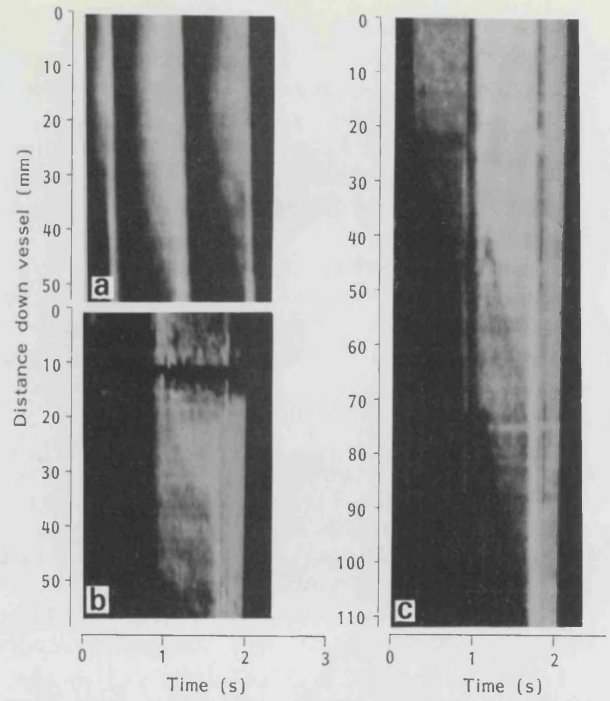

Figure 6 Parametric image showing contrast medium concentration (grey scale) at different positions down the blood vessel (the vertical axis) and at different times (the horizontal axis) pre-angioplasty for **a**, the left common femoral; **b**, the left superficial femoral; and **c**, the left profunda femoris arteries

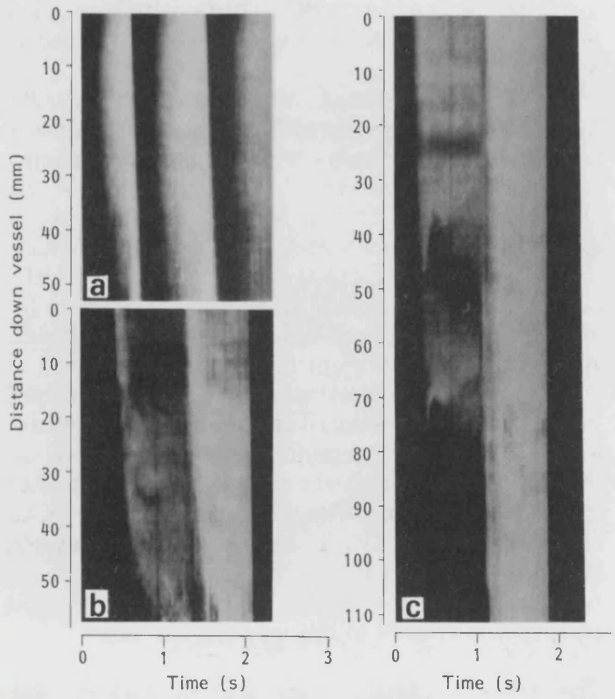

Figure 7 As in *Figure 6* but for post-angioplasty

in fair agreement with the blood flow waveform measured by an independent method, the EMF, for mean velocities of 147, 303 and 733 mm s^{-1} and peak flow velocities of 540, 964 and 1899 mm s^{-1}, respectively. The shape of the blood flow waveform is faithfully reproduced but there is an overestimation of peak flow of 40% at low flow rates (peak velocity of 540 mm s^{-1}), reducing to 19% at peak velocities of 964 mm s^{-1}, with an underestimation of 16% at the

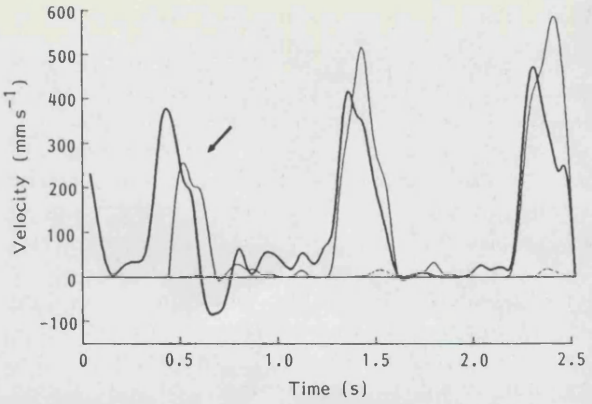

Figure 8 Plots of the flow velocity waveforms derived from the parametric images shown in *Figure 6*. The waveforms were extracted from the parametric images constructed for the left common femoral artery (———), the left superficial femoral artery (·····) and the profund femoris artery (———)

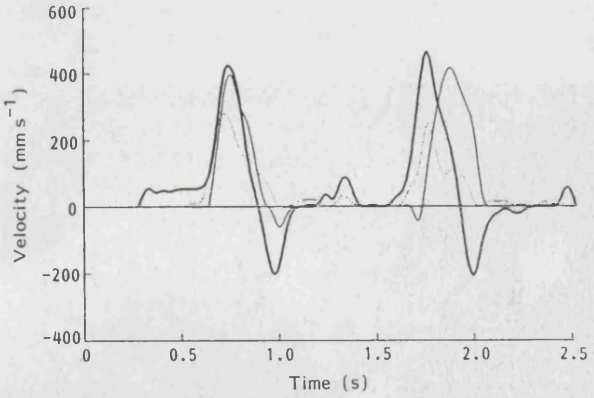

Figure 9 Plots of the flow velocity waveforms post angioplasty. The waveforms were extracted from the parametric images shown in *Figure 7* for the left common femoral artery (———), superficial femoral artery (· · · · ·) and profunda femoris artery (———)

peak flows rate of 1899 mm s^{-1}. *Table 2* shows that the injection site has little effect on the accuracy of the technique over the range of 130 to 230 mm between the injection and measurement site. Calculation of the mean difference and standard deviation of the difference confirm that the technique was independent of catheter position over this range.

The mean flow estimates showed a systematic fall as the length of tube analysed was reduced. For smaller tube length the tracking algorithm was more likely to fail. In the current implementation, if the tracking algorithm fails to find an adequate match, it will return zero flow, hence underestimating true flow.

Although the X-ray angiographic method for pulsatile flow measurements extracted reasonable velocity waveforms for a wide range of flow velocities, the results demonstrated its limitations. First, the technique became inaccurate at very high velocities. If peak fluid flow along the vessel is greater than about half the length of the vessel segment analysed per frame interval, then the tracking algorithm will fail. Second, we found a consistent overestimate of peak flow velocities at low flow rates. This overestimate reduced as the flow increased, becoming an underestimate until finally the tracking algorithm failed at very high velocities.

Some of the discrepancy could be explained by:

RESULTS

In the phantom study, the mean flow velocities measured by the EMF were 147, 303 and 733 mm s^{-1}, and the peak flow velocities were 540, 964 and 1899 mm s^{-1}. *Figure 3* shows the waveforms acquired simultaneously using the EMF and radiographic method for the three flow rates. A comparison of radiographic and EMF estimates of mean, peak and back flow velocities are shown in *Table 1*. *Table 2* shows the effect of the distance between the injection site and imaging site on the flow velocity estimates. Data were analysed for a 100 mm length of tube, beginning at a distance of between 130 and 230 mm from the injection site. *Table 3* shows the effect that reducing the length of the tube analysed had on the fluid velocity estimation. The length of vessel analysed ranged from 200 to 20 mm. All data were derived from the parametric images constructed for the experiments with mean flow velocities of 147 and 303 mm s^{-1} through the tube.

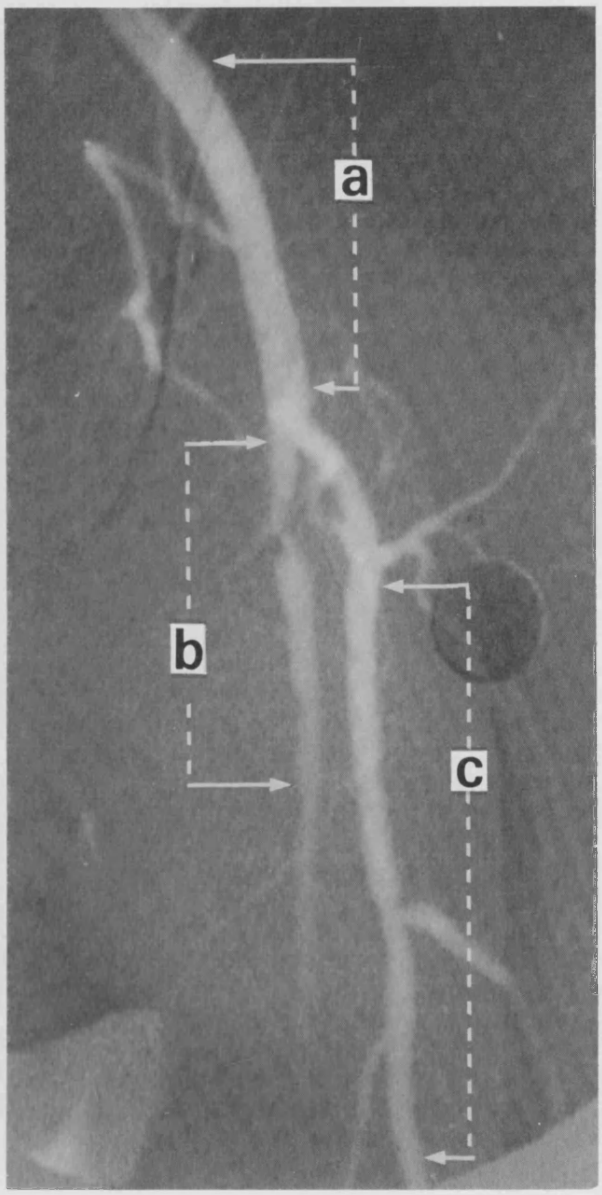

Figure 4 X-ray angiogram showing the left femoral arteries. The arrows indicate the positions of the selected arterial segments for generation of the parametric images. a = left common femoral; b = left superficial femoral; and c = left profunda femoris arteries

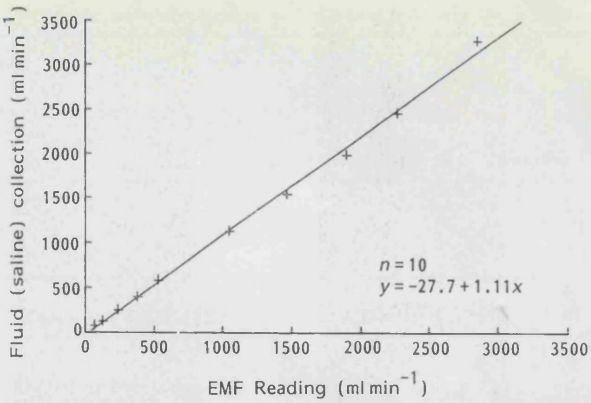

Figure 5 Relationship between flow determined by timed fluid collection and mean flow determined from the electromagnetic flowmeter

Results of the calibration of the EMF by comparison of the actual flow rates using fluid collection and the EMF readings are shown in *Figure 5*. Flow rates computed from fluid collection ranged from 75 to 3270 ml min^{-1}, with corresponding EMF readings ranging from 68 to 2850 ml min^{-1}. The best-line fit for the data is described by the equation:

$$Y = -27.7 + 1.11X$$

where Y is the fluid collection in ml min^{-1} and X is the EMF reading in ml min^{-1}. The standard deviation of the slope was 0.021 and of the intercept to the Y axis was 30.21.

In the clinical study, the blood flow velocity measurements showed a change of flow waveforms after PTA of the stenosis in the superficial femoral artery. Changes between pre- and post-PTA are apparent in the parametric images (*Figures 6* and *7*, respectively), derived from (*a*) approximately 53 mm of the left common femoral artery, (*b*) approximately 57 mm of the left superficial femoral artery and (*c*) approximately 112 mm of the left profunda femoris artery (*Figure 4*).

Figures 8 and *9* show plots of the flow velocity waveforms *versus* time. The waveforms were extracted from the parametric images shown in *Figures 6* and *7*. The plot in *Figure 8* demonstrates that there was negligible flow through the superficial femoral artery pre-PTA due to almost complete stenosis.

DISCUSSION AND CONCLUSIONS

The purpose of this study was to evaluate the accuracy of an X-ray angiographic technique for the measurement of instantaneous pulsatile blood flow velocity. The technique is based on the matching of concentration distance profiles along a vessel. We used a flow phantom constructed to simulate normal arterial flow in order to generate angiographic data. The experiments covered a wide range of flow rates, similar to physiological values found in the human circulation.

Figure 3 and *Table 1* demonstrate that results obtained using our X-ray angiographic technique for the matching of contrast concentration profiles are

Table 1 Summary of results of flow estimates in phantom

Experiment	Mean velocity ($mm\,s^{-1}$) EMF	Mean velocity ($mm\,s^{-1}$) Angiographic measurement	Peak velocity ($mm\,s^{-1}$) EMF	Peak velocity ($mm\,s^{-1}$) Angiographic measurement	Peak back flow velocity ($mm\,s^{-1}$) EMF	Peak back flow velocity ($mm\,s^{-1}$) Angiographic measurement	Mean difference between flow estimates (EMF-angiographic) ±standard deviation of difference ($mm\,s^{-1}$)
I	147.2	219.7	540.5	757.0	−233.7	−237.2	−72.4 ± 96.2
II	303.3	364.9	964.1	1152.4	−306.8	−338.9	−61.7 ± 160.4
III	733.0	371.5	1899.0	1581.7	−438.0	0.0	361.4 ± 634.0

Table 2 Effect of the distance between injection site and measurement site on angiographic flow estimates using the experimental phantom

Measurements	EMF	Injection distance to blood flow sampling site (mm)					
		130	150	170	190	210	230
Mean velocity flow rate of 147.2 $mm\,s^{-1}$							
Mean velocity ($mm\,s^{-1}$)	147.2	199.7	201.6	200.7	190.5	185.8	184.5
Mean difference (EMF-angiographic) ±standard deviation of difference ($mm\,s^{-1}$)		−52.5 ±106.3	−54.4 ±107.7	−53.6 ±104.9	−43.4 ±114.7	−38.6 ±127.8	−37.3 ±138.9
Peak velocity ($mm\,s^{-1}$)	540.5	756.9	756.9	756.9	756.9	711.8	711.8
Peak back flow ($mm\,s^{-1}$)	−233.7	−266.0	−237.2	−237.2	−237.2	−237.2	−237.2
Mean velocity flow rate of 303.3 $mm\,s^{-1}$							
Mean velocity ($mm\,s^{-1}$)	303.3	297.0	236.0	177.3	174.8	161.8	202.7
Mean difference (EMF-angiographic) ±standard deviation of difference ($mm\,s^{-1}$)		8.1 ±190.0	69.1 ±211.6	127.8 ±223.1	130.3 ±232.4	143.3 ±249.4	102.4 ±256.8
Peak velocity ($mm\,s^{-1}$)	964.1	1163.7	903.9	903.9	768.3	768.3	836.1
Peak back flow ($mm\,s^{-1}$)	−306.8	−226.0	−316.4	−361.5	−339.0	−339.0	−339.0

Table 3 Effect of reducing sampled length on angiographic flow estimates

Measurements	EMF	Length of vessel analysed (mm)					
		200	150	100	50	40	20
Mean velocity flow rate of 147.2 $mm\,s^{-1}$							
Mean velocity ($mm\,s^{-1}$)	147.2	219.7	204.3	185.5	132.8	141.5	98.1
Mean difference (EMF-angiographic) ±standard deviation of difference ($mm\,s^{-1}$)		−72.5 ±96.2	−57.2 ±112.7	−38.4 ±140.1	−14.3 ±196.9	−5.6 ±202.3	−49.0 ±218.3
Peak velocity ($mm\,s^{-1}$)	540.5	757.0	757.0	700.5	700.5	700.5	700.5
Peak back flow ($mm\,s^{-1}$)	−233.7	−237.3	−237.3	−237.3	−237.3	−203.3	−203.3
Mean velocity flow rate of 303.3 $mm\,s^{-1}$							
Mean velocity ($mm\,s^{-1}$)	303.3	365.0	298.1	233.8	201.8	195.7	134.3
Mean difference (EMF-angiographic) ±standard deviation of difference ($mm\,s^{-1}$)		−61.7 ±160.8	5.2 ±225.5	69.5 ±267.6	101.5 ±306.0	107.6 ±308.6	169.0 ±337.7
Peak velocity ($mm\,s^{-1}$)	964.1	1152.4	1039.42	915.1	881.3	881.3	881.3
Peak back flow ($mm\,s^{-1}$)	−292.1	−338.9	−338.9	−338.9	−338.9	−338.9	−338.9

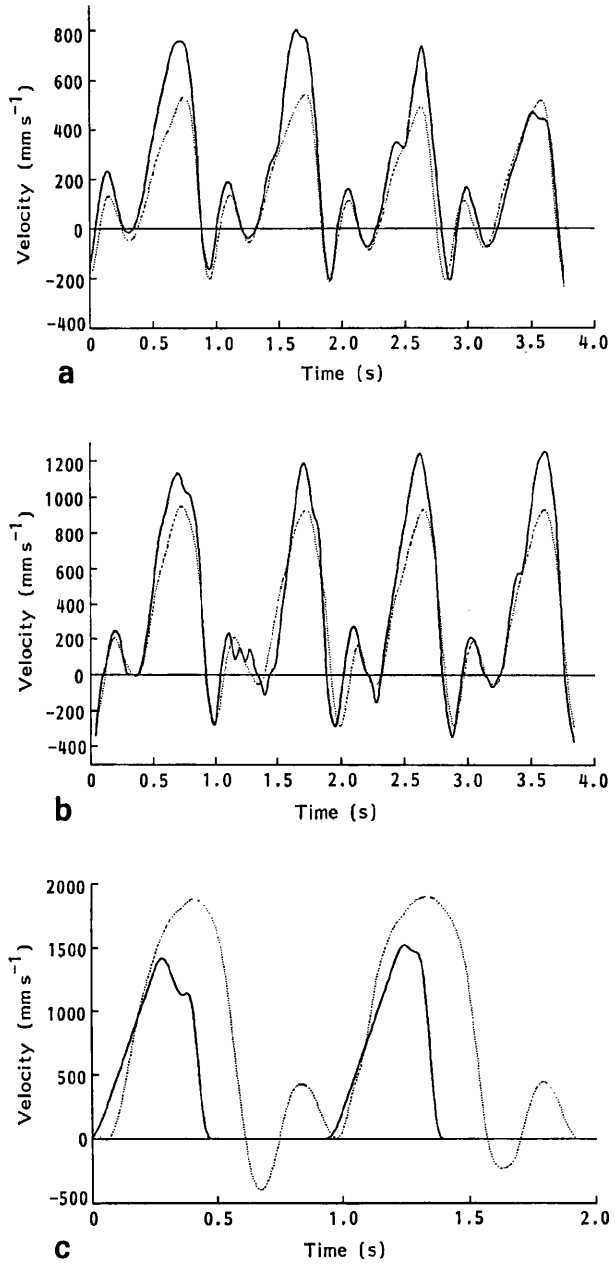

Figure 3 Direct comparison of flow velocity waveforms measured simultaneously with the new X-ray radiographic method (———) and the standard electromagnetic method (· · · · ·) for a mean flow velocity of **a**, 147.2 mm s^{-1}; **b**, 303.3 mm s^{-1}; and **c**, 733.0 mm s^{-1}

connector, was used to inject contrast material. Data were collected for three flow rates with corresponding mean flow rates of 147, 303 and 733 mm^{-1}, and peak flow rates of 540, 964 and 1899 mm s^{-1}, respectively. Instantaneous velocity flow was calculated at 0.04 s intervals, corresponding to the X-ray framing rate, and compared with the output of the EMF flowmeter. The flowmeter zero value and full-scale deflection were checked before each experiment in order to compensate for DC drift. The probe was calibrated for zero flow by clamping the flexible plastic tube both up- and down-stream of the meter.

Data from two runs (mean flow rates of 147 and 303 mm s^{-1}) were used to assess the effect of the distance between the catheter tip and the measurement site on the accuracy of the measurement. Data corresponding to a 100 mm section of the tube were analysed for distances ranging from 130 to 230 mm between the catheter tip and the start of the analysis site. The same data sets were used to investigate the effect on the accuracy of the velocity measurement of reducing the vessel length analysed from 200 to 20 mm.

For phantom studies, Urografin 370 (370 mg of iodine/ml) was injected into the phantom via the 8 French catheter with a power injector (Simtrac C; Siemens). The injector delivered contrast material at a rate of 3 ml s^{-1} (total volume 9 ml for each injection) during the image acquisition. The point of injection was 130 mm upstream from the images section of tubing.

We validated the EMF reading against the fluid collection by using normal saline (0.9% sodium chloride). With the available equipment it was not possible to calibrate the instantaneous flow response of the EMF for pulsatile flow, although its mean flow response was calibrated at several steady flow rates up to 3270 ml min^{-1}, both before and after the radiographic experiments.

Clinical study

To assess the clinical applicability of the technique we attempted to measure blood velocity in the femoral artery of one patient before and after PTA. PTA for the treatment of obliterating atherosclerosis was first described by Dotter and Judkins in 1964[29]. In the late 1970s, the technique was refined by the introduction of an inflatable polyvinyl double-lumen balloon catheter by Gruentzig[30–32]. One of the main indications for this procedure has been localized stenosis of the femoral artery. In such cases the early evaluation of the procedures has been largely based on the angiographic appearances immediately following PTA[33–36]. There might be considerable clinical benefit in measuring blood flow before and after PTA using angiographic data derived as part of the standard PTA procedure.

For the clinical study, we injected contrast material (Urografin 370, 370 mg of iodine ml^{-1}) at a rate of 3 ml s^{-1} for a total of 9 ml into the left common femoral artery via a 5 French catheter positioned approximately 10 mm above the imaging site. One patient who had a localized stenosis of the left superficial femoral artery was studied. Blood flow was measured using the X-ray angiographic technique before and immediately after PTA. Blood flow measurements were obtained in the left common femoral artery, left superficial femoral artery and left profunda femoris artery. The arterial segment analysed had lengths of approximately 53, 67 and 112 mm, respectively (*Figure 4*). The patient was positioned such that the analysed segments of the arteries lay approximately parallel to the imaging plane. X-ray magnification and image scaling were determined using a small metallic disc of 23.5 mm diameter, which was attached to the skin surface of the inner thigh at a position estimated to be the same distance from the image intensifier as the femoral arteries. The catheter tip was placed approximately 73 mm proximal to the bifurcation of the superficial femoral artery and profunda femoris. After injection of contrast material, X-ray images were taken using the Siemens Digitron 2 DSA system.

functions are computed for each point along the TDP. The edge is identified as the positions on each side of the centre line where the sum of the moduli of the first and second differentials is a maximum. The edge point locations are averaged by median filtering, which removes individual, significantly erroneous points.

Generation of parametric image. A parametric image is generated using the detected edges and the masked dynamic angiographic data as follows. The area of each TDP between the edge points is calculated and used to construct a single vertical column of a parametric image. This calculation is repeated for each frame, producing a time–distance plot proportional to the mass of contrast material within the artery, assuming the Lambert–Beer Law applies. (Detailed discussion of the validity of the Lambert–Beer Law is provided in Hawkes *et al.*[28].) The grey values along each row correspond to a plot of contrast material mass against time at a particular point along the vessel. The values in each row are normalized by dividing by the maximum value in each row. This generates a parametric image approximately proportional to contrast material concentration and reduces errors that result from the breakdown of the Lambert–Beer Law due to beam hardening, X-ray scatter, non-linearities in the TV system and non-uniform grey-scale response to iodine across the field of view. An example of such a parametric image is shown in *Figure 1*.

Flow velocity calculations. The flow velocity waveform was calculated by translating adjacent concentration–distance profiles in the parametric image along the direction of the blood vessel until a match occurred. A match was defined as the point where the sum of squares of the differences in the two profiles was a minimum. Estimated blood velocity is equal to the distance translated per frame interval.

Phantom studies

To assess the performance of our technique, a phantom was constructed to simulate pulsatile blood flow and hence to permit correlation of flow velocity derived from X-ray angiography with independent flow measurements using an electromagnetic flowmeter (EMF). The phantom consisted of a variable-speed pump (Bio Medicus, Bio-Medicus Inc., Minnetonka, MN, USA), a 7.00 m length of flexible plastic tubing with an internal diameter of 6.6 mm, a tubular probe of an electromagnetic flowmeter (Nycotron Blood Flow Meter 376, A/S Nycotron, Drammen, Norway) and a solenoid (*Figure 2*) to simulate a pulsatile flow waveform, which includes reverse flow (*Figure 3*). We used normal saline (0.9% sodium chloride) throughout the flow circuit. Instantaneous flow rates were measured with a 9.5 mm calibre tubular flow probe placed in series downstream of the imaging site, and Nycotron EMF connected to a strip chart recorder.

A 200 mm section of the flexible plastic tube was laid in the X-ray field of view on a Perspex tray in an approximately straight line with its long axis parallel to the X-ray table. An ion chamber, to synchronize the EMF flow reading with X-ray exposure, was placed to one side of the tube. The ion chamber output was recorded on the same paper trace as the EMF reading. Synchronization of the frame number of the angiographic run with the EMF trace was obtained by counting pulses derived from the ion chamber on the paper trace. Our technique is dependent on the accuracy of the timing of the pulsed exposure from the DSA system. The number of pulses recorded on the paper trace in a 10 s sequence was counted and the timing was found to be accurate to within 1.02%. Although measurable, this error tends to an insignificant increase in the error of the angiographic flow estimates. The error in the paper trace output was negligible.

The flexible plastic tube was taped to the plastic tray to prevent movement caused by pulsatile flow. X-ray magnification and image scaling was determined using a small metal disc and metal rods placed every 10 mm alongside the tube. The markers were visible on the X-ray image. A catheter (8 French) inserted upstream of the imaging site, by means of a Y

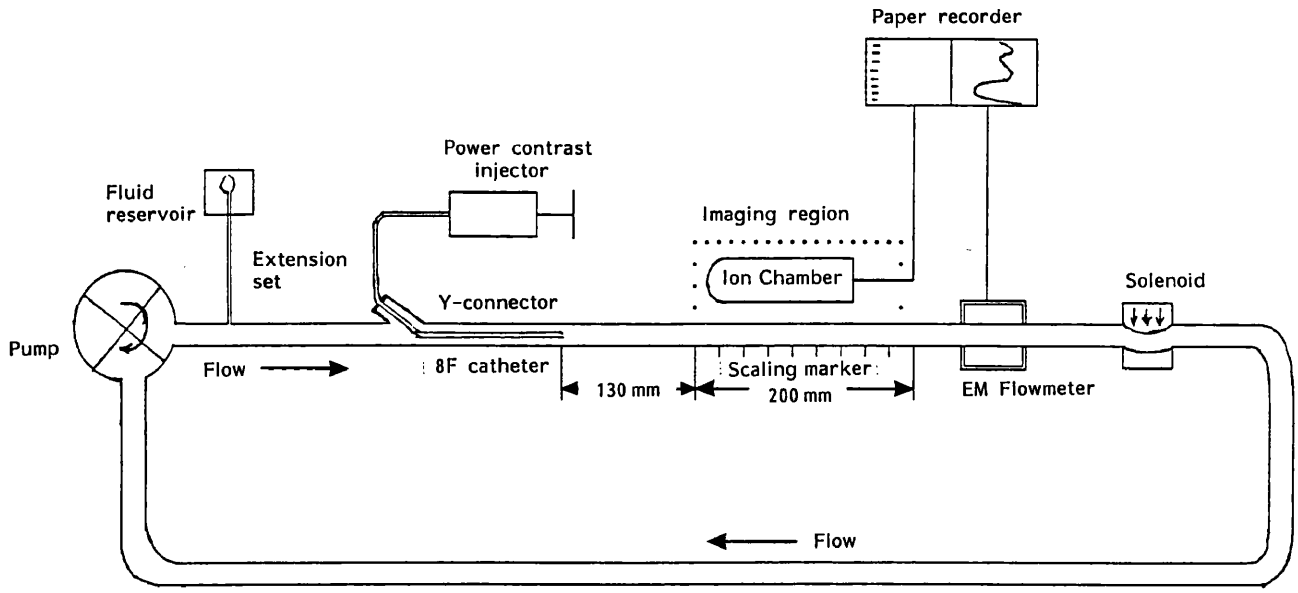

Figure 2 Block diagram of flow phantom

projection of the contrast material mass along the X-ray beam.

Various attempts have been made to use angiographic image data for the measurement of blood velocity. Many of the methods were based on the time-of-flight technique[16–22], which compares the time–density data at two different locations along the vessel and measures the mean transit time required for the bolus to travel between them. Unfortunately, precise timing of the passage of a dispersing bolus is difficult to achieve and, more importantly, the velocity estimates will depend markedly on the precise phase of the cardiac cycle that is sampled[23–26].

We recently described a new X-ray angiographic method for determining pulsatile flow waveform patterns from computer-simulated dynamic X-ray angiographic data[27]. We report here the experimental validation of the method and initial results of the clinical application of the technique. Phantom studies were used to compare simultaneous measurements of blood flow using X-ray angiographic data with measurements using an electromagnetic flowmeter (EMF).

To demonstrate the applicability of the technique in clinical practice we measured flow in the left femoral arteries of a 69-year-old male patient with severe superficial femoral artery stenosis and pre- and post-PTA. The angiographic images were collected as part of the routine digital femoral anteriography for the PTA procedure.

MATERIALS AND METHODS

Radiography

All X-ray images were acquired on a Digitron 2 DSA system (Siemens, Erlangen, Germany). Images used for flow studies were obtained with a tube voltage between 70 and 80 kVp, with a small focal spot in the pulsed X-ray exposure mode (18 ms/exposure). The digital image grey values, proportional to the logarithm of the X-ray image brightness, were recorded. For the phantom experiments, the X-ray beam was filtered by an additional 1 mm of copper. The digital images were acquired at 512 × 512 pixels/frame and 10 bits per pixel, at a rate of 25 frames s^{-1}. Up to 4 s of data were included in a single image series.

Image analysis

The image information was transferred to a Sun 4/260 Graphics workstation for further analysis. An image 'mask' was generated by averaging four frames before the appearance of contrast material. This mask was subtracted from all subsequent images in the study.

Identification of blood vessel outline. We implemented an interactive program[28] to detect the edges of an identified segment of blood vessel. The program operates as follows. The sum of about 20 frames of mask-subtracted images are calculated. A region is marked to include the blood vessel under consideration but to exclude artefact, crossing vessels, nearby vessels and bifurcating vessels. This ensures that the region used to calculate the residual background grey-level contribution contains only valid data. An approximate vessel width is entered and a few sample points along the approximate vessel centre line are marked. The system then joins these with a straight line and computes the centre of gravity of the grey-level distribution perpendicular to this line. The position of the vessel centre line is estimated as the locus of this centre of gravity. A smooth line is calculated to go through these centre line locations and the image is sampled along perpendiculars to the new centre line to yield the transverse density profile (TDP).

The edge points of the blood vessel are then calculated. A second-order polynomial is fitted successively to three, five or seven points of the TDP and the first and second differentials of these fitted

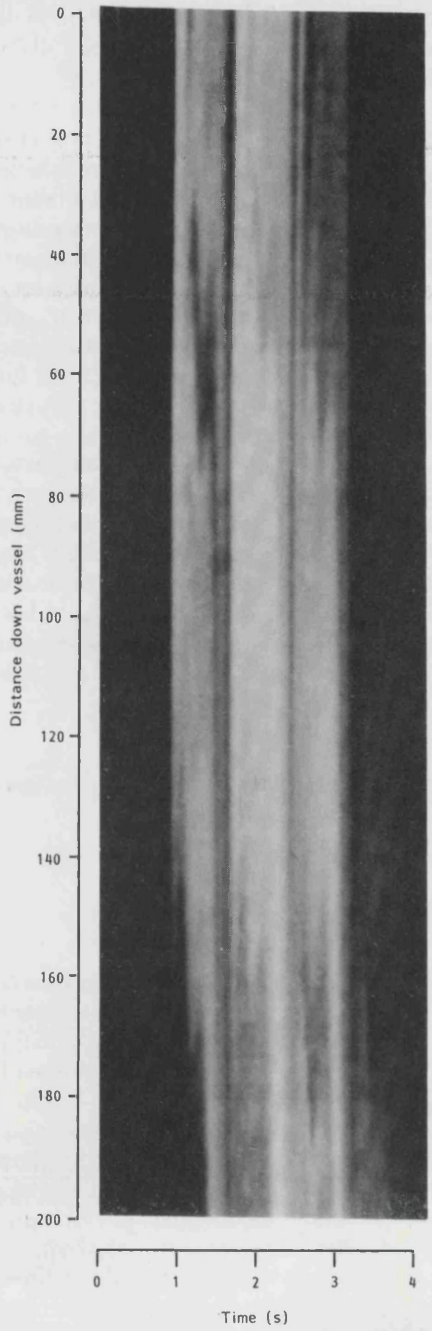

Figure 1 Example of parametric image showing contrast medium concentration (grey scale) at different positions down the blood vessel (vertical axis) and at different times (horizontal axis) in the experiment with mean flow of 147.2 mm s^{-1}

Validation of a quantitative radiographic technique to estimate pulsatile blood flow waveforms using digital subtraction angiographic data

A.M. Seifalian*, D.J. Hawkes†, C.R. Hardingham†, A.C.F. Colchester‡ and J.F. Reidy†

*Academic Department of Surgery, Royal Free Hospital School of Medicine, Pond Street, London NW3 2QG; †Division of Radiological Sciences and ‡Department of Neurology UMDS, Guy's Hospital School of Medicine, London SE1 9RT, UK

ABSTRACT

We have validated a new radiographic technique for determining pulsatile volume flow in arteries following an intra-arterial injection of contrast material. Instantaneous blood velocities were estimated by generating a parametric image from dynamic angiographic images in which the image grey level represents contrast material concentration as a function of time and distance along a vessel segment. Adjacent concentration–distance profiles in the parametric image were shifted with respect to distance until a match occurred. A match was defined as the point where the sum of squares of the differences in the two profiles was a minimum. The distance translated per frame interval gives the instantaneous contrast material bolus velocity. We have validated the technique using an experimental phantom of blood circulation, consisting of a pump, flexible plastic tubing, the tubular probe of an electromagnetic flowmeter (EMF) and a solenoid, to simulate a pulsatile flow waveform, which includes reverse flow. Small boluses of contrast material can be injected at various positions in the circuit. Measurements of pulsatile velocity flow were taken at 40 ms intervals, using a tube of 6.6 mm internal diameter and an imaged tube length of 200 mm. The shape of the flow velocity waveform was faithfully reproduced but there was an overestimation of peak velocity of 40% at low velocities (peak velocity of 540 mm s^{-1}), reducing to 19% at peak velocities of 964 mm s^{-1} with an underestimation of 16% at the peak velocities of 1899 mm s^{-1}. The validation was repeated for distances ranging from 130 to 230 mm between injection and measurement sites and for imaged tube lengths varying from 200 to 20 mm. Calculation of the mean difference and standard deviation of the difference between angiographic velocities and velocities calculated from EMF readings confirmed that the technique was independent of catheter position over this range, but that reduction of tube length resulted in a systematic reduction in mean flow velocity measurements. To demonstrate the use of this technique in a clinical context, we have measured blood flow waveforms in a patient immediately before and after percutaneous transluminal angioplasty of a stenosis in the superficial femoral artery.

Keywords: Blood flow, X-ray angiographic, image processing, blood flow velocity, digital subtraction angiographic, femoral artery, percutaneous transluminal angioplasty

INTRODUCTION

The non-invasive measurement of blood flow '*in vivo*' has long been a goal of clinicians and scientists investigating the vascular system. Blood flow measurements in individual vessels would be of value in a variety of clinical circumstances, including the assessment of the effect of atherosclerosis and other sources of vessel narrowing on flow in individual vessels; assessing the haemodynamic effects of percutaneous transluminal angioplasty (PTA) and other interventions; the investigation of bypass graft patency; the measurement of total blood flow to an organ; the partition of flow between different vessels; and assessment of changes in pulsatile flow waveforms in vascular disease.

The ideal method would provide an accurate assessment of flow through a particular vessel at any instant without disturbing the flow itself. Although no currently available system meets these requirements, there is on-going work in ultrasound[1–6], X-ray angiography and nuclear magnetic resonance (NMR)[7–10] to develop such a technique. X-ray angiographic imaging techniques are widely used in medicine for both diagnostic and prognostic purposes. Recent developments in computing have made digital subtraction angiography (DSA) a popular tool for patients who have vascular disease[11,12]. Its superior contrast resolution permits visualization of vascular structures after injection of small quantities of contrast material. Using these digital images, quantitative data on arterial dimensions can be extracted[13–15]. After careful calibration the subtracted image grey value or density is approximately proportional to the

Correspondence to: Mr Alexander M. Seifalian

0141–5425/91/030225–09

Neuroradiology (1989) 31: 263-269

Neuro-radiology

Experimental work

A new algorithm for deriving pulsatile blood flow waveforms tested using simulated dynamic angiographic data

A. M. Seifalian[1], D. J. Hawkes[2], A. C. F. Colchester[2], and K. E. F. Hobbs[1]

[1] Academic Department of Surgery, Royal Free Hospital School of Medicine, London
[2] United Medical and Dental Schools, Guy's Hospital, London, England

Summary. In vascular pathology the assessment of disease severity and monitoring of treatment requires quantitative and reproducible measurements of arterial blood flow. We have developed a new technique for processing sequences of dynamic digital X-ray angiographic images. We have tested it using computer simulated angiographic data which includes the effect of pulsatile blood flow and X-ray quantum noise. A parametric image was formed in which the image grey-level represents dye concentration as a function of time and distance along a vessel segment. Adjacent concentration - distance profiles in the parametric image were re-registered along the vessel axis until a match occurred. A match was defined as the point where the sum of squares of the differences in the two profiles was a minimum. The distance translated per frame interval is equal to the bolus velocity. We have tested several contrast medium injection methods including constant flow and a range of discrete pulses per second. The technique proved to be robust and independent of injection technique. Average blood flow was measured for simulated pulsatile waveforms with mean flows of up to 650 ml/min (peak velocities up to 186 cm/s) in a range of diameters from 2 mm to 6 mm. The standard deviation of the error in the mean flow estimates over the whole range of velocities and vessel sizes was ±1.4 cm/s.

Key words: Blood flow - X-ray angiograhic - Image processing - Blood flow velocity - Blood volume determination - Digital subtraction angiography (DSA)

Blood flow measurements in individual vessels would be of value in a variety of clinical circumstances, including the assessment of the effect of atherosclerosis and other sources of vessel narrowing on flow in individual vessels; the investigation of bypass graft patency; the measurement of total blood flow to an organ; the partition of flow between different vessels; and assessment of changes in pulsatile flow waveforms in vascular disease.

Currently available methods include the electromagnetic flowmeter which has been used to estimate blood flow in animals and man [1]. The technique is invasive, requiring placement of probes on the blood vessels [2, 3]. Doppler ultrasound has been used mainly in quantitative analysis of blood flow in vessels near the body surface [4-6] and can be used to measure aortic flow [7, 8], but it lacks the necessary resolution both in space and time in smaller deep-seated vessels [9-11]. Magnetic resonance techniques are developing rapidly [12-14] but present methods are time consuming and have poor spatial resolution. X-ray angiography remains the imaging modality which gives the highest spatial and temporal resolution and is widely used in clinical practice for obtaining high quality vessel images. The ability to derive quantitative flow data from the procedure would be a useful clinical tool. Numerous publications have shown its potential [15-21] but it has not been widely used due in part, we believe, to the use of inappropriate algorithms to process the image data.

Conventional angiographic techniques to measure flow require the measurement of the time difference between the passage of a bolus of contrast material between two sites, a known distance apart along the vessel. Unfortunately precise timing of the passage of a dispersing bolus is difficult to achieve and, more importantly, the velocity estimates will depend markedly on the precise phase of the cardiac cycle which is sampled [22].

The objectives of this paper are, firstly, to demonstrate the errors inherent in conventional "bolus-

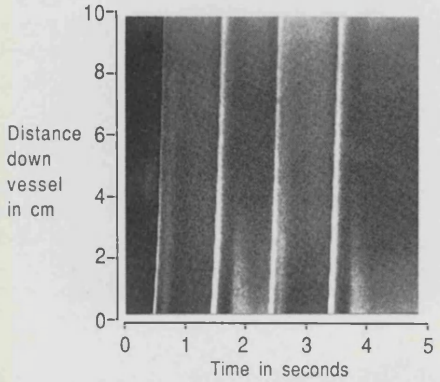

Fig. 1. Parametric image showing contrast medium concentration *(grey scale)* at different positions down the blood vessel *(vertical axis)* at different times *(horizontal axis)*

transport-time" angiographic techniques and, secondly, to assess other strategies for deriving pulsatile blood flow by analysis of time sequences of profiles of contrast medium concentration along the vessel. In particular we propose a new algorithm for deriving pulsatile blood flow. We have chosen to assess these techniques using simulated angiographic data [23] as this allowed greater flexibility in designing suitable experiments, more control of experiments, and less cost in capital equipment and material. In addition, it is of interest to predict the X-ray quantum limited precision of our technique, for a wide range of blood vessel calibres and blood flows, with data that is free from non-random errors and artefacts.

To assist in the evaluation of these techniques we generated parametric images where the image grey level represents contrast medium concentration as a function of time and distance along a vessel segment (Fig. 1). Instantaneous blood velocity measurements may be derived by analysing this image [24–26]. Volume blood flow is found by multiplying these blood velocity estimates by the blood vessel cross sectional area obtained by quantitative analysis of the densitometric data [27].

Methods

Bolus transport time

Several methods have been reported which analyse plots of contrast medium mass versus time obtained at several sites along the blood vessel [17, 19]. Blood velocity is calculated from the plots by determining the transport time for the passage of a bolus of contrast between the sites. Distinct points on the curve, such as the peak, the leading edge or the centre of gravity, are usually identified to determine the mean moment of transit past each site [17, 28, 29]. Thompson et al. [30] and Starmer and Clark [31] found that a least-squares gamma variate function closely fitted a single transport curve. Others have also used this model to estimate transport time [32–34].

The transport time is taken as the time difference between corresponding points at the two sites under study. The blood flow is then calculated as the product of the average cross-sectional area of the vessel between the two sites under study and the distance between the measurement sites, divided by the transport time.

Tracking of the segment of the vessel lumen which contains the same mass of contrast material (tracking of bolus mass)

Swanson et al. [26] suggested a technique for determining the blood velocity by tracking the position of a fixed length of vessel which contains the same mass of contrast material in time sequences of radiographic images.

The following procedure was used. The integrated radiographic density was determined along a defined length (80 mm) of the total arterial segment imaged (100 mm), on the first angiographic image. The integrated radiographic densities of regions of the same length (80 mm) in the next frame were then calculated for all positions from the most proximal site to the most distal site in single pixel intervals. For each shift the density in the first frame was subtracted from the density at each position on the second frame. The shift for which the absolute difference in the integrated radiographic density was a minimum was then determined. The length between this point and the previous point provides a measure of the distance moved by the blood during one frame period.

Registering plots of contrast medium concentration versus distance (matching of contrast concentration profiles)

We propose a new technique which operates by matching the amplitude of the plot of contrast medium concentration versus distance in adjacent images in a time sequence of radiographic images (Fig. 2). Adjacent concentration - distance profiles in the parametric image of iodine concentration versus distance and time were shifted along the vessel axis until a match occurred. A match was defined as the point where the sum of the squares of the difference between the two profiles was a minimum. The dis-

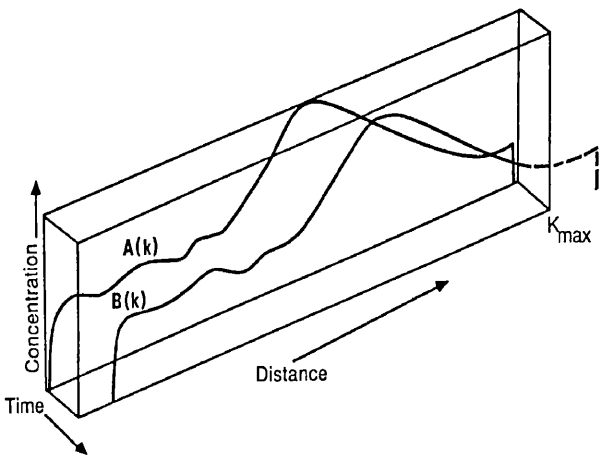

Fig. 2. Graphical representation of the method for the matching of contrast concentration profiles

tance of translation per frame interval is equal to the bolus velocity.

The match criteria in the forward flow direction is given when the function

$$\sum_{K=n}^{K_{max}} [(A(K)-B(K-n)]^2$$

is a minimum with respect to n.

The integer n is the spatial shift in pixels and A and B are the profiles of contrast concentration along the blood vessel. A similar relationship applies to back flow.

Generation of dynamic angiographic data

The algorithms were tested using data generated from a computer model that we have developed [23] as the generation of sufficient experimental data is expensive and time consuming. In addition in experimental work it is very difficult to vary one factor while keeping all others constant.

The computer model took as input the function of blood velocity versus time, details of the injection, blood vessel dimensions and radiographic parameters. The output from the model is a parametric image of contrast medium concentration versus time and distance (Fig. 1). The model generates parametric images similar in appearance to those generated experimentally. The major limitation of the model is the assumption of an axial flow profile appropriate to that found for steady state laminar flow in an infinite, straight tube of uniform, circular cross section. If the Womersley constant α [35] is less than 0.5, the blood vessel, by analogy with an electrical conductor, acts as a pure resistance to flow and flow would be described by Lamb's equations [36]. If α is greater than about 10, the axial flow velocity is approximately constant across the vessel lumen ('plug flow'). For most arteries the value of α is intermediate. We may, however, generate parametric images for both plug flow and laminar flow using the model. Hence we can investigate the effect and significance of either extreme of flow pattern in the artery. As laminar flow patterns are likely to produce greater errors due to dispersion of the bolus, all results presented here have assumed this "worst case" flow pattern.

The model generates the parametric image of iodine versus time and distance along the vessel axis. X-ray quantum noise is added according to the radiographic parameters simulated. For the parametric images generated we have assumed a monoenergetic X-ray beam of energy 50 KeV giving 3.344×10^2 photons/mm^2/μR/frame incident on the imaging plane, an exposure of 20 μR/frame at the imaging plane, a quantum detection efficiency of 50% and that the mass attenuation coefficient of iodine is equal to 1.225 m^2/kg.

The computer model for generation of dynamic angiographic images is based on the following additional assumptions: that the blood vessel cylinder is rigid and non-branching; and that there is perfect mixing of contrast medium at the injection site.

These assumptions were made to simplify calculations and reduce computation time [23]. It is thought unlikely that these assumption will significantly affect the results.

The precision of angiographic blood flow measurements potentially depends on a large number of parameters [23]; it is impractical to design experiments which cover sufficient combinations of factors to validate the technique for all possible variations of these parameters. Computer modelling permits study of the accuracy of flow measurement while these parameters are varied one at a time. This enables us to determine the accuracy of the blood flow measurements for each algorithm investigated under a wide range of experimental condition. The effect of varying experimental parameters individually and in combinations with each other is possible.

Effect of contrast medium injection technique

In order to study whether the injection technique was likely to have an effect on accuracy, we examined 4 different injection techniques.

The first injection technique consisted of a linear increase in flow up to a constant rate of injection of contrast medium which continued for a period of three seconds followed by a linear decrease down to zero flow [37]. In the second technique there was a linear increase in the flow of contrast material in-

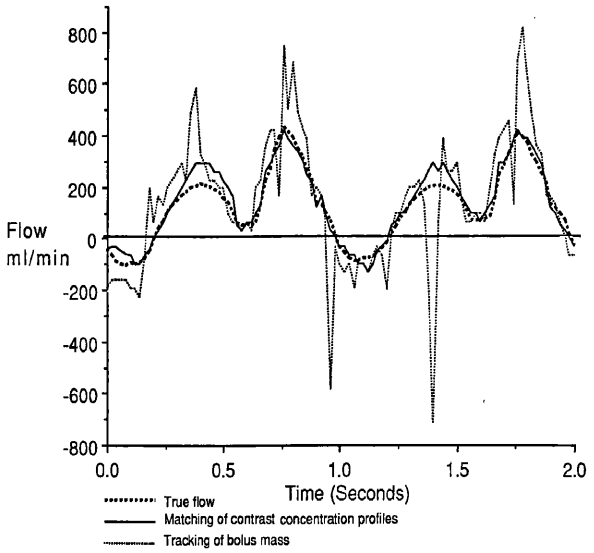

Fig.3. True and estimated blood flow waveforms vs time for low blood flow (mean 139 ml/min) with vessel internal diameter of 6 mm

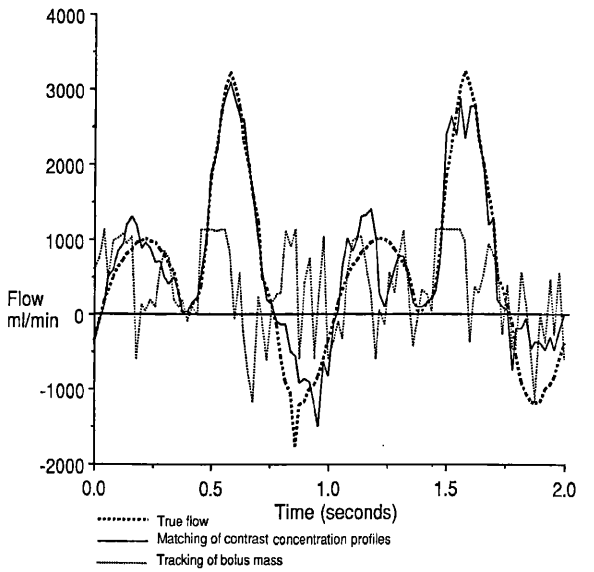

Fig.4. True and estimated blood flow waveforms vs time for high blood flow (mean 650 ml/min) with vessel internal diameter of 6 mm

jected over a period of four seconds. This was the injection strategy adopted by Swanson [26]. The third and fourth techniques consisted of 2 and 5 pulses per second. Five pulses per second is probably the highest that is achievable in practice. The total injected bolus volume was kept small (less than 2 ml) to have a minimal disturbing effect on the blood flow.

Statistical methods

All the data generated in this study were analysed using simple regression modelling with one predictor and one outcome variable. The degree of linearity

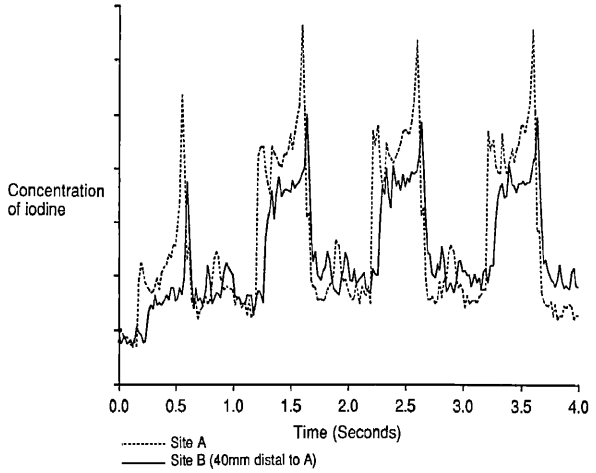

Fig.5. Plots of typical contrast concentrations versus time generated from synthetic data at two sites A and B, 40 mm apart, along a blood vessel with an internal diameter of 6 mm and mean blood flow of 367 ml/min

between the two variables was expressed by the correlation coefficient, with 1.00 as perfect linearity. The mean error (ME) of the calculated data from the true values is presented with ±1 SD [38]. Error bars in the figures represent 95% confidence limits (±2 SD).

Generation of data

We assessed these techniques for a range of blood flows, with mean blood velocity ranging from 3 to 36 cm/s, and peak velocity ranging from 15 to 186 cm/s, for different injection strategies and different sizes of vessels diameters (2, 4 and 6 mm). The length of vessel segment analysed was 100 mm and the injection point was 10 mm proximal to the segment. A total of 96 different experiments were simulated.

Figures 3 and 4 show plots of the flow waveform vs time which we used in our simulation. The low blood flow waveform (Fig.3), had a mean flow of 139 ml/min and the high blood flow waveform (Fig.4), had a mean of 650 ml/min. For both the vessel diameter was 6 mm. This flow waveform was used to generate the parametric images and is taken from the results of McDonald [39] which were measured in a canine femoral artery.

Results

Figure 5 shows contrast mass, averaged over two windows covering a 1.2 mm length of vessel, 40 mm apart, plotted against time for 4 s (four cardiac cycles). The mean blood flow was 367 ml/min and

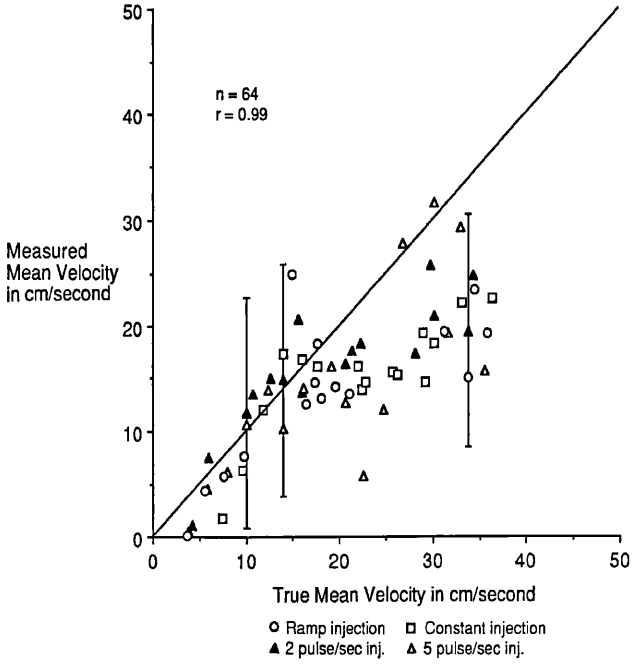

Fig. 6. Scatter plot showing the relationship between true mean velocity and mean velocity estimated by the method of the tracking of bolus mass for a 6 mm diameter vessel. The results for ramp, constant, 2 and 5 pulse/s injection techniques are plotted. Error bars represent 95% confidence limits

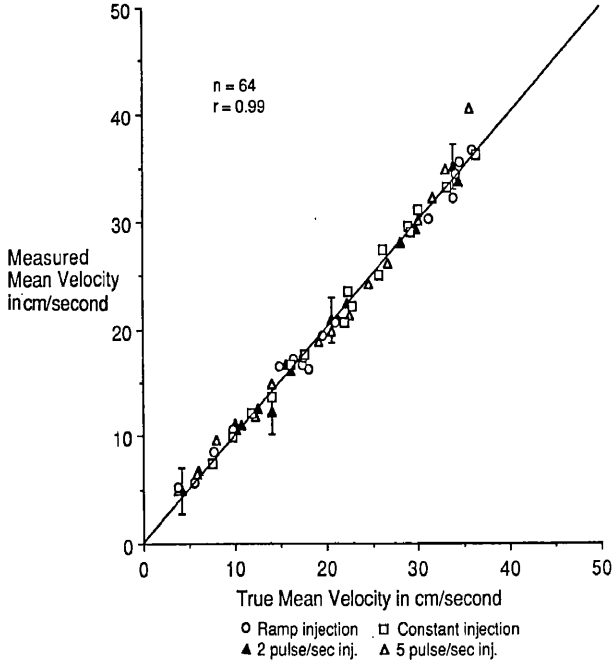

Fig. 7. Scatter plot showing the relationship between true mean velocity and mean velocity estimated by the proposed method matching contrast concentration profiles, for a 6 mm diameter vessel. The results for ramp, constant, 2 and 5 pulse/s injection techniques are plotted. Error bars represent 95% confidence limits

the internal diameter of the blood vessel was 6 mm. A parabolic axial flow profile was assumed. The flow rate of injected contrast material was uniform and equal to 1.10 ml/s.

The features visible in these plots were generated entirely by the rapid changes in bolus velocity over the cardiac cycle. These features have different shapes as the bolus disperses and to identify corresponding points on the two plots, in order to calculate the time of transport of the bolus, was not possible.

Figures 3 and 4 shows the superimposition of our estimates of the instantaneous measures of blood flow, on the flow waveform used to generate the simulated data. Flow was estimated using both Swanson's technique, the tracking of bolus mass, and our new algorithm, the matching of contrast concentration profiles.

Scatter plots were generated relating mean calculated velocity against mean input velocity, averaged over two cardiac cycles, for a vessel of 6 mm diameter. The scatter plot is generated using the bolus mass tracking of Swanson's technique shown on Fig. 6. The correlation coefficient of instantaneous blood flow input to the model and measured blood flow was 0.735 ($P<0.001$; ME $=4.86\pm6.62$ cm/s). The scatter plot generated using our technique, the matching of contrast concentration profiles, are shown on Fig. 7. There was excellent correlation ($r=0.995$, $P<0.001$; ME $=0.237\pm1.03$ cm/s) between input flow from the model and the

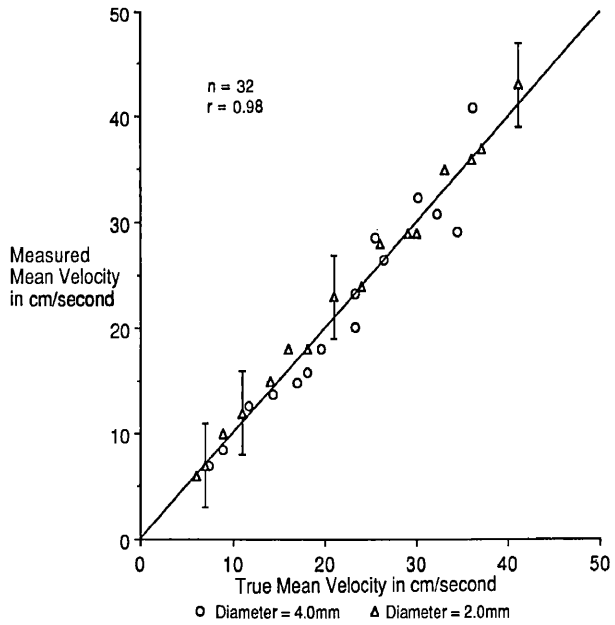

Fig. 8. Scatter plot showing the relationship between true mean velocity and the mean velocity estimated by the proposed method matching contrast concentration profiles, for 2 and 4 mm diameter vessel. Error bars represent 95% confidence limits

measured blood flow. Results for all four injection techniques are shown on the scatter plots.

Figure 8 shows plots of mean estimated velocity compared with mean input velocity for vessels of 4 and 2 mm diameters for our technique, the matching of contrast concentration profiles (r=0.98, P<

0.001; ME = 0.218 ± 1.87 cm/sec). Only results for the injection of 2 pulses of contrast material per second were calculated.

Discussion and conclusion

The pulsatility of the blood flow waveform produces wide variations in contrast medium concentration over time. These variations produce marked features in the time - concentration plots of Fig. 5. As stated above, matching these features between different measurement sites was not possible. In addition the velocity estimates will vary considerably with the timing of the appearance of features due to the pulsatile blood flow waveform. These results confirm observations from previous work by ourselves and others [22, 24-26, 29, 40]. Generally transport time methods are not suitable for measuring highly pulsatile blood flow.

The tracking of bolus mass method is in fair agreement with the input profile for low blood flow (Fig. 3) but fails at high flow rates (Fig. 4). Either no match is found or incorrect matches are found. Figure 6 shows that the tracking of bolus mass method is able to estimate the mean velocity at low flow rates of up to approximately 15 cm/s but it underestimates high flow rates for all four types of injection. These results are due to there being only a finite difference between (a) the total length of blood vessel which is visible within the image and (b) the length of blood vessel which is within the averaging window. This limits the maximum velocity, or distance travelled by the bolus, which can be measured in one frame time interval. If the window were to be reduced in size to detect higher velocities then the statistical error in the calculated velocities would increase significantly.

Figures 3 and 4 demonstrate that results obtained using our proposed technique for the matching of contrast concentration profiles, is in good agreement with the blood flow waveform over the whole range of blood flow rates investigated.

For a 6 mm diameter vessel our technique gives excellent results ($r = 0.995$, $P < 0.001$; ME = 0.237 ± 1.03 cm/s) over the entire range of flow rates, with mean blood velocities ranging from 3-36 cm/s, and peak velocities ranging from 15 to 186 cm/sec. Within the limits of the experiment, the technique is independent of the four injection strategies.

We have also obtained good agreement ($r = 0.98$, $P < 0.001$; ME = 0.218 ± 1.879 cm/s) for mean flow velocities of up to 41 cm/sec (mean volume flow rates of 307 ml/min) for 4 mm diameter vessels and up to 36 cm/s (mean volume flow rates of 68 ml/min) for 2 mm diameter vessels.

We have included the effect of X-ray quantum noise in our parametric images. We have not investigated problems such as the effect of X-ray scatter on image contrast, image artefacts due to mis-registration resulting from patient motion, or beam hardening effects resulting from overlying organs on the image of the vessel of interest. These effects may require additional pre-processing steps before applying our algorithm.

We have not investigated varying the site of injection with respect to the imaging site. For injection of contrast material at more remote sites we would expect greater dispersion of the bolus and hence some reduction in accuracy for both the bolus mass tracking method and the matching of contrast concentration profiles.

We have not presented here the effect of varying the length of blood vessel analysed. The shorter the blood vessel segment that is analysed the lower the peak velocity that may be measured and the greater the statistical uncertainly in the result for both techniques.

In conclusion, the estimation of instantaneous and mean volume blood flow by matching profiles of contrast material concentration along the blood vessel axis is a robust technique when applied to synthetic data. It is superior to other methods we have evaluated. We propose that the technique could be applied over the full range of pulsatile flows expected in clinical practice in vessels 2 to 6 mm diameters.

Acknowledgements. We have been collaborating with Mr. D. A. Wicks and Dr. J. N. H. Brunt of the Department of Medical Biophysics at Manchester University and Professor G. H. du Boulay of the Institute of Neurology, Queen Square, London, (who are investigating the use of gradient operators [41] to derive blood flow from the parametric image). We are grateful to the Leverhulme Trust for supporting one of us (DJH).

References

1. Richardson PDI, Withrington PG (1981) Liver blood flow. I. Intrinsic and nervous control of liver blood flow. Gastroenterology 81: 159-173
2. Wyatt DG (1984) Review: Blood flow velocity measurement in vivo by electromagnetic induction. Med Biol Eng Comput 22: 193-211
3. O'Sullivan VT (1982) Effect of blood vessels on electromagnetic flowmeter sensitivity. Phys Med Biol 27: 277-284
4. Nimura Y, Mastsuo H, Hayashi T, Kitabatake A, Mochizuki S, Sakakibara H, Kato K, Abe H (1974) Studies on arterial flow patterns - instantaneous velocity spectrums and their phasic changes - with directional ultrasonic Doppler technique. Br Heart J 36: 899-907
5. Johnston KW, Maruzzo BC, Cobbold RSC (1978) Doppler methods for quantitative measurement and localization of peripheral arterial occlusion diseases by analysis of the blood flow velocity waveforms. Ultrasound Med Biol 4: 209-223
6. Marquis C, Meister JJ, Mooser E, Mosimann R (1986) Quanti-

tative pulsed Doppler measurement of common femoral artery blood flow variables during postocclusive reactive hyperemia. J Clin Ultrasound 14: 165-170
7. Light H, Cross G (1972) Cardiovascular data by transcutaneous aortovelography. In: Roberts C, Strandness DE (eds) Blood flow measurement. Sector Publishing Limited, London
8. Sequeira RF, Light LH, Cross G, Raftery EB (1976) Transcutaneous aortovelography, A quantitative evaluation. Br Heart J 38: 443-450
9. Taylor KJW (1985) Blood flow in deep abdominal and pelvic vessels: Ultrasonic pulsed Doppler analysis. Radiology 154: 487-493
10. Burns PN (1987) The physical principles of doppler and spectral analysis. J Clin Ultrasound 15: 567-590
11. van Merode T, Hick P, Hoeks APG, Reneman RS (1983) Limitations of Doppler spectral broadening in the early detection of carotid artery disease due to the size of the sample volume. Ultrasound Med Biol 9: 581-586
12. Shimizu K, Matsuda T, Sakurai T, Fujita A, Ohara H, Okamura S, Hashimoto S, Mano H, Kawai C, Kiri M (1986) Visualization of moving fluid: Quantitative analysis of blood flow velocity using MR imaging. Radiology 159: 195-199
13. Ridgway JP, Turnbull LW, Smith MA (1987) Demonstration of pulsatile cerebrospinal-fluid flow using magnetic resonance phase imaging. Br J Radiol 60: 423-427
14. West DJ, Tarnawski M, Graves MJ, Taylor MG, Padayachee TS, Ayton VT, Smith MA (1988) Blood flow imaging by magnetic resonance. Medicamundi 33: 101-111
15. Nordenstrom B, Grim S (1965) A method for determination of blood flow with use of roentgen contrast medium. Radiology 84: 644-655
16. Rutishauser W, Simon H, Stucky JP, Schad N, Noseda G, Wellauer J (1967) Evaluation of roentgen cinedensitometry for flow measurement in models and in the intact circulation. Circulation 36: 951-958
17. Silverman NR, Rosen L (1977) Arterial blood flow measurement: Assessment of velocity estimate methods. Invest Radiol 12: 319-324
18. Heintzen PH (1978) Review of research into and some aspects of the modern development of densitometry, particularly roentgen-video-computer techniques. Ann Radiol (Paris) 21: 343-348
19. Kedem D, Kedem D, Smith CW, Dean RH, Brill AB (1978) Velocity Distribution and blood flow measurements using videodensitometric methods. Invest Radiol 13(1): 46-56
20. Bürsch J, Hahne HJ, Brennecke R, Grönemeier D, Heintzen PH (1981) Assessment of arterial blood flow measurements by digital angiography. Radiology 141: 39-47
21. Forbes G (1984) Quantitative blood flow analysis with digital technique. In: Harrison RM, Isherwood I (eds) Digital radiology - physical and clinical aspects. IPSM Publishing, London, pp 137-145
22. Colchester ACF (1985) The effect of changing $PaCo_2$ on cerebral artery calibre estimated by a new technique of dynamic quantitative digital angiography. PhD Thesis, University of London, pp 136-142
23. Hawkes DJ, Colchester ACF, Brunt JNH, Wicks DAG, du Boulay GH, Wallis A (1988) Development of a model to predict the potential accuracy of vessel blood flow measurements from dynamic angiographic recordings. In: Viergever MA, Todd-Pokropek A (eds) Mathematics and computer science in medical imaging. Springer, Berlin Heidelberg New York, pp 469-478
24. du Boulay GH, Brunt J, Colchester A, Hawkes D, Wallis A, Wicks D (1987) Volume flow measurement of pulsatile flow by digitised cine angiography. Acta Radiol [Suppl] XIII: Symposium Neuroradiologicum 59-62
25. Colchester ACF, Hawkes DJ, Brunt JNH, du Boulay GH, Wallis A (1986) Pulsatile blood flow measurements with the aid of 3-D reconstruction from dynamic angiographic records. In: Bacharach SL (ed) Information processing in medical imaging. Nijhoff, Dordrecht, pp 247-265
26. Swanson DK, Myerowitz PD, Hegge JO, Watson KM (1986) Arterial blood-flow waveform measurement in intact animals: New digital radiographic technique. Radiology 161: 323-328
27. Hawkes DJ, Colchester ACF, de Belder MA, Norbury RN, Camm AJ, Davies MJ (1988) The measurement of absolute lumen cross sectional area and lumen geometry in quantitative angiography. In: Todd-Pokropek A, Viergever MA (eds) The formation, handling and evaluation of medical images. Proceedings of NATO ASI (Portugal), September 1988
28. Bürsch JH, Hahne HJ, Brennecke R, Hetzer R, Heintzen PH (1979) Functional-angiograms derived from densitometric analysis of digitized x-ray picture series. Biomed Engineering (Berlin) [Suppl] 24: 189-190
29. Kruger RA, Bateman W, Liu PY, Nelson JA (1983) Blood flow determination using recursive processing: a digital radiographic method. Radiology 149: 293-298
30. Thompson HK, Starmer CF, Whalen RE, McIntosh HD (1964) Indicator transit time considered as a gamma variate. Circ Res 14: 502-515
31. Starmer CF, Clark DO (1970) Computer computations of cardiac output using gamma function. J Appl Physiol 28: 219-220
32. Burbank FH (1983) Determinants of contrast enhancement for intravenous digital subtraction angiography. Invest Radiol 18: 306-316
33. Harpen MD, Lecklitner ML (1984) Derivation of gamma varite indicator dilution function from simple convection dispersion model of blood flow. Med Phys 11: 690-692
34. Forbes GS, Earnest F, Kinspert DB, Folger WN, Sundt TM (1982) "Digital angiography": Introducing digital techniques to clinical cerebral angiography practice. Mayo Clin Proc 57: 673-693
35. Womersley JR (1955) Method for the calculation of velocity, rate of flow and viscous drag in arteries when the pressure gradient is known. J Physiol 127: 553-563
36. Lamb H (1932) Hydrodynamics, 5th edn (reprinted 1953). University Press, Cambridge
37. Link DP, Lantz BMT, Foerster JM, Holcroft JW, Reid MH (1979) New videodensitometric method for measuring renal artery blood flow at routine arteriography: Validation in the canine model. Invest Radiol 14: 465-470
38. Bland JM, Altman DG (1986) Statistical methods for assessing agreement between two methods of clinical measurement. Lancet I: 307-310
39. McDonald DA (1974) Blood flow in arteries, 2nd edn. Edward Arnold, London, p 130
40. Bogaard JM, van Duyl WA, Versprill A, Wise ME (1985) Influence of random noise on the accuracy of the indicator-dilution method. Clin Phys Physiol Meas 6: 59-64
41. Wicks DA, Brunt JN, Colchester ACF, du Boulay GH, Hawkes DJ, Wallis A (1986) A quantitative cineangiographic technique to estimate blood flow in identified vessels. Proc 26th Annual Conference Biological Engineering Society, Abstract, p 60

Received: 1 April 1989

A. M. Seifalian
Academic Department of Surgery
Royal Free Hospital School of Medicine
Pond Street
London, NW3 2QG
England